University of Strathclyde

Department of Mechanical and Aerospace Engineering

A Numerical and Analytical Study of Size Effects in Free Vibration of Heterogeneous Materials

Bahman Hassanati

2019

A thesis submitted in partial fulfilment of the requirements for the degree of Doctor of Philosophy

Declaration of Authenticity and Author's Rights

‘This thesis is the result of the author’s original research. It has been composed by the author and has not been previously submitted for examination which has led to the award of a degree.’

Signed: B. Hassanati

Date:

Abstract

In this thesis, the influence of the periodic microstructure on the dynamic mechanical behaviour of geometrically similar heterogeneous samples, namely 2D beams and 3D plates, with different dimensions and boundary textures but constant aspect ratio has been numerically investigated. Beam samples of a representative material comprised of 2D unit-cells were created using the conventional finite element analysis (FEA) to identify and quantify size effects existing in flexural modal frequencies when the scale of microstructure becomes comparable to the macroscopic dimensions. The unit cells were created so as to keep the overall properties of the material at the macroscopic scale constant despite variations in the void or inclusions volume fraction. The finite element numerical results were then compared against the analytical results obtained from the enhanced nonlocal Timoshenko beam which incorporates the Eringen small length scale coefficients, but the values obtained for the coefficient exhibited size dependency. Accordingly, 2D analysis using a novel finite element method (MPFEM) or, alternatively, the control volume based finite element method (CVFEM) was carried out by incorporating micropolar constitutive behaviour into their formulation. The numerical predictions using either MPFEM or CVFEM were then matched with the FEA results to obtain additional constitutive parameters featuring in planar micropolar elasticity theory.

The 2D models were then extruded to form square 3D plates as a straightforward progression. These samples demonstrated a moderate degree of anisotropy, which increased with volume fraction. Nevertheless, the 3D-MPFEM models which assume isotropy agreed with the dynamic behaviour of FEA nonhomogeneous models with low volume fractions, which were mildly anisotropic. Subsequently, to reduce the anisotropy, 3D square plate samples with a square-pyramidal geometry, or a body-centred cubic, arrangement of spherical voids and inclusions were modelled which demonstrated approximately isotropic characteristics for which the 3D-MPFEM results agreed with the finite element results at lower mode numbers.

Acknowledgements

Those who went in pursuit of knowledge
Soared up so high, stretched the edge
Were still encaged by the same dark hedge
Brought us some tales ere life to death pledge.[1]

I am very grateful and would like to thank all those who supported me during the course of my Ph.D. research studies and their supportive role contributed to knowledge in general and my Ph.D. research specifically. My supervisor, Dr. Marcus Wheel made this possible by his guidance and supervision and support.

I would like to express my special gratitude to the technical staff of the University of Strathclyde namely IT group of MAE (Department of Mechanical and Aerospace Engineering). MAE administration staff members were of great support during this project and always were prepared to help and support me especially our postgraduate administrator Diane McArthur.

The three dimensional analysis results were obtained using the EPSRC funded ARCHIE-WeSt High-Performance Computer (www.archie-west.ac.uk). EPSRC grant no. EP/K000586/1. I also want to express my appreciation to the Archie-WeSt personnel for training and educational support that I received during the course of the project. I especially thank Dr. Richard Martin and Dr. Karina Kubiak-Ossuka for their support.

Bahman Hassanati

Summer 2019

[1] **Omar Khayyám** ; 1048 – 1131, was a Persian polymath, scholar, mathematician, astronomer, philosopher, and poet

Table of Contents

List of Figures

List of Tables

List of Symbols (Nomenclature)

Roman Symbols

A	Cross section area of the beam
$\hat{A}$	Area of the triangular element
A^*	Mid-plane surface area of the plate
AR	Aspect ratio
APDL	ANSYS Parametric Design Language
$\bar{a}$	Internal characteristic length in the NLT beam
B	Matrix of derivatives of the shape functions
CBT	Classical beam theory (Euler-Bernoulli)
C_{NLT}	An empirical constant for nonlocal Timoshenko curve fitting
C_i	Multiplying coefficient
CVFEM	Control Volume Finite Element Method
D	Flexural rigidity
$\mathbb{D}$	Matrix of the material properties
DOF	Degree of Freedom
d	Beam or plate depth
E	Modulus of Elasticity
E_m	micropolar modulus of elasticity
FE	Finite Element
FEA	Finite Element Analysis
FF	Free-Free boundary conditions of Beams
FFFF	Free-Free-Free-Free boundary conditions of Plates
ENA	Element-Node adjacency table
e_0	A constant specific to each material
$\boldsymbol{e}_{ijk}$	Permutation tensor
f	Flexural or longitudinal modal frequency in Hz
G	Shear Modulus
h	Beam or plate depth
I	Second moment of area
J	Micro-inertia density
$\hat{\mathrm{J}}$	Jacobian matrix

$\mathbf{J}_{ji}$	Microinertia tensor
K_G	Global stiffness matrix
K_e	Element stiffness matrix
L, l	Length of beam or plate
l_b	Characteristic length in bending
l_t	Characteristic length in torsion
M, $\boldsymbol{M}_{xz}$	Bending moment
M_C	Consistent mass matrix
M_G	Global mass matrix
M_L	Lumpped mass matrix
M_T	Template mass matrix
MPFEM	Micropolar Finite Element Method
m	Mass
$\boldsymbol{m}_{ij}$	Couple stresses
N	Coupling number
$\mathbb{N}$	Shape function
NCy	The number of unit-cells across the depth of beam and plate models
NLT	Non-local Timoshenko beam
n	Mode number
Q	Shear force
R	Radius of curvature
R^2	The coefficient of determination of the Polyfit approximation
RBT	Rayleigh's Beam Theory
r	Void/inclusion radius
S_x, S_y, S_z	Dimensions of the unit cell in Cartesian coordinates
s	Square root of the second order differential equations
T	Transposed
TBT	Timoshenko beam theory
t	Time
$\bar{\boldsymbol{U}}$	Displacement and micro rotation vector
$\boldsymbol{u}$	Displacements
$\mathbb{V}$	Volumetric domain
V_r	The radius of void or inclusions
V_f	Cylindrical void or inclusion volume fraction

W	Transverse or lateral deflection
x,y,z	Cartesian coordinates
Y_{Mean}	The mean square value

Greek Symbols

α	Scaling effect parameter
$\alpha^*, \beta^*, \gamma^*, \kappa^*$	Micropolar elastic constants
β, γ	The roots of second order differential equation
Γ	Mass scaling coefficient
$\boldsymbol{\delta}_{ij}$	Kronecker delta
δ, η, ξ, ζ	Natural coordinates
$\boldsymbol{\varepsilon}_{ij}$	Strain tensors
$\bar{\varepsilon}$	Strain field
$\boldsymbol{\phi}$	Micro rotation
$\boldsymbol{\theta}$	Macro rotation
$\hat{\kappa}$	Timoshenko shear correction factor
$\boldsymbol{\kappa}_{xz}$	Curvature of the cubic micro-element
Λ	Normalised frequency
λ^* and μ^*	The Lamé constants
λ	Nondimensional frequency parameter
λ_0	Non-dimensional frequency of homogeneous beam
μ	Mass per unit length
ν_m	Micropolar Poisson's ratio
$\hat{\xi}$	Slenderness ratio
ρ	Mass density of the material
$\boldsymbol{\tau}_{ij}$	Stress (force stress)
Ψ	Polar ratio
$\widehat{\Psi}_{\beta}$	A function of β
$\widehat{\Psi}_{\gamma}$	A function of γ
ω	Circular frequency, $rad.s^{-1}$
Ω	Non-dimensional modal frequency of the plate
$\hat{\Omega}$	Shear deformation parameter

Research output

The ouput of this PhD project are as follows:

- **Journal paper (Published):**

Article title: Quantifying Numerically Forecast Size Effects in the Free Vibration of Heterogeneous Beams
Authors: B Hassanati, M Wheel
Journal title: International Journal of Mechanical Sciences
DOI information: 152.10.1016/j.ijmecsci.2019.01.009.

- **Journal paper (In progress):**

Article title: On the Influence of Micro-inertia on Free Vibration of Heterogeneous Beams

Authors: B Hassanati, M Wheel

- **Conference paper (Published):**

Article title: Size Effects on Free Vibration of Heterogeneous Beams

Authors: B Hassanati, M Wheel
Issue: MATEC Web Conf., Volume 148, 2018, International Conference on Engineering Vibration (ICoEV 2017)
Article Number : 07003
Section : Vibration of Beams, Plates and Shells, from Nano to Macro
DOI: https://doi.org/10.1051/matecconf/201814807003
Published online: 02 February 2018

1. Introduction

1.1 Motivations

In recent decades, technological advances in many areas such as in the biomedical and biomechanical, nanotechnology, bio-inspired and especially aero-space technologies have rapidly revealed the necessity of achieving in-depth knowledge in the application of micro-scaled structures and materials. Structures in which their microstructural dimensions are comparable to the overall size make the classical deformation theories in mechanics invalid and inapplicable. This has created a whole new era for researchers to investigate the dynamic behaviour of structures where the classical theories of elasticity become increasingly invalid such as in the case of the flexural or transverse vibration of small-scale heterogeneous beams and plates.

If materials are macroscopically examined and show that they consist of undistinguishable phases which are mechanically inseparable, they are then called homogeneous. Now, if the mechanical properties of a homogeneous material remain constant in all directions, the material is then classified as homogeneous isotropic, for example steel, aluminium and ceramics. Therefore, the static and dynamic behaviour of homogeneous isotropic materials can be explained by the classical deformation theories. These classical deformation theories applicable to 2D beams such as Euler-Bernoulli and Timoshenko theories provide formulations for a beam's static and dynamic behaviour when undergoing small displacements. These theories are categorised as local because the strain at any given point in the material is only related to the stresses at that specific point and is independent of the stresses at all other points in the body which will be further discussed in chapters two and three where these theories are applied and solved for specific beam models. On the other hand, if the overall dimensions of the specimen reduced significantly, down to the microstructural scale, the material becomes inhomogeneous, and the significance of the changes of the material properties in different locations of the specimen becomes inevitable. These types of materials are therefore classified as heterogeneous. Generally, heterogeneity is regarded as a discontinuity of physical properties of the material in either a specific direction or multi-directionally. The heterogeneity may consist of porosities, particles, fibres, polycrystalline, and so forth. Also, the specimen may consist of one or more isotropic or orthotropic materials.

The heterogeneity may also appear in a periodic manner. Four different heterogeneous materials are shown figure 1-1 as examples:

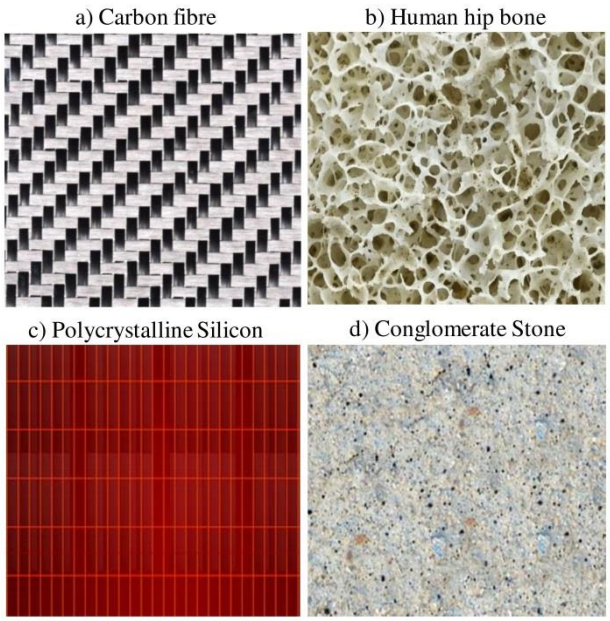

Figure 1-1: Examples of heterogeneous materials

It is clearly evident that the heterogeneity is a microstructural characteristic of materials. Almost all solid materials are non-homogeneous at some scale: if they are measured and it is found that the overall dimensions of the material specimen under investigation become so small that the microstructure becomes a measurable dimension it is thus not ignorable. Therefore, there is no exact prescription to define when precisely a specimen is considered heterogeneous, but it is widely understood that when a material shows unusual size dependent static or dynamic behaviour at a certain size, then the specimen is categorised as non-homogeneous. One option is to model the specific microstructure of the specimen in complete detail such as voids, inclusions or impurities; the other option is to consider the material a continuous but heterogeneous mass and take advantage of more general deformation theories which can anticipate size effects in microscopic scaled specimens.

Most research publications focus on beam or plate structures and the application of the more advanced and higher order deformation theories to justify the validity and usefulness of more generalised continuum mechanics, but there are always shortcomings especially the complexity of these higher order theories and the additional material constants they incorporate which make them less attractive. For instance, the micropolar theory, which will be discussed in more details in chapters two and four, has long been studied and exploited in a variety of applications especially in two-dimensional static cases in which fewer

complications are involved. 2D micropolar elasticity incorporates two additional elastic constants while the 3D version contains four. But the question is whether this theory is adaptable to dynamic cases, specifically modal analysis? If yes, are the assumptions which are made in static cases also valid in dynamic cases? Are the micropolar elastic constants accurately obtained? How much are the results sensitive to the accuracy of the micropolar constants? Unfortunately, information is scarce and the material constants are not widely available for many material types. In recent decades, numerical methods and high performance computers have made it easier to find answers to these questions which were previously impossible to solve. This has inspired and motivated us to adopt a numerical approach in making the most out of technology and exploit the advanced and higher order mechanical deformation theories in a wider range of applications, specifically the vibration of plates and beams which while apparently a small step, is nonetheless significant.

1.2 Research aim and objectives

The primary goal of this thesis is to investigate, understand and quantify the size effects arising from the microstructure of heterogeneous materials, periodic voids and inclusions, in a dynamic regime namely modal analysis and determine whether more generalised continuum elasticity may or may not anticipate the size effect in such materials by using numerical methods. The following objectives are set to achieve the project goal:

1) Size effects in dynamic behaviour, specifically modal analysis, of heterogeneous beams and plates will be quantified which could not be seen through applying other analytical or numerical methods e.g., size effect detected in beams or plates with same volume fraction and aspect ratio but varying depth;
2) Limitations of the classical elasticity theories will be investigated;
3) The applicability and relevance of modified theories such as the Eringen non-local theory in explaining size effect in the material models will be investigated and its shortcomings will be identified.
4) The applicability of micropolar theory in the modal analysis of heterogeneous beams and plates will be investigated to reveal any shortcomings that may exist in the theory as applied to modal analysis and its advantage over other theories will then be highlighted.

1.3 Methodology

1.3.1 General approach

Finite element (FE) modelling was used as the prime method to model 2D beams and 3D plates for numerical analysis of dynamic behaviour of heterogeneous materials. The advantage of this method is that detailed microstructure of representative heterogeneous material can be modelled by constructing unit cells and repeated regeneration of the unit cells results in a complex heterogeneous beam or plate model. FE modelling provides versatility to model almost any nonhomogeneous solid material consisting of different isotropic materials. Modal analysis, as a means of dynamic analysis, with free boundary conditions in the absence of external loads with small displacements was used for both beams and plates.

As the primary objective of this project was to see whether continuum elasticity can explain size effects in heterogeneous material, therefore, unconstrained 2D and 3D beam and plate structures were considered. This choice of boundary conditions eliminates the complications in the finite element analysis of constraining the structure, e.g., simply supported or clamped edges and the effect of these boundary conditions on the analysis are avoided. Other reasons are that in finite element analysis there are many ways to constrain 3D plates and choosing one method in preference to another would not help the objectives of this project.

Correction to the material properties was carried out for each unit cell volume fraction. This facilitates the study of beams and plates of various sizes with varying void or inclusions volume fraction while keeping the overall homogenised properties of the material constant. In theory, this allowed the study of the dynamic behaviour of specimens and thereby identifies the size effect with respect to the variation of specimen size and the volume fraction of voids or inclusions. Therefore, this method permits having a range of volume fractions in a specific specimen model while the overall properties of the sample are kept similar. This homogenisation concept used throughout this work as the basis for numerical analysis which is a novel methodology in modelling and FE analysis of heterogeneous materials because it reveals size effects in non-homogeneous beams and plate without changing their aspect ratio. Maintaining the homogenised properties provides a rational basis for normalising the predicted dynamic behaviour of the representative heterogeneous materials. The size effect was quantified based on the effects of changes that the specimen depths and volume fractions have on the extracted normalised modal frequencies, although the aspect ratio of the specimens remained unchanged.

Modal analysis by finite element method results in generating the full spectrum of frequencies such as longitudinal, transverse and torsion modes and thus it is not possible to perform a dynamic analysis by finite element to generate, for instance, transverse or longitudinal modes independently. Therefore post-processing and categorisation of the modal frequencies were conducted. For this reason a database comprising of an Excel spreadsheet was created to store modal frequencies and screen captures of mode shapes for further investigation. Then modal frequencies were categorised into mode shape groups. 2D analysis for beams was used to isolate some of the modal frequencies and generate longitudinal and transverse frequencies. 2D modal analysis also helps to reduce the number of micropolar constants which makes it possible to identify them by analytical and numerical methods suitable for micropolar models.

Analytical methods were used to develop a one-dimensional model for the free vibration of the nonlocal Timoshenko beam. Analytical methods were also used to derive useful equations to obtain characteristic length of bending using the primary modal frequency of 2D beams. The coupling number was obtained by an iterative method. The micro-inertia parameter is also derived and obtained analytically. A combination of numerical and iteration method was used to obtain the coupling number. Thus both analytical and numerical methods were employed to obtain the relevant micropolar constants.

The micropolar theory was incorporated into conventional finite element method (MPFEM) as well as using the existing control volume based finite element method (CVFEM) to investigate the dynamic behaviour of two-dimensional heterogeneous beams. The MPFEM and its control volume counterpart, CVFEM, were implemented in MATLAB codes developed during the course of this research. For three-dimensional plates, only the finite element method incorporating micropolar elasticity was used. The applicability of the micropolar theory was investigated by comparing the modal frequencies resulted from the application of this theory with those obtained from the finite element analysis.

1.3.2 Thesis overview

In chapter two, the previous work in the beam theories were first reviewed before focussing on the review of literature in which the size effects on the mechanical behaviour of the heterogeneous beams and plates have been examined.

In chapter three, specific beam models with voids and inclusions of various volume fractions were modelled using the finite element method, then the dynamic behaviour of the models were investigated which lead to quantifying size effect in heterogeneous beams.

Appropriate corrections were made to material properties while keeping the overall properties unchanged. Then non-dimensional modal frequencies (λ) of beams with free-free boundary conditions, in the absence of any external load, were investigated with regard to the influence of any size effect. The normalized frequencies (Λ) were also compared at each of the modal frequencies for particular beam models and volume fractions.

The widely used non-local theory of Eringen was studied with the aim of identifying whether it could explain the influence of the size effect in the dynamic behaviour of non-homogeneous beams. The Eringen non-local theory incorporates a length scale parameter in its formulation. Therefore, the Eringen non-local theory was considered and formulated for a Timoshenko beam with free-free boundary conditions. Then the results from FEA and Eringen non-local Timoshenko beams were compared, and shortcomings of non-local theory for the beam models considered in this work were highlighted.

In chapter four, formulations based on micropolar theory were conducted for beam models, and a useful equation was derived which helps to identify one of the micropolar constants, namely characteristic length of bending, from the beams overall dimensions, and the primary modal frequency.

In chapter five, the micropolar constituent parameters were incorporated into the conventional FE method, namely micropolar finite element method (MPFEM), and then an already existing control volume finite element method (CVFEM) was enhanced to provide an alternative procedure for the dynamic analysis of two-dimensional beams, with regard to the application of micropolar theory, and the difference between the two methods has been discussed. Then an iterative process was defined to identify the other micropolar constant, namely the coupling number. Then the effect of micro-inertia in micropolar theory in transverse modal frequencies of micropolar beams was investigated. The micro-inertia was analytically derived and numerically investigated, and the impact of changing the value of micro-inertia on the transverse modal frequencies of beams was investigated.

In chapter six, the second micropolar constant namely coupling number was obtained for beam models and the results based on micropolar theory and dynamic analysis of Two-dimensional beams were compared with FEA results.

In chapter seven, the work, then, expanded to 3D models. The micropolar constituent parameters were incorporated into the FE method for three-dimensional dynamic problems (modal analysis) and two types of finite elements were employed and compared.

In chapter eight, detailed 3D plate models incorporating cylindrical shaped voids and inclusions were generated using commercial finite element software. Modal analysis was performed on all models for which the micropolar constants were available. The size effect was also investigated in detail for plates with unconstrained boundaries. The micropolar finite element procedure (MPFEM) was applied to some of the plate models for which the micropolar constants were available, and the results were compared with those from FEA.

In chapter nine, analyses similar to those in chapter eight were conducted but plate models with spherical voids and inclusions were modelled, and detailed finite element analysis was carried out for the plate models. The FE results were then compared with the results obtained from the three-dimensional MPFEM.

In chapter ten, Summary and Conclusions and further work are discussed.

Appendices provide:

- Dimensionless frequency parameter for various 2D beam and three-dimensional plate models with different surface conditions, volume fractions obtained numerically from finite element analysis and application of micropolar beam theory,
- The first five longitudinal frequencies of 2D beam models,
- Analytical solution for the local and nonlocal Timoshenko beams,
- Finite element results in terms of dimensionless frequency parameter for various three-dimensional plate models with different surface conditions, volume fractions and corresponding results obtained from micropolar beam models. The numerical results include both plates with cylindrical and body-centred types of voids and inclusions.

2. Literature Review of Previous Work

Beams and plates represent arguably the simplest but most fundamental mechanical structures for which the concept of the size effect can be studied, developed and expanded to more involved structures. Therefore, in this chapter, firstly previous work in the well-known beam theories such as Euler-Bernoulli and Timoshenko beams will be reviewed and then the focus will be on the review of literature in which the size effects on the mechanical behaviour of the heterogeneous beams and plates have been examined.

2.1 Analytical methods and exact solutions for FF beam vibration

Euler-Bernoulli beam theory provides reasonably accurate predictions of modal frequencies if the aspect ratio of the beam specimen is greater than 20 but less than 100, but this theory neither considers the shear deformation nor the rotary inertia. Rayleigh's beam theory (RBT), on the other hand, considers rotary inertia but not shear deformation (Dolph 1954). The shear beam model takes into account the shear distortion but ignores the rotary inertia (Strutt and Rayleigh 1877). Timoshenko beam theory takes into account both shear deformation and rotary inertia and can be used for moderately thick beams with smaller length, L, to depth, d, aspect ratio , L/d, and is thus a more accurate beam theory when compared with the other theories (Dolph 1954; Stephen 1981; Stephen and Puchegger 2006; Elishakoff, Kaplunov, and Nolde 2015), but it is still a single layer (one-dimensional) theory and does not consider variation of properties and layers across the beam depth or along the length of the beam. The methods to solve the above theories are provided in ref. (Han, S., Benaroya, and Wei 1999).

2.1.1 Transverse Vibration of the Classical Beam Theory (CBT)

Here, Euler-Bernoulli's beam theory which is sometimes called Euler, Bernoulli, or classical beam theory is considered for free-free boundary conditions. Euler-Bernoulli beam theory in absence of external loads and damping can be stated as in equation (2.1):

$$EI\frac{d^4\boldsymbol{W}}{dx^4} - \mu\omega^2\boldsymbol{W} = 0 \tag{2.1}$$

$$\mu = \rho A = mass\ per\ unit\ length \tag{2.2}$$

where EI is the flexural rigidity; E is the modulus of elasticity, I is the second moment of area, ρ is the mass density, **W** is the transverse displacement and μ is the linear mass or mass per unit length.

The general solution for the equation (2.1) according to ref. (Avcar 2014) is:

$$\boldsymbol{W}(x) = Asin(\lambda x) + Bcos(\lambda x) + Csinh(\lambda x) + Dcosh(\lambda x) \tag{2.3}$$

where "λ" is the transverse non-dimensional frequency. A, B, C and D are constants which depend on the initial and boundary conditions.

Now to solve the above equation boundary conditions must be applied for a free-free beam where the second and third derivative of equation (2.3) equals zero as in equation (2.4) to eliminate bending moments and shear forces at the free ends:

$$\boldsymbol{W}''(0) = \boldsymbol{W}''(L) = \boldsymbol{W}'''(0) = \boldsymbol{W}'''(L) = 0 \tag{2.4}$$

This leads to the following equation for a free-free beam flexural vibration Sawant (2013):

$$cos(\lambda L)cosh(\lambda L) - 1 = 0 \tag{2.5}$$

2.1.2 Transverse Vibration of Timoshenko beam (Timoshenko beam theory)

Among all beam theories, the Timoshenko beam theory is the most widely used and thoroughly investigated by researchers as it includes both rotary inertia and shear deformation. The Timoshenko beam theory can be written in the following format in equations (2.6) to (2.7) as presented in references (Han, S., Benaroya, and Wei 1999; Wang, Zhang, and He 2007):

$$\frac{\partial}{\partial x}\boldsymbol{M} + \boldsymbol{Q} = \rho I \frac{\partial^2 \boldsymbol{\theta}}{\partial t^2} \tag{2.6}$$

$$\frac{\partial}{\partial x}\boldsymbol{Q} = \rho d \frac{\partial^2 \boldsymbol{W}}{\partial t^2} \tag{2.7}$$

Thus:

$$\frac{\partial}{\partial x}\left(EI\frac{\partial \boldsymbol{\theta}}{\partial x}\right) + \hat{\kappa}Gd\left(\frac{\partial \boldsymbol{W}}{\partial x} - \boldsymbol{\theta}\right) = \rho I \frac{\partial^2 \boldsymbol{\theta}}{\partial t^2} \tag{2.8}$$

$$and \quad \frac{\partial}{\partial x}\left(\hat{\kappa}Gd(\frac{\partial \boldsymbol{W}}{\partial x} - \boldsymbol{\theta})\right) = \rho d \frac{\partial^2 \boldsymbol{W}}{\partial t^2} \tag{2.9}$$

where $\boldsymbol{\theta}$ and $\boldsymbol{W}$ are the beam's rotation and transverse deflection:

$$\boldsymbol{\theta}(x,t) = \boldsymbol{\theta}(x)\cos \omega t \qquad rotation\ of\ the\ normal\ line \tag{2.10}$$

$$\boldsymbol{W}(x,t) = \boldsymbol{W}(x)\cos \omega t \qquad transverse\ or\ lateral\ deflection \tag{2.11}$$

while $\boldsymbol{M}$ is the bending moment, $\boldsymbol{Q}$ is the shear force, G denotes the shear modulus of the beam, $\hat{\kappa}$ (Kappa with hat) is the shear correction factor, $\boldsymbol{\theta}$ is the rotation, ρI is the rotary inertia, A is the cross section area of a rectangular beam and d is the beam's depth, sometimes denoted by h in other literature.

The fundamental difference between the Timoshenko and the classical beams with regard to the rotation of the cross section perpendicular to the bending line is shown in figure 2-1. As seen in the CBT the cross-section remains perpendicular to the mid-plane line after beam deformation while in the Timoshenko beam, the cross section also rotates and does not necessarily remain perpendicular to the mid-plane this being due to the shear deformation.

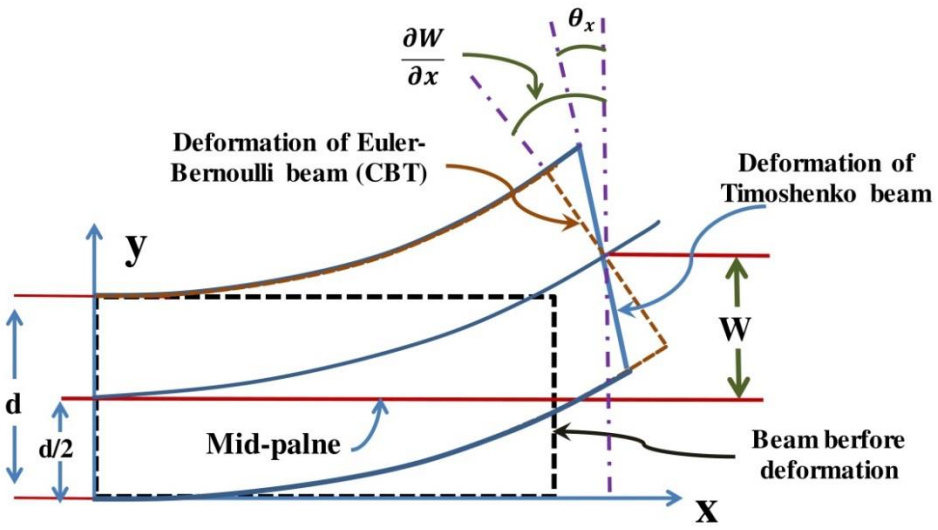

Figure 2-1: Representation of the rotation and deflection in the CBT and Timoshenko beam cases

Equation (2.8) and (2.9) can be written in the following forms:

$$EI\frac{d^2\boldsymbol{\theta}}{dx^2} + \hat{\kappa}Gh\left(\frac{d\boldsymbol{W}}{dx} - \boldsymbol{\theta}\right) = -\omega^2\rho I\boldsymbol{\theta} \tag{2.12}$$

$$\hat{\kappa}Gh\frac{d^2\boldsymbol{W}}{dx^2} - \hat{\kappa}GA\frac{d\boldsymbol{\theta}}{dx} = -\omega^2\rho h\boldsymbol{W} \tag{2.13}$$

Equations (2.12) and (2.13) can be decoupled for **W**, x and t (Han, S., Benaroya, and Wei 1999) to form:

$$EI\frac{\partial^4\boldsymbol{W}}{\partial x^4} + \rho A\frac{\partial^2\boldsymbol{W}}{\partial t^2} - \left(\frac{\rho EI}{\hat{\kappa}G} + \rho I\right)\frac{\partial^4\boldsymbol{W}}{\partial x^2\partial t^2} + \left(\frac{\rho^2 I}{\hat{\kappa}G}\right)\frac{\partial^4\boldsymbol{W}}{\partial t^4} = 0 \tag{2.14}$$

The Timoshenko beam theory tends to be less reliable for cases were the transverse modal frequencies are higher than the first eleven modes or so, as the results of Stephen et al. (2006) show, but can identify the first few modes accurately. The reason is that as the wavelength approaches the beams height, the lower and the upper surface of the beam would not vibrate simultaneously and therefore they will not stay parallel as seen in the lower mode shapes. This phenomenon will be discussed further in chapter three.

Méndez-Sánchez and Franco-Villafañe (2005; 2016) performed experiments on an aluminium beam with Length/height ratio of 19.841 and obtained normal-mode frequency percentage error for the first 24 modes. Their results show a dramatic and reverse shift in the modal frequencies after mode 11 and this shift in the results they obtained also depends on the value of '$\hat{\kappa}$', the Timoshenko shear correction factor, before and after this critical frequency and therefore they suggested that: 'the value of $\hat{\kappa}$ above the critical frequency is different from below it'. Critical frequency is the frequency at which the wavelength approaches the beam depth of homogeneous materials in beam models. In Timoshenko beam theory the cross sectional area is assumed to be planar[2] and unchanged during beams deformation but this is not a valid assumption for higher mode frequencies.

The surface morphology may also have a great impact on the results. This complicates the dynamic behaviour of the beam structures.

In summary, the dynamic behaviour of the heterogeneous beams strongly depends to the following issues:

[2] In Timoshenko beam theory, the original cross-section of the beam remains straight although it does not necessarily remain vertical to the mid-plane after beam deformation (Stephen 1981; Garcea, Madeo, and Casciaro 2012; Dolph 1954; Asghari et al. 2011).

- Beam/ plate's aspect ratio (AR)
- Mode numbers for which frequencies are obtained
- Material discontinuity across the height and length of the structure
- Structures surface morphology

These issues are addressed in chapters 3 to 6.

2.2 Continuum mechanics descriptions of heterogeneous beams

In the literature, homogenisation methods are sought to represent the properties of materials comprised of periodic assemblies of a specified unit cell. Della and Shu (2006) used Eshelby's equivalent inclusion method to investigate the vibration of piezoelectric beams, and their analytically obtained results indicate that a size effect arising from the size of the piezoelectric inclusions, their location in the structure of the beam and their volume fraction is anticipated in their dynamic behaviour. Rabboh et al. (2013) thus used the rule of mixtures to calculate the elastic constants and Poisson's ratio for functionally graded material sandwich beams and investigated the effect of the functional grading on the beams' dynamic behaviour. They also reported that increasing the thickness of the beam results in the increase of natural frequencies.

Homogenisation methods also become increasingly problematic when the size of constituent materials such as inclusions and/or voids becomes comparable to the overall size of the beam structure. Modifications to classical elasticity theories are only useful when the internal length scale parameters associated with the microstructure are considered very small. The size-dependent behaviour of materials has been reported by many researchers (Groh and Weaver 2015), (Gherlone 2013), and (Schulze et al. 2012) in laminated beams. The results presented by Dasgupta et al. (2000) in modelling active damping of adaptive structures show how the beam's time to decay varies as the device aspect ratio, inclusion shape, location and volume fraction are altered, and also show how changes in host stiffness result in changes in time to decay and electrical field. Timoshenko beam theory is regarded as nonlocal if Eringen's small-scale effect (Wang, Zhang, and He 2007) is incorporated in the governing equations. In Eringen non-local elasticity (A. Cemal Eringen 1972) 'the stress state at a given point is a function of the strain states at all points in the body.'. Wang et al. (2007) , solved the nonlocal Timoshenko beam theory (NTB) incorporating the scale coefficient 'α' in Nano-beams. In chapter three the NTB will be extended to the case of free-free beam models and examined against the FEA results for 2D heterogeneous beam.

The Eringen nonlocal theory of elasticity has also been used to analyse Euler-Bernoulli beams by researchers but it may show inconsistencies depending on whether the differential form or integral form of the theory is solved which has been reported by Fernández-Sáez et al (2016) in the investigation of size effects in static bending of heterogeneous Euler-Bernoulli beams.

C M Wang et al. (2013) used a finite segments method to calibrate Eringen's small length scale coefficient for initially stressed vibrating nonlocal beams and stated that 'e_0 does not depend on buckling or vibration modes' where e_0 is a constant specific to each material in non-local Timoshenko beam theory which will be discussed in further details in chapter three. Available results on the presence of size effects in the deformation of heterogeneous materials reported by researchers show deviation from elastic theories in static loading cases when the beam or plate length, L, to depth, d, aspect or slenderness ratio ,L/d, reduces (A. Riahi Dehkordi 2008; Riahi and Curran 2009; Beveridge, Wheel, and Nash 2013b; 2013a; Frame 2013b; Waseem et al. 2013; M. a. Wheel, Frame, and Riches 2015)

2.3 Higher order deformation theory of the micropolar (Cosserat) type

The classical and local Timoshenko beam theories do not include asymmetry of shear stresses (Hassanpour and Heppler 2017). On the other hand, the Eringen micropolar theory as described by Lakes (1996; 2003), which will be discussed further in chapter four to six, incorporates additional couple stresses and an associated additional degree of freedom, a micro-rotation, and thus accounts for material size effects but requires the specification of additional constitutive parameters including a characteristic length.

The micropolar elasticity theory is just one member of a family of theories that incorporate additional degrees of freedom to account for higher order deformation. Other members include couple stress and micromorphic elasticity (Toupin 1964; Tekoğlu and Onck 2008; Hassanpour and Heppler 2017).

In classical elasticity the stress-strain relations are given by:

$$\boldsymbol{\tau_{ij}} = \lambda^* \boldsymbol{\varepsilon}_{kk}\, \boldsymbol{\delta}_{ij} + 2\mu^* \boldsymbol{\varepsilon}_{ij} \tag{2.15}$$

where λ^* and μ^* are the Lamé constants, $\boldsymbol{\varepsilon}_{kk}$ and $\boldsymbol{\varepsilon}_{ij}$ are strain tensors, and $\boldsymbol{\tau}_{ij}$ is the force stress, $i, j, k = 1,2,3$, and $\boldsymbol{\delta}$ is the Kronecker delta which is equal to one if $i = j$ otherwise it

is zero . However, in linear, three dimensional, micropolar elasticity the force stresses, $\boldsymbol{\tau}_{ij}$, and couple stresses, $\boldsymbol{m}_{ij}$, are related to the deformations by equations (2.16) and (2.17) as defined by Lakes (1996):

$$\boldsymbol{\tau_{ij}} = \lambda^* \boldsymbol{\varepsilon}_{kk}\boldsymbol{\delta}_{ij} + (2\mu^* + \kappa^*)\boldsymbol{\varepsilon}_{ij} + \kappa^* \boldsymbol{e}_{ijk}(\boldsymbol{\theta}_k - \boldsymbol{\phi}_k) \tag{2.16}$$

$$\boldsymbol{m_{ij}} = \alpha^* \boldsymbol{\phi}_k, \boldsymbol{\delta}_{ij} + \beta^* \boldsymbol{\phi}_i, + \gamma^* \boldsymbol{\phi}_j, \tag{2.17}$$

where $\boldsymbol{\phi}$ is the microrotation and $\boldsymbol{\theta}$ is the conventional macro rotation. $i, j, k = 1,2,3$, and $\boldsymbol{\delta}$ is again the Kronecker delta and $\boldsymbol{e}_{ijk}$ is the permutation tensor. For even permutation of ijk, $\boldsymbol{e_{ijk}} = +1$, for the odd permutation of ijk, $\boldsymbol{e}_{ijk} = -1$ and otherwise zero. α^*,β^*, γ^* and κ^* are the additional moicropolar elastic constants.

Thus the equations (2.16) and (2.17) may be written in matrix form in a general equation as in equation (2.18) for the 3D cases:

$$\begin{bmatrix} \boldsymbol{\tau}_{ij} \\ \boldsymbol{m}_{ij} \end{bmatrix} = \mathbb{D} \begin{bmatrix} \boldsymbol{\varepsilon}_{ij} \\ \boldsymbol{\phi}_{i,j} \end{bmatrix} \tag{2.18}$$

Here $\mathbb{D}$ is the matrix of the material properties of size 18 by 18:

$$\mathbb{D} = \begin{bmatrix} A1 & 0 & [0]_{9\times 9} \\ 0 & A2 & \\ & & T1 \quad 0 \\ [0]_{9\times 9} & & 0 \quad T2 \end{bmatrix} \tag{2.19}$$

The stresses and strains in equation (2.18) are related as follows:

$$[\boldsymbol{\tau}_{ij}] = \begin{bmatrix} A1 & 0 \\ 0 & A2 \end{bmatrix} [\boldsymbol{\varepsilon}_{ij}] \tag{2.20}$$

where matrices $A1$ and $A2$ are:

$$A1 = \begin{bmatrix} \lambda^* + 2\mu^* + \kappa^* & \lambda^* & \lambda^* \\ \lambda^* & \lambda^* + 2\mu^* + \kappa^* & \lambda^* \\ \lambda^* & \lambda^* & \lambda^* + 2\mu^* + \kappa^* \end{bmatrix} \tag{2.21}$$

$$A2 = \begin{bmatrix} A3 & 0 & 0 \\ 0 & A3 & 0 \\ 0 & 0 & A3 \end{bmatrix} \tag{2.22}$$

and matrix $A3$ is:

$$A3 = \begin{bmatrix} \mu^* + \kappa^* & \mu^* \\ \mu^* & \mu^* + \kappa^* \end{bmatrix} \tag{2.23}$$

In the 3D micropolar medium, assuming that the displacements and micro-rotations act independently, the matrix of the material properties will be of rank 18. The micro-rotation and macro-rotation are not considered as equal, and this is apparent in equations (2.18), (2.19), (2.22) and (2.23) when $\kappa^* \neq 0$. The shear stresses in equation (2.18), $\boldsymbol{\varepsilon}_{ij}$ when $i \neq j$, are also related to the derivatives of displacements and micro-rotation which will be later discussed in section 4.1 where the relations of macro and micro rotations will be addressed.

Now matrix A3 in equation (2.23), relates the shear stress and strain in a 3-dimensional situation.

Similarly:

$$[\boldsymbol{m}_{ij}] = \begin{bmatrix} T1 & 0 \\ 0 & T2 \end{bmatrix} [\boldsymbol{\phi}_{i,j}] \tag{2.24}$$

where matrices T1 and T2 are:

$$T1 = \begin{bmatrix} \alpha^* + \beta^* + \gamma^* & \alpha^* & \alpha^* \\ \alpha^* & \alpha^* + \beta^* + \gamma^* & \alpha^* \\ \alpha^* & \alpha^* & \alpha^* + \beta^* + \gamma^* \end{bmatrix} \tag{2.25}$$

$$T2 = \begin{bmatrix} T3 & 0 & 0 \\ 0 & T3 & 0 \\ 0 & 0 & T3 \end{bmatrix} \tag{2.26}$$

and matrix T3 is:

$$T3 = \begin{bmatrix} \gamma & \beta \\ \beta & \gamma \end{bmatrix} \tag{2.27}$$

The matrix of the material properties, $\mathbb{D}$, in equation (2.18), is easily reducible to a 2D plane stress form (to form a matrix of the material properties of rank 6) in terms of four practical engineering constants which will be discussed in chapter four. Further, two more engineering constants which are applicable in 3D cases will be defined and used in chapter seven.

Nakamura and Lakes (2003) used a two dimensional FE method to investigate the localised end loads applied on a strip sample and the influences of elastic constants, especially characteristic length and coupling number, were studied. They concluded that as the characteristic length increases, the rate of decay of stress and strain energy reduces. They also concluded that for a significantly small characteristic length (in comparison with the strip's width), the rate of stress/or strain energy decreases as the characteristic length increases. In the dynamic case, this may be shown by wave dispersion. Their work predominantly included studying the models for various characteristic lengths and coupling numbers, N; but provide no method to determine them. However, in an earlier work by Lakes (1996), an extensive comparison was made between various theories, e.g. micropolar and Eringen's nonlocal theories. This shows that the elastic constants can be obtained by means of a dynamic wave propagation method. Nevertheless, in any field or wave based method that relies on determining size effects, there are limitations concerning the smallest characteristic length. Also, caution is required when one of the practical engineering constants, the coupling number, N, is close to its lower and upper bound values of zero and one when performing numerical analysis otherwise errors in computation may result.

Beveridge et al. (2013a) also studied the micropolar behaviour of perforated beams in the static 3 point bending case and determined the micropolar constants using 3 point bending test results and a control volume based finite element technique to inversely identify the constants by matching numerical predictions to experimental results.

Waseem et al. (2013) investigated the influence of void size on the constitutive properties of circularly shaped samples containing voids (Perforated rings), and derived the final equation linking the stiffness to the specimen size by relating the diametrically applied loads, displacement and stored strain energy. They concluded that in models with smooth specimen surface (rings circumference), the stiffness changes linearly with sample size measure. McGregor (2014) provides the same conclusions.

Wheel et al. (2015) studied the influence of model size in heterogeneous beams when loaded in 3 point bending. They investigated size effects in beams with voids and showed that sample stiffness relates to the beam sample size, as measured by the reciprocal of its depth

squared, in a linear manner. They also reported that there are both negative and positive effects of beam size depending on the beam boundary topology. The majority of previous work is confined to static loading cases.

There are also other more generalised elasticity theories such as strain gradient theories in which the potential energy density depends on the gradient of the strain in addition to the strain (R. D. Mindlin and Eshel 1968). The strain gradient theory was first introduced by Touplin (1964) in a non-linear form. The strain gradient theories have been subject of studying size effects in materials, such as the work that has been done in (Lam et al. 2003; Tekoğlu and Onck 2008; Askes 2009; Neff, Jeong, and Ramézani 2009; Gitman et al. 2010; Aifantis 2011; Askes and Aifantis 2011; Trinh et al. 2012; Rafii-tabar, Ghavanloo, and Fazelzadeh 2016; Lurie and Solyaev 2018; Gortsas et al. 2018; Faghidian 2018; Apuzzo et al. 2018; Fu, Zhou, and Qi 2019). An excellent comparison between higher order theories incorporating additional degrees of freedom and additional gradients is given in (Tekoğlu and Onck 2008).

2.4 Incorporation of micropolar theory in the finite element method

As briefly discussed in section 2.3, micropolar elasticity had previously been applied to static mechanical problems by researchers incorporating the theory often into 2D but rarely in 3D finite element formulations. These studies mostly included stress concentration around a circular hole in a plate or beam under uniform tension applied to two opposite edges, or bending of 2D slender beams. Eremeyev et al. (2016) used an 8-node isoparametric finite element to analyse a contact problem and their numerically obtained results showed that couple stress appears almost in the vicinity of the contact zone. Although they included the micropolar elasticity in the finite element formulation, the 8-node element itself is not discussed in detail. Forest et al. (1998) replaced a heterogeneous Cauchy medium by a homogeneous micropolar (Cosserat) continuum and studied the deformation of a multi-layered 2D cantilever beam and concluded that the Cauchy continuum is seen to give a poor prediction of the real deformation state and is not able to take the clamping conditions into account. On the contrary, the additional boundary condition in the Cosserat continuum in which micro-rotation is set to zero at one end of the specimen provides a more precise approach to the actual situation. They also stated that in the Cosserat computation, the free end of the specimen is also free of couples.

The micropolar elasticity model has also been used in models which represent rocks, blocks, granular, composite and layered materials as seen in (Vardoulakis 1989; S. Forest and Sab 1998; Buhan et al. 2002; Pasternak and Mühlhaus 2005; Stefanou, Sulem, and I. Vardoulakis 2008; Salerno and Felice 2009;Sulem, Stefanou, and Veveakis 2011; Veveakis et al. 2013), in biomechanics especially in the mechanical behaviour of bones (Park and Lakes 1986; Fatemi, Keulen, and Onck 2002; Goda, Assidi, and Ganghoffer 2014) and in other microstructures such as in the description of biological tissues (Sanchez-Molina 2014). Hongxiang et al. (2016) utilised an eight noded finite element discretisation with the incorporation of the Cosserat continuum model for soil and implemented it to simulate the strain localisation phenomena due to strain softening or non-associated plasticity of the material. Their numerical results indicated that the classical continuum finite element may suffer from uncontrollable mesh dependence and may be incapable of completing the analysis of the whole failure process, while the Cosserat continuum finite elements possess better performance in preserving the well-posed problem of localization and in completing the simulation of the entire progressive failure process occurring in geotechnical engineering structures.

Nakamura et al. (1984) developed a planar finite element method for orthotropic, micropolar solids using 3-node triangular plane stress and plane couple stress for computing the stress concentration around a hole in strips of isotropic and orthotropic micropolar elastic materials under tension. They used arbitrary micropolar constants in their analysis, and their work showed that the numerically and analytically predicted stresses were in agreement for circular holes smaller than the finite strip width. In another pertaining work, Nakamura et al. (1995) employed 4-node elements to investigate the decay of strain energy in a 2D strip and found that for the strip geometry a Cosserat solid exhibits slower stress decay than an elastic solid, and the rate of decline of strain energy becomes slower in a 2D strip as the micropolar characteristic length, l_b, is increased when the characteristic length sufficiently less than the strip width. Lei et al. (2004) used 2D 4-node and 8-node finite elements and numerically studied the scale effects in pure bending of very-thin beams. They also studied the stress concentration problem of a plate with a circular hole. Their study indicated that the bending stiffness of beams increased significantly when the beam's thickness is close to the material characteristic length parameter. They also found that the stress concentration factor decreased when the radius of the hole is close to another of the engineering constants, the material characteristic length in bending, l_b. However, their research did not consider the

shear locking problem that is a ubiquitous phenomenon which may exist and can affect the results in bending using 4-node elements.

Although the above literature survey shows that the micropolar theory has been applied to many mechanical problems using finite element analysis, the details of how exactly the formulation of micropolar theory exploited in the finite element procedure is only partially explained, and there is no procedure describing how the micro-inertia, in dynamic cases, would be included into the finite element code. Thus this lack of information would question the general applicability of such formulations to dynamic situations.

Godio et al. (2015) utilised an eight-noded shell-type finite element discretisation with six degrees of freedom per node incorporating the Cosserat finite element that may be used for different applications in structural and materials engineering.

Providas et al. (2002) also studied the stress concentration around a circular hole in a plate of an isotropic material under uniform tension and thus exploited both 3-node linear and 6-node quadratic triangular elements integrating micropolar elasticity. Their study shows that for a hole with a specific radius, the error between analytically and numerically obtained maximum stress at the circular hole increases by the ratio of radius to the characteristic length parameter. Wheel (2008) developed a numerical procedure for predicting deformations and stresses in a loaded 2D membrane which exhibited micropolar constitutive behaviour by employing a conventional finite element mesh together with a dual mesh of interconnected control volumes; the control volume based finite element method (CVFEM) which was then validated through a series of patch tests. The numerically obtained maximum stress at circular hole predicted by the CVFEM (M. A. Wheel 2008) was in good agreement with analytical and conventional FE results previously obtained by Lakes et al. (1984) and Providas et al. (2002). Beveridge et al. (2013b) also incorporated the micropolar elasticity into a higher order control volume procedure, which led to the development of a CVFEM code for static 3 point bending. However, their work includes static cases only. The algorithm for the stiffness matrix based on incorporating the micropolar theory in two dimensional cases using control volume finite element method (CVFEM) which was previously developed by Beveridge et al (2013b) showed satisfactory performance for static three-point bending. Therefore the readily available stiffness matrixes of CVFEM as well as the micropolar finite element method MPFEM, as detailed in chapter five, are both used for modal analysis in chapter six. In the control volume FE, a dual mesh is introduced which incorporates control volumes paved over a finite element mesh. Since an exact solution for

the transverse vibration of a 2D micropolar beam is not available, a 2D numerical method based on the CVFEM was developed. The difference between the two-dimensional MPFEM and CVFEM is that the MPFEM enforces equilibrium in a global sense only whereas the CVFEM enforces it locally to each control volume. The diagram in figure 2-2 represents the construction of the dual mesh around vertices of finite element nodes belonging to a six node triangular element:

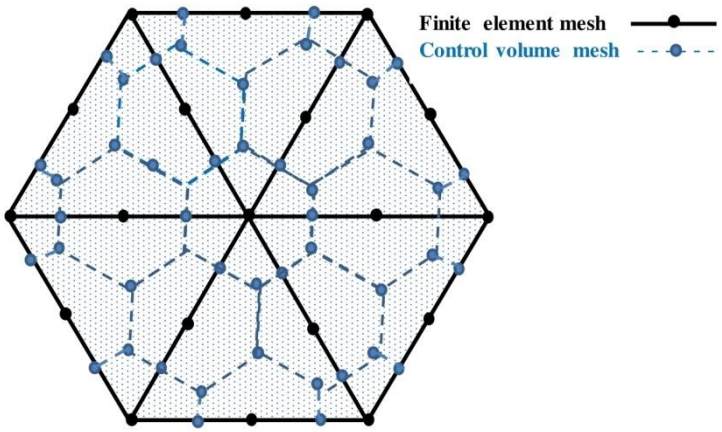

Figure 2-2: The construction of the dual control volume mesh around finite element nodes

Thus control volumes are constructed around each node of six-node triangular finite elements. Discrete equilibrium equations are developed for each control volume by integrating the stress resultants around each volume to yield the stiffness matrix. The method was originally developed for predicting static deformations by Beveridge et al. (2013b) where full details of the derivation of the stiffness matrix are available. This work exploits the method used to derive the stiffness matrix since it is already validated for the static case by Beveridge et al. However, the method has now been significantly enhanced through the incorporation of mass and micro inertia matrices to facilitate the dynamic analysis of micropolar media. Micro inertia is an extra parameter in dynamic problems that must be considered in the governing equations of micropolar theory which were initially derived by Eringen (1966). Although the term micro inertia is frequently referred to in the literature, the value of micro inertia and how it was obtained remains ambiguous. Usually, in the literature, a minimal value is selected for micro inertia which eliminates the effect of it. However, de Borst et al. (1991) derived this additional material parameter analytically as a function of characteristics length of bending by introducing a micro-element.

The micro-inertia is typically assumed to be of order of $10^{-8}m^2$ e.g. a value for aluminium of $0.325 \times 10^{-7}m^2$ was used by Abadikhan et al (2015; 2017). However, there is no

extensive work on how the micro-inertia might be obtained or its influence on the coupling number. The effect of varying micro-inertia is considered in chapter 5.

2.5 Heterogeneous plates

Plates are also subject to vast research activity and the understanding of the dynamic behaviour of plates has become a significant area of research in recent years due to its importance in advanced technological structures within industries which exploit them especially when the overall size of the plates under dynamic loading becomes so small that the constitutive microstructure of the plate become comparable to the overall size. In some applications, researchers suggest a modification of the available theories such as introducing penalty factors into the governing equations when micro inertia is involved (Lombardo and Askes 2012; Askes, Nguyen, and Tyas 2011) or, alternatively taking advantage of less complicated theories for which the unknown elastic constants are limited to one or two, as for instance in the application of Eringen's non-local theory in nanoplates, beams, and tubes. However, despite the simplicity and validity of these methods, they are limited to specific applications, and they are not necessarily valid for all situations (Hassanati and Wheel 2019). In this thesis, considerable effort has been made to understand the behaviour of heterogeneous plates from a dynamic perspective.

Much of the work undertaken by researchers and reported in many scientific papers agree that the micropolar theory provides more accurate results compared to the classical theory of elasticity if micropolar elastic constants are available, however most work is restricted to static cases, and the means of identification of micropolar elastic constants are still questionable. Determination of micropolar elastic constants for the material is an active research area in itself. Despite suggestions that micropolar elastic constants can be obtained through bending and torsion in the static case or from wave dispersion in a dynamic case (Lakes 1996), the sources for such material elastic constants are rare (Hassanpour and Heppler 2017); especially if a dynamic method using 3D methods in combination with finite element methods is proposed. The static analysis of structures is usually limited to simple cases of bending, torsion, contact problems and so forth with known boundary conditions. Furthermore static analysis demands less computation. This raises some fundamental questions regarding size effects such as: if the assumptions made to simplify the theories and the use of presumable constants resulted in promising and convincing outcomes in the static case, would they also be valid in a dynamic case to verify such a method?

In this work, unconstrained square plates with three types of heterogeneities and continuous or textured boundaries where investigated which are categorised in chapter eight. In fact, there are 21 different choices of boundary conditions, as defined by Kitipornchai (1998). Finally, the aim of this project is to study size effect in heterogeneous material in dynamic regimes rather than the influence of boundary conditions or modal frequency. Free, unconstrained boundary conditions at all plate edges in the absence of external load, provide a unique condition in which the size effect is not compromised by local loads or constraints, and therefore the applicability of the micropolar theory can be better studied and understood.

Eremeyev et al. (2016) used 8-node isoparametric element to analyse a contact problem and used the micropolar constant of the polar ratio equal to 1.5 as obtained from Lakes work (1991). Their work showed that couple stress distribution appears in the contact zone of two elastic solids which can be explained by the micropolar elasticity.

Since Mindlin plate theory was proposed by Mindlin (1955;1951;1986), many researchers tried to solve the midline plate theory by the exact solution for various boundary conditions. However the exact solution for unconstrained boundaries (FFFF or all-edges-free boundary conditions) has not been found and if one edge is free, the neighbouring edges must be constrained such as in references (Xing and Liu 2009; Wu, Liu, and Chen 2007). Shen et al. (2001) used the Rayleigh-Ritz method and analysed the free vibration of Mindlin plate with FFFF edges but resting on Pasternak-type elastic foundations.

Aksencer et al. (2011) incorporated an internal characteristic length in Eringen non-local plate theory, to obtain the governing equations for vibration analysis of Mindlin plates and considered size effect in nano-plates. The non-local theory has been applied to simple 2D beam cases and its validity in dynamic cases is investigated and discussed in chapter three as well as in reference (Hassanati and Wheel 2019).

The size effect becomes even more influential when the plates aspect ratio (Length or width to thickness) decreases, and the specimen becomes a Mindlin plate. Thus in this work exact square plates were investigated with equal length and width, and aspect ratio of length to height at 8.083:1 for plates with cylindrical voids or inclusions and 7.071:1 for plates with spherical voids or inclusions.

Liew et al. (1995) applied the Ritz energy method with boundary characteristics orthogonal polynomials (the transverse deflection function and the cross-sectional rotation functions are expressed in terms of sets of separable orthogonally generated polynomial functions) to

analyse the vibration of Mindlin plates for a variety of boundary conditions except for FFFF (all edges free and unconstrained) boundary conditions. Lim et al. (1998;1998) also used an energy method to formulate three dimensional thick plates into a two dimensional Mindlin domain. Liew et al. (1995) have done an extensive literature survey on various thick plate vibration cases including rectangular plates. Considering the amount of work done on Mindlin plates with a moderate thickness in recent years, it is clear that there is no exact method available to perform modal analysis on square plate models when all plate edges are unconstrained.

Shimpi and Petal (2006) used two-dimensional plate theory to avoid the use of shear correction factor such as ,$\hat{\kappa}$, in Mindlin plate theory. Their work, despite the proposed refined plate theory, indicates that the percentage error of the non-dimensional frequency parameter compared with the values from exact theory increases for higher modes. According to the work of Xing and Liu (2009) which covers the direct separation of variables and provides characteristic equations for various types of boundary conditions, the characteristic equations for exact solution of Mindlin plate, when edges are unconstrained, are only available for cases where two opposite edges of the plate are constrained with simply supported boundary conditions. Xiang et al. (2010) developed and applied a DSC-Ritz element method for rectangular plates with mixed boundary conditions. They discretised a plate into the equal sectioned 5 by 5 grid and applied the DSC-Ritz method. This method is numerical, and therefore the accuracy of the method greatly depends on the grid size.

Liu et al. (2017) modelled the plate's boundary conditions by assuming spring-shaped supports for which the stiffness changes from zero to infinity and then used improved Fourier series to represent three displacements fields and then via Rayleigh-Ritz method derived an eigenvalue problem which was solved for various boundary conditions including unconstrained plate edges. By modifying the stiffness and mass matrix of this method to incorporate micropolar constants, this method has the potential to be modified to a numerical micropolar method as it has only previously been applied to the isotropic material and classical elasticity. However, the advantage of this method over finite element methods remains to be proven; that is one of the reasons, that in this work micropolar theory was used with the finite element method to represent the three-dimensional plates.

There are numerous literature published in recent years showing the extensive work carried out to apply the micropolar theory into real plate problems most of which are related to static

and two-dimensional cases. Hassanpour (2017) has carried out an extensive survey on micropolar theory literature. The main problem is that there are 6 independent elastic constants in full 3D micropolar theory and for most materials, these constants are not available. The micropolar theory sounds promising with regard to the static problems such as bending, but due to unavailability of micropolar elastic constants, similar material constants are repeatedly used by researchers that were originally given by Lakes (1996).

2.6 Summary

Based on the literature review of previous work, as stated in this chapter, it has become clear that the influence of microstructure on the dynamic behaviour of materials, when the overall properties of the specimen are fixed but different at the microstructural level, in terms of material properties, has not been previously studied and this suggests that there is a gap in this research area which require further research. Therefore, in the next chapter, a set of beam models with periodic heterogeneities will be modelled, and the effects of beam size and volume fraction on their dynamic behaviour will be investigated, then more generalised higher-order theories such as Eringen nonlocal and micropolar theories will be investigated to see if they may explain any size effect that may exist in the dynamic behaviour of the representative heterogeneous beam models.

3 Investigation into the Effect of Size in Two-dimensional Heterogeneous Beam Structures

In this chapter, first two widely used theories namely the classical or Euler-Bernoulli beam and the Timoshenko beam theories will be solved for homogeneous beam models and compared, then the focus will be on modelling a set of two-dimensional beams with detailed periodic heterogeneities comprised of one or two isotropic materials, and their dynamic behaviour will be investigated to study any effects that may arise from the microstructure of the specimens. Then the Eringen nonlocal theory will be examined to see if it may explain any identified size effect that may exist in the dynamic behaviour of the representative heterogeneous beam models.

3.1 A comparison between CBT and local Timoshenko beam models

3.1.1 Obtaining the frequency parameters for classical beam

By solving equation (2.5) using the Newton-Raphson method, the first 10 flexural modal frequencies can be determined using an iterative sequence as listed in table 3-1 and non-dimensionalised using equation (3.1):

$$\omega_n = (\lambda)^2 \sqrt{\frac{EI}{\mu L^4}} \tag{3.1}$$

Since the units of ω are rad.s^{-1}, this must be divided by 2π to get frequency, in Hz.

Table 3-1: Frequency parameters for beams using the solution for the classical beam theory (Euler-Bernoulli). The CBT frequency parameters are independent of the beams aspect ratio

Mode	1	2	3	4	5	6	7	8	9	10
CBT	4.73004	7.8532	10.9956	14.1372	17.2788	20.4204	23.5619	26.7035	29.8451	32.9867

The mode shapes of an Euler beam may be obtained using equation (3.2):

$$\boldsymbol{W}(x) = \big(sin(\lambda x) + sinh(\lambda x)\big) + [\frac{sin(\lambda L) - sinh(\lambda L)}{cos(\lambda L) - cosh(\lambda L)}](cos(\lambda x) + cosh(\lambda x)) \tag{3.2}$$

For a given λ, equation (3.2) would produce a specific mode shape for that particular transverse modal frequency from $\boldsymbol{W} = -1$ to $+1$ and from $x = 0$ to L. The first to fifth

mode shapes of a free-free beam based on the classical beam theory (CBT) are shown in figure 3-1:

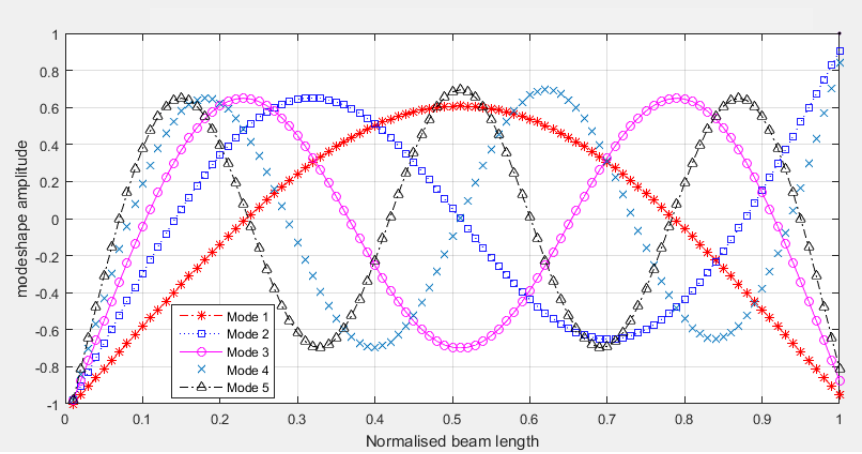

Figure 3-1: First to fifth mode shapes of a free-free beam based on the CBT

These mode shapes are used to identify associated modal frequencies.

3.1.2 Frequency parameters for Timoshenko beam

The solution for the governing equation (2.14) for FF boundary conditions when moment and shear forces at each end of the beam are zero is provided in Appendix A which results in the polynomial equation below:

$$\left\{\left[cos(sl)\times\left(\frac{1}{e^{sl}}+e^{sl}\right)\right]-2\right\} i\frac{4\rho^4}{\hat{\kappa}^4G^4s^2}\lambda^8+\left[\left(\frac{1}{e^{sl}}-e^{sl}\right)\times sin(sl)\right]i\frac{8\rho^3}{\hat{\kappa}^3G^3}\lambda^6+ \left[2-cos(sl)\times\left(\frac{1}{e^{sl}}+e^{sl}\right)\right]i\frac{4s^2\rho^2}{\hat{\kappa}^2G^2}\lambda^4=0 \tag{3.3}$$

where s is the square root of the second order form of the differential equation (2.14). Equation (3.3) is a polynomial equation of order 8 and it can be solved by iterative techniques. Here, by using the bisection method the non-dimensional parameters (λ) have been generated for the Timoshenko beam of aspect ratio 10.4 and these are provided below in table 3-2.

Table 3-2: Frequency parameters for beams using the solution for the Timoshenko beam theory (TBT)

Mode	1	2	3	4	5	6	7	8	9	10
TBT	4.6530	7.5166	10.1714	12.5904	14.7956	16.8130	18.6676	20.3807	21.9687	23.4418
Relative difference with CBT	1.64%	4.38%	7.79%	11.57%	15.48%	19.38%	23.18%	26.86%	30.40%	33.83%

Figure 3-2 shows clearly that the CBT overestimates the modal frequencies after mode three and this indicates that the numerical beam models are Timoshenko beams.

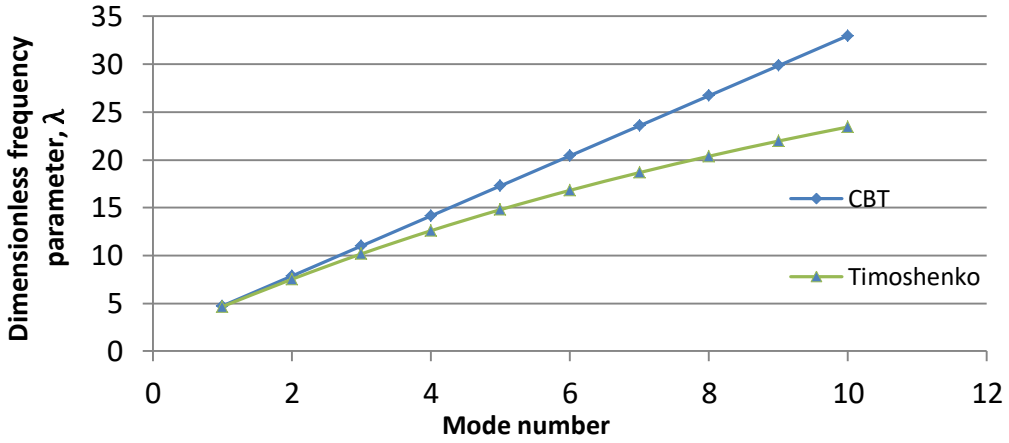

Figure 3-2: Frequency parameter for a homogenised beam with aspect ratio equal to10.4 and depth equal to 0.866 mm using CBT and Timoshenko.

Although the Euler-Bernoulli beam theory (CBT) provides fairly acceptable forecasts of flexural modal frequencies for slender beams, for the short beams of L/d<20, it over estimates the frequency values especially for modes 3 and above.

The shortcomings of the Timoshenko beam theory in modal analysis are as follow:

a) Size effect is not anticipated;
b) Only effective below the critical frequencies

The critical frequency as described in section 2.1.2 occurs in beams' transverse vibration when the wavelength approaches the beam depth of homogeneous materials. However, in heterogeneous materials, the critical frequency depends highly on the specimen's microstructure and the beam's boundary conditions; consequently it may occur at lower frequencies compared with homogeneous cases.

3.2 Finite element modelling of 2D heterogeneous beams

3.2.1 Unit-cells consisting of two isotropic materials

In this chapter, the procedure for FE modelling of 2D heterogeneous beams is discussed. In homogenisation methods the ultimate aim is to model unit cells which have the following characteristics in order to be amenable to analysis and reveal any potential size effect in their dynamic behaviour:

1. The unit-cells must be large enough to contain all the material information in the specimen.
2. The unit-cell must be small enough in order not to cause distortions in the stress gradient across the depth of the beam.

However, there are some challenges involved which highlight the potential difficulties with the application of such methods. Firstly, when the smallest scale of specimen is intended to be studied, the second condition will not be satisfied as the depth of the beam might be as little as one unit-cell. Secondly, a variation of void or inclusion's radius would affect the constituent materials volume fraction thus the overall properties of the specimens will consequently change which thereby undermines the identification of any size effect present in the specimen. Therefore, as the radius of the void or inclusion changes, so does the mass and stiffness of the unit-cell, correcting for this is discussed in section 3.3. In this research, three distinct types of 2D beams were modelled:

- those with perforations (voids)
- those with compliant inclusions
- and those with a compliant matrix

By considering two possible beam surface conditions, namely smooth, continuous surfaces and textured surfaces there will be six possible beam types as follows:

I. beams with perforations (voids) and continuous boundaries (BVOCB);
II. beams with perforations (voids) and textured boundaries (BVOTB);
III. beams with compliant inclusions and continuous boundaries (BINCB)
IV. beams with compliant inclusions and textured boundaries (BINTB)
V. beams with compliant matrix and continuous boundaries (BCMCB)
VI. beams with compliant matrix and textured boundaries (BCMTB)

ANSYS APDL version 16.2 was used to perform geometric modelling and finite element analysis (FEA) on each beam type. Figure 3-3 shows the two unit-cell configurations containing either voids or inclusions that were used to construct individual beam models. The height of the modelled unit cell is 0.866 mm, and the length of the unit cells is 1mm respectively. The void or inclusion centres are thus located on an equilateral triangular array. Models containing various void/inclusion volume fractions were generated. For unit-cells containing inclusions rather than voids, the cells consist of two isotropic materials with the included material surrounded by matrix material.

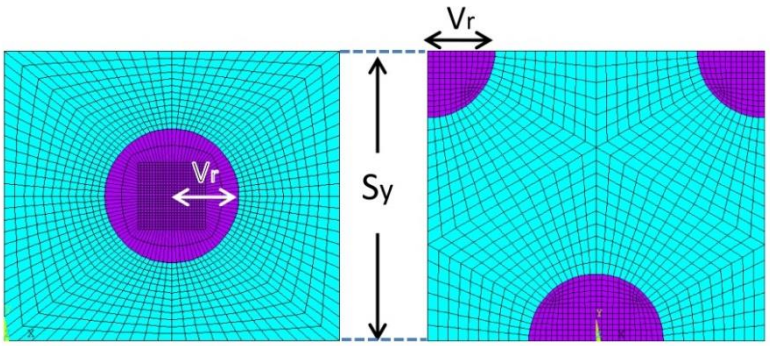

Figure 3-3: Unit cell consisting of two isotropic materials r = 0.2 mm; the unit cell on the left is used in generating beams with continuous surfaces and the unit cell on the right is used for when inclusions intercept the surface of the beam.

Figure 3-3 shows unit-cells with the inclusion of 0.2 mm in radius. For the unit cells used to generate beam models with continuous boundaries as seen in figure 3-3, left, a quarter unit cell was first modelled and then reflected appropriately to produce a full unit cell. Therefore, all sides of the matrix section are divided by 12 parts and mapped so that the sizes of elements decrease on approaching the inclusion's border. The circular area containing the inclusion incorporates a squared area which is divided into a 12 by 12 element meshed area and the remaining area is divided into two concentric rings. 8-node solid elements were used for meshing the areas. 8-node solid element is a quadrilateral element with four corner nodes plus four mid-side nodes, and this element choice uses full integration that will not cause shear locking problems. By reflecting the quarter unit cell in both x and y-directions, a complete unit cell was created which contained 1920 elements and 6068 nodes.

The beams with textured boundaries were modelled so that inclusions or voids were located at the centre of a hexagonal array as seen in figure 3-3, right. The hexagonal sides are divided into 12 equal parts. The diagonal lines connecting the hexagon's vertices to the circle are divided into ten parts. Such a mesh arrangement provides 1260 elements and 3925 nodes per unit cell.

Void or inclusion radius was varied from 0.1 to 0.3 mm in 0.05 mm increments. The corresponding void or inclusion volume fractions are listed in table 3-3 along with the equivalent radius normalised with respect to the unit cell height (V_r/S_y), where V_r is the void or inclusion radius, and S_y is the height of the unit cell. Throughout this work, void or inclusions radius, volume fraction and normalised radius are used interchangeably.

Table 3-3: Changes in void or inclusion volume fraction with radius and/or normalised radius of void or inclusion

Void/inclusion radius, r mm	Void/inclusion volume fraction, V_f %	Normalised void/inclusion radius, V_r/S_y
0.1	4	0.12
0.15	8	0.17
0.2	15	0.23
0.25	23	0.29
0.3	33	0.35

In order to create the macroscopic scale beam models, the unit cells were repeatedly regenerated to produce four different beam sizes consisting of one, two, three or four layers of cells through beam depth, NCy=1,2,3 and 4 e.g. when NCy=1 then d=1*0.866 mm and NCy=2 then d=2*0.866 mm and so forth. The length, L, to depth, d, aspect ratio, (L/d) was kept constant at 10.4:1 so that all four sizes of the beam of a given volume fraction remained geometrically similar. Two variants of each beam were created: those based on the first unit cell contained boundaries comprised continuously of matrix material, figure 3-4a and 3-4b, while those incorporating the second unit cell contained textured boundaries intersected by the voids or inclusions, as seen in figures 3-4c and 3-4d. The successive layers of voids and inclusions are such that the center points of every three neighboring voids or inclusions forms an equilateral triangle aimed to minimise anisotropic characteristics of the material.

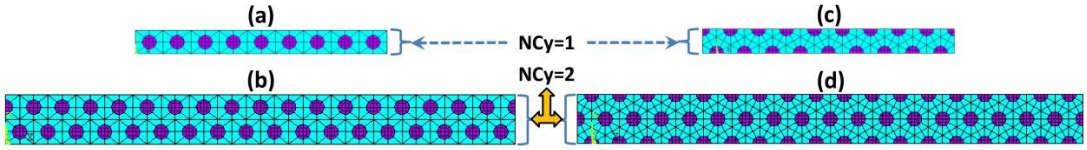

Figure 3-4: Models showing the arrangement of unit cells in beams; (a) Beam size 1 with 9 unit cells with continuous boundaries (top, left); (b) Beam size 2 with 18 unit cells in length with continuous boundaries (bottom, left); (c) Beam size 1 with 9 unit cells with textured boundaries (top, right); (d) Beam size 2 with 18 unit cells in length with textured boundaries (bottom, right)

A schematic of the beams overall dimensions is shown in figure 3-5.

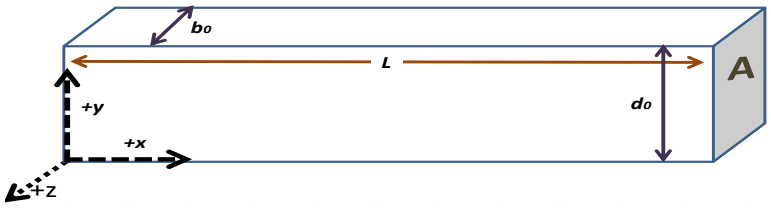

Figure 3-5: Schematic representation of the coordinates and dimensions on a homogeneous beam

3.2.2 Mesh convergence in modal analysis.

To analyse the effect of mesh refinement, beams with 28, 156, 528, 898, 1920 and 7680 elements per unit cell were modelled by changing the number of line divisions, and it was observed that the average error of the frequencies of each model for the first ten modes compared with the next model refinement in sequence are 5.6740E-03, 4.6611E-05, 1.6991E-06, 1.1951E-06 and 1.1950E-06. Therefore, beams with 1920 elements per unit cell satisfied the requirements for mesh convergence for the beams with continuous boundaries. Beams with textured boundaries and 108, 276, 1260 and 5040 element/Unit-Cell were modelled and the average error for the first ten modes reduced to 7.8101E-03, 2.1102E-03, 6.2110E-04, 6.2102E-04 upon refinement. Therefore unit cells with 1260 elements have a 6.00E-06 difference comparing with unit cells containing 5040 elements. The choice of tolerance was set at 1E-5 for the first ten modal frequencies because in dynamic analysis, firstly the meshed models must represent an idealised geometry, secondly the average error increases for the higher modal frequencies.

3.3 Adjusting the modulus of elasticity (E) and mass density (ρ) of the unit-cells

When changing the volume fraction of each material, the homogenised mass and stiffness properties of the beam were kept fixed. This enabled the size effect on the free vibration to be identified for various volume fractions when the unit cell mass and overall homogenised properties were kept constant.

The aim is to investigate the frequency changes for various beam sizes and void/or inclusions volume fractions for transverse vibration modes. Therfore, the ratio of modulus of elasticity of matrix to inclusion was set at 10:1 for the beams with compliant inclusions and 1:10 for the beams with the compliant matrix. The modulus of elasticity at the macroscopic scale was fixed at 70 GPa, see table 3-4.

The adjustment of the modulus of elasticity for each beam model has been done by conducting appropriate static tensile test simulations which involved constraining all degrees of freedom at one end of the beams like clamped conditions and applying a constant tensile force on the opposite end and then obtaining the changes in length which is then used to adjust modulus of elasticity. FEA made it possible to easily model various beam types with the volume fractions and material constants associated with the constituent unit-cells being altered while keeping the properties of the equivalent homogenized beam unchanged. This

approach resulted in identifying the influence of the size effect on the flexural frequencies in the beam models which would not be possible with other approaches such as practical experimental testing. Using corrected values of modulus of elasticity of matrix and inclusion, the beam models were again examined for the level of accuracy in comparison with the original assumption of the overall modulus of elasticity which is 70 GPa. Therefore the values in table 3-5 show the relative difference between the overall modulus of elasticity of heterogeneous beam models and the modulus of elasticity of corresponding homogeneous beams. As seen, in table 3-5, the relative difference for all beam models remains about or below 1E-3.

The matrix and inclusion densities were also altered according to the void or inclusion volume fraction, as detailed in table 3-6 while keeping the mass density of the unit cells constant at 2700 kg/m^3 as a strategy during analysis. For beams with voids, the mass of the matrix material was increased proportionally to its volume fraction. Therefore, the value of 2700 kg/m3 was divided by the volume fraction of the matrix as the void's radius increased, which resulted in creating beam models with an equal mass of the unit cell. For beams with inclusions, the mass of inclusions kept as 1/10 of the mass of the matrix, therefore achieving the overall density of 2700 kg/m^3 for such beams required a nominal value of 2454.5 kg/m^3 to be divided by the volume fraction of the matrix.

Although the matrix and inclusion's density altered, the overall mass density of the beam models are very close to the homogeneous beam models and the relative difference remains below 1E-6, as seen in table 3-6. Poisson ratio, ν, is equal to 0.3 throughout this work.

Table 3-4: Correction of modulus of elasticity of beams matrix by void or inclusions radius for various beam models

Void or inclusion radius, mm	**The modulus of elasticity of matrix, MPa**					
	Perforated beams		**Beams with compliant inclusions**		**Beams with compliant matrix**	
	Continuous boundaries	**Textured boundaries**	**Continuous boundaries**	**Textured boundaries**	**Continuous boundaries**	**Textured boundaries**
0	7.000E+04	7.000E+04	7.000E+04	7.000E+04	7.000E+04	7.000E+04
0.1	7.796E+04	7.814E+04	7.590E+04	7.600E+04	6.679E+04	6.681E+04
0.15	8.892E+04	8.915E+04	8.382E+04	8.394E+04	6.292E+04	6.295E+04
0.2	1.064E+05	1.063E+05	9.600E+04	9.599E+04	5.775E+04	5.776E+04
0.25	1.338E+05	1.328E+05	1.139E+05	1.135E+05	5.142E+04	5.142E+04
0.3	1.796E+05	1.767E+05	1.404E+05	1.397E+05	4.412E+04	4.413E+04

Table 3-5: The relative difference of the overall modulus of elasticity of beams models provided in table 3-4 with the modulus of elasticity of the homogeneous beam

Void or inclusion radius, mm	The relative difference of the overal modulus of elasticity of the heterogeneous beams with homogeneous beam					
	Perforated beams		Beams with compliant inclusions		Beams with compliant matrix	
	Continuous boundaries	Textured boundaries	Continuous boundaries	Textured boundaries	Continuous boundaries	Textured boundaries
0	0	0	0	0	0	0
0.1	3.394E-05	1.238E-04	1.096E-05	1.238E-04	1.096E-05	5.587E-05
0.15	7.885E-05	1.687E-04	3.394E-05	1.238E-04	5.587E-05	1.096E-05
0.2	5.587E-05	1.906E-04	7.885E-05	2.136E-04	7.885E-05	7.885E-05
0.25	2.585E-04	1.457E-04	3.483E-04	2.803E-04	1.096E-05	7.885E-05
0.3	6.179E-04	2.136E-04	4.382E-04	1.687E-04	1.008E-04	1.096E-05

Table 3-6: Correction of density by void or inclusions radius

Void or inclusion radius, mm	The mass density of matrix and inclusions, kg/m^3				
	Perforated beams		Beams with inclusions		
	For matrix	Relative difference with homogeneous beam	For matrix	For inclusions	Relative difference with homogeneous beam
0	2700.00	0	2700.00	N/A	0
0.1	2801.64	1.852E-07	2546.94	6766.11	1.852E-07
0.15	2939.97	1.852E-07	2672.70	3007.16	1.852E-07
0.2	3158.29	1.852E-07	2871.18	1691.53	1.852E-07
0.25	3491.67	1.852E-07	3174.25	1082.58	1.852E-07
0.3	4008.87	1.852E-07	3644.43	751.79	1.852E-07

The adjustment of modulus of elasticity and mass of the unit cells with the volume fraction of void and inclusions has the following benefits:

- To identify any size effect within the structure of the heterogeneous models that may exist on the dynamic behaviour of specimens due to the changes in void or inclusion's volume fraction as well as size effects due to changes in beam depths with a constant aspect ratio;
- The effects of the size of the voids and inclusions near the boundaries on the dynamic behaviour of beams and also when they intercept the boundaries can be investigated;
- This approach is particularly useful for studying the size of the voids and inclusions on the flexural frequencies in the heterogeneous beam models when experimental testing is not physically possible.

This approach can be useful for future research studies mainly when two different materials with similar macroscopic geometries and overall observable properties but different in microstructural scale are studied. Consequently, the industrial application of such materials may be their functionality rather than overall similarities among them.

3.4 Modal analysis (Flexural vibration)

3.4.1 2D model and boundary conditions choices

In modelling the dynamic behaviour of the beams, two dimensional analyses were initially preferred rather than three dimensional, the main reason being that in a two dimensional analysis, the in-plane modes are only identified, such as in-plane transverse and longitudinal modal frequencies. In-plane modal analysis will automatically exclude torsional and out-of-plane bending modes. This reduced the required computational time and resources for analysis.

In this work the study of the size effect in nonhomogeneous materials was the primary goal and the effect of boundary conditions was of lesser importance. Therefore, free-free (FF) boundary conditions were chosen for the two dimensional modal analyses. This means that there are no bending moments or shear forces acting at either ends of the beam. The reason is that in the FF case the effect of boundary conditions are totally eliminated and, in addition, the mode shapes are distinctively recognisable for categorising. Thus, in order to categorise the transverse modes, it just requires counting the number of wave lobes and subsequently distinguishing the mode number, e.g. primary mode shape has one lobe, second mode shape has two opposite lobes, and so forth; see for example the five mode shapes shown in figure 3-1.

3.4.2 FEA Solver used, the number of modal frequencies, and the benefits of Block Lanczos

In 2D FE modal analysis initially about 63 modal frequencies were extracted using the Block Lanczos solver. This solver is capable of extracting modes from a lower to a prescribed upper frequency and it is very reliable and would not omit any of the modal frequencies within the specified range. This solver is the preferred option when the number of DOF is less than one million. The main issue in modal analysis using finite element software is that it does not distinguish longitudinal from transverse frequencies and all the modal frequencies are produced in ascending order. Therefore, the mode shapes were investigated individually and divided into three categories: transverse modes, longitudinal modes and mixed modes. Transverse modal frequencies were distinctly recognisable below the critical frequency, before the wave length approached the beams depth. Therefore, to be certain, 10 transverse modal frequencies were identified along with 4 to 6 longitudinal frequencies. The majority of the modes above the critical frequency showed very complicated in-plane mode shapes in

which the bending modes were not clearly recognizable from the longitudinal ones; therefore they were separated and named mixed-modes.

3.5 Finite element results and size effect predictions

3.5.1 Beams with continuous boundaries

The finite element results which are presented in this section and shown in figures 3-6 to 3-8 and also tabulated in Appendix B, provide size effect information for beams with continuous surfaces. For this purpose, three types of beams listed in section 3.2.1 are modelled and analysed.

Modal frequencies are nondimensionalised using the equation (3.4):

$$\lambda = L(2\pi f)^{1/2}(\frac{12\rho}{Ed^2})^{1/4} \tag{3.4}$$

where λ is the non-dimensional frequency parameter, L is the beams length; f is the numerically predicted flexural modal frequency in Hz; ρ is the mass density; E is the modulus of elasticity, and d is the depth of the beam. The values for λ for the first ten flexural modal frequencies of homogeneous beams ($V_r/S_y = 0$) predicted using finite element analysis are compared to the analytically derived values based on Timoshenko beam theory in table 3-7. These frequency parameters are dimensionless and are used for normalisation of the flexural frequency values of all heterogeneous beams considered in this thesis. The procedure to obtain the dimensionless frequency parameters of Timoshenko beam is explained in section 3.1.2. However, Timoshenko beam theory proved to provide good predictions for the first ten flexural modal frequencies which are corroborated by the FEA results for homogeneous cases.

Table 3-7: The non-dimensional modal frequencies (λ) for homogeneous beams and with aspect ratio 10.4:1

Mode	FEA	Timoshenko	Relative diff. of FEA with Timoshenko
1	4.655455	4.653041	0.05%
2	7.527076	7.516596	0.14%
3	10.194069	10.171415	0.22%
4	12.626892	12.590439	0.29%
5	14.84537	14.795647	0.34%
6	16.874623	16.813016	0.37%
7	18.739625	18.667635	0.38%
8	20.461702	20.380707	0.40%
9	22.057553	21.968693	0.40%
10	23.538186	23.441844	0.41%

The normalised values (Λ) when presented in figure 3-6 to 3-14 were obtained by dividing the non-dimensional frequency parameter (λ) at each modal frequency by its corresponding non-dimensional frequency from column two of table 3-7, that is, the FEA derived values for λ.

Figure 3-6 shows the normalised primary bending modal frequency of four beam sizes for beams with various volume fractions of voids and continuous boundaries (BVOCB). This behaviour is highly size dependent as seen in figure 3-6. The homogeneous case is represented by the blue lines (dotted lines with solid square markers) and the FE results show that in this case, the normalised modal frequency is size independent. For any given mode the size effect becomes more pronounced with diminishing beam size and is greatest for the smallest size of beams. The size effect is also more pronounced for beams with a higher void volume fraction. The non-dimensional frequency parameters (λ) information for the first ten transverse vibration modes of beams with voids is provided in table B-1 in Appendix B. Interestingly, the size effect is apparently mode dependent; there is a distinct change in its nature such that after mode three changes in void radius causes a decrease rather than an increase in normalised frequencies (Λ). Figure 3-7 shows how the normalised frequencies for the beams with voids and height of one unit-cells (First smallest beam sample) vary with mode number.

Results in figure 3-8 show that beams with compliant inclusions behave similarly although the size effect appears to be slightly less pronounced. The smaller values of normalised frequencies for beams with compliant inclusions is because the matrix is less stiff in comparison with the perforated beam models which is related to the reduction of the flexural rigidity, EI, at any given cross-section of the beams.

According to these results in figures 3-6 and 3-8, for the primary modes (first flexural mode), it appears that variations in the normalised frequencies have an approximately linear relationship with reciprocal size measure given by the inverse of the square of the depth of the beam ($1/d^2$), except for the smallest beam sizes where the ratio of the radius of void or inclusion to overall beam thickness approaches the maximum. The smallest beam models lack the triangular arrangements of void or inclusions within the beam structures. Therefore the size effect not only increases dramatically but also deviates from the linear pattern as seen for the larger models.

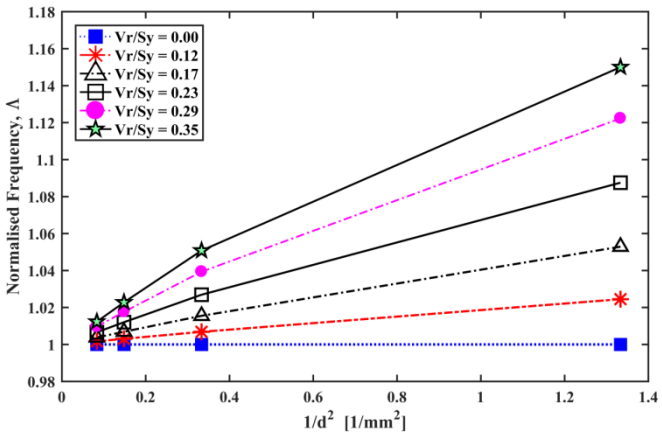

Figure 3-6: Normalised primary bending modal frequency of four beam sizes for beams with various volume fractions of voids and continuous boundaries (BVOCB)

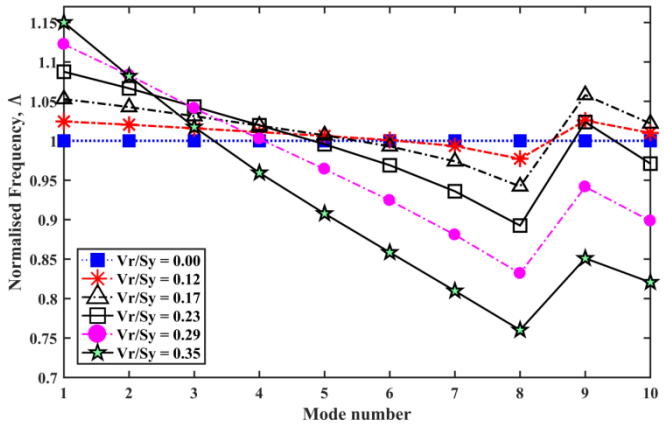

Figure 3-7: The first ten normalised bending modal frequency of the smallest beam sample (NCy=1 or depth=0.866 mm) with various volume fractions of voids and continuous boundaries (BVOCB)

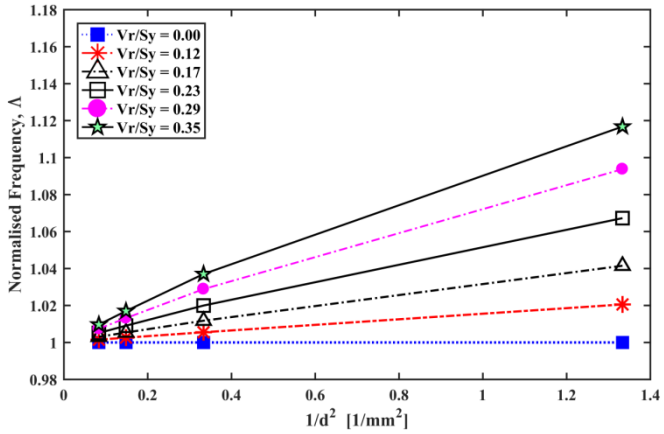

Figure 3-8: Normalised primary bending modal frequency of four beam sizes for beams with various volume fractions of compliant inclusion and continuous boundaries (BINCB)

The results for specimens with stiff inclusions and continuous surfaces, BCMCB, show an entirely different dynamic behaviour; Here, a distinctly different size effect indicating that increasing volume fraction causes a decrease in Λ at a given mode number for this sample size. Figure 3-9 shows the inverse size effect on normalised frequencies for the primary mode when the inclusions have a higher modulus of elasticity than the matrix. The size effect although inverted once more remains approximately linear across the three larger samples but again this does not extrapolate to the smallest sample size. Figure 3-10 shows changes in Λ with mode number for the beams with height of one unit-cell (the smallest beam sample).

The dynamic behaviour of the beam models with a compliant matrix as modelled in this chapter may seem counterintuitive because of the inverse size effects that they indicate. In structures with a matrix of a specific modulus of elasticity, stiffer inclusions are expected to make the entire structure stiffer. But here, on the contrary, the matrix material is not the same as the beams with compliant inclusions; here the matrix is more compliant than the previous models and reduces with volume fraction too. The second reason is that as the models are two-dimensional, only in-plane transverse vibrations are analysed, which is not in the direction of cylindrical shaped inclusions. The third reason is that in beam models with or less than four layers of unit cells in depth of the beams, the compliant matrix may dictate the overall behaviour of the structure and generates inverse size effects on normalised frequencies. Note that the matrix modulus of elasticity is ten times lower than the modulus of elasticity which was explained earlier in section 3.3 and shown in table 3-4.

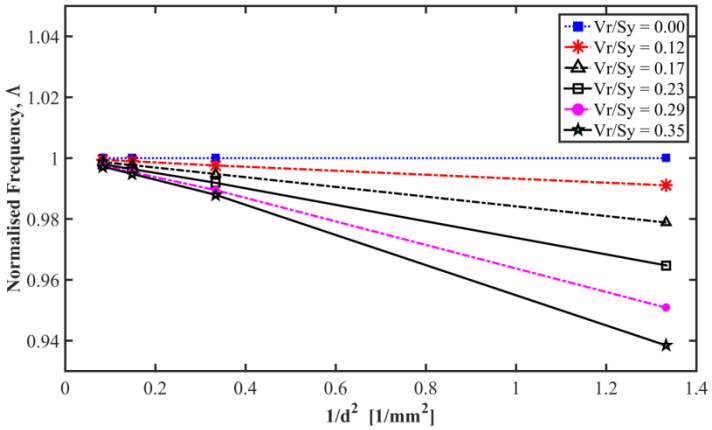

Figure 3-9: Normalised primary bending modal frequency of four beam sizes for beams with compliant matrix and continuous boundaries (BCMCB)

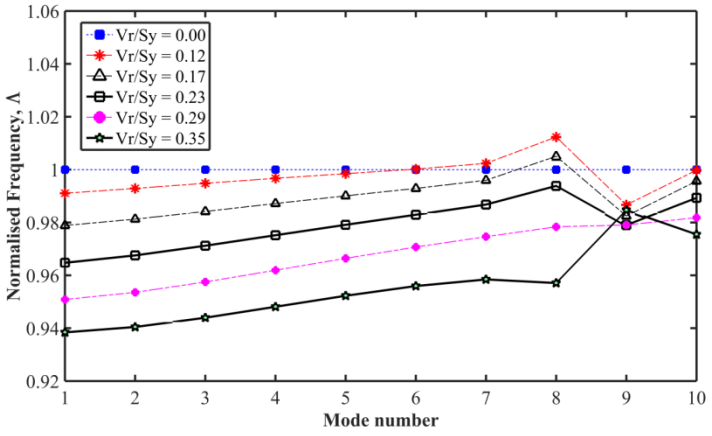

Figure 3-10: The first ten normalised bending modal frequency of the smallest beam sample (NCy=1) with compliant matrix and continuous boundaries (BCMCB)

As seen in figures 3-7 and 3-10, the normalised frequency values are also mode related, and that means the frequency values change at any specific mode number which also depends on the void or inclusions volume fraction. If the void or inclusion's volume fraction is reduced then the dynamic behaviour of the specimen becomes closer to a homogeneous case. The mode related frequencies show a clear pattern for the lower modal frequencies, e.g., mode numbers one to eight. As the frequency values approach the critical frequency, then a clear trend is not visible any longer since the wavelength approaches the beam depth, so mode shapes are not categorically distinguishable. This phenomenon is observed in FE results as seen in figure 3-11 for the transverse modes numbers 12, 13 and 14 for the beam with 0.2 mm voids, depth equal to 1.732 mm, aspect ratio (Length to depth) equal to 10.4 and continuous boundaries.

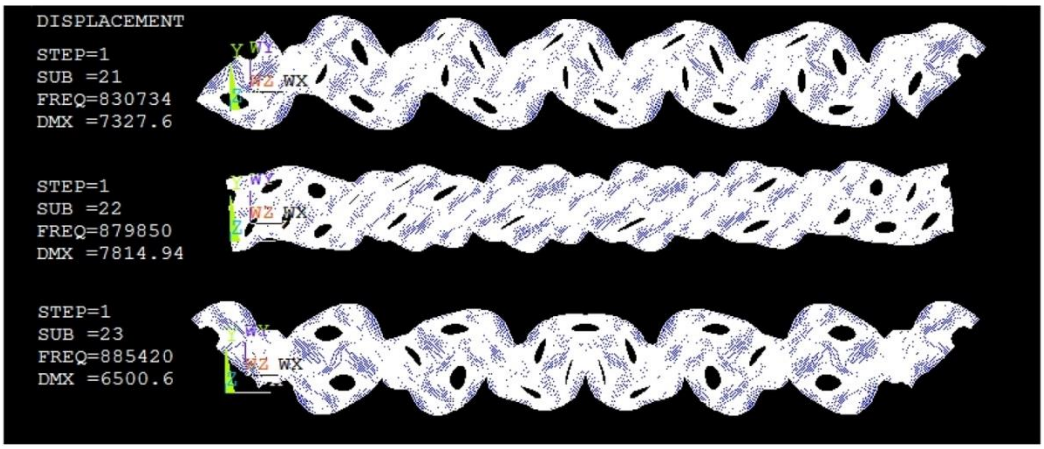

Figure 3-11: Mode Number: At modal frequency of Hz, beam sample with voids and continuous boundaries, depth =1.732 mm, R=0.2mm

3.5.2 Beams with textured boundaries

If the upper and lower boundaries of the beams are not continuously comprised of matrix but textured due to their intersection with the voids or inclusions, there is a significant difference in dynamic behaviour. Beams with voids or compliant inclusions and textured boundaries showed similar behaviour to the beams with compliant matrix and continuous boundaries already discussed in section 3.5.1 and therefore are not discussed any further in this section. Figures 3-12 and 3-13 show normalised flexural frequencies of beams with voids and textured boundaries.

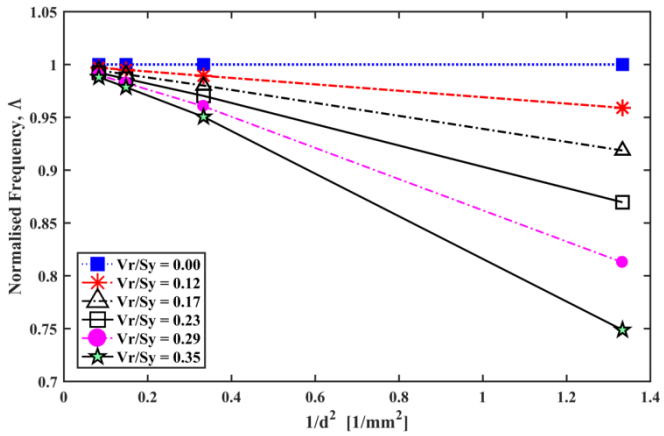

Figure 3-12: Normalised primary bending modal frequency of four beam sizes for beams with voids and textured boundaries (BVOTB) for which the micropolar constants were not obtainable

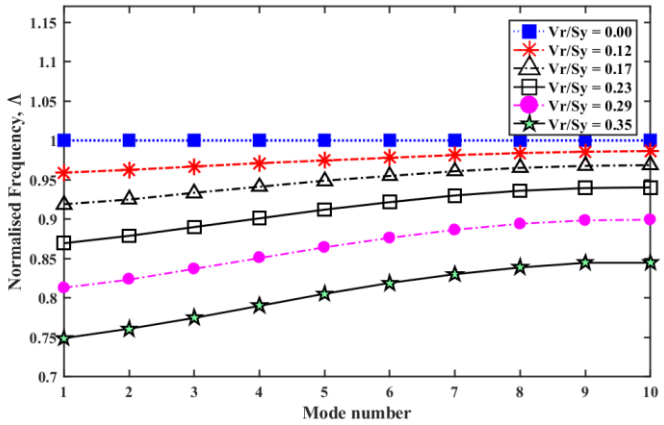

Figure 3-13: The first ten normalised bending modal frequency of the smallest beam sample (NCy=1) with voids and textured boundaries (BVOTB) for which the micropolar constants were obtainable

Finally, beams with textured boundaries and a matrix comprised of compliant material with a lower modulus of elasticity exhibit a more conventional size effect with normalised frequency increasing as beam size reduces as seen in figure 3-14.

The location of the inclusions concerning the boundaries of the specimens causes an inverse dynamic behaviour. As explained in section 3.5.1, for beam models with or less than four layers of unit cells in depth of the beams, the compliant matrix may dictate the overall behaviour of the structure. However, when the boundaries of the specimen are intercepted with stiff inclusions, the beams' borders will be more rigid in general. Therefore, the actual cause of inverse size effects in beam models with textured boundaries is due to changes in the material properties in near the surface of the specimen. If voids or compliant inclusions intercept the models, then the near-surface area becomes less stiff than inner parts of the sample. On the contrary, if stiffer inclusions intercept the surface of the beam, then the near-

surface area becomes stiffer than internal components of the specimen. Such dynamic behaviour will be maximised by reducing the total number of the constitutive layers across the beam depth to only one unit cell, as well as changing the shape of the void or inclusion's which is not circular any longer.

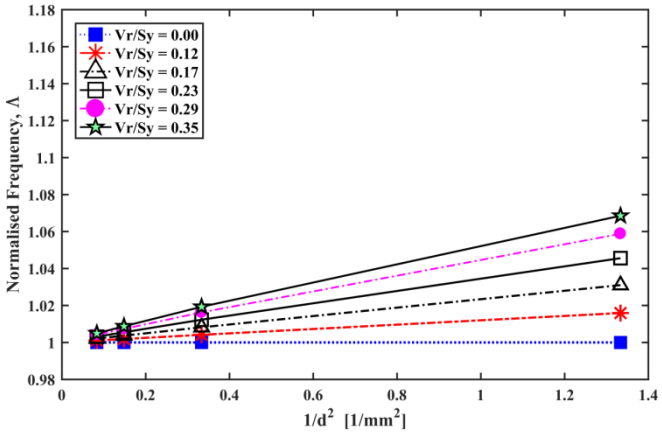

Figure 3-14: Normalised primary bending modal frequency of four beam sizes for beams with compliant matrix and textured boundaries (BCMTB) for which the micropolar constants were obtainable

In summary, the numerical results shown in figures 3-6 to 3-14 and provided in tables B-1 to B-6 Appendix B indicate that the forecast size effect depends on:

a) Beam depth
b) Void/inclusions volume fraction
c) The relative stiffness of matrix and inclusions
d) Beam surface morphology

The remainder of this chapter considers whether various theoretical beam models, especially models incorporating an intrinsic length scale in their formulations to account for size effects are capable of predicting these numerical results by means of analytical or numerical solution methods.

3.6 An analytical nonlocal Timoshenko beam model and size effect

In this section the characteristic equations for nonlocal Timoshenko beams will be derived and solved for free-free boundary conditions. The local and nonlocal Timoshenko beam mode shapes will also be discussed. In addition, the results will be compared with FEA results.

3.6.1 The nonlocal Timoshenko beam model

In this section, the nonlocal Timoshenko (NLT) beam model is used to study the size effect in a Timoshenko beam by incorporating Eringen's nonlocal theory. This approach has been widely used in nanotechnology because it can be solved analytically for various boundary conditions, e.g., (Wang, Zhang, and He 2007; Z. Zhang, Challamel, and Wang 2013; Zhen Zhang, Wang, and Challamel 2015). However, it must be noted that the Timoshenko beam theory is one dimensional and Eringen's small-scale coefficient is only really applicable to the longitudinal direction.

Here the work of Wang et al. (2007) is extended to include the free-free boundary condition: Axial normal stresses, $\boldsymbol{\sigma}_{xx}$, can be stated in the following forms:

$$\boldsymbol{\sigma}_{xx} - (e_0\bar{a})^2 \frac{d^2\boldsymbol{\sigma}_{xx}}{dx^2} = E\boldsymbol{\varepsilon}_{xx} \tag{3.5}$$

where the $\boldsymbol{\varepsilon}_{xx}$ is the corresponding strain. Equation (3.5) indicates that NLT is a gradient type nonlocal theory.

The governing equations for nonlocal Timoshenko beam can be obtained by applying Hamilton's principle and incorporating Eringen's small-scale coefficient $e_0\bar{a}$ into the Timoshenko beam model as defined by Wang et al.(2007):

$$EI\frac{d^2\boldsymbol{\theta}}{dx^2} - \hat{\kappa}GA\left(\boldsymbol{\theta} + \frac{d\boldsymbol{W}}{dx}\right) + \rho I\omega^2\boldsymbol{\theta} - (e_0\bar{a})^2\left(\rho A\omega^2\frac{d\boldsymbol{W}}{dx} + \rho I\omega^2\frac{d^2\boldsymbol{\theta}}{dx^2}\right) = 0 \tag{3.6}$$

$$\hat{\kappa}GA\left(\frac{d\boldsymbol{\theta}}{dx} + \frac{d^2\boldsymbol{W}}{dx^2}\right) + \rho A\omega^2\boldsymbol{W} = 0 \tag{3.7}$$

where $\boldsymbol{\theta}$ is the rotation, $\boldsymbol{W}$ is the transverse displacement, ω is the circular frequency, $\hat{\kappa}$ is the Timoshenko's shear correction factor, G is the shear modulus, A is the cross-section of the beam, I is the second moment of area, e_0 is a constant specific to each material and $\bar{a}$ is the internal characteristic length in the NLT beam. In equation (3.5), $e_0\bar{a}$ can be normalised and represented by α, alpha. After decoupling equations (3.6) and (3.7) and applying free-free boundary conditions, the following equation (3.8) may be derived:

$$cosh\beta cos\gamma + \left(\frac{[(H_2H_3)^2 - (H_1H_4)^2]}{2H_1H_2H_3H_4}\right) sinh\beta sin\gamma = 1 \tag{3.8}$$

where:

$$H_1 = \alpha^2\lambda^2 + \left(\frac{\alpha^2\lambda^2}{\hat{\xi}^2} - 1\right)\beta\hat{\Psi}_\beta \tag{3.9}$$

$$H_2 = \alpha^2\lambda^2 + \left(\frac{\alpha^2\lambda^2}{\hat{\xi}^2} - 1\right)\gamma\hat{\Psi}_\gamma \tag{3.10}$$

$$H_3 = \hat{\Psi}_\beta + \beta \tag{3.11}$$

$$H_4 = \hat{\Psi}_\gamma + \gamma \tag{3.12}$$

and

$$\binom{\beta}{\gamma} = \left(\frac{\pm b + \sqrt{b^2 - 4ac}}{2a}\right)^{1/2} \tag{3.13}$$

in which

$$a = \left(1 - \frac{\alpha^2\lambda^2}{\hat{\xi}^2}\right) \tag{3.14}$$

$$b = \lambda^2\left(\hat{\Omega} + -\frac{1 - \hat{\Omega}\alpha^2\lambda^2}{\hat{\xi}^2} + \alpha^2\right) \tag{3.15}$$

$$c = \lambda^2\left(\frac{\lambda^2\hat{\Omega}}{\hat{\xi}^2} - 1\right) \tag{3.16}$$

with a, b and c being the usual quadratic formula constants. Finally:

$$\hat{\Psi}_\beta = -\frac{\beta^2 + \lambda^2\hat{\Omega}}{\beta} \tag{3.17}$$

$$\hat{\Psi}_\gamma = \frac{\gamma^2 + \lambda^2\hat{\Omega}}{\gamma} \tag{3.18}$$

The parameters H_1 to H_4 are defined by C. M. Wang et al. (2007) while the derivation of equation (3.8) is entirely new. The full mathematical procedure to derive equation (3.8) is given in Appendix C.1.

The non-dimensional parameters used in the above equations are:

$$\lambda = \omega^{(1/2)}(\rho AL^4/EI)^{1/4} \tag{3.19}$$

$$\hat{\Omega} = EI/(K_s GAL^2) \tag{3.20}$$

$$\alpha = e_0\bar{a}/L \tag{3.21}$$

$$\hat{\xi} = L(A/I)^{1/2} \tag{3.22}$$

in which λ is the dimensionless frequency parameter, $\hat{\Omega}$ is the shear deformation parameter, α is the scaling effect parameter, $\bar{a}$ is the internal characteristic length, and finally, $\hat{\xi}$ is the slenderness ratio.

The equations (3.6) and (3.7) where solved with the assumption that $e_0\bar{a}$ is effective in the axial, x, direction. The solutions to equations (3.6) and (3.7) with alpha effective in this direction, as shown in equation (3.5), and when Eringen's nonlocal effect is also applicable in axial and transverse, y, directions are provided in the Appendices C.1 and C.2.

Equation (3.8) can be solved by iteration which produces an infinite number of Eigenvalues giving the transverse frequencies for a free-free beam.

It must be stated that small scale effects are considered when the overall length scales of the beam are comparable to the microstructural scale and thus appear to affect the resulting eigenvalues. Therefore, if 'α' is taken as equal to zero, then the characteristic length is ignored and so the governing equations will be reduced to that of conventional local Timoshenko beams and the results from equation (3.8) will be the exact results for a local Timoshenko beam where there is no small scale effect.

3.6.2 Local and nonlocal Timoshenko beam mode shapes

Having obtained the transverse frequencies, the Eigen vectors or mode shapes at each modal frequency can be determined by equation (3.23):

$$\overline{\boldsymbol{W}} = \left[sinh(\beta\overline{x}) - \frac{H_1}{H_2}sin(\gamma\overline{x})\right] - \frac{\left[\beta^2 sinh(\beta) + \left(\frac{H_1}{H_2}\right)\gamma^2 sin(\gamma)\right]}{[\beta^2 cosh(\beta) - (\frac{H_3}{H_4})\gamma^2 cos(\gamma)]}\left[cosh(\beta\overline{x}) + \frac{H_3}{H_4}cos(\gamma\overline{x})\right] \quad (3.23)$$

where $\overline{x}$ and $\overline{\boldsymbol{W}}$ are the position in the axial, x, and displacements in the transverse, y, direction normalised with respect to length, L. The full mathematical procedure to derive equation (3.23) is given in Appendix C.3.

If the frequency parameter is known then the associated mode shape for a free-free beam can be depicted using the equation (3.23) for $\overline{x}$ between $0 < \overline{x} < 1$ knowing that $\overline{\boldsymbol{W}} = \frac{\boldsymbol{W}}{L}$ and $\overline{x} = \frac{x}{L}$. The first to fifth mode shapes of a free-free beam based on the Timoshenko beam theory (TBT) are shown in figure 3-15 which are the same for local and nonlocal Timoshenko beams:

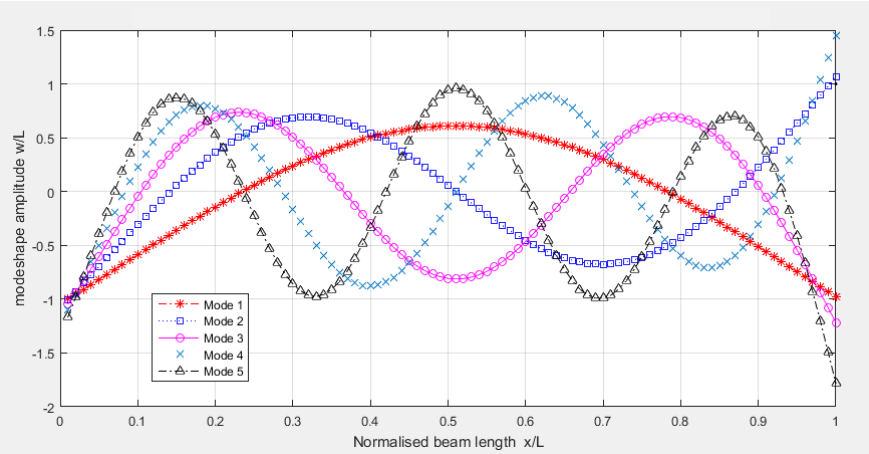

Figure 3-15: First to fifth mode shapes of a free-free beam based of the TBT, AR=10.4. The mode shapes are used to identify modal frequencies associated with each mode shape.

3.6.3 Comparison with FE results to identify α

Equation (3.8) was solved by applying the bisection method to identify the normalised transverse modal frequencies for the first 37 modes of a beam with aspect ratio L/d=10.4:1. The results are provided in figure 3-17-a. By comparing the finite element results and these analytical NLT results, it is possible to obtain Eringen's scale parameter for some of the heterogeneous beam models considered previously. Direct comparison between the results in

figure 3-17-a and the finite element results given in section 3.5 suggests that it is not always possible to determine α for all cases considered. However, by applying a constant shift:

$$(\lambda/\lambda_0)_{FE,n,after} = (\lambda/\lambda_0)_{FE,n,before} - [C_{NLT} \times (1 - (\lambda/\lambda_0)_{FE,\ Mode\_1})] \qquad (3.24)$$

where n, $n > 1$, is the mode number and λ_0 is the non-dimensional frequency of homogeneous beam obtained using ANSYS. The FE results for perforated beams with continuous boundaries could be compared with the results obtained from solving the Eringen non-local theory, as seen in figure 3-16.

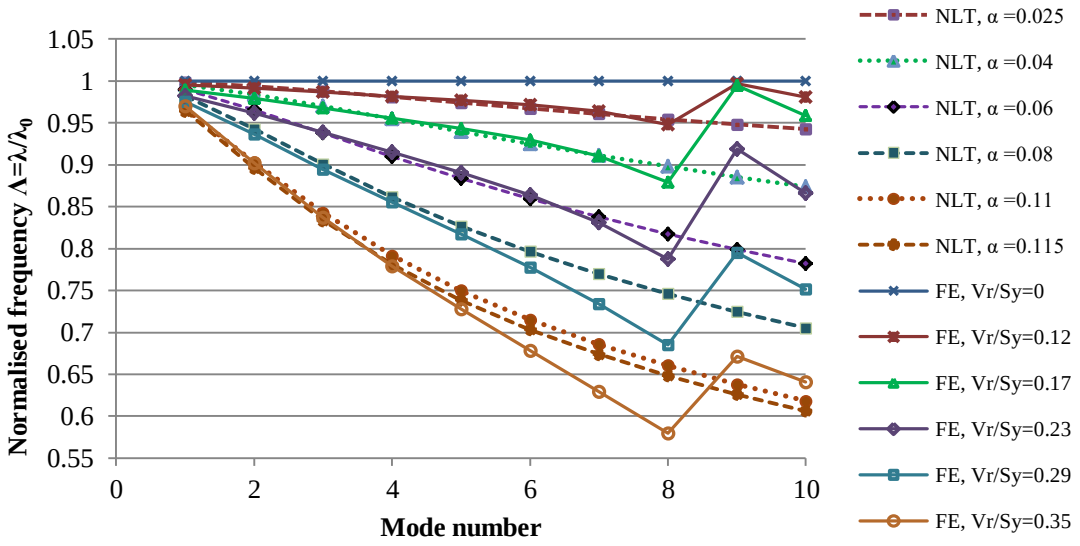

Figure 3-16: Numerically obtained normalised frequency parameter vs. mode numbers
Beam model: Perforated beam (BVOCB), Size 1(1/d^2=1.33), BC: Free-Free

Equation (3.24) is only used to shift the FE normalised frequencies at any given volume fraction and fit them onto the NLT transverse frequency results to obtain α. Therefore, $(\lambda/\lambda_0)_{FE,n,after}$ is the normalised frequency parameter of the n^{th} mode after shifting, $(\lambda/\lambda_0)_{FE,n,before}$ is the normalised frequency parameter of the mode number n^{th} before shifting from the FE results and C_{NLT} is an empirical constant for the beam type and is equal to 1.2 which relates FE and NLT results. The value of C_{NLT} was obtained by curve fitting and changing the C_{NLT} value until the NLT beam results match those obtained from FE. Thus, by shifting the results below the line representing the homogeneous case, obtaining α for beams with either voids or inclusions is possible.

The values for α obtained via this curve fitting method for beams with continuous surfaces show that for a given volume fraction α is not size independent as illustrated in figure 3-17-b

and therefore, it cannot be considered as a unique property of the material. For the samples with textured boundaries, it is not possible to identify α because of the inverted size effect.

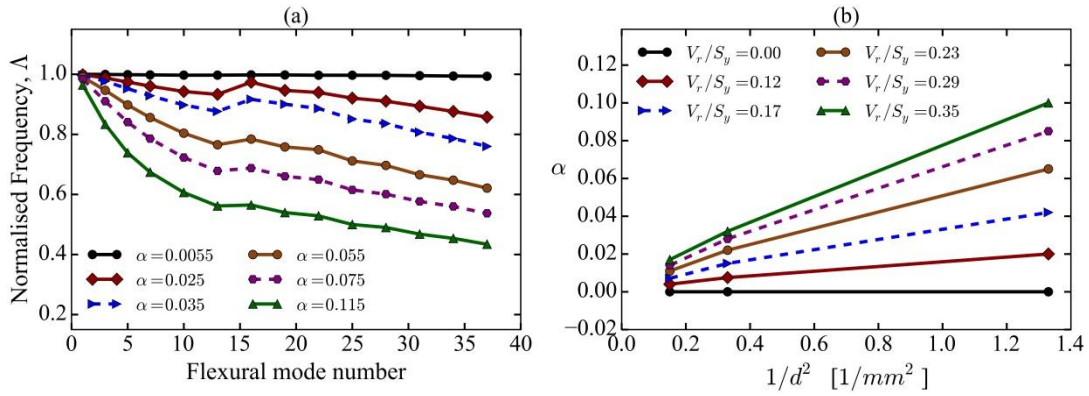

Figure 3-17: Results for perforated beam models with continuous boundaries and F-F boundary conditions using NLT beam theory; a) Normalised non-local Timoshenko frequency parameters for various α's. Eringen's nonlocal parameter is influenced in only x directions ($d^{-2} = 1.33,\ AR = 10.4$) (graph on the left); b) Scale Coefficient 'α' (Alpha), Obtained by curve fitting FE results with NLT and V_r/S_y is the normalised void radius changing from 0 to 0.35 (graph on the right).

Further investigation into the nonlocal Timoshenko beam theory such as including the Eringen's nonlocal parameter in both x and y directions in the formulations did not overcome this fundamental problem. See figures 3-18-a, 3-18-b and the solution procedure in Appendix C.2.

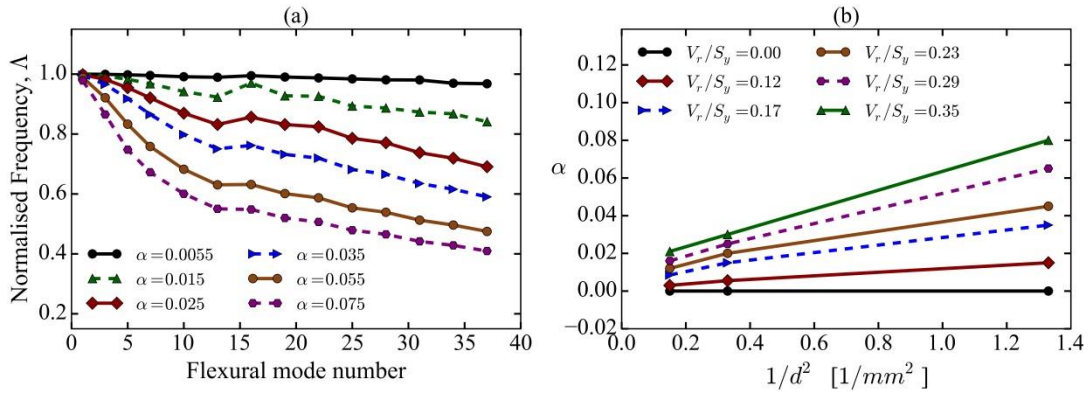

Figure 3-18: Results for perforated beam models with continuous boundaries and F-F boundary conditions using NLT beam theory (including the Eringen's nonlocal parameter in x and y directions); a)Normalised non-local Timoshenko frequency parameters for various α's for perforated beam models with continuous boundaries and F-F boundary conditions using NLT beam theory. Eringen's nonlocal parameter is effective in x and y directions ($1/d^2 = 1.33, AR = 10.4$). b) Scale Coefficient 'α' (Alpha), Obtained by curve fitting FE results with NLT and V_r/S_y is the normalised void radius changing from 0 to 0.35 (graph on the right).

As seen in figures 3-17-b and 3-18-b, increasing the beam depth will require a different value of 'α' which indicates that the Eringen's scale coefficient for the beam models with constant aspect ratio is thus size-dependent. This confirms that the NLT beam is not applicable for modal analysis in cases when increasing the beam depth is accompanied by an increase in number of unit cells across the beam depth.

3.7 Conclusions:

Geometrically similar beam samples of different sizes that contained periodic heterogeneities were modelled using finite element analysis, and modal analyses were performed to identify the unconstrained flexural natural frequencies. Contrary to the homogeneous case where these frequencies are size independent, the FE results indicate that in the heterogeneous case they are size dependent. Moreover, this size effect depends on both the specification of the periodic heterogeneity and its location relative to the sample boundaries.

Eringen's enhanced nonlocal Timoshenko beam was also solved analytically for FF boundary condition and mode shapes were extracted. For cases where the finite element results exhibit a consistent size effect, Eringen's nonlocal Timoshenko beam (NLT) analysis was considered in attempting to explain the dynamic behaviour observed. However, the NLT appears to have shortcomings since the small-scale coefficient was not constant for all model sizes of the same aspect ratio. The size dependency of the coefficient value thus implies that it cannot be interpreted as an independent constitutive property and, therefore, the Eringen nonlocal theory was not applicable for the models presented in this chapter.

In the light of the above points which describe, in detail, the inability of the classical and non-local beam deformation theories to explain the dynamic behaviour of heterogeneous models, in the next chapter, the theory of micropolar elasticity will be studied and its applicability and abilities in explaining the dynamic response of the heterogeneous beams and plates will be investigated.

4 Application of Micropolar Theory to 2D Beams

In chapter three, the Eringen non-local Timoshenko beam could not explain the dynamic behaviour of two-dimensional heterogeneous beams. Therefore a more suitable theory must be used which should be able to explain the size effect in the dynamic behaviour of the heterogeneous materials. The micropolar theory, as briefly discussed in chapter two, has an additional degree of freedom: a micro rotation vector which allows the constituent material particles to rotate individually. Additional couple stresses, as well as the stresses, are taken into considerations in the micropolar theory (Lakes 1996) and orthogonal shear stresses may therefore be symmetric or asymmetric. In this chapter, two-dimensional plane-stress formulation of micropolar theory will first be discussed and one of the micropolar constants, namely the characteristic length of bending, will be analytically obtained.

4.1 2D micropolar formulation

Equation (4.1) defines the strain components, $\boldsymbol{\varepsilon}$, in terms of the displacements, $\boldsymbol{u}$, and micro-rotations, $\boldsymbol{\phi}$, by (Hossein Abadikhah and Folkow 2015; Hassanpour and Heppler 2017):

$$\boldsymbol{\varepsilon}_{ij} = \boldsymbol{u}_{j,i} - \boldsymbol{e}_{ijk}\,\boldsymbol{\phi}_k \tag{4.1}$$

The micro-rotation occurs due to the effects of asymmetric components of shear stresses on infinitesimal material particles which causes these material points to rotate individually and is different from the macro rotation when the slope of the displacement is considered. The micro and macro rotations are shown in figure 4-1.

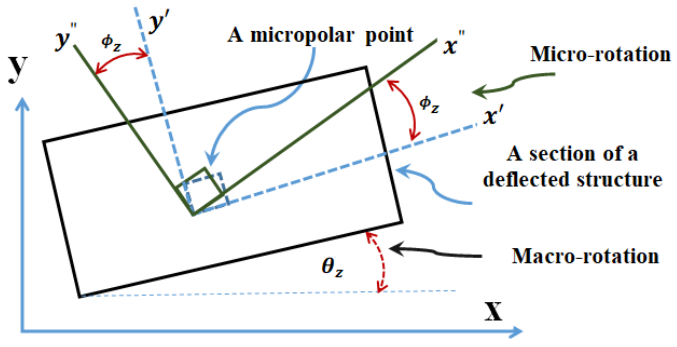

Figure 4-1: Representation of micro and macro rotations in a micropolar medium

The macro-rotation is:

$$\boldsymbol{\theta}_k = (\boldsymbol{e}_{ijk}\, \boldsymbol{u}_{k,j})/2 \tag{4.2}$$

The strain tensor in equation (4.1) is composed of symmetric and asymmetric strain tensors as in (Hassanpour and Heppler 2017):

$$\boldsymbol{\varepsilon}_{ij} = \boldsymbol{\varepsilon}_{ij}^{sym} + \boldsymbol{\varepsilon}_{ij}^{asy} \tag{4.3}$$

Thus:

$$\boldsymbol{\varepsilon}_{ij}^{sym} = \frac{1}{2}(\boldsymbol{u}_{i,j} + \boldsymbol{u}_{j,i}) \tag{4.4}$$

$$\boldsymbol{\varepsilon}_{ij}^{asy} = \frac{1}{2}(\boldsymbol{u}_{i,j} - \boldsymbol{u}_{j,i}) - \boldsymbol{e}_{ijk}\, \boldsymbol{\phi}_k = \boldsymbol{e}_{ijk}(\boldsymbol{\theta}_k - \boldsymbol{\phi}_k) \tag{4.5}$$

Therefore equation (4.1) can be expanded in a 2D matrix form in Cartesian coordinates with indices substituted i, j, k=x, y, and z as follows:

$$\begin{bmatrix} \boldsymbol{\varepsilon}_{xx} \\ \boldsymbol{\varepsilon}_{yy} \\ \boldsymbol{\varepsilon}_{xy} \\ \boldsymbol{\varepsilon}_{yx} \end{bmatrix} = \begin{bmatrix} \boldsymbol{u}_{x,x} \\ \boldsymbol{u}_{y,y} \\ \boldsymbol{u}_{y,x} - \boldsymbol{\phi}_z \\ \boldsymbol{u}_{x,y} + \boldsymbol{\phi}_z \end{bmatrix} \tag{4.6}$$

In the dynamic case micro inertia also needs to be included into the equations of dynamic equilibrium for linear and angular momenta. Therefore the equations of equilibrium to satisfy the micropolar linear elasticity balance will be according to:

$$\boldsymbol{\tau}_{\mathrm{ij,i}} = \rho \frac{\partial^2 \boldsymbol{u}_j}{\partial t^2} \tag{4.7}$$

$$\mathbf{m}_{\mathrm{ij,i}} + \mathbf{e}_{\mathrm{jik}}\, \boldsymbol{\tau}_{\mathrm{ij}} = \rho\, \mathbf{J}_{\mathrm{ji}} \frac{\partial^2 \boldsymbol{\phi}_k}{\partial t^2} \tag{4.8}$$

where $\mathbf{J}_{\mathrm{ji}}$ is the microinertia tensor. In the literature, the value of the micro-inertia is taken constant (Hossein Abadikhah and Folkow 2015) but in the next chapter, it will be shown that

the micro inertia depends on volume fraction through the characteristic length of bending and its influence on another constitutive parameter, the coupling number, will be discussed.

In the plane stress case, the micro-rotation vector is only perpendicular to the plane and the shear stresses relating to z coordinates vanish. Therefore, $\boldsymbol{\phi}_x = \boldsymbol{\phi}_y = 0$ and $\boldsymbol{\tau}_{zz} = \boldsymbol{\tau}_{xz} = \boldsymbol{\tau}_{zx} = \boldsymbol{\tau}_{yz} = \boldsymbol{\tau}_{zy} = 0$

The stress and strain tensors are define by:

$$\boldsymbol{\tau} = [\boldsymbol{\tau}_{xx}\ \boldsymbol{\tau}_{yy}\ \boldsymbol{\tau}_{xy}\ \boldsymbol{\tau}_{yx}]^T \tag{4.9}$$

$$\boldsymbol{\varepsilon} = [\boldsymbol{\varepsilon}_{xx}\ \boldsymbol{\varepsilon}_{yy}\ \boldsymbol{\varepsilon}_{xy}\ \boldsymbol{\varepsilon}_{yx}]^T \tag{4.10}$$

where T stands for transposed.

Stress and couple stress are linked to the strain and curvature as follows:

$$\begin{pmatrix} \boldsymbol{\tau} \\ \boldsymbol{m}_{xz} \\ \boldsymbol{m}_{yz} \end{pmatrix} = \mathbb{D}_{2D\ Plane\ Stress} \begin{pmatrix} \boldsymbol{\varepsilon} \\ \boldsymbol{\phi}_{z,x} \\ \boldsymbol{\phi}_{z,y} \end{pmatrix} \tag{4.11}$$

$$\mathbb{D}_{2D\ Plane\ Stress} = \begin{bmatrix} \mathbb{D}1 & [0]_{4\times 2} \\ [0]_{2\times 4} & \mathbb{D}2 \end{bmatrix} \tag{4.12}$$

where the material constitutive matrix "$\mathbb{D}1$" and "$\mathbb{D}2$" can be derived from equations (2.16) and (2.17) and reduced for a 2-D micropolar in plane stress case are given by Lake (2003) as:

$$\mathbb{D}1 = \begin{bmatrix} \dfrac{(2\mu^* + \kappa^*)(2\lambda^* + 2\mu^* + \kappa^*)}{(\lambda^* + 2\mu^* + \kappa^*)} & \dfrac{(2\mu^* + \kappa^*)\lambda^*}{(\lambda^* + 2\mu^* + \kappa^*)} & 0 & 0 \\ \dfrac{(2\mu^* + \kappa^*)\lambda^*}{(\lambda^* + 2\mu^* + \kappa^*)} & \dfrac{(2\mu^* + \kappa^*)(2\lambda^* + 2\mu^* + \kappa^*)}{(\lambda^* + 2\mu^* + \kappa^*)} & 0 & 0 \\ 0 & 0 & \mu^* + \kappa^* & \mu^* \\ 0 & 0 & \mu^* & \mu^* + \kappa^* \end{bmatrix} \tag{4.13}$$

$$\mathbb{D}2 = \begin{bmatrix} \gamma^* & 0 \\ 0 & \gamma^* \end{bmatrix} \tag{4.14}$$

Equations (4.13) and (4.14) may be written in terms of 4 independent engineering constants as defined by Lake (1996) in a generalised plane stress form thus:

$$\mathbb{D}1 = \frac{E_m}{1-{\nu_m}^2}\begin{bmatrix} 1 & \nu_m & 0 & 0 \\ \nu_m & 1 & 0 & 0 \\ 0 & 0 & \frac{1-\nu_m}{2}\left(\frac{1}{1-N^2}\right) & \frac{1-\nu_m}{2}\left(\frac{1-2N^2}{1-N^2}\right) \\ 0 & 0 & \frac{1-\nu_m}{2}\left(\frac{1-2N^2}{1-N^2}\right) & \frac{1-\nu_m}{2}\left(\frac{1}{1-N^2}\right) \end{bmatrix} \tag{4.15}$$

$$\mathbb{D}2 = \begin{bmatrix} \frac{2E_m l_b^2}{1+\nu_m} & 0 \\ 0 & \frac{2E_m l_b^2}{1+\nu_m} \end{bmatrix} \tag{4.16}$$

where the engineering constants relate to the micropolar constants as follows:

$$E_m = \frac{(2\mu^* + \kappa^*)(3\lambda^* + 2\mu^* + \kappa^*)}{(2\lambda^* + 2\mu^* + \kappa^*)} \tag{4.17}$$

$$\nu_m = \frac{\lambda^*}{(2\lambda^* + 2\mu^* + \kappa^*)} \tag{4.18}$$

$$l_b^2 = \frac{\gamma^*}{2(2\mu^* + \kappa^*)} \tag{4.19}$$

$$N^2 = \frac{\kappa^*}{2(\mu^* + \kappa^*)} \tag{4.20}$$

Here E_m is the micropolar modulus, ν_m is the micropolar Poisson's ratio and l_b is a length scale parameter termed the characteristic length in bending that should reflect the microstructural scale. N is the coupling number that quantifies the shear stress asymmetry.

The characteristic length of bending, l_b , in equation (4.16) can be obtained analytically for a slender beam which is now described in section 4.2.

According to equation (4.15), the shear stress and strain relationship may be written in matrix form:

$$\begin{bmatrix}\boldsymbol{\tau}_{yx}\\ \boldsymbol{\tau}_{xy}\end{bmatrix} = \begin{bmatrix} G_{11} & G_{12} \\ G_{21} & G_{22}\end{bmatrix}\begin{bmatrix}\boldsymbol{\varepsilon}_{yx}\\ \boldsymbol{\varepsilon}_{xy}\end{bmatrix} \tag{4.21}$$

$$G_{11} = G_{22} = \mu^* + \kappa^* \tag{4.22}$$

$$G_{12} = G_{21} = \mu^* \tag{4.23}$$

or

$$\begin{bmatrix}\boldsymbol{\tau}_{yx}\\ \boldsymbol{\tau}_{xy}\end{bmatrix} = \frac{E_m}{(1+\nu_m)}\begin{bmatrix}\dfrac{1}{2(1-N^2)} & \dfrac{(1-2N^2)}{2(1-N^2)} \\ \dfrac{(1-2N^2)}{2(1-N^2)} & \dfrac{1}{2(1-N^2)}\end{bmatrix}\begin{bmatrix}\boldsymbol{\varepsilon}_{yx}\\ \boldsymbol{\varepsilon}_{xy}\end{bmatrix} \tag{4.24}$$

indicating that the asymmetric components of the shear stress are controlled by N according to:

$$G_{sy} = (G_{11} + G_{12}) = 2\mu^* + \kappa^* = \frac{E}{1+\nu_m} \tag{4.25}$$

$$G_{asy} = G_{11} - G_{12} = \kappa^* = \frac{E}{1+\nu_m}\left(\frac{N^2}{1-N^2}\right) \tag{4.26}$$

This parameter can be identified from the higher order modes using an iteration method that will be described in chapter five since these involve increased shear deformation.

The solid behaves in a classical homogeneous manner if $\alpha^*, \beta^*, \gamma^*$ and κ^* equal zero, while if N=1 and therefore, microrotation and macrorotation are not kinematically distinct implying that, they are equal, such that $\boldsymbol{\phi}_z \cong \boldsymbol{\theta}_z$ and this limiting case is usually referred to as couple stress elasticity.

4.2 Characteristic length in bending, l_b

As shown in equations (4.11), (4.12), (4.15) and (4.16), the couple stress tensors are related to the micro rotations which allow identification of one of the micropolar constants, namely the characteristic length of bending, analytically through the primary transverse frequency of slender beams. E_m and ν_m can be determined from static tensile tests where no size effect is anticipated while l_b can be obtained from mode 1 dynamic behaviour as outlined here.

In a slender beam where $d/L \ll 1$, the micro and macro-rotations actually become indistinguishable (Hadjesfandiari, Hajesfandiari, and Dargush 2016):

$$Microrotation\ \boldsymbol{\phi}_z \cong Macrorotation\ \boldsymbol{\theta}_z \tag{4.27}$$

The bending moment, **M**, is related to the internal force stress,$\boldsymbol{\tau}_{xx}$, and couple stress,$\boldsymbol{m}_{xz}$, thus:

$$\boldsymbol{M} = \int_A (y\boldsymbol{\tau}_{xx} + \boldsymbol{m}_{xz})dA \tag{4.28}$$

Also,

$$\frac{1}{R} = \frac{d\boldsymbol{\theta}}{dx} = \frac{d\boldsymbol{\phi}_z}{dx} = -\frac{d^2\boldsymbol{W}}{dx^2} \tag{4.29}$$

where R is the radius of curvature and **W** is the transverse displacement.

The in-plane couple stress $\mathbf{m}_{xz}$ and the normal stress $\boldsymbol{\tau}_{xx}$ are:

$$\boldsymbol{m}_{xz} = \gamma^* \frac{d\boldsymbol{\phi}_z}{dx} \tag{4.30}$$

$$\boldsymbol{\tau}_{xx} = \frac{E_{mf} y}{R} \tag{4.31}$$

where E_{mf} is the micropolar flexural modulus which is assumed to be equal to the micropolar tensile modulus E_m.

If $\boldsymbol{\phi}_z \cong \boldsymbol{\theta}_z$ then:

$$\boldsymbol{m}_{xz} = \frac{\gamma^*}{R} \tag{4.32}$$

The second moment of area is defined as:

$$I = \int_A y^2 dA \tag{4.33}$$

where A is the cross-section of the slender beam:

$$A = \int_A dA \tag{4.34}$$

Substituting for $\frac{1}{\mathrm{R}} = -\frac{\mathrm{d}^2\mathbf{W}}{\mathrm{dx}^2}$ in the moment-curvature relationship:

$$\frac{d^2\boldsymbol{W}}{dx^2} = -\frac{\boldsymbol{M}}{E_{mf}I + \gamma^* A} = -\frac{\boldsymbol{M}}{D_{mf}} \tag{4.35}$$

$$D_{mf} = E_{mf}I + \gamma^* A \tag{4.36}$$

where D_{mf} is the micropolar flexural rigidity

For an unloaded Euler-Bernoulli beam in the dynamic case:

$$D_{mf}\frac{d^4\boldsymbol{W}}{dx^4} - \mu\omega^2\boldsymbol{W} = 0 \tag{4.37}$$

where μ is the mass per unit length given by:

$$\mu = \rho A \tag{4.38}$$

and

$$\omega = \lambda^2\sqrt{\frac{D_{mf}}{\rho A L^4}} \tag{4.39}$$

$$\rightarrow \omega = \lambda^2\sqrt{\frac{E_{mf}I + \gamma^* A}{\rho A L^4}} \tag{4.40}$$

Also, $D_{mf} = D = EI$ in absence of any couple stress.

The equations (4.33) and (4.34) may also be written as:

$$I = \frac{bd^3}{12} \tag{4.41}$$

$$A = bd \tag{4.42}$$

for a rectangular sectioned beam. By combining the equations (4.17) and (4.19) it follows that:

$$\gamma^* = \frac{E_{mf} l_c^2}{12} \tag{4.43}$$

Note that parameter l_c (Beveridge, Wheel, and Nash 2013a) differs from the conventional characteristic length in bending, l_b , by a factor of 24.

By substituting equations (4.41), (4.42) and (4.43) into equation (4.40):

$$\omega^2 = \frac{E_{mf}\lambda^4}{12\rho L^4}\left(d^2 + l_b^2\right) \tag{4.44}$$

Rearrange the equation (4.44) regarding mass and frequency:

$$m.\omega^2 = \frac{E_{mf}\lambda^4 b}{12}\left(\frac{d}{L}\right)^3\left(1 + \left(\frac{l_c}{d}\right)^2\right) \tag{4.45}$$

Note that if γ^* is taken as in the equation (4.16), the resulting characteristics length will be about $\sqrt{24}$ or 4.3 times smaller. By applying γ^* as it appears in equation (4.16), the equation (4.45) can be modified to:

$$m.\omega^2 = \frac{E_{mf}\lambda^4 b}{12}\left(\frac{d}{L}\right)^3\left(1 + \left(\frac{24}{1+\nu_m}\right)\left(\frac{l_b}{d}\right)^2\right) \tag{4.46}$$

Equation (4.45) thus relates the characteristic length, l_c, non-dimensional frequency, λ, micropolar flexural modulus, E_{mf}, and beam dimensions, to the product of beam's mass, m (m without subscript is scalar and stands for mass), multiplied by squared frequency. Thus, if this product is determined for beams of various size and plotted against the beam's reciprocal size measure, $(1/d^2)$, then it is possible to obtain E_{mf} or λ from the intercept and the characteristic length from the slope. See table 4-1. Since equation (4.45) and (4.46) assume the beam is slender, they are only applied to mode one here where this assumption is presumed valid.

The FE results, as presented in chapter three, indicated that in some cases, the size effect appears to be consistent with more generalised continuum descriptions of dynamic constitutive behaviour such as micropolar elasticity in that an increase in frequency with reducing size is observed while in other cases the effect is contradictory. Therefore, Equation (4.45) was applied to all four sizes of sample to obtain results, the characteristic length of bending, listed in table 4-1 for the following beam types:

1) Perforated beams with continuous boundaries
2) Beams with compliant inclusions and continuous boundaries
3) Beams with compliant matrix and textured boundaries

Other beam types did not satisfy the micropolar theory since the size effect is not as anticipated.

The characteristic length does not vary with beam size and only depends on volume fraction. See table 4-1 below:

Table 4-1: Characteristic length changes with volume fraction, V_f . Based on all four sizes of beam model

Void or inclusion vol. fraction	l_c for beams with continuous boundaries, mm				l_c for beams with textured boundaries, mm	
	Perforated beams	R^2	Beams with compliant inclusions	R^2	Beams with compliant matrix	R^2
4%	0.2717	98.99%	0.2555	99.99%	0.2218	99.70%
8%	0.4139	99.77%	0.3612	99.97%	0.3126	99.76%
15%	0.5432	99.78%	0.4681	99.95%	0.3829	99.91%
23%	0.6522	99.88%	0.5621	99.94%	0.4379	99.95%
33%	0.7334	99.83%	0.6367	99.93%	0.4759	99.91%

The coefficients of determination, denoted R^2, in table 4-1 indicate the accuracy of the Polyfit approximation for in obtaining the values of characteristic length for various volume fractions.

Beveridge et al. (2013a) identified the characteristic length of bending through static mechanical 3 point bending experiments on four slender beams of high mass density aluminium (HMD) with periodic perforations of radius equal to 3.5 mm, breadth 12.7 mm, depths of 12.7, 25.4, 38.1, and 50.8 mm and aspect ratio of 10:1. Although their test pieces were scaled up and that their results are available for only one volume fraction equal to 0.23, however, the normalised value of the characteristic length of bending that they identified is in good agreement with the value that was determined through dynamic procedure for the same volume fraction in this chapter, as seen in table 4-2:

Table 4-2: The normalised characteristic length of bending, l_c , for perforated beams of volume fraction equal to 0.23

	Void radius	Unit-cell depth	Normalised void radius	The characteristic length of bending	The normalised characteristic length of bending
	$V_r\ mm$	$S_y\ mm$	V_r/S_y	$l_c\ mm$	l_c/S_y
This work, Modal FEA	0.25	0.866	0.289	0.652	0.753
Experimental, 3 Point bending case, Ref: (Beveridge, Wheel, and Nash 2013a)	3.5	12.7	0.276	8.750	0.689

As seen in figure 3-6 and 3-8, the variations in the normalised frequencies have an approximately linear relationship with $(1/d^2)$, except for the smallest beam sizes where the ratio of the radius of void or inclusion to overall beam thickness approaches the maximum. Therefore, in this work, the three largest sizes of beam model were considered in identifying the characteristic length of bending, as given in table 4-3 to avoid complications relevant to the smallest beam sample. However, while the values change from table 4-1 to 4-3, they don't change dramatically. Therefore, values listed in table 4-3 of were subsequently used to estimate the coupling number in chapter 5.

Table 4-3: Characteristic length changes with V_f . Based on the three largest sizes of beam model

Void or inclusion vol. fraction, V_f	l_c for beams with continuous boundaries, mm				l_c for beams with textured boundaries, mm	
	Perforated beams	R^2	Beams with compliant inclusions	R^2	Beams with compliant matrix	R^2
4%	0.332	97.12%	0.254	99.99%	0.256	99.92%
8%	0.464	99.64%	0.377	99.99%	0.32	93.76%
15%	0.608	99.41%	0.496	99.99%	0.412	99.77%
23%	0.709	99.55%	0.601	99.99%	0.455	99.04%
33%	0.817	99.93%	0.684	99.99%	0.479	97.70%

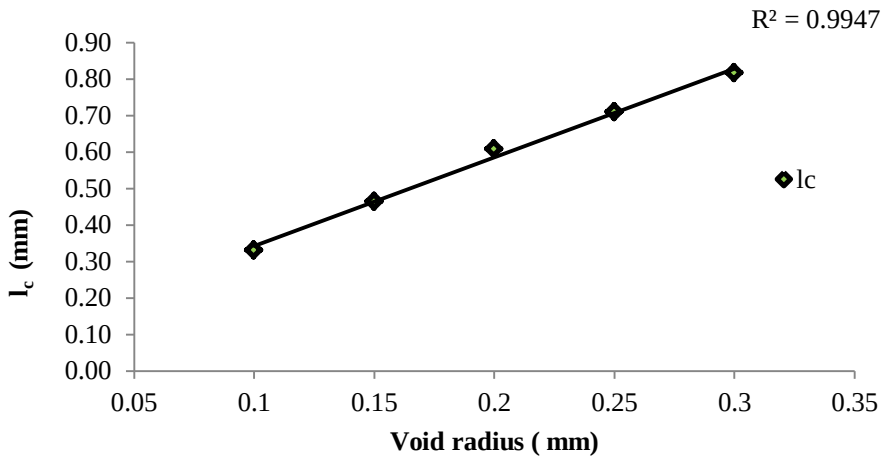

Figure 4-2: Linear changes of the characteristic length void radius for beams with continuous boundaries. Based on the three largest beam models

l_b may be obtained directly from the equation (4.46) or simply multiplying the values in the above table by $\frac{1}{\sqrt{24}}$ or 0.233 and they are listed below in table 4-4. The R^2 values here are exactly equal to those listed in table 4-3.

Table 4-4: Characteristic length (l_b) changes with volume fraction. Based on the three largest sizes of beam model

Void or inclusion vol. fraction	l_b for beams with continuous boundaries, mm		l_b for beams with textured boundaries, mm
	Perforated beams	Beams with compliant inclusions	Beams with compliant matrix
4%	0.077	0.059	0.060
8%	0.108	0.088	0.075
15%	0.142	0.115	0.096
23%	0.165	0.140	0.106
33%	0.190	0.159	0.112

4.3 Summary and conclusions

The FE results presented in chapter 3 were used to estimate the characteristic length in bending. A useful equation was derived analytically which relates the beam's primary modal frequency to the inverse of the depth squared and then used to obtain the characteristic length of bending. This result agrees with the results of Frame (2013b) that were obtained through FE analysis of statically loaded perforated beams. The characteristic length of bending , l_b, was found to behave linearly, in proportion to the void and inclusions radius but it was noticed that the smallest sample with one layer of voids/inclusions departs slightly from linearity. It was also found that the inverse of beams depth squared varies approximately

linearly with the mass multiplied by the square of the frequency of the primary mode but it deviates from linearity for the smallest sample.

Equation (4.45) only facilitates the identification of the characteristic length parameter from the first flexural natural frequency based on the assumption of slender beam behaviour for which shear deformation is negligible.

Therefore, in order to have a more conservative approach towards deviation from linearity of length scale, the characteristic lengths based on the three largest sample models were obtained.

As there was no analytical method available to relate the coupling number to modal frequency similar to the method used for obtaining the characteristic length, the coupling number may therefore be obtained with known parameters such as characteristic length of bending and the micro-inertia in an iterative process employing a numerical procedure as outlined in the next chapter.

5 Development of Algorithms for the Numerical CVFEM and 2D-MPFEM and Investigation into the Effect of Micro Inertia on the Coupling Number "N"

5.1 Introduction

Now that the characteristic lengths of bending for beam models have been identified, the linear isotropic micropolar theory will be incorporated into conventional finite element and control volume finite element methods (MPFEM and CVFEM) through a set of mathematical models and algorithms which facilitates the modal analysis of heterogeneous beam models. Therefore, the methods of construction of the main matrices, namely the stiffness, mass and micro-inertia matrices along with the step-wise algorithms needed for numerical analysis will be presented. These algorithms can be used in future to develop useful codes in any programing language for modal analysis. Besides this, another algorithm will be developed which is useful for the identification of the coupling number, N, which is named the "Parameter Identification Algorithm" will be described in details which benefits from the modelling and modal analysis of MPFEM or CVFEM and the linear regression method for the iteration process and obtaining the coupling number specific to the heterogeneous beam models. The parameter identification algorithm will be used later in chapter six to obtain the coupling number, N, for various beam types. The effect of micro inertia on the coupling number will also be described in section 5.5.

5.2 Formulation of the numerical CVFEM (and 2D-MPFEM)

In this section, the formulation which incorporates the micropolar theory into two different numerical procedures for dynamic analysis is discussed. Both the control volume finite element method (CVFEM) incorporating micropolar elasticity and two-dimensional micropolar finite element method (2D-MPFEM) used in obtaining the required stiffness matrix are described. Derivation of the mass and micro inertia matrices and solution process are explained in detail. The formulations will be later used in section 5.3 for development of algorithms which are used for modal analysis of micropolar beams.

5.2.1 Modelling 6-node triangular element

In a 6-node linear strain triangular element, figure 5-1, there are three nodes at the corners plus three mid-side nodes. In conventional, displacement-based finite element procedures, each node has two degrees of freedom but here nodes can also rotate independently as well

as undergoing displacement in the coordinates of the plane. Therefore, an extra degree of freedom called the micro rotation is associated with each node.

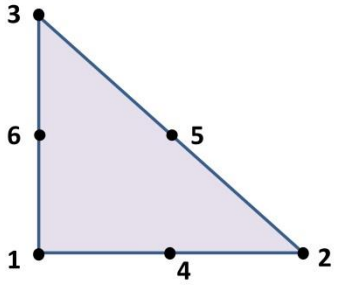

Figure 5-1: The conventional mode numbering in a 6-node triangular element in Cartesian coordinates

The displacements in 6-node triangular element are quadratic functions. $\boldsymbol{U}_x$ and $\boldsymbol{U}_y$ are assumed to be displacements in x and y directions. Therefore:

$$\boldsymbol{U}(x,y) = a_1x^2 + a_2x + a_3xy + a_4y + a_5y^2 + a_6 \tag{5.1}$$

in which the polynomials are of the second order.

The overall displacement field of the triangular element can be expressed in the following way:

$$\boldsymbol{U}(x,y) = \mathbb{N}_i \begin{Bmatrix} x \\ y \end{Bmatrix} \tag{5.2}$$

where $\mathbb{N}$ is the shape function of a specific node i , $i = 1,2,\dots 6$ in the natural coordinate system in which internal location coordinates are defined based on the fraction of the sub-triangles areas to the overall area of the triangular element; as seen in figure 5-2:

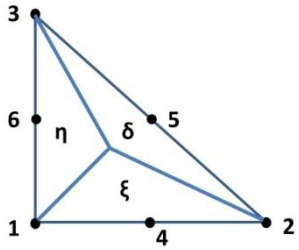

Figure 5-2: The illustration of natural coordinate system for triangular element

5.2.2 Stiffness matrix based on micropolar elasticity (2D-MPFEM)

The six-node triangular element is used in the development of a finite element code incorporating the aforementioned micropolar theory and each shape function is identified as $\mathbb{N}^i$, for i=1,2,…6; Shape functions for six-node triangular element can be found in reference (Bathe 2006; Zienkiewicz and Taylor 2000; Vladimir and Tomic 2015; Kaltenbacher 2015) and are as follows:

$$\mathbb{N} = [\delta(2\delta - 1)\ \ \xi(2\xi - 1)\ \ \eta(2\eta - 1)\ 4\delta\xi\ \ 4\xi\eta\ \ 4\eta\delta\ ] \tag{5.3}$$

where

$$\delta = 1 - \xi - \eta \tag{5.4}$$

By substituting equation (5.4) in (5.3), the shape functions may also be written as:

$$\mathbb{N} = [(1 - \xi - \eta)(1 - 2\xi - 2\eta) \quad \xi(2\xi - 1) \quad \eta(2\eta - 1) \quad 4(1 - \xi - \eta)\xi \quad 4\xi\eta \quad 4\eta(1 - \xi - \eta)] \tag{5.5}$$

The derivatives of the shape functions with regard to the area coordinates are:

$$\begin{bmatrix} \mathbb{N}^i{}_{,\delta} \\ \mathbb{N}^i{}_{,\xi} \\ \mathbb{N}^i{}_{,\eta} \end{bmatrix} = \begin{bmatrix} 4\delta - 1 & 0 & 0 & 4\xi & 0 & 4\eta \\ 0 & 4\xi - 1 & 0 & 4\delta & \eta & 0 \\ 0 & 0 & 4\eta - 1 & 0 & 4\xi & 4\delta \end{bmatrix} \tag{5.6}$$

For any point with coordinates (x, y) in the 6-node triangular and isoparametric elements we may write:

$$x = \sum_{i=1}^{6} \mathbb{N}_i x_i \tag{5.7}$$

$$y = \sum_{i=1}^{6} \mathbb{N}_i y_i \tag{5.8}$$

The derivatives of the shape functions in the Cartesian and natural coordinates are related according to equation (5.9):

$$\begin{bmatrix} \mathbb{N}^i_{,x} \\ \mathbb{N}^i_{,y} \end{bmatrix} = \begin{bmatrix} \delta_{,x} & \eta_{,x} \\ \delta_{,y} & \eta_{,y} \end{bmatrix} \begin{bmatrix} \mathbb{N}^i_{,\delta} \\ \mathbb{N}^i_{,\eta} \end{bmatrix} = \hat{\mathrm{J}}^{-1} \begin{bmatrix} \mathbb{N}^i_{,\delta} \\ \mathbb{N}^i_{,\eta} \end{bmatrix} \tag{5.9}$$

where $\hat{\mathrm{J}}^{-1}$ represents the inverse of the Jacobian matrix and is used to transform the derivatives of shape functions from natural to Cartesian coordinates. The Jacobian matrix can be calculated as follows(Zienkiewicz and Taylor 2000; Zienkiewicz, Taylor, and Zhu 2013; Zienkiewicz and Taylor, n.d.; Bathe 2006):

$$\hat{\mathrm{J}} = \begin{bmatrix} \sum_{i=1}^{6} x_i \mathbb{N}^i_{,\delta} & \sum_{i=1}^{6} y_i \mathbb{N}^i_{,\delta} \\ \sum_{i=1}^{6} x_i \mathbb{N}^i_{,\eta} & \sum_{i=1}^{6} y_i \mathbb{N}^i_{,\eta} \end{bmatrix} \tag{5.10}$$

Thus

$$\hat{\mathrm{J}}^{-1} = 2\hat{A} \tag{5.11}$$

i.e.

$$\therefore \quad \hat{\mathrm{J}} = 1/(2\hat{A}) \tag{5.12}$$

where $\hat{A}$ is the area of the triangular element.

Referring to equation (4.11), the strain field as described by $\left[\boldsymbol{\varepsilon_{ij}} \;\; \boldsymbol{\phi}_{i,j}\right]^T$, can be related to the displacement field and micro rotation by matrix B, see equation (5.13). Let $\bar{\varepsilon}$ represent the strain field and $\overline{\boldsymbol{U}}$ represent the displacement and micro rotation vector:

$$[\bar{\varepsilon}] = [B][\overline{\boldsymbol{U}}] \tag{5.13}$$

where:

$$[\bar{U}] = \left[\boldsymbol{u}_x,\ \boldsymbol{u}_y,\ \boldsymbol{\phi}_z\right]^T \tag{5.14}$$

Knowing the derivatives of the shape functions $\mathbb{N}^i$, the matrix B can be constructed as follows:

$$[B] = \begin{bmatrix}[P1]\\ [P2]\end{bmatrix} \tag{5.15}$$

where the matrices P1and P2 are:

$$[P1] = \begin{bmatrix} \mathbb{N}^i_{,x} & 0 & 0 \\ 0 & \mathbb{N}^i_{,y} & 0 \\ \mathbb{N}^i_{,y} & 0 & +\mathbb{N}^i \\ 0 & \mathbb{N}^i_{,x} & -\mathbb{N}^i \end{bmatrix} \tag{5.16}$$

$$[P2] = \begin{bmatrix} 0 & 0 & \mathbb{N}^i_{,x} \\ 0 & 0 & \mathbb{N}^i_{,y} \end{bmatrix} \tag{5.17}$$

and $\mathbb{N}$ is the shape function of the 6-node triangular element at node i, where i=1, 2… 6

Now the stiffness matrix for the 6-node triangular element, K_e , can be calculated:

$$K_e = \int_0^1 \int_0^{1-\eta} B^T \mathbb{D} B det[\hat{\jmath}]\, d_\xi d_\eta \tag{5.18}$$

where K_e has the size of 18×18. Equation (5.18) was solved by symbolic integration in MATLAB. T stands for transposed.

5.2.3 Determination of mass and micro inertia matrices

In this section a full description of the mass and micro-inertia matrices and how they actually were used to construct the element mass matrix is given.

5.2.3.1 Mass matrix for 6-node triangular element

The mass matrix for a 6-node triangular element must be constructed such as to form an 18 by 18 template mass matrix for a six-node triangular element which incorporates consistent and lumped mass matrices. The consistent mass matrix, M_C, interpolates nodal masses within the area of the triangle while in the lumped mass matrix, M_L, the element mass is equally spread over all element nodes as lump masses.

First a lumped mass matrix M_L was defined,

$$M_L = \frac{\rho \hat{A}}{6} diag[1\ 1\ 1\ \dots 1]^{18\times 18} \tag{5.19}$$

Then a consistent mass matrix was obtained for the 6-node triangular element using equation (5.20):

$$M_C = \int_{\Omega} \rho (\mathbb{N})^T N \, d\mathbb{V} \tag{5.20}$$

where $\mathbb{N}$ is the shape function, and T stands for transposed. M_C, the consistent mass matrix, is thus an integration of mass over the domain $\mathbb{V}$ which is the area of a triangular element within the mesh, figure 5-1.

In equation (5.20), the shape function $\mathbb{N}$ and its transpose have been multiplied as in equation (5.21):

$$(\mathbb{N})^T\mathbb{N} = \begin{bmatrix} \mathbb{N}_1 & 0 & 0 \\ 0 & \mathbb{N}_1 & 0 \\ 0 & 0 & \mathbb{N}_1 \\ \mathbb{N}_2 & 0 & 0 \\ : & : & : \\ 0 & 0 & \mathbb{N}_6 \end{bmatrix} \begin{bmatrix} \mathbb{N}_1 & 0 & 0 & \mathbb{N}_2 & 0 & 0 & \dots \mathbb{N}_6 & 0 & 0 \\ 0 & \mathbb{N}_1 & 0 & 0 & \mathbb{N}_2 & 0 & \dots 0 & \mathbb{N}_6 & 0 \\ 0 & 0 & \mathbb{N}_1 & 0 & 0 & \mathbb{N}_2 & \dots 0 & 0 & \mathbb{N}_6 \end{bmatrix} \tag{5.21}$$

Note that $\mathbb{N}$ is the shape function and is different from the coupling number N associated with shear stress asymmetry.

The elements in the third column of the first matrix and the third row of the second matrix in equation (5.21) are introduced to account for the mass which is associated with the micro-inertia. The micro inertia is described in section 5.2.3.2. The integration of equation (5.21**)** required the multiplication of the shape functions and integration over the area of the triangular element (Huebner et al. 2001) as follows:

$$\int_{\mathbb{V}} \mathbb{N}_i \mathbb{N}_j d\mathbb{V} = \int_{\mathbb{V}} \xi_1^i \xi_2^j \xi_3^k d\mathbb{V} \tag{5.22}$$

where $i, j \; and \; k \geq 0$ and indicate the node numbers; and $\mathbb{V}$ is the volumetric domain which becomes an area in the 2D case, thus the integration of the shape functions over the area coordinates, according to Stricklin (1968) and Eisenberg et al. (1973), are obtained using the equation (5.23):

$$\int_{A} \xi_1^i \xi_2^j \xi_3^k d\mathbb{V} = 2\hat{A}\left(\frac{i!\, j!\, k!}{(i+j+k+2)!}\right) \tag{5.23}$$

Thus, for example:

$$\begin{aligned} \int_{\mathrm{A}} \mathbb{N}_1 \mathbb{N}_1 \mathrm{d}\widehat{\mathrm{A}} = \int_{\mathrm{A}} (4\delta^4 - 4\delta^3 + \delta^2)\mathrm{d}\widehat{\mathrm{A}} &= \int_{\mathrm{A}} 4\delta^4 \,\mathrm{d}\widehat{\mathrm{A}} - \int_{\mathrm{A}} 4\delta^3 \,\mathrm{d}\widehat{\mathrm{A}} + \int_{\mathrm{A}} \delta^2 \mathrm{d}\widehat{\mathrm{A}} \\ &= 2\mathrm{A}\left[\frac{4!}{(4+2)!} - \frac{3!}{(3+2)!} + \frac{2!}{(2+2)!}\right] = \frac{\mathrm{d}\widehat{\mathrm{A}}}{30} \end{aligned} \tag{5.24}$$

The rest of the integrals are calculated accordingly and listed below:

Table 5-1: Integration of the matrix elements of the area domain

i	j	$\int_{A} \mathbb{N}_i \mathbb{N}_j d\widehat{A}$	i	j	$\int_{A} \mathbb{N}_i \mathbb{N}_j d\widehat{A}$
1	2	$\frac{-\widehat{\mathrm{A}}}{180}$	3	3	$\frac{\widehat{\mathrm{A}}}{30}$
1	3	$\frac{-\widehat{\mathrm{A}}}{180}$	3	4	$\frac{-\widehat{\mathrm{A}}}{45}$
1	4	0	3	5	0
1	5	$\frac{-\widehat{\mathrm{A}}}{45}$	3	6	0
1	6	0	4	4	$\frac{8\widehat{\mathrm{A}}}{45}$
2	2	$\frac{\widehat{\mathrm{A}}}{30}$	4	5	$\frac{4\widehat{\mathrm{A}}}{45}$
2	3	$\frac{-\widehat{\mathrm{A}}}{180}$	4	6	$\frac{4\widehat{\mathrm{A}}}{45}$
2	4	0	5	5	$\frac{8\widehat{\mathrm{A}}}{45}$
2	5	0	5	6	$\frac{4\widehat{\mathrm{A}}}{45}$
2	6	$\frac{-\widehat{\mathrm{A}}}{45}$	6	6	$\frac{8\widehat{\mathrm{A}}}{45}$

In order to have both the lumped, M_L, and consistent masses considered, a template matrix M_T with a scaling coefficient Γ equal to 0.5 was introduced, see equation (5.25) and reference (Colorado 2010). Therefore, the template mass matrix is obtained for each element within the mesh using the equation below:

$$M_T = \Gamma M_L + (1 - \Gamma) M_C \tag{5.25}$$

According to Felippa et al. (2015), where the details of this method are discussed, as beams depth increases, the consistent mass matrix causes an overestimation of frequencies and, on the contrary, a diagonally constructed mass matrix underestimates frequencies. Therefore, a linear combination of the two mass matrices with Γ equal to 0.5 has been chosen to overcome these problems.

The values in table 5-1 were used in equation (5.20) to determine the consistent mass matrix. Now that the mass matrix of a triangular element is defined according to equation (5.25), the micro inertia, which is described in section 5.2.3.2, needs to be incorporated into the mass matrix. In equation (4.8), the micro-inertia tensor, $\mathbf{J}_{ji}$ is considered as equal in all directions for simplicity. Therefore, in order to include micro-inertia into the formulation, it must be assembled into the elements of an overall mass matrix that are associated with the micro rotation accelerations. Thus, the micro-inertia matrix is incorporated into the overall mass matrix. Deriving the micro-inertia matrix is explained in further detail in section 5.2.3.2.

5.2.3.2 Micro-inertia matrix in the 2D field

As referred in section 2.4, there is no extensive work on how the micro-inertia might be obtained or on its influence on the coupling number. In this work, periodic voids or inclusions are introduced into the representative material which requires a method for obtaining an appropriate micro-inertia value for the beam models. In this section, the relation of the micro-inertia to the characteristic length of bending will be shown. The determination of micro-inertia in finite element applications is rather complex to visualise and understand as the FE elements do not undergo micro-rotation but the individual nodes presumably do. On the other hand, the nodes have no physically spatial dimensions and are defined as the point of masses and their mass are interpolated throughout the element. Therefore to quantify the micro-inertia the nodal mass must be multiplied by a value which represents the square of a length dimension and at the same time be independent of the dimensions of the triangular element.

In a pertinent work, de Borst et al. (1991) related the micro inertia density to the square of the characteristic length in bending by defining a microelement. In this work, a cubic micro-element, not to be confused with a conventional finite element, is considered and it is stated that the rotational inertia depends on the shape and size of the microelement. However, in the finite element method elements are defined by nodes which are considered as the points of mass. As said, the finite element models in this chapter incorporate the linear isotropic micropolar elasticity using triangular finite elements, but they do not represent individual microelements that rotates independently as seen in other models such as, for example, materials with granular particles where micro-inertia can be directly identified by the mass and radius of the constituent particles. In fact, in the finite element method, the micro-inertia is applied to the models but independently from the mesh density and size or the type of the finite element, e.g., FE triangular or brick elements. Therefore the micro-inertia density will be constant for each material with a specific characteristic length in bending.

If the micro-element dimensions, despite the shape of the element, approach zero, then the micro inertia becomes independent of the shape and dimensions of the micro-element and only depends on the characteristics length. Such a three-dimensional micro element is shown in figure 5-3.

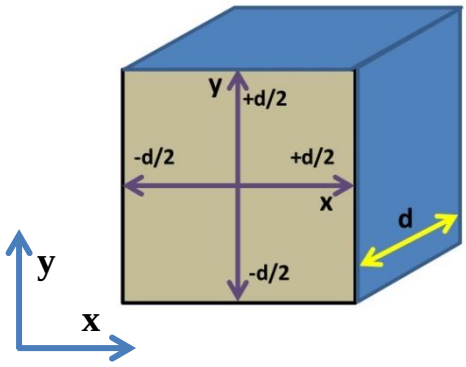

Figure 5-3: Representation of a cubic micro element

If we consider the rotation of a cubic micro-element of edge length equal to d, in a 2D x-y plane, as identified in figure 5-3, then the rotational inertia per unit volume, J, may be stated as:

$$J = \frac{\left(\int_A \rho(x^2 + y^2)\,(d)dxdy\right)}{(d)^3} \tag{5.26}$$

where d is the edge length of a cube element in which all edge lengths are equal. x and y are coordinates of any point in the x-y plane of the front face of the micro element which vary from $-d/2$ to $d/2$. Thus:

$$J = \frac{\rho d^2}{6} \tag{5.27}$$

The bending moment for a cubic micro-element can be stated as:

$$\boldsymbol{M}_{xz} = EI\boldsymbol{\kappa}_{xz} \tag{5.28}$$

where

$$I = \frac{1}{12}bh^3 = \frac{d^4}{12} \tag{5.29}$$

i.e.

$$\boldsymbol{M}_{xz} = \frac{1}{12}E_m d^4 \boldsymbol{\kappa}_{xz} \tag{5.30}$$

where $\boldsymbol{\kappa}_{xz}$ is the curvature of the cubic micro-element and can be represented by the derivative of the micro-rotation:

$$\boldsymbol{\kappa}_{xz} = \boldsymbol{\kappa}_{zx} = \frac{d\boldsymbol{\phi}_z}{dx} \tag{5.31}$$

The couple stress can be obtained by:

$$\boldsymbol{m}_{xz} = \frac{\boldsymbol{M}_{xz}}{A} = \frac{E_m d^2}{12}\frac{d\boldsymbol{\phi}_z}{dx} \tag{5.32}$$

From the micropolar theory which was described in chapter four and equation (4.11) to (4.16) in particular, the couple stress is:

$$\boldsymbol{m}_{xz} = \gamma^* \frac{d\boldsymbol{\phi}_z}{dx} \tag{5.33}$$

where

$$\gamma^* = 2G l_b^2 \tag{5.34}$$

Then since

$$\frac{E_m l_b^2}{1+\nu_m} = \frac{E_m d^2}{12} \tag{5.35}$$

It follows that

$$d^2 = \frac{12 l_b^2}{1+\nu_m} \tag{5.36}$$

By substituting the equation (5.36) into equation (5.27):

$$J = \frac{\rho d^2}{6} = \frac{\rho \frac{12 l_b^2}{1+\nu_m}}{6} \tag{5.37}$$

Thus:

$$J = \frac{2 l_b^2}{(1+\nu_m)}\ \rho \tag{5.38}$$

Note that in some literature γ^* in equation (5.34) is taken equal to $\frac{2E_m l_b^2}{1+\nu_m}$ and this will cause the micro-inertia to be doubled. It will be shown in the section 4.6 that the coupling number, N, will not be greatly affected by this.

The micro-inertia term in equation (5.38), if assumed to be independent of the direction it applies to, will thus be a parameter which is related to the square of the characteristic length of bending.

In section 5.5, a set of numerical trials have been performed to investigate the validity of the equation (5.38).

5.2.4 Solution to eigen problem

Having obtained stiffness and mass matrices for an element, assembly of global mass and stiffness matrixes can then be carried out by following standard finite element procedures. Finally, the eigenvalue equation below can be solved in the absence of external loads:

$$K_G - \omega^2 M_G = 0 \tag{5.39}$$

to obtain the natural frequencies. Here K_G and M_G are the global stiffness and overall mass matrices respectively.

By solving the eigenvalue problem, equation (5.39), ω^2 will be an array comprised of the diagonal elements of the resulting matrix. The square root of the array elements provides the frequency spectrum. Once the modal frequencies are obtained the normalised displacement components can be extracted, and the mode shapes obtained.

5.3 Algorithms used for modal analysis of micropolar beams

In this section the mathematical formulations which were defined in section 5.2 are used to develop algorithms which are used to develop MATLAB codes for the modal analysis and they can also be used in future to create codes in any programing language.

5.3.1 The 2D beam modelling process

Straight-sided and equal-sized triangular elements were used for modelling the micropolar beams. The numbering of elements begins from left to right side of the beam, counting both triangles on a line division as seen in figure 5-4 for example:

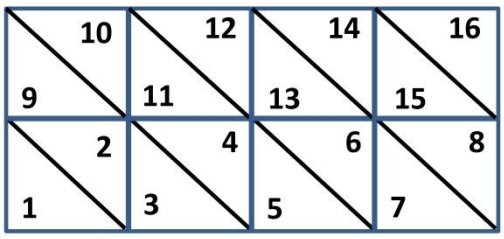

Figure 5-4: An example of element counts in a beam with four and two line divisions in length and depth to generate one sample beam with sixteen elements

The beam modelling procedure is conducted according to the following algorithm:

Step 1: Start [Start of algorithm];
Step 2: Enter the overall dimensions beam model: e.g., beam depth, width;
Step 3: Enter the number of layers (NCy), number of line divisions across the depth and length of the beam;
Step 4: Enter the beam's length to depth aspect ratio (AR);
Step 5: Create and save Element-Node adjacency table (ENA);
Step 6: Create and save the list of coordinates, nodal-coordinates (GNC), for all nodes in the beam in ascending order;
Step 7: Generate a 2D plot representing the actual beam dimensions for visual confirmation;
Step 8: Normalise the nodal coordinates by the maximum length and depth;
Step 9: Save the number of elements (nel);
Step 10: Save the number of nodes per element (nnel);
Step 11: Save nodal degree of freedom (ndof);
Step 12: Save the number of nodes (nnode);
Step 13: Calculate the element's degree of freedom edof=ndof*nnel;
Step 14: Save the element's degree of freedom sdof;
Step 15: Calculate the system's degree of freedom sdof= ndof*nnode;
Step 16: Save the system's degree of freedom sdof;
Step 17: Stop [End of algorithm];

The beam mesh comprised of 2 and 18 element divisions through the depth and along the length respectively for the smallest sample size. Overall dimensions of each model correspond to the beam sizes used in chapter three for finite element models. For example, the second smallest sample size, which is comprised of two layers of unit cells, has NCy=2. Therefore its micropolar counterpart will consist of 4 and 36 element divisions across the

depth and along length of the beam model. Figure 6-3 shows the mesh assembled from triangular elements by the CVFEM or MPFEM analysis. So, every unit cell which was created through detailed finite element modelling in chapter three, are represented by eight triangular elements.

5.3.2 Algorithm for constructing the element stiffness matrix

Here the mathematical model in section 5.2.2 is presented in the form of an algorithm through which the stiffness matrix, mainly 2D-MPFEM, can be constructed and used for modal analysis. This algorithm can be implemented for beam modelling. Note that the difference between CVFEM and MPFEM is only in the construction of the element's stiffness matrix. Therefore, if the CVFEM is intended instead of MPFEM, the already existing algorithm shall be used as briefly discussed in 2.4 and provided by Beveridge et al. (2013b). Thus, the general algorithm to derive the global stiffness matrix using the 2D-MPFEM is defined as follows:

Step 1: Start [Start of algorithm]

Step 2: Entre the engineering micropolar constants: $E_m, \nu_m, N, and\ l_b$

Step 3: Construct the matrix of the material properties, $\mathbb{D}$, (matrix of material properties), using the micropolar engineering constants as in equation (4.12), (4.15) and (4.16)

Step 4: Select the first element of the finite element model from section 5.3.1;

Step 5: Select the nodal coordinates of all six nodes in the triangular element in Cartesian coordinate system e.g., x_1, x_2, x_3, ... and y_1, y_2, y_3, ...;

Step 6: Calculate the nodal distances of the vertex nodes:

$x_{23} = (x_2 - x_3)$; $x_{31} = (x_3 - x_1)$; $x_{12} = (x_1 - x_2)$;

$y_{23} = (y_2 - y_2)$; $y_{31} = (y_3 - y_1)$; $y_{12} = (y_1 - y_2)$;

Step 7: Calculate the area of the triangular element:

$\hat{A} = (x_{31}y_{12} - x_{12}y_{31})/2$;

Step 8: Calculate the matrix of derivatives of the shape functions, equation (5.3) with respect to area coordinates, $\delta,\ \eta\ and\ \xi$. According to the equation (5.6)

Step 9: Calculate the Jacobian ($\hat{J}$) and the inverse of the Jacobian matrix using the derivatives of shape functions and the coordinates from step 5 as in equation (5.10) and (5.11); or:

For 2D analysis: $Jacobian = 1/2\hat{A}$ as in equation (5.12)

Step 10: Calculate the matrix of derivatives of the shape functions with respect to Cartesian coordinates ($dN_x \; and \; dN_y$) according to the equation (5.9)

Step 11: Construct the matrix B using the derivatives of shape functions[3] from step 10 to generate matrix B of size 6×18 as in equations (5.15), (5.16), and (5.17) using the following pseudo code:

```
B=sym (zeros (6, 18));
For n=1:6
   B (1, (3*n-2)) = dNx (n);
   B (2, (3*n-1)) = dNy (n);
   B (3, (3*n-2)) = dNy (n);
   B (3, (3*n))   = N (n);
   B (4, (3*n-1)) = dNx (n);
   B (4, (3*n))   = -N (n);
   B (5, (3*n))   = dNx (n);
   B (6, (3*n))   = dNy (n);
End
```

Step 12: Calculate the element stiffness matrix using equation (5.18) and the following pseudo code:

B1=substitute δ with 1- η - ξ in B matrix;

B2=$\mathbb{D}$*B1*(determinant of $\hat{J}$);

B3= multiply the inverse of B1by B2;

k=integrate from B3 with respect to ξ from 0 to 1- η;

k= integrate from k with respect to η from 0 to 1; Note: k will be a matrix of size 18×18

Step 13: Insert the element stiffness matrix into the global stiffness matrix, K_G;

Step 14: Continue the steps (2) to (13) for the subsequent element till the last element stiffness matrix is included into the global stiffness matrix;

Step 15: Stop [End of algorithm]

5.3.3 Algorithm for constructing element mass and micro-inertia matrices

The template mass matrix is a weighed combination of the lumped and consistent mass matrices as described in section 5.2.3. The mass matrix for the 6-node triangular element

[3] B (Row, Column)= The shape function or derivative of the shape function.

also incorporates the micro-inertia matrix. Thus, the general algorithm to derive the global mass matrix using the 2D-MPFEM is defined as follows:

Step 1: Start [Start of algorithm]

Step 2: Entre the material mass density, ρ;

Step 3: Select the first element of the finite element model;

Step 4: Define the nodal coordinates of all six nodes in the triangular element in Cartesian coordinate system e.g., x_1, x_2, x_3, ... and y_1, y_2, y_3, ...;

Step 5: Calculate the nodal distances of the vertex nodes:

$x_{23} = (x_2 - x_3)$; $x_{31} = (x_3 - x_1)$; $x_{12} = (x_1 - x_2)$;

$y_{23} = (y_2 - y_2)$; $y_{31} = (y_3 - y_1)$; $y_{12} = (y_1 - y_2)$;

Step 6: Calculate the area of the triangular element:

$A = (x_{31}y_{12} - x_{12}y_{31})/2$

Step 7: Calculate the volume of the triangular element;

Step 8: Create an (18×18) identity matrix;

Step 9: Multiply the element volume by its mass density and divide the product by 6;

Step 10: Multiply the product of step (9) to the identity matrix from step (8) to generate lumped mass matrix;

Step 11: Generate an (18×18) matrix using equation (5.21) and the values in table 4-1;

Step 12: Multiply the element volume by mass density and the matrix from step (11) to generate the consistent mass matrix;

Step 13: Having the lumped and consistent mass matrices obtained from steps (10) and (12), generate the template mass matrix using equation (5.25);

Step 14: Calculate the micro-rotation $J/\rho = \frac{2l_b^2}{(1+\nu_m)}$ from equation (5.38); and inject into the rows and columns and rows in the matrix generated from step (13) which represent the micro-rotations.

Step 15: Insert the element mass matrix into the global mass matrix, M_G;

Step 16: Select the next element;

Step 17: Continue the steps (4) to (16) for the subsequent element till the last element stiffness matrix is included into the global stiffness matrix;

Step 18: Stop [End of algorithm]

5.3.4 Solution process to eigenvalue problem

The solution process begins with defining the system matrices which are zero matrices for reserving memory spaces for stiffness, mass and forces based on the total number degrees of freedom of all nodes comprising the beam geometry. The next step in the process is to generate element stiffness, mass and micro-inertia matrices. The micro-inertia matrix will be merged into the element mass matrix. The element stiffness matrix is calculated based on the selection made between CVFEM and MPFEM by the operator. The matrices are then globalised and assembled into the system matrices. The process continues in a loop for all elements. The boundary conditions take effect in the global matrices by setting the selected rows and columns to zero as appropriate. Finally, the eigen problem is solved according to equation (5.39). Following the solution of the eigen problem, the list of eigen values, ω^2 , and the matrix of eigen vectors are saved for post-processing.

The algorithm of the solution stage is as follows:

Step 1: Start [Start of algorithm]

Step 2: Call M_G, (the global mass matrix including micro-inertia matrix);

Step 3: Call K_G, (the global stiffness matrix);

Step 4: Solve the eigen problem by applying equation (5.39) using the pseudo code:
[Eigen vectors, Eigen values]=eig (K_G, M_G);

Step 5: Save eigenvectors;

Step 6: Save eigenvalues;

Step 7: Stop [End of algorithm]

5.3.5 Post-processing of data for extracting the modal frequencies and mode shapes

The frequency values are obtained by taking the square root of the eigen values and multiplied by 2π then arranged in ascending order. The normalised displacement of each node in the system in x and y directions is defined by identifying row and column number in the matrix of eigen vectors for that specific frequency and, after arranging them in ascending order, saving the values as vectors for x and y displacements for each node. The eigen vector values contain normalised values which could be zero, positive or negative. These eigen vector values are then added to the normalised GNC coordinates which result in mode shape coordinates.

The algorithm of the post-processing stage is as follows:

Step 1: Start [Start of algorithm]

Step 2: Take the square root of the eigenvalues;

Step 3: Multiply the eigenvalues by 2π to obtain ω values;

Step 4: Arranged the in ascending order;

Step 5: Extract corresponding row and column associated with each frequency from the matrix of eigenvectors;

Step 6: Add the eigenvector to the normalised nodal coordinates obtained from Step (8) section 5.3.1;

Step 7: Generate a 2D plot representing the mode shape for any of the specified modal frequency in step (5);

Step 8: Stop [End of algorithm]

Note that the use of these algorithms will result in generating the full frequency spectrum including both flexural and longitudinal modes. Therefore, to identify the flexural frequencies, every individual frequency and its corresponding mode shape must be visually investigated for categorisation of the modal frequencies.

5.4 A parameter identification algorithm for obtaining the coupling number "N" using CVFEM

Before embarking on the investigation into the effect of micro-inertia on the coupling number, which will be discussed in section 5.5, a numerical method must be introduced to obtain the coupling number.

N will be estimated through linear regression implemented in an iteration method. This method was used by Beveridge et al (2013a) for the static three point bending problem. The linear regression is a fairly standard method and is used for curve fitting. Therefore an algorithm for identification of the coupling number, N, is used. For this purpose, the values of characteristic length of bending which were previously estimated for beam models in table 4-3 will be used and then the iteration process will only be carried out to identify the coupling number for beams with specified volume fractions.

The first two transverse modes are used in the process to iterate for coupling number, N, which, as a constitutive property, should satisfy all modal frequencies and all model depths. Therefore, the mass of each beam specimen is calculated, the higher flexural frequencies (modes 1 and 2) which were previously obtained through finite element analysis in chapter three will be selected and the values for $m.\omega^2$ against d^{-2} will be derived. As seen already the $m.\omega^2$ values are on the same lines when plotted against d^{-2}. Therefore, this line will be

set as the reference and the linear regression attempts to fit the $m.\omega^2$ values using the numerical control volume finite element method (CVFEM) to those obtained from detailed FEA as best as possible. 2D-MPFEM can alternatively be used to derive $m.\omega^2$. The parameter identification algorithm is therefore linked to the algorithms described in section 5.3 through the use of CVFEM or MPFEM methods to obtain $m.\omega^2$ for micropolar beams. A value is specified for N as the initial guess which must be near but not equal to one such as N=0.95. A set of $m.\omega^2$ are calculated for all required beam models (beam depth: NCy=2, 3 and 4) and then the mean square value is calculated using the sequence of equation (5.40) to (5.46):

$$Y_{FEA} = (m.\omega^2)_{FEA} \tag{5.40}$$

$$Y_{CVFEM} = (m.\omega^2)_{CVFEM} \tag{5.41}$$

$$Y_{Mean} = \frac{1}{length(Y_{FEA})} * \sum (Y_{FEA})\,; \tag{5.42}$$

$$Error = (Y_{FEA} - Y_{CVFEM})^2 \tag{5.43}$$

$$Total = (Y_{FEA} - Y_{Mean})^2 \tag{5.44}$$

The coefficient R_i which is used to check the necessity of repeating the iteration loop is:

$$R_i = \frac{\sum Total - \sum Error}{\sum Total} \tag{5.45}$$

If $R_{n+1} > R_n$, then the iteration stops, otherwise it repeats. At each iteration point, the value of the coupling number is updated as follows:

$$N_{n+1} = \left\{\left(\frac{1}{length(Y_{FEA})}\right)\sum \frac{Y_{FEA}}{Y_{CVFEM}}\right\} \times N_n \tag{5.46}$$

So the parameter identification algorithm attempts to find the best fit for the coupling number, N, by taking average values for beams with depths of two, three and four unit cells by iteration. Beams with one array of unit-cells were not considered for the reason of deviation from linearity seen with the beams of larger depths and shown in figure 3-6 and 3-8.

The above method is time consuming because the CVFEM is numerical and the above method uses iteration over the CVFEM outcome results. Therefore the mesh density used for meshing the beams in the process of parameter identification must be as low as reasonably possible. Three divisions in depth of the beam were found to satisfy the requirement of mesh density in this case.

The parameter identification algorithm is as follows:

Step 1: Start [Start of algorithm]

Step 2: Entre the first and second flexural frequencies from FEA for the three largest samples with equal v_f;

Step 3: Construct matrix of modal frequencies against beam sizes d^{-2};

Step 4: Construct matrix square of frequencies ω^2 from step (3)

Step 5: Specify l_b corresponding to the v_f in step (2);

Step 6: Calculate the mass of each beam sample;

Step 7: Construct matrix of $m.\omega^2$ against beam sizes d^{-2} for FEA models;

Step 8: Save $m.\omega^2$ values as Y_{FEA} , (equation 5.40);

Step 9: Calculate mean value, Y_{Mean}, equation (5.42);

Step 10: Entre the initial guessed value for N, equal to 0.95;

Step 11: Go to algorithm for CVFEM or MPFEM described in section 5.3 to generate ω^2 for three largest beam depths;

Step 12: Construct matrix of $m.\omega^2$ against beam sizes d^{-2} for CVFEM/ MPFEM models;

Step 13: Save $m.\omega^2$ values as Y_{CVFEM} , equation (5.41);

Step 14: Calculate error, equation (5.43);

Step 15: Calculate Total, equation (5.44);

Step 16: Calculate the coefficient R_i, equation (5.45);

Step 17: Stop if $R_{n+1} > R_n$, then the iteration stops, Go to Step (19);

Step 18: Estimate new N, equation (5.46); Go to Step (11);

Step 19: Report N;

Step 20: Stop [End of algorithm]

Now that the parameter identification algorithm has been defined, the effect of changing the micro-inertia value on the coupling number, N, and the validity of the equation (5.38) can be studied and is discussed in detail in section 5.5.

5.5 The effect of micro-inertia on the coupling number "N"

As described in chapter four, in order to perform a two-dimensional modal analysis using the micropolar theory, the material micropolar engineering elastic constants were identified except the coupling number N which is to be determined in chapter six but first the influencing parameters must also be investigated. In two-dimensional beam vibrations, the characteristic length of bending is not the only parameter which influences the coupling number. The other important influencing parameter is the micro inertia. Therefore, in this section the effect of micro-inertia on the coupling number will be investigated. The appropriate coupling numbers for the beam models will subsequently be obtained in chapter six.

5.5.1 Validation of the analytically determined micro-inertia

For the validation of the equation (5.38), the value of the micro inertia was varied from a small fraction of l_b^2 to a much higher bound as follows:

$$C_{i(Lower\ bound)}\frac{l_b^2}{(1+\nu_m)} \leq J/\rho \leq C_{i(Upper\ bound)}\frac{l_b^2}{(1+\nu_m)} \tag{5.47}$$

The multiplying coefficient, C_i , varied from a lower bound $\frac{1}{96}$ to an upper bound 52 by doubling the value of C_i each time and evaluating the coupling number using the MPFEM procedure for different volume fractions of voids, three unit cells in depth and continuous boundaries. In figure 5-5 the value of N is drawn against J/ρ while in figure 5-6 the value of N is drawn against an arbitrary coefficient C_i. The values for coupling number with C_i being equal to 2 are identified by a dotted rectangle in both graphs for which the equation (5.38) has been used to derive micro-inertia and consequently to identify the coupling

number, N. It can be readily seen that if $C_i < 2$, then the coupling number become much less dependent on micro-inertia or the characteristic length and tends to remain constant. On the other hand for $C_i > 4$, the value of the coupling number is highly affected by and sensitive to the micro-inertia and becomes unstable. Therefore, the derived micro-inertia appears to be a threshold above which the coupling number will be affected largely by the volume fraction. However, in the next section, two values of micro-inertia from the higher bound region are chosen, the related coupling numbers are obtained for two beam types with various volume fractions, see table 5-2, and the effect of using higher values of micro-inertia and on modal frequencies are discussed.

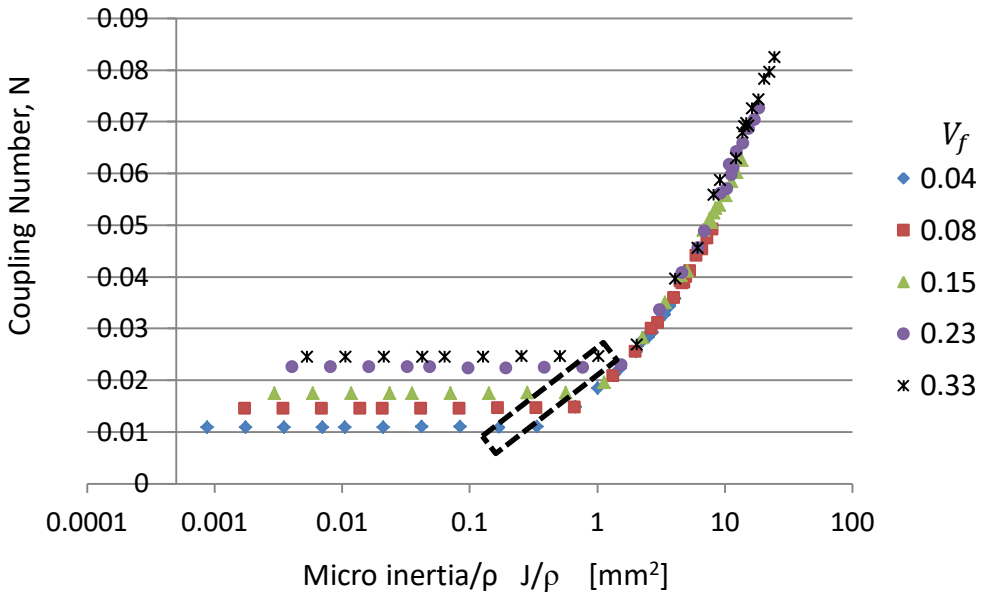

Figure 5-5: The value of the coupling number, N, for different values of J/ρ and volume fractions. The beam has three unit cells in depth and continuous boundaries.
($V_f = 0.04\ to\ 0.33\ \ corresponds\ to\ l_c = 0.332\ to\ 0.817\ mm$)

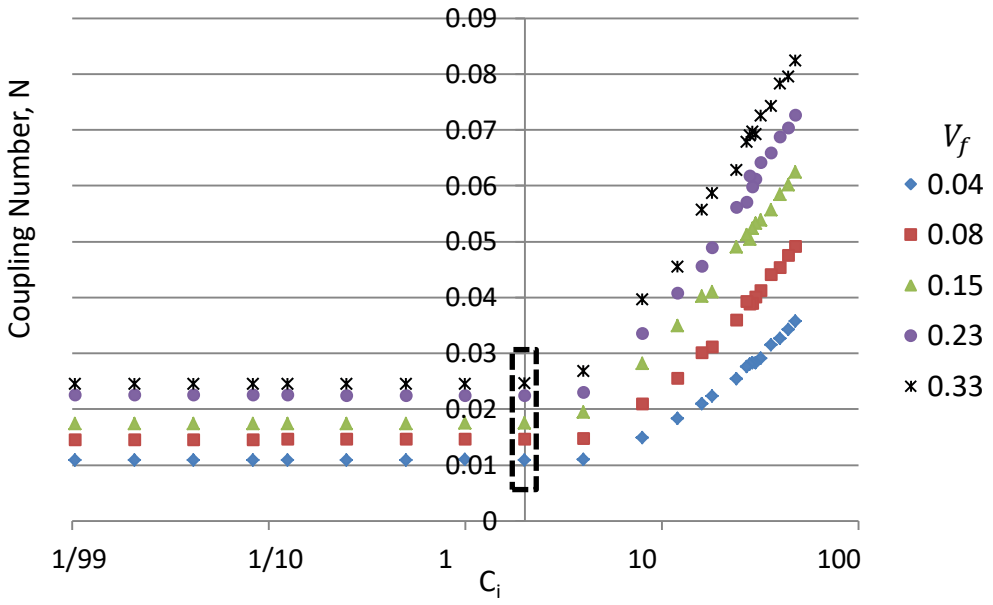

Figure 5-6: The value of the coupling number, N, for different values of an arbitrary coefficient C_i and volume fractions. The beam has three unit cells in depth and continuous boundaries. ($V_f = 0.04\ to\ 0.33\ \ corresponds\ to\ l_c = 0.332\ to\ 0.817\ mm$)

5.5.2 The effect of increased micro inertia on the coupling number

In this section the effect of increasing the micro-inertia on coupling number and therefore the transverse modal frequencies is investigated. This, in fact, validated the analytical method which was used to define the micro-inertia in the MPFEM and the CVFEM algorithms and shows that increasing the micro-inertia beyond the values of the equation (5.38) will not improve the accuracy of the results. To do this, beams with continuous boundaries with voids or inclusions with three layers depth (NCy=3) were considered and the coefficient C_i equal to 36 and 44 have been tried using both MPFEM and CVFEM stiffness matrices in the parameter identification algorithm. So, a set of values for coupling number at different volume fractions were obtained to study how increasing the micro inertia, by increasing the value of C_i, will affect the coupling number and if these positively affect the modal frequency results. Thus, the values of coupling number corresponding to different volume fractions are obtained and listed in table 5-2 which indicate that the choice between MPFEM and CVFEM does not matter too much as the resulting coupling numbers are very close but the obtained coupling numbers become very sensitive to the volume fraction.

Table 5-2: Coupling number, N, if micro inertia increased by 36 and 44 times for a beams with continuous boundaries (Averaged over the three largest sample models) Sample size (NCy=3)

		C_i \ V_f	**0.04**	**0.08**	**0.15**	**0.23**	**0.33**
Beams with voids and continuous boundaries	l_c , mm	-	0.332	0.464	0.608	0.709	0.817
	2D CVFEM	36	0.031	0.044	0.057	0.067	0.073
	2D MPFEM		0.032	0.044	0.056	0.066	0.074
	2D CVFEM	44	0.034	0.047	0.062	0.070	0.079
	2D MPFEM		0.034	0.048	0.060	0.070	0.080
Beams with inclusions and continuous boundaries	l_c , mm	-	0.254	0.377	0.496	0.601	0.684
	2D CVFEM	36	0.024	0.036	0.046	0.057	0.065
	2D MPFEM		0.024	0.035	0.047	0.055	0.063
	2D CVFEM	44	0.028	0.039	0.051	0.061	0.067
	2D MPFEM		0.026	0.039	0.051	0.061	0.068

Furthermore, to investigate how the changes in micro inertia affects the transverse modal frequencies, again a sample model of three unite cells in depth (NCy=3) was investigated with respect to the influence of the higher values of the micro-inertia equal to C_i=36 and the five transverse modal frequencies were extracted for beams with voids using both CVFEM and MPFEM. The primary analysis showed clearly that increasing the micro-inertia by altering the coefficient, C_i, has more influence on the primary mode rather than on the higher transverse modal frequencies. This suggests that, increasing the micro-inertia would only significantly affect the primary mode and provides results for the primary mode which approximately matched the values that were obtained by detailed FEA but the rest of the modal frequencies are less affected. Figure 5-7 show the micropolar CVFEM results (Primary normalised modal frequency) for a specimen with C_i equal to 36 which clearly shows the development of nonlinearity in anticipating the size effect and the coupling numbers become more sensitive to volume fraction as the values in table 5-2 confirm. The higher modes showed that increasing the C_i has less influence on the results with regard to anticipation of the size effect. Figure 5-7 also indicates that increasing the micro-inertia via increasing the C_i causes nonlinearity in normalised primary frequency changes with the inverse of beam depth squared.

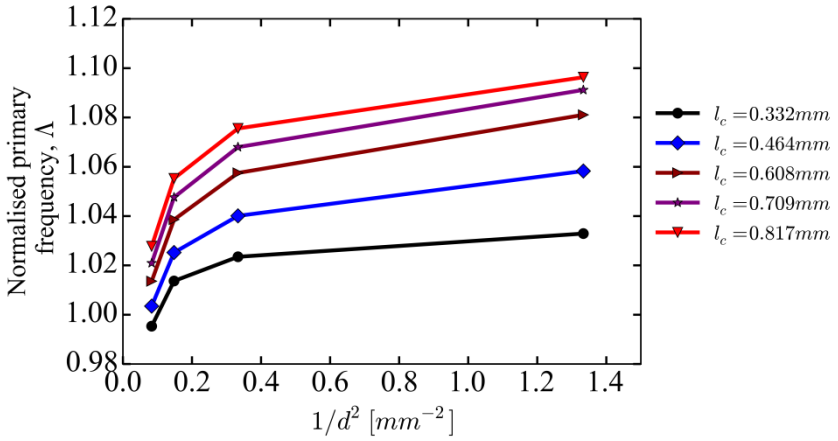

Figure 5-7: Normalised primary frequency changes with the inverse beams depth squared for beams with voids and continuous boundaries and various volume fractions using CVFEM when $C_i = 36$ ($l_c = 0.332\ to\ 0.817\ mm\ corresponds\ to\ V_f = 0.04\ to\ 0.33$)

Using the 2D MPFEM also resulted in the same dynamic behaviour with increasing the micro-inertia by changing C_i to 36 which indicated that 2D-MPFEM produced results similar to the CVFEM method and that increasing the micro inertia mainly affects the modal frequencies at mode one. Therefore the value of C_i is equal to 2 and the equation (5.38) is valid and, therefore, incorporated into the algorithms. Note that for this additional reason only the first two modal frequencies were used for iteration process to obtain the coupling number using the parameter identification algorithm.

5.6 Summary and conclusions

This chapter resulted in development of algorithms which incorporate the micropolar theory into a numerical method for dynamic analysis. However, in order to obtain the coupling number, N, a parameter identification algorithm has also been developed and described. In two dimensional beam vibrations, the characteristic length of bending is not the only parameter which influences the coupling number. The other important influencing parameter is the micro inertia. Therefore, in this chapter, a procedure for obtaining mass and micro-inertia matrices and the coupling number, N, were introduced and the effect of micro-inertia on the coupling number was investigated.

The general conclusion is that the micro-inertia is very much related to the parameter of characteristics length of bending, l_b, mass density, ρ, and the Poisson ratio, ν_m. As the mass density and Poisson ratio are considered constant, therefore, the only influencing parameter is the characteristic length of bending.

Now that the aditional micropolar constant, the characteristic length of bending and the micro inertia are detemined, and that the algorithm for parameter identification has been developed for obtaining the second additional micropolar constant namely coupling number, N, it is now possible to generate modal frequencies using either the CVFEM or MPFEM procedures and compare the results with those from detailed FE analysis from chapter three. Therefore, in chapter six, first the coupling number for some of the beam models will be obtaind using the parameter identification algorithm which incorporates micro-inertia as described in this chapter then three types of beam models, for which micropolar constants are available, will be modeled and modal frequencies will be obtained using both the CVFEM and 2D-MPFEM and the size effects will be compared with the detailed finite element results which were previously obtained in chapter three.

6 Two-dimensional CVFEM and MPFEM Results, Comparison with FEA Results, and Validation

Recalling from chapter three, FEA was used for creating geometrically detailed beam models of a representative heterogeneous material, which are considered to exhibit realistic beam vibration modes, generating corresponding modal frequencies that can be used as the basis for comparison with suitable theory. Therefore, in this chapter, two-dimensional beam models are created using the CVFEM and MPFEM methods presented in the previous chapter to generate modal frequencies. The results will then be compared with the aforementioned FEA results.

Note that for 2D beams modal analysis incorporating the micropolar elasticity, not only the characteristic length of bending is needed, but the coupling number value is also required for running the analysis. Therefore, in section 6.1, the coupling number will be identified for some of the beam models.

6.1 Identification of the coupling number, N, for the representative material

Previously in chapter four, an analytical method was introduced for obtaining the characteristic length in bending from the size dependency of the first natural frequency. Then in chapter five a parameter identification algorithm was developed which enables the coupling number to be identified by an iterative approach based upon matching multiple flexural frequency forecasts provided by the FEA results. In this section, the additional micropolar constant, coupling number, will be identified for the representative materials.

6.1.1 Estimation of N for beams with continuous boundaries (BVOCB and BINCB)

Using the CVFEM, and the parameter identification procedure which uses the linear regression as described in section 5.4, unique values for N were identified. In figures 6-1-a and 6-1-b, the FEA results and the results predicted for mode one and two by the CVFEM through the parameter identification procedure are compared after convergence of the iteration process with $m\omega^2$ being obtained within the range of N from 0 to 0.9. The first value represents the lower bound on N and corresponds to the classical case while the second value is an approximation to the upper bound on N of 1 corresponding to the constrained micropolar or so called couple stress elasticity case. Note that setting the upper bound for N

at 1 would give rise to numerical error. In figures 6-1-a and 6-1-b, the linear regression method was applied to the first and second modal frequencies (obtained from ANSYS finite element analysis) for all beam sizes and a void or inclusion volume fraction of 0.23.

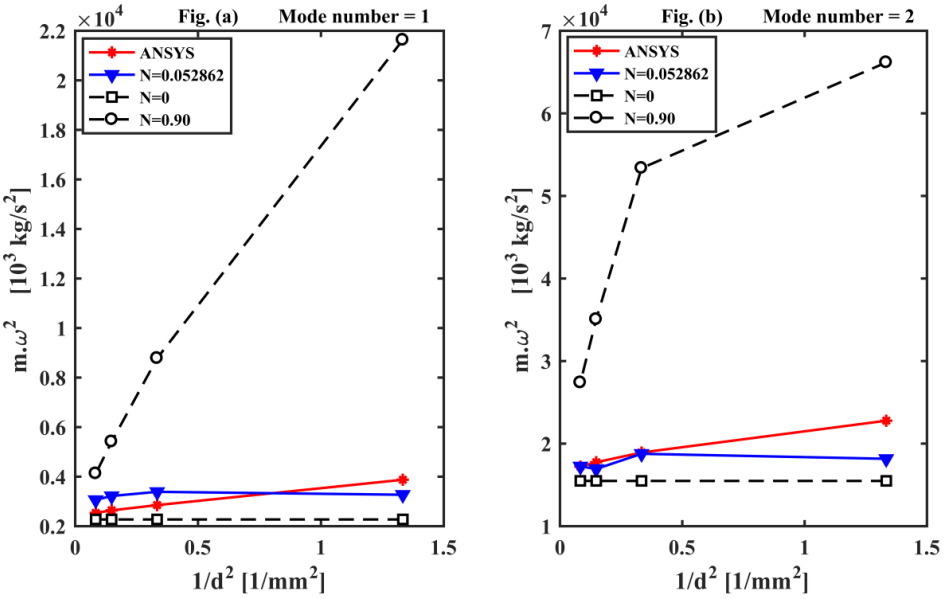

Figure 6-1: The variation of $m\omega^2$ with beam size for beams with voids and continuous surface and volume fraction equal to 0.23; a) The variation of $m\omega^2$ at flexural mode 1 (on the left); b) The variation of $m\omega^2$ at flexural mode 2 (on the right).

In theory, the more mode numbers used within the iterative identification, the more accurate the coupling number estimate should be, but as the frequency spectrum which is identified by the CVFEM also includes longitudinal modes above mode 2, only the first two modal frequencies were used in the iteration process. The second reason is that micropolar flexural frequencies approach the homogenised case frequencies after mode 3 or 4.

The values of N identified in this way are given in table 6-1 for both beams with voids and compliant inclusions. The iteration process was similarly performed for all other inclusion volume fractions from 4% to 33%. This revealed that N changes only slightly with volume fraction. Waseem et al. (2013) have reported that the value of coupling number in perforated ring samples decreasing slightly as the void radius is increased but, here, for perforated beam models as can be seen in table 6-1, the value of coupling number, N, increases slightly with changes in volume fraction.

The regression method was not useful for beams with continuous boundaries but compliant matrix and therefore the coupling numbers are not available for such beam types. This is due

to the fact that the value of $m\omega^2$ fall either below or above the values of $m\omega^2$ obtained with coupling numbers 0 and 1 and thus their behaviour is apparently not anticipated by micropolar theory.

6.1.2 Estimation of N for beams with compliant matrix and textured boundaries (BINTB)

When the boundary of the beam is intercepted by voids or inclusions, the coupling number could also not be identified by the iterative method because the values of $m\omega^2$ obtained from the finite element analysis exhibit a size effect that is not anticipated by the micropolar theory. While the size effect in beams with compliant matrix and continuous surfaces contradicts the micropolar theory, when the boundaries are textured by intersection with the stiffer inclusions the size effect is as expected. Thus for this type of beam, a value for the coupling number can also be identified by the linear regression based iterative procedure.

Table 6-1 shows the coupling numbers estimated using CVFEM for various beam types and C_i equal to 2:

Table 6-1: Coupling numbers obtained for various beam types by taking $J = \frac{2l_b^2}{(1+\nu_m)}\rho$

V_f	**0.04**	**0.08**	**0.15**	**0.23**	**0.33**
BVOCB	0.042	0.047	0.051	0.053	0.055
BINCB	0.043	0.046	0.048	0.051	0.053
BCMTB	0.0459	0.0460	0.0451	0.0452	0.0477

The values in table 6-1 above are obtained by using the three largest sample sizes with the CVFEM to match the first two modes and averaging them (With C_i=2, as identified in chapter five). Therefore the coupling number values based on the CVFEM were also selected for 3D-MPFEM modal analysis in chapters eight and nine. Note that values in table 6-1 are smaller than those that other researchers usually assume for example in the work by Beveridge et al.(2013a), the value that has been identified for coupling number through static 3 point bending is equal to 0.12. The coupling number values obtained are towards the lower bound of the anticipated range and thus show some agreement with those obtained previously for similar materials when undergoing static deformation (Frame 2013a). However, later in chapter eight, in three dimensional modal analysis of plates it will be shown that the major influencing parameter in modal frequencies is the characteristic length

rather than the coupling number and that increasing the coupling number affectes the primary modal frequency more significantly than the higher modes.

6.2 Modelling 2D homogeneous beams with MPFEM and CVFEM

Before using the constitutive parameters identified in section 6.1 to predict the full frequency spectrum of the representative heterogeneous materials in this section, both the MPFEM and CVFEM methods were first used to model 2D homogeneous beams. Thus four beam sizes were modelled and all with the aspect ratio of 10.4 similar to the overall beam dimensions as the FEA models with one, two, three and four unit-cells in depth as described in section 3.2.

6.2.1 Applying the free-free boundary conditions in micropolar beam models

In beams with free-free boundary conditions (FF), both changes in the moment and shear forces at each end of the beam are equal to zero; and in finite element analysis, it can be achieved by not constraining any of the nodes at each side of the beam and allowing them to move freely. Such condition is not completely achievable practically but using the finite element method, it is feasible and the CVFEM and MPFEM results for the full frequency spectrum can be generated and compared with the finite element results which supposedly represent realistic dynamic behaviour.

6.2.2 Modelling beams and mesh convergence study of micropolar beam models

By dividing the micropolar beam depth and length into subsections, it was possible to run a modal analysis for various DOF's and investigate the mesh convergence of a meshed micropolar beam. The graph in figure 6-2 below shows that the smallest beam (NCy=1) with 225 degrees of freedom converges with an error below 0.2 percent while the smallest sample model, which is modelled for modal analysis micropolar beams in this chapter, has 555 degrees of freedom with the height of 2 and length of 18 divisions which satisfies the requirement of mesh convergence. This convergence study was conducted for the homogeneous case. In fact the unit-cells employed by FEA are here represented by a 2 by 2 divisions which include eight 6-node triangular elements, see figure 6-3.

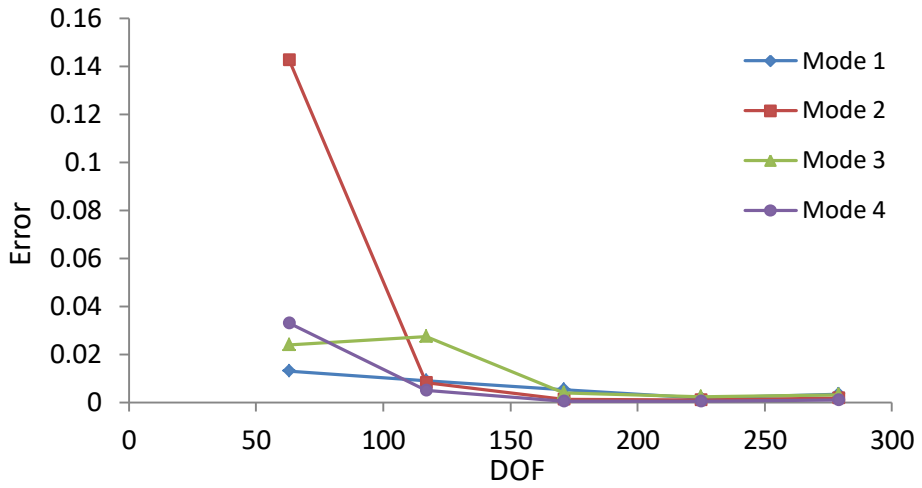

Figure 6-2: Mesh convergence for a homogeneous beam (NCy=1) using the CVFEM (α^*,β^*, γ^* *and* κ^* *are equal to zero*)

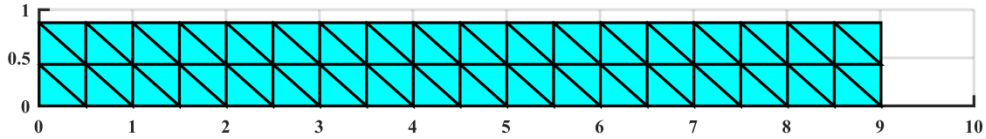

Figure 6-3: Micropolar beam model, NCy=1

6.2.3 Non-dimensional transverse frequencies for homogeneous micropolar beam with N and the characteristic length of bending to zero

In order to solve the micropolar beam for a homogeneous case, the parameters α^*,β^*, $\gamma^*$and κ^* are set to zero. Therefore, the coupling number and the characteristic length of bending must also be taken equal zero. The results for a homogeneous beam model are used to first of all check the validity of the CVFEM and MPFEM methods and then to use these values for normalisation of the transverse modal frequency values of the results for the heterogeneous beam models presented later in sections 6.3.2.1 to 6.3.2.3.

The FEA modal frequencies for homogeneous cases were already compared with the Classical, Timoshenko and non-local Timoshenko beams in chapter three. Here, in table 6-2 the relative difference of the CVFEM and MPFEM results are given in comparison with the FEA and Timoshenko beam results for the homogeneous cases listed in chapter three table 3-7.

While the dimensionless frequency parameters for the homogeneous beams with aspect ratio of 10.4:1, which are listed in table 6-2, are used to normalise the transverse modal

frequencies of the micropolar beams in the next sections, the longitudinal frequencies presented in section 6.3.1 are normalised by the frequency of the longitudinal modes of the homogeneous beam models.

As can be observed in table 6-2 the relative difference between values for the primary modal frequency irrespective of the solution method is well below 0.1% although this difference increases slightly with mode number. However, even for the 10 modal frequencies the difference value still remains below 0.5% for the homogeneous beams. This therefore validates the performance of the code for the implementation of the CVFEM and 2D MPFEM algorithms.

Table 6-2: Dimensionless frequency parameters generated for a homogeneous beam model using CVFEM and MPFEM (Based on beams with NCy=4) and the relative differences (absolute values) with FEA and Timoshenko values given in chapter three table 3-7

Mode number	Transverse Modes		Relative diff. of CVFEM with FEA	Relative diff. of CVFEM with Timoshenko	Relative diff. of MPFEM with FEA	Relative diff. of MPFEM with Timoshenko
	Non-dimensional Frequency, λ					
	CVFEM	MPFEM				
1	4.649946	4.654824	1.18E-03	6.65E-04	1.36E-04	3.83E-04
2	7.531761	7.525683	6.22E-04	2.02E-03	1.85E-04	1.21E-03
3	10.20287	10.19205	8.63E-04	3.09E-03	1.98E-04	2.03E-03
4	12.64783	12.62462	1.66E-03	4.56E-03	1.80E-04	2.71E-03
5	14.85686	14.84335	7.74E-04	4.14E-03	1.36E-04	3.22E-03
6	16.90657	16.87354	1.89E-03	5.56E-03	6.42E-05	3.60E-03
7	18.79062	18.74023	2.72E-03	6.59E-03	3.23E-05	3.89E-03
8	20.51416	20.4649	2.56E-03	6.55E-03	1.56E-04	4.13E-03
9	22.12443	22.06447	3.03E-03	7.09E-03	3.14E-04	4.36E-03
10	23.42212	23.55009	4.93E-03	8.41E-04	5.06E-04	4.62E-03

6.2.4 Extracting the transverse and longitudinal mode shapes using CVFEM and MPFEM

The transverse mode shapes below the critical frequency, are easily recognizable by the lobe (wave) counts on the beams surface so that a full wave length in mode two, generates two lobes, one positive and one negative (or one up and one down). In order to create the mode shapes in 2D MPFEM or CVFEM, the eigen vectors are normalised by the corresponding maximum eigen vector value then each normalised value is added to the normalised coordinated of the same node. This method will result in generating mode shapes for further analysis. However, it must be noted that while the eigen vectors are useful for generating

mode shapes they do not provide any information regarding the actual displacement of the nodal points.

Increasing the mode number is associated with an increase in frequency and the number of lobes is increased and the wave length decreases. When the length of the wave approaches the beams depth, then it is hard to distinguish the modal frequencies in the 2D plane and that is when the transverse modal frequency is approaching the critical frequency. Another point to note is that after mode numbers three or four, the CVFEM and/or MPFEM results do not show any size effect and, therefore, micropolar theory would not apply. The first fourteen mode shapes predicted by MPFEM (CVFEM) are shown in figures 6-4 to 6-17 which include ten transverse and 4 longitudinal mode shapes of a homogeneous beam with depth equal to two unit cells.

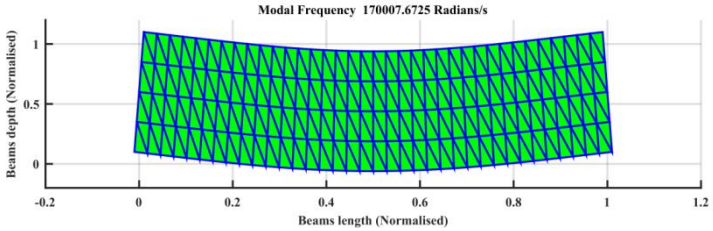

Figure 6-4: Mode shape of beam with $d = 1.732\ mm$, Mode 1, Transverse 1

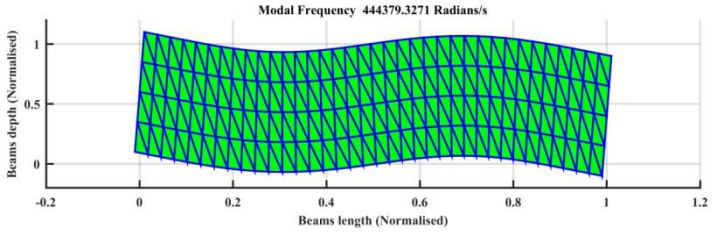

Figure 6-5: Mode shape of beam with $d = 1.732\ mm$, Mode 2, Transverse 2

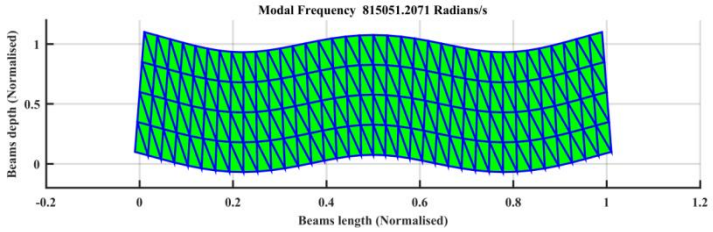

Figure 6-6: Mode shape of beam with $d = 1.732\ mm$, Mode 3, Transverse 3

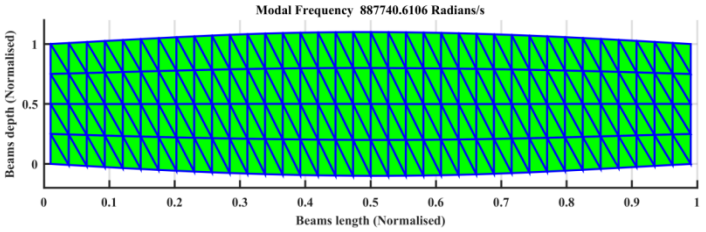

Figure 6-7: Mode shape of beam with $d = 1.732\ mm$, Mode 4, Longitudinal 1

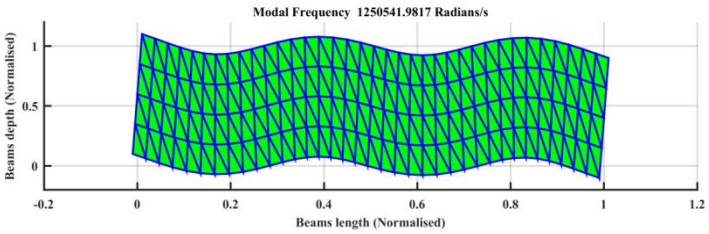

Figure 6-8: Mode shape of beam with $d = 1.732\ mm$, Mode 5, Transverse 4

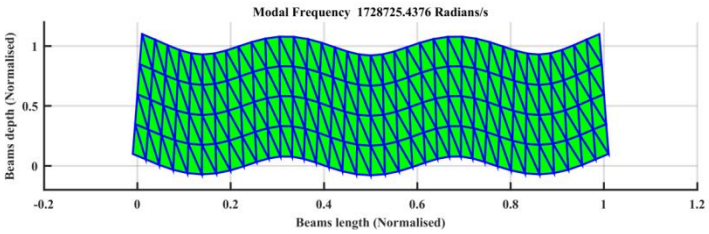

Figure 6-9: Mode shape of beam with $d = 1.732\ mm$, Mode 6, Transverse 5

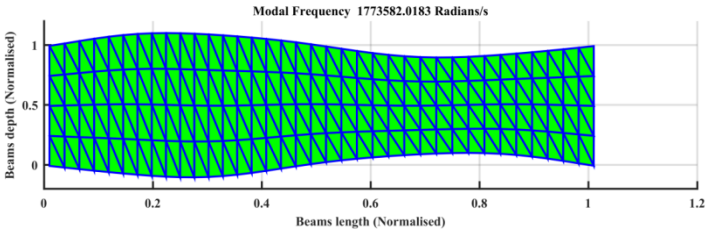

Figure 6-10: Mode shape of beam with $d = 1.732\ mm$, Mode 7, Longitudinal 2

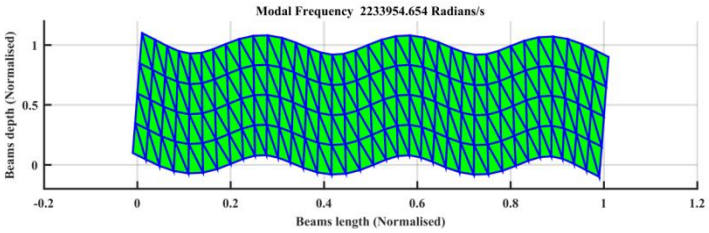

Figure 6-11: Mode shape of beam with $d = 1.732\ mm$, Mode 8, Transverse 6

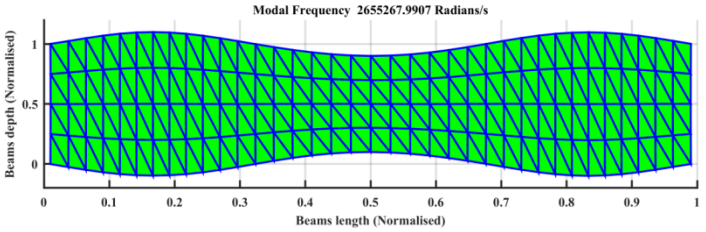

Figure 6-12: Mode shape of beam with $d = 1.732\ mm$, Mode 9, Longitudinal 3

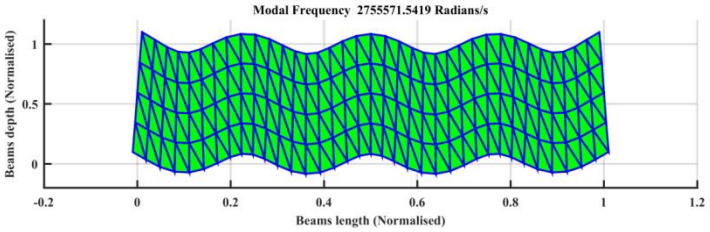

Figure 6-13: Mode shape of beam with $d = 1.732\ mm$, Mode 10, Transverse 7

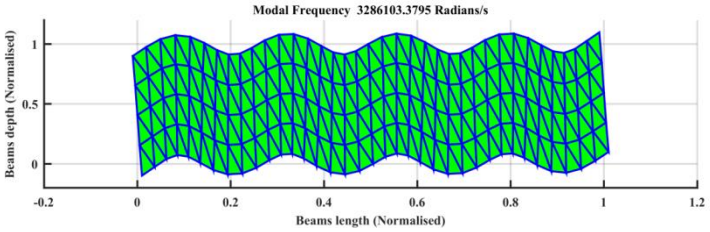

Figure 6-14: Mode shape of beam with $d = 1.732\ mm$, Mode 11, Transverse 8

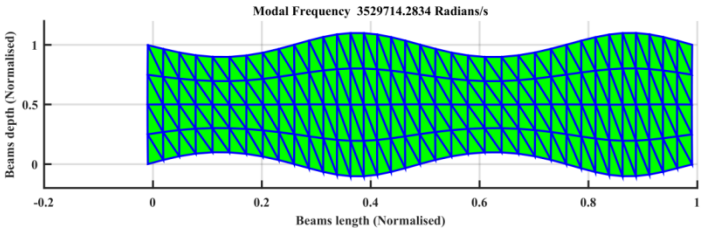

Figure 6-15: Mode shape of beam with $d = 1.732\ mm$, Mode 12, Longitudinal 4

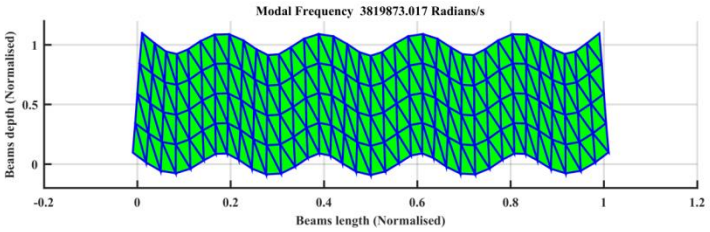

Figure 6-16: Mode shape of beam with $d = 1.732\ mm$, Mode 13, Transverse 9

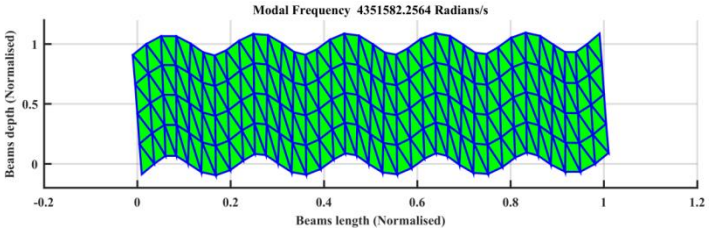

Figure 6-17: Mode shape of beam with $d = 1.732\ mm$, Mode 14, Transverse 10

6.3 Full frequency spectrum modal analysis of 2D beams models using CVFEM and MPFEM incorporating identified micropolar constants

In this section, both CVFEM and MPFEM were employed for modelling 2D beams exploiting the identified micropolar constants, N and l_b, to generate all modal frequencies. The results are then compared with the FEA results of chapter three, and the capabilities and shortcomings of the micropolar elasticity in predicting the size effects in heterogeneous beam models are discussed.

6.3.1 Longitudinal modal frequencies of heterogeneous materials and size effects

The finite element results for heterogeneous beam models also indicated the existance of size a effect in longitudinal modes, but unfortunately the micropolar theory is not capable of anticipating any size effects in longitudinal displacements because the characteristic length parameters, l_b and l_t, only influence the transverse and torsional displacements and thus have no influence on longitudinal displacement. The finite element results for the first two longitudinal frequencies for the perforated beams with continuous boundaries are provided in figure 6-18 and 6-19 confirming the existance of the size effect phenomenon in the heterogeneous beams for longitudinal modes. Other beam models showed similar size effects too. The first five longitudinal frequencies for beams with voids and compliant inclusions and continuous boundaries, and also beams with compliant matrix and textured boundaries are provided in tables D-1 to D-3 in Appendix D.1. Although the finite element results indicate that there is a longitudinal size effect, it is small compared to the flexural size effect. The results for other type of beams are not included because although the tabulated results for those beams confirm the existance of a size effect in longitudinal modes, the micropolar theory is again not capable of predicting these effects.

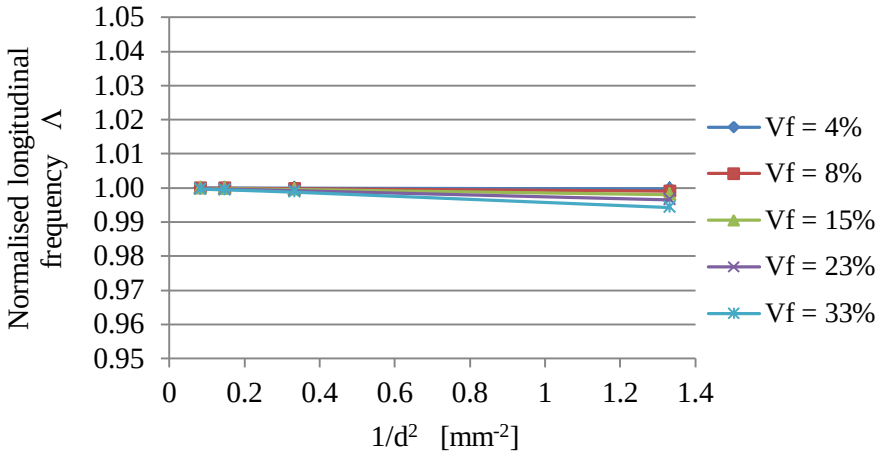

Figure 6-18: Normalised primary longitudinal frequency of four heterogeneous beam sizes for beams with voids and continuous boundaries from FEA

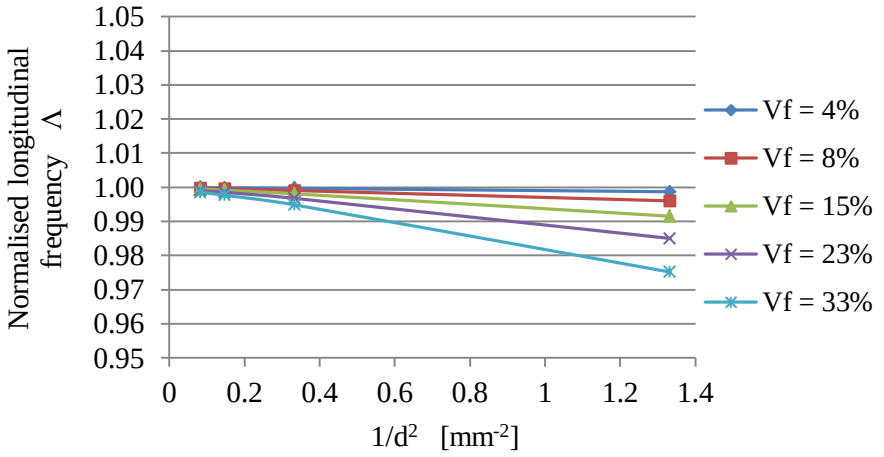

Figure 6-19: Normalised 2nd mode longitudinal frequency of four heterogeneous beam sizes for beams with voids and continuous boundaries from FEA

The CVFEM and MPFEM results for the longitudinal modal frequencies showed no size effect with beam thickness or volume fraction, Figure 6-20, and that is because the micropolar theory does not account for any size effect in the longitudinal direction, therefore, only the transverse (bending) modes have been extracted and investigated. This required checking every mode shape and selecting the transverse modal frequencies from the entire frequency spectrum up to the 33rd modal frequency.

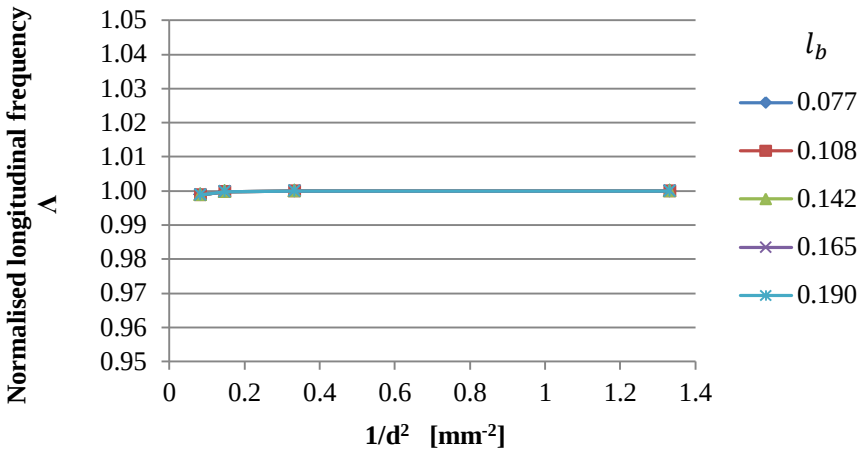

Figure 6-20: Normalised longitudinal frequency (for modes 1 to 5) of four beam sizes for beams with voids and continuous boundaries using MPFEM ($V_f = 0.04\ to\ 0.33$ correspond to $l_b = 0.077\ to\ 0.19\ mm$)

6.3.2 Transverse modal frequencies of micropolar beams in comparison with heterogeneous F. E. models

Based on the equation 4.46 and the iteration process which was introduced in section 5.4, the characteristic length of bending and the coupling number for various beam types are obtained and provided previously in tables 4-4 and 6-1. Having quantified the characteristic length parameter analytically and the coupling number numerically, the CVFEM and MPFEM procedures were used to predict the full frequency spectrum for all sizes of beams with inclusions or perforated by voids at all volume fractions considered. The only difference between CVFEM and MPFEM procedures is the process with which the stiffness matrix for the triangular element is obtained. These procedures showed significant agreement for lower mode numbers.

6.3.2.1 Beams with voids and continuous boundaries (BVOCB)

The discussions regarding the size effect which was provided in chapter three for finite element results are valid here too. The MPFEM and CVFEM reasonably forecast the same explanation for size effect of beams with voids and continuous boundaries (BVOCB).

In figures 6-21 and 6-22, the variations in normalised frequency, Λ, with size measure for the primary flexural modes are displayed. According to these results, variations in the normalised frequencies have an approximately linear relationship with the inverse of the square of the depth of the beam ($1/d^2$) just the same as what had been observed from FEA

results in chapter three figure 3-6 and 3-8, except for the smallest beam sizes where the ratio of the radius of void or inclusion to beam thickness reaches the maximum. The Λ value for the smallest beam sample size is slightly underestimated in comparison with the FEA results.

Figure 6-23 and 6-24 shows how the first five transverse normalised frequencies for the beams with voids and height of one unit-cell vary with mode number and how the behaviour is highly size dependent, as seen in figures 6-21 and 6-22, for mode one. The CVFEM and MPFEM results[4] show that the normalised modal frequency of the homogeneous beams is size independent.

Tables D-4 and D-7 in Appendix D provide non-dimensional frequency parameter (λ) information for the first ten transverse vibration modes of beams with voids and continuous boundaries predicted using MPFEM and CVFEM procedures. For any given mode the size effect becomes more pronounced with diminishing beam size and is greatest for the smallest size of beams. The size effect is also more pronounced for beams with a higher void volume fraction.

Similar to the beam behaviour based on the FEA results; here too, the size effect is mode dependent; but the micropolar results do not provide much information regarding the size effect in modal frequencies for after mode 3 or 4. This issue must be investigated in future work but in the meantime, it appears to be one of the shortcomings of the micropolar theory.

All of the CVFEM and MPFEM results provided in figures 6-21 to 6-31 are obtained using the characteristic length in bending, l_b, and the coupling number, N, from tables 4-4 and 6-1 as input parameters which correspond to normalised void radius $(V_r/S_y) = 0, 0.12, . . , 0.35$ in heterogeneous beam models using FEA.

[4] Here on after it's called micropolar beam when it meant either of CVFEM or MPFEM or both as a general expression.

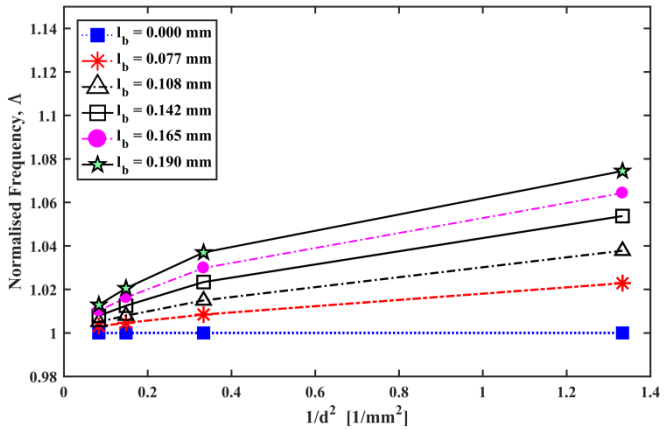

Figure 6-21: Normalised primary bending modal frequency of four beam sizes for beams with voids and continuous boundaries using CVFEM ($l_b = 0\ to\ 0.19\ mm$ corresponds to $V_r/S_y = 0\ to\ 0.35$)

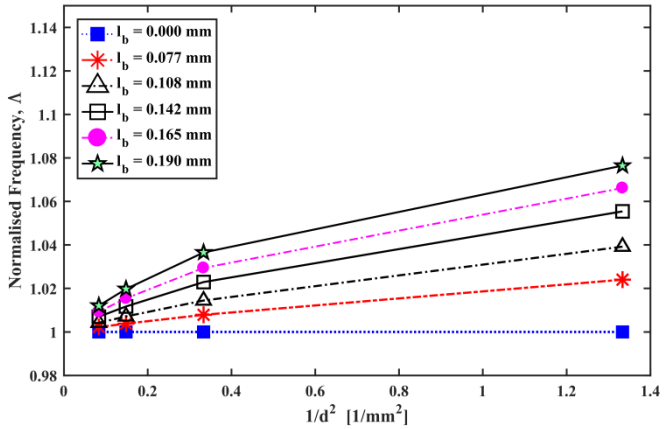

Figure 6-22: Normalised primary bending modal frequency of four beam sizes for beams with voids and continuous boundaries using MPFEM ($l_b = 0\ to\ 0.19\ mm$ corresponds to $V_r/S_y = 0\ to\ 0.35$)

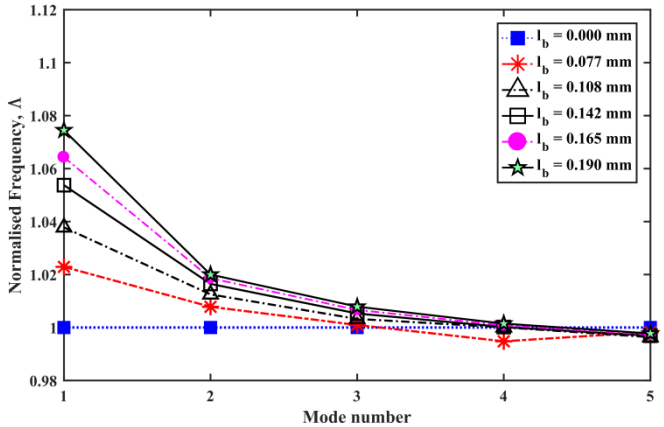

Figure 6-23: First five normalised bending modal frequencies of the smallest beam sample with voids and continuous boundaries using CVFEM ($l_b = 0\ to\ 0.19\ mm$ corresponds to $V_r/S_y = 0\ to\ 0.35$)

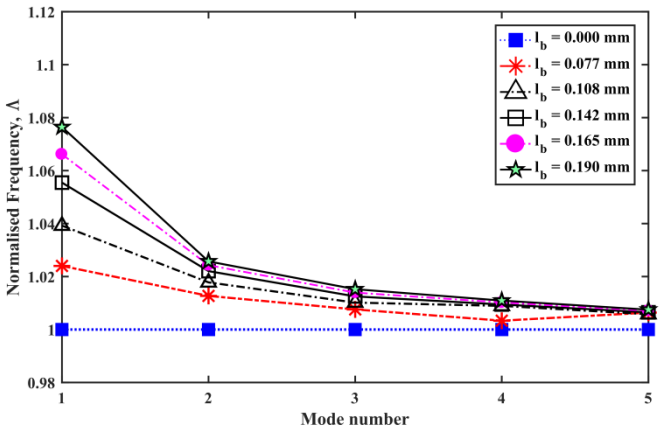

Figure 6-24: First five normalised bending modal frequencies of the smallest beam sample with voids and continuous boundaries using MPFEM ($l_b = 0\ to\ 0.19\ mm$ corresponds to $V_r/S_y = 0\ to\ 0.35$)

The results in figures 6-21 and 6-22 indicate that the MPFEM and CVFEM results show little difference for the beams with one layer in depth ($NCy = 1$) although the frequency values obtained from using CVFEM are slightly higher.

An overall comparison with the results from FE analysis, as shown in figure 6-25 for mode one, indicates that both CVFEM and MPFEM under estimate the normalised frequency values for the smallest sample size with the difference increasing as the volume fraction increases. For example for volume fractions above $V_f = 0.08$ in figure 6-25; the maximum Λ reads 1.15 for the smallest beam sample size with the highest volume fraction at mode one but the predicted value is only around 1.075.

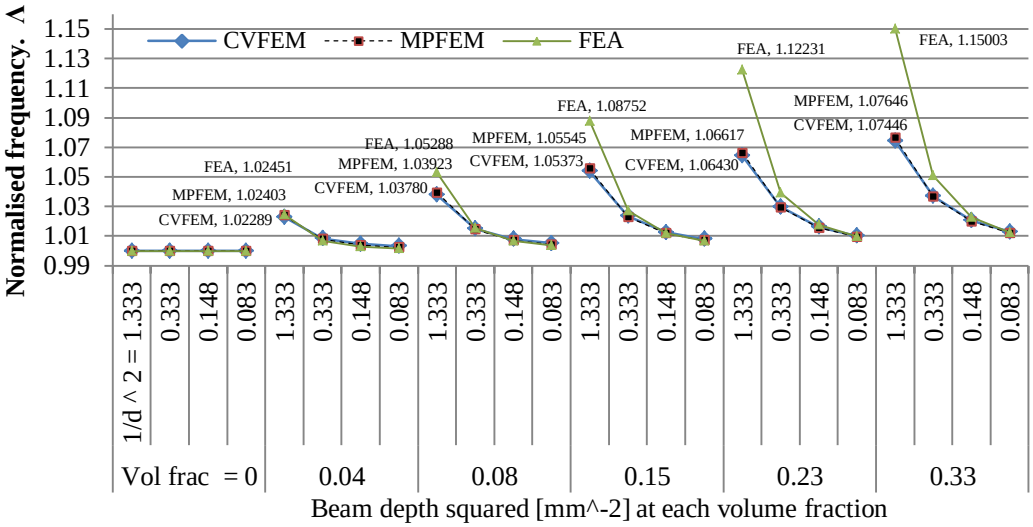

Figure 6-25: Primary normalised modal frequencies, mode 1, for beams with voids and continuous boundaries, BVOCB

6.3.2.2 Beams with inclusions and continuous boundaries (BCICB)

As seen in the previous section, the choice between CVFEM and MPFEM does not alter the results significantly. Therefore, while all the CVFEM results have been tabulated in Appendix D, the MPFEM results are sufficient for investigating and making conclusions regarding the size effect in micropolar beams in dynamic cases.

The dynamic behaviour of micropolar beams with compliant inclusions and continuous boundaries, as shown in figures 6-26 to 6-27, show similar size effect behaviour as beams with voids. However, the normalised frequencies are smaller and the graphs show a better fit with the FE results as seen in figure 6-28. Thus, according to figure 6-28, Λ reads 1.12 for the smallest beam sample size with the highest volume fraction at mode one which is smaller than the corresponding specimens in figure 6-25 for BVOCB.

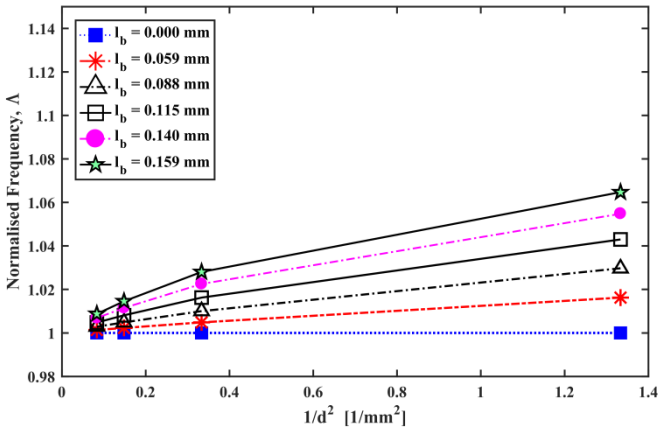

Figure 6-26: Normalised primary bending modal frequency of four beam sizes for beams with compliant inclusions and continuous boundaries using MPFEM
($l_b = 0\ to\ 0.159\ mm$ corresponds to $V_r/S_y = 0\ to\ 0.35$)

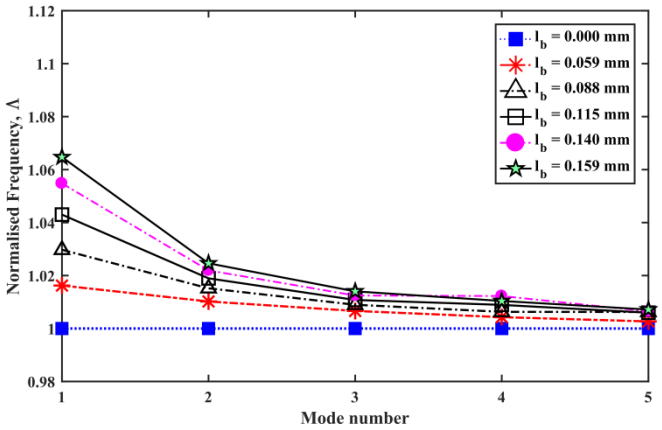

Figure 6-27: First five normalised bending modal frequencies (modes 1 to 5) of the smallest beam sample for beams with compliant inclusions and continuous boundaries using MPFEM ($l_b = 0\ to\ 0.159\ mm$ corresponds to $V_r/S_y = 0\ to\ 0.35$)

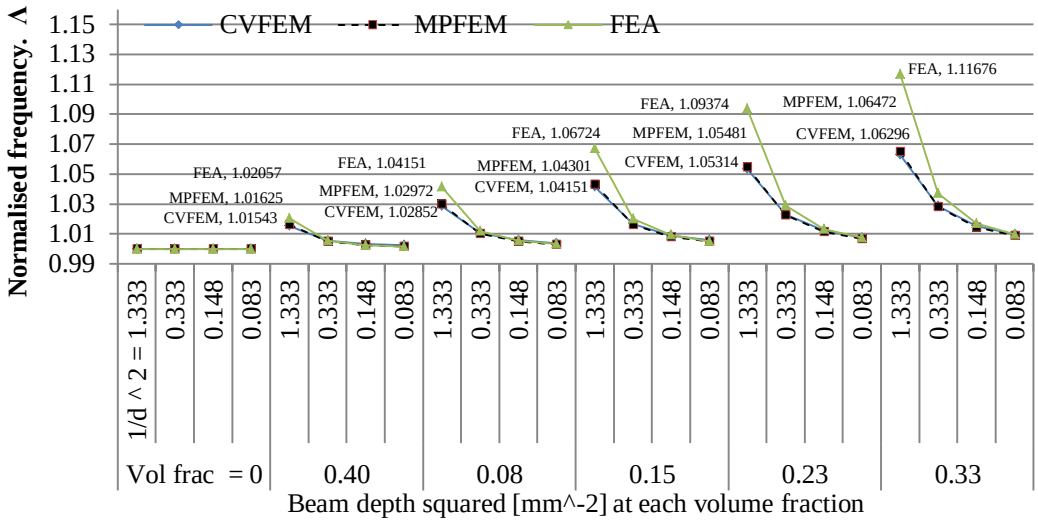

Figure 6-28: Primary normalised modal frequencies, mode 1, for beams with compliant inclusions and continuous boundaries, BCICB

6.3.2.3 Beams with compliant matrix and textured boundaries (BCMTB)

Beams with compliant matrix and textured boundaries also show size effects consistent with micropolar theory but comparatively less pronounced than the previously discussed beam models, see figure 6-29. The normalised primary modal frequency is equal to 1.04 even for the largest volume fraction of 0.33 ($V_r/S_y = 0.35$) and this reduces with diminishing volume fraction, see figure 6-29 and 6-30. For example, the normalised frequency, Λ, for the smallest beam sample with $V_r/S_y = 0.12$ is about 1.01.

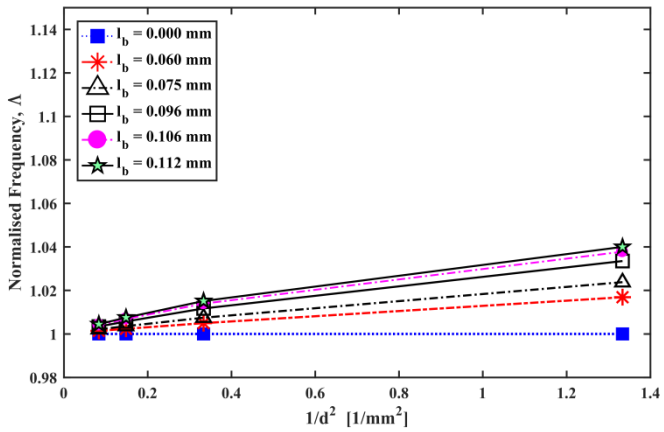

Figure 6-29: Normalised primary bending modal frequency of four beam sizes for beams with compliant matrix and textured boundaries using MPFEM
($l_b = 0\ to\ 0.112\ mm$ corresponds to $V_r/S_y = 0\ to\ 0.35$)

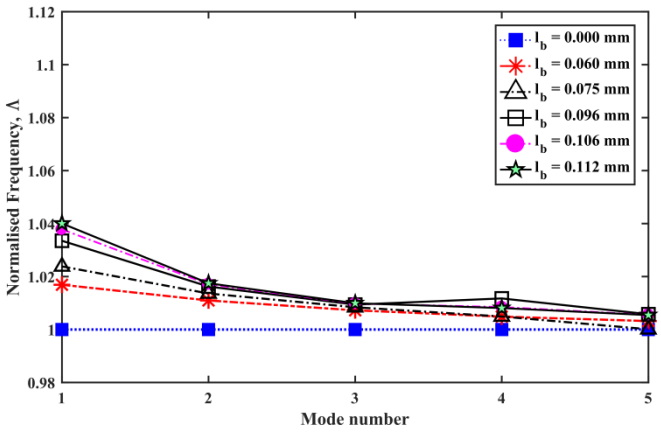

Figure 6-30: First five normalised bending modal frequencies (modes 1 to 5) of the smallest beam sample for beams with compliant matrix and textured boundaries using MPFEM
($l_b = 0\ to\ 0.112\ mm$ corresponds to $V_r/S_y = 0\ to\ 0.35$)

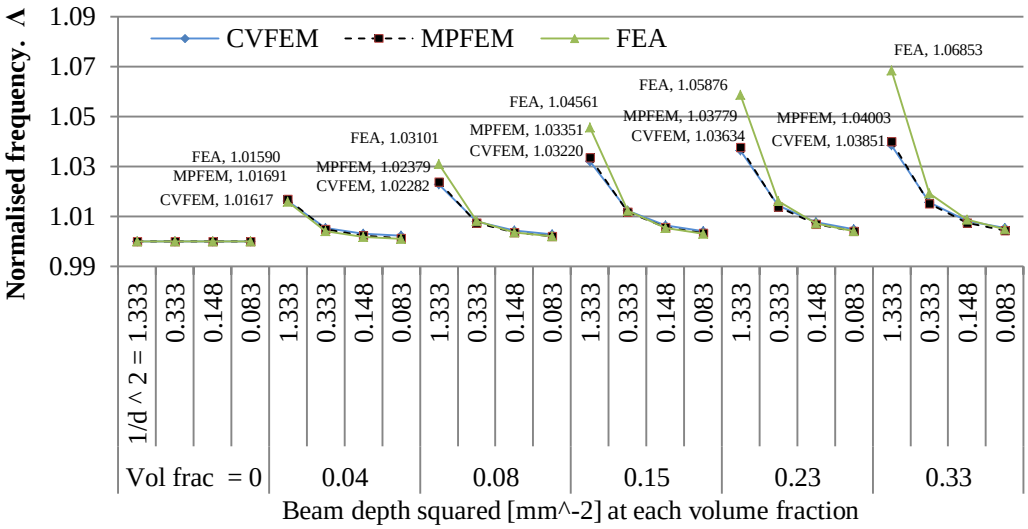

Figure 6-31: Primary normalised modal frequencies, mode 1, for beams with compliant matrix and textured boundaries, BCMTB

According to the results shown in figure 6-31 above, the normalised frequency value, Λ reads 1.07 (using FEA) for the smallest beam sample size with the highest volume fraction for mode one which clearly indicates that the size effect in these type of beams are less marked in comparison with the size effect seen for both beams with voids and inclusions with continuous boundaries as shown previously in figures 6-25 and 6-28.

6.4 Summary and conclusions

FEA was used for creating beam models of a representative heterogeneous material and generating modal frequencies and using them as the basis for comparison with those from CVFEM and MPFEM. This approach is different from the usual techniques in the literature but has some benefits. First of all, as shown in chapter three, the analytical methods in the literature were not applicable to those beam models. Secondly, changing the volume fraction in beam models with a periodic array of voids or inclusions, as described in detail in chapter three, required changing material constants such as modulus of elasticity in order to keep the overall dimensions and the properties of the homogenized equivalent beam unchanged which was achieved by performing tensile test simulations using finite element analysis while keeping each cell's mesh configurations fixed.

In studying the longitudinal modal frequencies category, the FEA results revealed that there is a smaller yet nevertheless identifiable size effect present in non-homogeneous beams which indicate that normalised frequencies decreases on increasing the modal frequency and this becomes more discernible in smaller beam samples. Nevertheless, the micropolar theory was incapable of predicting this size effect in such longitudinal modes for non-homogeneous beam models due to the fact that there is no length scale parameter in micropolar theory related to size effects in axial strain states associated with longitudinal displacement.

In the flexural modal frequencies category of dynamic behaviour, when the micropolar predictions are compared to the results obtained from finite element analysis, a number of similarities and differences are evident. The MPFEM (CVFEM) modal analysis results indicate that in the micropolar beam, the modal frequencies decreased quickly and consequently after the first few modes the size effect is rapidly suppressed which thus limits the utility of the higher modes in the investigation of any size effect. On the other hand, the FEA results indicate that the size effect remains more pronounced and may even change in nature.

Micropolar analyses were conducted for both beams with void and inclusions with continuous boundaries and beams with compliant matrix in which boundaries were textured. Micropolar analysis for other beam types are not obtained due to unavailability of the micropolar constants as explained in chapter four. For the beam types for which the constants were available, the values identified were subsequently for micropolar modal analysis to predict the full frequency spectrum covered by the FE results. Discernible differences were still present with these becoming more marked as frequency increased.

Thus, while micropolar theory appears to have some capacity to forecast the size effect at low frequencies of beams with lower volume fractions, its predictive ability becomes progressively compromised as the volume fraction increases or beam depth reduced to one unit cell or the frequency is increased towards the critical value. Comparable similarities and differences are seen in the cases where the beams contain compliant inclusions and where the inclusions, although more rigid, intersect the boundaries. Full numerical results are tabulated and presented in Appendices B and D.

However, despite some shortcomings as stated above, the linear isotropic micropolar theory demonstrated good capabilities to:

- capture size effect in beams with different sizes despite having the same length to depth aspect ratio;
- forecast size effects for the first few flexural frequencies, especially modes 1 and 2, in some of the 2D heterogeneous beam models;
- show that size effect also depends on the volume fraction similar to FEA results;
- predict the flexural frequencies for beam models with low to moderate volume fractions;
- Predict the flexural frequencies for beam models with more than one layer of unit cells across the depth of the heterogeneous beam models.

The above listed positive aspects of employing the micropolar theory raise the necessity to investigate the extent to which the theory is still applicable. Therefore, in the next three chapters the application of micropolar theory is extended to three-dimensional plate vibration to verify the existence of size effects in plate models and to identify and investigate size effects in three-dimensional representative materials as well. The three-dimensional heterogeneous plate models discussed in chapter eight will demonstrate some anisotropy but the more isotropic 3D micropolar plate presented in chapter nine is expected to be able to explain the dynamic behaviour of the heterogeneous 3D models with a lower degree of anisotropy. Therefore, in chapter seven the 3D micropolar theory will be formulated and introduced through a 3D MPFEM procedure for modal analysis which will later be used to generate the modal frequency data presented in chapters eight and nine.

7 Development of Algorithms for the Numerical 3D-MPFEM

This chapter covers the incorporation of the linear isotropic micropolar theory in the conventional finite element method and its application to the three-dimensional (3D) context and the development of appropriate algorithms defining the 3D linear isotropic micropolar finite element method (3D-MPFEM) which will be used subsequently to extract eigenvalues of heterogeneous plates in chapters eight and nine. Thus, in the development of the 3D-MPFEM algorithms, two types of solid elements, namely, 8-node and 15-node solid elements are formulated, and consequently their features are therefore discussed in some detail here. Therefore, from this section onward, the accuracy of micropolar theory in a specific dynamic problem, the free vibration of square plates with free-free-free-free (FFFF) boundary conditions, is investigated to see if the theory can also explain the size effect in 3-dimensional plates[5] in the dynamic case.

7.1 Stiffness matrix for 3D micropolar plate

As explained in chapter two, for the 3D cases, the stiffness matrix will be of rank 18, see equation (2.19). The strain components in the micropolar govering equations (2.16) and (2.17) can be related to micro rotation tensor, $\boldsymbol{\phi}$, and the displacements tensor , $\boldsymbol{u}$, as in equation (4.1) while the strain tensors and the macro rotations in terms of displacements are given in equations (4.2). Therefore the micro-rotation and macro-rotation are not taken as equal which is clearly seen in the above equations and also reflected in the matrix expansion of the equations as seen in equations (2.18) to (2.27).

The extra engineering constants in 3D micropolar elasticity are l_t, the characteristics length of torsion (l_t reflect the microstructural scale similar to l_b but in torsion), and Ψ is the polar ratio which is conceptually similar to Poisson ratio but now represents the ratio of orthogonal rotations. Energetically Ψ may vary from zero to 1.5. In almost all literature, the value of Ψ is assumed to be 1.5; thus also throughout the analysis in this project. The characteristic length of torsion and the polar ratio are defined as:

$$l_t^2 = \frac{\beta^* + \gamma^*}{(2\mu^* + \kappa^*)} \tag{7.1}$$

[5] Sign conventions are according to the figure 7-1. The Cartesian coordinates may also be indicated by integers 1, 2 and 3.

$$\Psi = \frac{\beta^* + \gamma^*}{\alpha^* + \beta^* + \gamma^*} \tag{7.2}$$

If Ψ approaches one, then α^* approaches zero which is necessary for the material to behave in a classical manner but not sufficient since for the material to behave classically, all of four additional micropolar constants $\alpha^*, \beta^*, \gamma^*$ and κ^* must each equal zero. In a special case when N=1 in equation (4.15), the material behaves as in couple stress theory where micro rotation and macrorotation become equal.

The micropolar elastic constants may also be written as functions of the engineering constants by rearranging equations (4.17) to (4.20) and equations (7.1) and (7.2):

$$\alpha^* = \frac{E_m l_t^2}{1 + \upsilon_m}\left(\frac{1 - \Psi}{\Psi}\right) \tag{7.3}$$

$$\beta^* = \frac{E_m}{1 + \upsilon_m}(l_t^2 - 2l_b^2) \tag{7.4}$$

$$\gamma^* = \frac{2E_m l_b^2}{1 + \upsilon_m} \tag{7.5}$$

$$\kappa^* = \frac{N^2}{1 - N^2}\left(\frac{E_m}{1 + \upsilon_m}\right) \tag{7.6}$$

$$\lambda^* = \frac{E_m}{1 + \upsilon_m}\left(\frac{\upsilon_m}{1 - 2\upsilon_m}\right) \tag{7.7}$$

$$\mu^* = \frac{E_m}{1 + \upsilon_m}\left(\frac{1 - 2N^2}{2(1 - N^2)}\right) \tag{7.8}$$

In the dynamic analysis, the micro inertia tensor, $\mathbf{J}_{ji}$, must be included into the governing equations as given in the equations of dynamic equilibrium (4.7) and (4.8).

7.2 Formulation of the 3D-MPFEM using 15-node wedge element for modal analysis

In this section the 3D micropolar elasticity theory is incorporated into a finite element method which leads to development of algorithms for the 3-D MPFEM for modal analysis of heterogeneous plates.

7.2.1 Formulation of stiffness matrix based on micropolar elasticity

There are 15 nodes in a wedge element, and each shape function is identified as $\mathbb{N}^i$, i=1,2,…15; Shape functions for 15-node wedge element are listed in table 7-1 which can be found in reference (Hanukah 2014):

Table 7-1: Shape function of a 15-node wedge elements based on the node numbering in figure 7-1

Node number	Shape function	Node number	Shape function
1	$\eta(1-\zeta)(2\eta-\zeta-2)/2$	9	$\delta(1-\zeta^2)$
2	$(-1)(1-\delta-\eta)(1-\zeta)(2\delta+2\eta+\zeta)/2$	10	$\eta(1+\zeta)(2\eta+\zeta-2)/2$
3	$\delta(1-\zeta)(2\delta-\zeta-2)/2$	11	$(1-\delta-\eta)(1+\zeta)(2\delta+2\eta-\zeta)/2$
4	$2\eta(1-\delta-\eta)(1-\zeta)$	12	$\delta(1+\zeta)(2\delta+\zeta-2)/2$
5	$2\delta(1-\delta-\eta)(1-\zeta)$	13	$2\eta(1-\delta-\eta)(1+\zeta)$
6	$2\delta\eta(1-\zeta)$	14	$2\delta(1-\delta-\eta)(1+\zeta)$
7	$\eta(1-\zeta^2)$	15	$2\delta\eta(1+\zeta)$
8	$(1-\delta-\eta)(1-\zeta^2)$		

Figure 7-1 shows the node numbering in a 15-node wedge element in a natural coordinate system. δ and η vary from zero to one and ζ varies from -1 to $+1$.

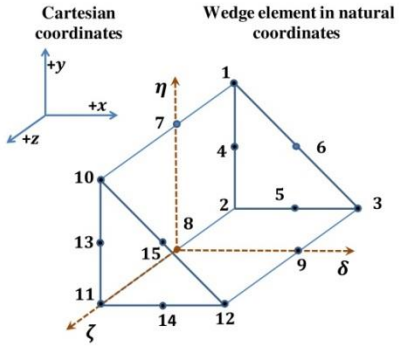

Figure 7-1 : Representation of a 15-node wedge element in natural coordinate system. The Cartesian coordinates may also be indicated by integers 1, 2 and 3.

The derivatives of the shape functions in the Cartesian and natural coordinates are related according to the equation (7.9):

$$\begin{bmatrix} \mathbb{N}^i_{,x} \\ \mathbb{N}^i_{,y} \\ \mathbb{N}^i_{,z} \end{bmatrix} = \begin{bmatrix} \delta_{,x} & \eta_{,x} & \zeta_{,x} \\ \delta_{,y} & \eta_{,y} & \zeta_{,y} \\ \delta_{,z} & \eta_{,z} & \zeta_{,z} \end{bmatrix} \begin{bmatrix} \mathbb{N}^i_{,\delta} \\ \mathbb{N}^i_{,\eta} \\ \mathbb{N}^i_{,\zeta} \end{bmatrix} = \hat{\mathbb{J}}^{-1} \begin{bmatrix} \mathbb{N}^i_{,\delta} \\ \mathbb{N}^i_{,\eta} \\ \mathbb{N}^i_{,\zeta} \end{bmatrix} \tag{7.9}$$

$\hat{\mathbb{J}}^{-1}$ represents the inverse of the Jacobian matrix and is used to transform the derivatives of shape functions from natural to Cartesian coordinates. The Jacobian matrix can be calculated as follows (Zienkiewicz, Taylor, and Zhu 2013; Kaltenbacher 2015):

$$\hat{\mathbb{J}} = \begin{bmatrix} \sum_{i=1}^{15} x_i \mathbb{N}^i_{,\delta} & \sum_{i=1}^{15} y_i \mathbb{N}^i_{,\delta} & \sum_{i=1}^{15} z_i \mathbb{N}^i_{,\delta} \\ \sum_{i=1}^{15} x_i \mathbb{N}^i_{,\eta} & \sum_{i=1}^{15} y_i \mathbb{N}^i_{,\eta} & \sum_{i=1}^{15} z_i \mathbb{N}^i_{,\eta} \\ \sum_{i=1}^{15} x_i \mathbb{N}^i_{,\zeta} & \sum_{i=1}^{15} y_i \mathbb{N}^i_{,\zeta} & \sum_{i=1}^{15} z_i \mathbb{N}^i_{,\zeta} \end{bmatrix} \tag{7.10}$$

Referring to equation (2.18), the strain field as described by $\left[\boldsymbol{\varepsilon_{ij}}\ \boldsymbol{\phi_{ij}}\right]^T$, can be related to the displacement field and micro rotation by matrix B, see equation (7.11). Let $\bar{\varepsilon}$ represent the strain field and $\overline{\boldsymbol{U}}$ represent the displacement and micro rotation vector:

$$[\bar{\varepsilon}] = [B][\overline{\boldsymbol{U}}] \tag{7.11}$$

where:

$$[\bar{\boldsymbol{U}}] = \left[\boldsymbol{u}_{\bar{j}} \;\; \boldsymbol{\phi}_{\bar{j}}\right]^{T} , \bar{j} = 1, 2 \; and \; 3 \tag{7.12}$$

Knowing the derivatives of the shape functions $\mathbb{N}^i$, the B matrix can be constructed as follows:

$$[B] = \begin{bmatrix} [Q1] & [Q2] \\ [0]_{9\times 3} & [Q3] \end{bmatrix} \tag{7.13}$$

where the matrices Q1, Q2, and Q3 are:

$$[Q1] = \begin{bmatrix} \mathbb{N}^i_{,x} & 0 & 0 \\ 0 & \mathbb{N}^i_{,y} & 0 \\ 0 & 0 & \mathbb{N}^i_{,z} \\ 0 & \mathbb{N}^i_{,x} & 0 \\ \mathbb{N}^i_{,y} & 0 & 0 \\ 0 & 0 & \mathbb{N}^i_{,x} \\ \mathbb{N}^i_{,z} & 0 & 0 \\ 0 & 0 & \mathbb{N}^i_{,y} \\ 0 & \mathbb{N}^i_{,z} & 0 \end{bmatrix} \tag{7.14}$$

$$[Q2] = \begin{bmatrix} [0]_{3\times 3} \\ 0 & 0 & -\mathbb{N}^i \\ 0 & 0 & +\mathbb{N}^i \\ 0 & +\mathbb{N}^i & 0 \\ 0 & -\mathbb{N}^i & 0 \\ -\mathbb{N}^i & 0 & 0 \\ +\mathbb{N}^i & 0 & 0 \end{bmatrix} \tag{7.15}$$

and

$$[Q3] = \begin{bmatrix} \mathbb{N}^i_{,x} & 0 & 0 \\ 0 & \mathbb{N}^i_{,y} & 0 \\ 0 & 0 & \mathbb{N}^i_{,z} \\ \mathbb{N}^i_{,y} & 0 & 0 \\ 0 & \mathbb{N}^i_{,x} & 0 \\ \mathbb{N}^i_{,z} & 0 & 0 \\ 0 & 0 & \mathbb{N}^i_{,x} \\ 0 & \mathbb{N}^i_{,z} & 0 \\ 0 & 0 & \mathbb{N}^i_{,y} \end{bmatrix} \tag{7.16}$$

$\mathbb{N}$ is the shape function of 15-node wedge element at node i, where i=1, 2… 15.

Now the stiffness matrix for the 15-node wedge element, K_e , can be calculated:

$$K_e = \int_{-1}^{+1} \int_{0}^{+1} \int_{0}^{+1} B^T \mathbb{D} B det[\hat{\mathrm{J}}] d_\delta d_\eta d_\zeta \tag{7.17}$$

where K_e is the element stiffness matrix which has the size of 90×90 . A Gauss quadrature method with three integration points was used to calculate the element stiffness matrix numerically. T stands for transposed.

7.2.2 Derivation of mass and micro inertia matrices

Similar to the procedure described in chapter five, a template mass matrix was constructed for a 15-node wedge element incorporating both consistent and lumped mass matrices using the equation (5.25). A full and comprehensive procedure on obtaining consistent and lumped matrices is provided in (Colorado 2010; Felippa, Guo, and Park 2015). The consistent and lumped mass matrices were obtained from the equations 7.18 and 7.19:

$$M_C = \int_{\mathbb{V}} \rho (\mathbb{N})^T \mathbb{N} \, d\mathbb{V} \tag{7.18}$$

$$M_L = \frac{\rho \mathbb{V}}{15} diag[1\ 1\ 1 \ldots 1]^{90\times 90} \tag{7.19}$$

The consistent mass matrix using shape functions of nodes within the wedge element interpolates the nodal mass within the element by integration of mass over the volume domain $\mathbb{V}$.

The micro-inertia, as introduced in equation (4.8), now has components in x, y and z directions. In this thesis, it is assumed that the micro-inertia tensors are equal in all directions. In the finite element method, a node is considered as a point of mass. Therefore the micro-inertia of a node must be independent of the physical dimensions of the elements which can cause some confusion, but in micropolar theory, however, it can be related to the square of the characteristics length in bending. As described in chapter five, in 3D the micro inertia is assumed to be given by equation (7.20):

$$Micro\ Inertia = J = \frac{2 l_b^2 \, \rho}{(1 + \upsilon_m)} \tag{7.20}$$

Thus the micro inertia matrix is considered as a 3 by 3 diagonal matrix:

$$Micro\ Inertia = \begin{bmatrix} J & 0 & 0 \\ 0 & J & 0 \\ 0 & 0 & J \end{bmatrix} \tag{7.21}$$

$\mathbf{J}_{ji}$ in equation (4.8) has three components in spatial coordinates but, as seen in equations (5.38) and (7.20), these components are assumed to be J/ρ when i=j and zero otherwise.

When the element mass matrix is constructed, it is possible to include the micro-inertia matrix into the mass matrix through those elements associated with the rotation of the nodes as in the 2D cases.

7.2.3 Solution to eigen problem

Finally the stiffness and mass matrices will be assebled in the global mass and stiffness matrixes, K_G and M_G, and the eigenvalue equation can be solved according to the equation (5.39). Similar to the algorithm for 2D eigen problem, the square root of the array of the diagonal elements of the resulting matrix provides the frequency spectrum, ω^2.

7.3 Algorithms used for modal analysis of 3D micropolar plates

In this section the mathematical formulations which were defined in sections 2.3, 7.1 and 7.2 are used to develop algorithms for modal analysis of three dimensional micropolar plates in a distinct process of 3D-MPFEM.

7.3.1 Plate modelling using 3D-MPFEM

The micropolar models are such that each plate unit-cell is represented by 8 wedge elements, figure 7-2 , and the modal frequencies of the primary mode for the plate shown in figure 7-4 shows that the number of elements (392 elements with 10350 DOF) satisfies the required mesh density for this, the smallest plate.

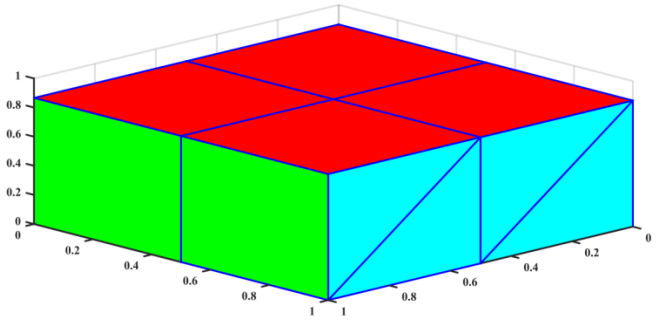

Figure 7-2 : Representation of one micropolar unit cell consisting of 8 wedge elements. $Height_{Unit\ Cell} = 0.866\ mm, Length_{Unit\ Cell} = 1\ mm\ and\ Width_{Unit\ Cell} = 1\ mm$

A micropolar plate model generated by 3D-MPFEM is provided in figure 7-3 which represents a plate with two layers of cells in depth. Note that in this work, free vibration with FFFF boundary conditions in the absence of external loads was exclusively investigated. This negates the problem of having to prescribe partially or fully constrained boundary conditions.

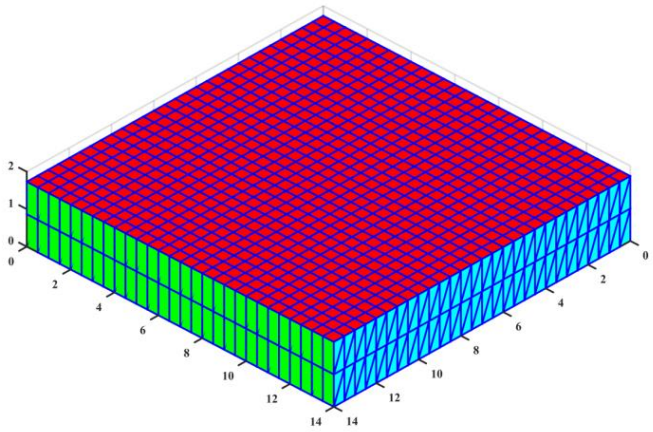

Figure 7-3 : MPFEM plate model with height doubled and AR=8.083

Figure 7-4 shows the reduction of the percentage of error with increasing DOF representing a micropolar plate albeit in a homogeneous test case in which all of the additional micropolar engineering parameters are each set to zero.

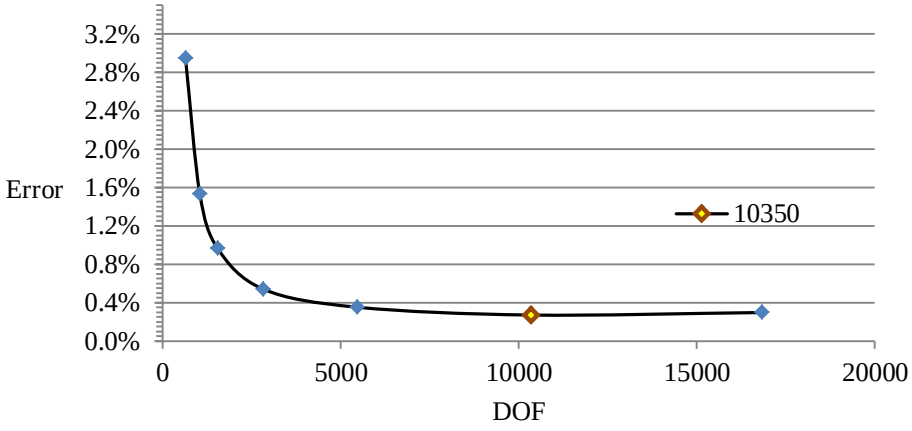

Figure 7-4 : The influence of DOF in decreasing the percentage of error in the micropolar plate in comparison with detailed FEA homogeneous plate model ; height=0.866 mm, Length=7 mm, Width=7 mm, AR=8.083 ; the error percentage was calculated by $error = \{|(\Omega_{MPFEM} - \Omega_{ANSYS})|/\Omega_{ANSYS}\} \times 100$

The process of modelling the micropolar plate begins with entering the overall plate dimensions by requesting the number of layers across the depth of the plate, number of line divisions along the depth, width and length of the plate layers and aspect ratios in both mid-plane directions. The micropolar constants are then required to be entered and finally the number of modal frequencies and mode shapes to be extracted which becomes important at post-processing stage as described in section 7.3.5.

In the process of modelling by 3D-MPFEM, a matrix denoted ENA (element node adjacency or element node connectivity table) is generated in which each row represents a wedge element and columns define the node numbers (first to fifteenth node) in that particular element. Neither the element nor the node numbers are repeated. The numbering sequence of elements proceeds from the left to the right side of the plate in the length direction counting both wedge elements on a line division, then moving on to the next layer until one slice of the plate is completed. Then the successive plate slices in the direction of the plate's width, z direction, will be generated until the plate model is completed.

Then, a list of coordinates for all nodes used in constructing the plate in an ascending will be generated. Having the matrices for elements-nodes (ENA) and nodes-coordinates (GNC), a 3-D plot representing the actual plate dimensions and showing the meshed plate model for visual confirmation will be generated. The nodal coordinates are also normalised by the maximum length, width and depth and saved to be used later in the post-processing stage in section 7.3.5.

The plate modelling procedure is conducted according to the following algorithm:

Step 1: Start [Start of algorithm];
Step 2: Enter the overall dimensions of the plate model: e.g., depth, width and length;
Step 3: Enter the number of layers (NCy), number of line divisions across the depth of the plate;
Step 4: Entre the number of unit-cells along the length and width of the plate model;
Step 5: Enter the plates's length to depth aspect ratio (ARx);
Step 6: Enter the plates's width to depth aspect ratio (ARz);
Step 7: Create and save Element-Node adjacency table (ENA);
Step 8: Create and save the list of coordinates, nodal-coordinates (GNC), for all nodes in the plate structure in ascending order;

Step 9: Generate a 3D plot representing the actual plate's dimensions for visual confirmation;

Step 10: Normalise the nodal coordinates by the maximum length, depth and width;

Step 11: Save the number of elements (nel);

Step 12: Save the number of nodes per element (nnel);

Step 13: Save nodal degree of freedom (ndof);

Step 14: Save the number of nodes (nnode);

Step 15: Calculate the element's degree of freedom edof=ndof*nnel;

Step 16: Save the element's degree of freedom sdof;

Step 17: Calculate the system's degree of freedom sdof= ndof*nnode;

Step 18: Save the system's degree of freedom sdof;

Step 19: Stop [End of algorithm];

7.3.2 Algorithm for constructing the element stiffness matrix

Here in this section the algorithm for obtaining the element stiffness matrix, K_e, in 3D-MPFEM is developed based on the mathematical formulations provided in sections 2.3, 7.1 and 7.2.1. This algorithm can be implemented for the construction of plate's element stiffness matrix incorporating the micropolar theory into conventional finite element method and used in construction of the global stiffness matrix, K_G. Thus, the general algorithm to derive the global stiffness matrix, using the 3D-MPFEM is defined as follows:

Step 1: Start [Start of algorithm]

Step 2: Entre the engineering micropolar constants: E_m, ν_m, N, l_b, l_t and Ψ.

Step 3: Convert the engineering micropolar constants to the original micropolar constants, $\alpha^*, \beta^*, \gamma^*, \kappa^*, \lambda^*, \mu^*$, using equations (7.3) to (7.8).

Step 4: Construct the matrix of the material properties, $\mathbb{D}$, using the micropolar constants, defined in step 3, as in equation (2.19) to (2.27).

Step 5: Select the first element of the finite element model from section 7.3.1;

Step 6: Select the nodal coordinates of all 15 nodes in the wedge element in Cartesian coordinate system e.g., $x_1, x_2, x_3, \ldots, y_1, y_2, y_3, \ldots$ and $z_1, z_2, z_3, \ldots$;

Step 7: Entre the three Gauss points and weights;

Step 8: Reserve a matrix of zeros of rank 90 for the element's stiffness matrix, K_e;

Step 9: Begin numerical integration using Gauss integration to implement the equation (7.17) over the following steps 10 to 17;

Step 10: Calculate the matrix of derivatives of the shape functions, 15 equations in table 7.1, with respect to area coordinates, $\delta,\ \eta\ and\ \zeta$.

Step 11: Calculate the Jacobian matrix ,$\hat{J}$, the $\hat{J}$ determinant and the inverse of the Jacobian matrix using the derivatives of shape functions and the coordinates from step 6 as in equation (7.10);

Step 12: Calculate the matrix of derivatives of the shape functions with respect to Cartesian coordinates ($dN_x\ , dN_y and\ dN_z$) according to the equation (7.9)

Step 13: Construct the partial matrix B using the derivatives of shape functions[6] from step 12 as in equations (7.13) to (7.16), using the following pseudo code:

```
For n=1 to 15
   B (1, (6*n-5))   = dNx (n);
   B (2, (6*n-4))   = dNy (n);
   B (3, (6*n-3))   = dNz (n);
   B (4, (6*n-4))   = dNx (n);
   B (4, (6*n))     = -N (n);
   B (5, (6*n-5))   = dNy (n);
   B (5, (6*n))     = N (n);
   B (6, (6*n-3))   = dNx (n);
   B (6, (6*n-1))   = N (n);
   B (7, (6*n-5))   = dNz (n);
   B (7, (6*n-1))   = -N (n);
   B (8, (6*n-3))   = dNy (n);
   B (8, (6*n-2))   = -N (n);
   B (9, (6*n-4))   = dNz (n);
   B (9, (6*n-2))   = N (n);
   B (10, (6*n-2)) = dNx (n);
   B (11, (6*n-1)) = dNy (n);
   B (12, (6*n))    = dNz (n);
   B (13, (6*n-2)) = dNy (n);
   B (14, (6*n-1)) = dNx (n);
   B (15, (6*n-2)) = dNz (n);
   B (16, (6*n))    = dNx (n);
   B (17, (6*n-1)) = dNz (n);
   B (18, (6*n))    = dNy (n);
End;
```

Step 14: Calculate $K_e = B^T \mathbb{D} B det[\hat{J}]$ *(Gauss weight1)*(Gauss weight2)*(Gauss weight3);

Step 15: Substitute the values in K_e matrix

Step 16: Update the Gauss point and weight

Step 17: Repeat the loop from step (9) till the K_e matrix of rank 90 is completed.

Step 18: Insert the element stiffness matrix into the global stiffness matrix, K_G;

[6] B (Row, Column) = the shape function or derivative of the shape function.

Step 19: Continue the steps (5) to (18) for the subsequent element till the last element stiffness matrix is included into the global stiffness matrix;

Step 20: Stop [End of algorithm]

7.3.3 Algorithm for constructing the element mass and micro-inertia matrices

The template mass matrix is described in section 7.2.2. The mass matrix for the 15-node wedge element also incorporates the micro-inertia matrix. Thus, the general algorithm to derive the global mass matrix for using in the 3D-MPFEM is defined as follows:

Step 1: Start [Start of algorithm]

Step 2: Entre the material mass density, ρ;

Step 3: Select the first element of the finite element model;

Step 4: Define the nodal coordinates of all 15 nodes in the wedge element in Cartesian coordinate system e.g., $x_1, x_2, x_3, \ldots, y_1, y_2, y_3, \ldots$ and $z_1, z_2, z_3, \ldots$;

Step 5: Calculate the volume of the wedge element;

Step 6: Create an (90×90) identity matrix;

Step 7: Multiply the element volume by its mass density and divide the product by 15;

Step 8: Multiply the product of step (7) to the identity matrix from step (6) to generate lumped mass matrix using equation (7.19);

Step 9: Generate an (90×90) matrix using $(\mathbb{N})^T\mathbb{N}$;

Step 10: Multiply the element volume by mass density and the matrix from step (9) to generate the consistent mass matrix as in equation (7.18);

Step 11: Having the lumped and consistent mass matrices obtained from steps (8) and (10), generate the template mass matrix using equation (5.25);

Step 12: Calculate the micro-rotation $J/\rho = \frac{2l_b^2}{(1+\nu_m)}$ from equation (5.38); and inject into the rows and columns and rows in the matrix generated from step (11) which represent the micro-rotations.

Step 13: Insert the element mass matrix into the global mass matrix, M_G;

Step 14: Select the next element;

Step 15: Continue the steps (4) to (14) for the subsequent element till the last element mass matrix is included into the global mass matrix;

Step 16: Stop [End of algorithm]

7.3.4 Solution of the discrete eigenvalue problem

Equation 5.39 in chapter five is also valid here for 3D plate's modal analysis and was solved by using a sparse matrix and parallel computation method[7]. The solution process[8] begins with defining the system matrices which are zero matrices for reserving memory spaces for stiffness, forces (if applicable) and mass matrices based on the total number of degree of freedom associated with all nodes in the constructed plate (also called the plate system matrix). The boundary conditions take effect in the global matrices by replacing the appropriate rows and columns with zeros which is not applicable here as no constrains are applied but are considered for future work. Finally the eigen problem is solved according to the equation 5.39. Following the solution of the eigen problem, the list of eigenvalues, ω^2, and the matrix of the eigenvectors are saved for post-processing.

The algorithm of the solution stage is as follows:

Step 1: Start [Start of algorithm]

Step 2: Define the number of modal frequencies and mode shapes to be extracted, e.g., Ext_mode=10 means that the first ten modal frequencies are to be extracted;

Step 3: Call M_G, (the global mass matrix including micro-inertia matrix);

Step 4: Call K_G, (the global stiffness matrix);

Step 5: Create sparse matrix from K_G;

Step 6: Create sparse matrix from M_G;

Step 7: Start a parallel pool for parallel solution;

Step 8: Solve the eigen problem by applying equation (5.39) using the pseudo code: [Eigen vectors, Eigen values]=eig (K_G, M_G, Ext_mode);

Step 9: Save eigen vectors;

Step 10: Save eigen values;

Step 11: Delete the parallel pool;

Step 12: Stop [End of algorithm]

7.3.5 Post-processing of data for extracting the modal frequencies and mode shapes

The frequency values are obtained by taking the square root of the eigenvalues and multiplied by 2π then arranged in ascending order. The displacement of each node in the

[7] The sparse matrix and parallel computation was carried out in MATLAB.
[8] MATLAB was used as the numerical computing environment and all numerical codes in this project are developed in this language.

system in x, y and z directions is defined by identifying row and column number in the eigenvectors matrix for that specific frequency and after arranging them in ascending order, saving the values as vectors corresponding to x, y and z coordinates for each node. The eigenvector values contain normalised displacement values which could be zero, positive or negative values. These eigenvector values are then added to the normalised GNC coordinates which result in mode shape coordinates.

The algorithm of the post-processing stage is as follows:

Step 1: Start [Start of algorithm]

Step 2: Take the square root of the eigenvalues;

Step 3: Multiply the eigenvalues by 2π to obtain ω values;

Step 4: Arranged the in ascending order;

Step 5: Extract corresponding row and column associated with each frequency from the matrix of eigenvectors;

Step 6: Add the eigenvector to the normalised nodal coordinates obtained from Step (10) of the algorithm which is provided in section 7.3.1;

Step 7: Generate a 3D plot representing the mode shape for any of the specified modal frequency in step (5);

Step 8: Stop [End of algorithm]

7.4 An alternative 8-node brick element and comparison with the 15-node wedge element

Here, in this section, an alternative but widely used solid element with fewer nodes (8-node brick element) is described which is simpler than a 15-node wedge element and, therefore, requires less computational time. The shortcomings of the 8-node brick elements and the advantages of using the 15-node wedge element in the modal analysis of plates are discussed.

7.4.1 Modelling and shape functions using 8-node brick element

The modelling process with the 8-node brick element is similar to the description that was provided in section 7.3 for the wedge element; the only difference is that the numbers of nodes are reduced to eight nodes per element. Note that two 15-nodes wedge elements construct a cuboid with 22 nodes in comparison with 8 nodes in a brick element. Another difference is there are no mid-side nodes in the 8-node brick elements. Therefore, the interpolation of dependent variables in the 8-node brick element is linear.

Figure 7-5 represents the node numbering in an 8-node brick element in a natural coordinate system. δ, η and ζ that vary from -1 to $+1$.

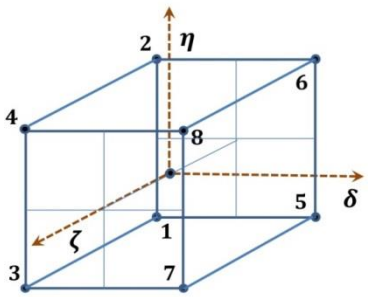

Figure 7-5: Representation of 8-node brick element in natural coordinate system

The shape functions in the 8-nodes brick element are identified as N^i, i=1,2,…8; Shape functions for brick element are listed in table 7-2:

Table 7-2: Shape function of 8-node brick elements based on the node numbering in figure 7-5

Node number	Shape function	Node number	Shape function
1	$(1-\delta)(1-\eta)(1-\zeta)/8$	5	$(1+\delta)(1-\eta)(1-\zeta)/8$
2	$(1-\delta)(1+\eta)(1-\zeta)/8$	6	$(1+\delta)(1+\eta)(1-\zeta)/8$
3	$(1-\delta)(1-\eta)(1+\zeta)/8$	7	$(1+\delta)(1-\eta)(1+\zeta)/8$
4	$(1-\delta)(1+\eta)(1+\zeta)/8$	8	$(1+\delta)(1+\eta)(1+\zeta)/8$

7.4.2 Solution of plate problem with 8-node brick element

The stiffness matrix for the 8-node brick element, K_e , can be calculated by equation (7.22):

$$K_e = \int_{-1}^{+1}\int_{-1}^{+1}\int_{-1}^{+1} B^T \mathbb{D} B det[\hat{\jmath}] d_\delta d_\eta d_\zeta \tag{7.22}$$

where K_e is the element stiffness matrix which has the size of 48×48. A Gauss quadrature method with two integration points was used to calculate the element stiffness matrix numerically. T again indicates transposed.

The mass and micro-inertia matrices are obtained as described in section 7.2.2 which also results in an overall mass-micro-inertia matrix of dimension 48×48.

Equation (5.39) was again solved by using a sparse matrix and parallel computation and then modal frequencies and mode shapes were extracted as required.

7.4.3 Comparing 15-node wedge element with 8-node brick element

The numerical solution of plates with an 8-node brick element mesh is expected to be performed faster than those with 15-node wedge elements since the dimensions of the mass and stiffness matrices are smaller for the 8-node brick element. But numerical investigation of a homogeneous plate, see figure 7-6, showed that plates with 15-node wedge element display very good accuracy with fewer elements needed to mesh the plate in comparison with plates of the same dimensions modelled using 8-node brick elements. Figure 7-6 indicates that the frequency results in a plate with wedge element and line division of $7 \times 7 \times 1$ which consist of 98 wedge elements is significantly more accurate than similar plate meshed with brick elements and a line division of $30 \times 30 \times 2$ which consists of 1800 brick elements. Therefore in order to achieve reliable results for plates using brick elements, the mesh density must increase substantially in all directions. The reason for the inaccuracy of the 8-node brick element when using a sparse mesh density is mainly due to the shear locking issue in the 8-node brick element which does not happen in the wedge element in which the interpolation of dependent variables is quadratic. The additional shear stress as a result of linearity of the brick element makes it stiffer than the actual plate model and therefore any given modal frequency of the plate increases.

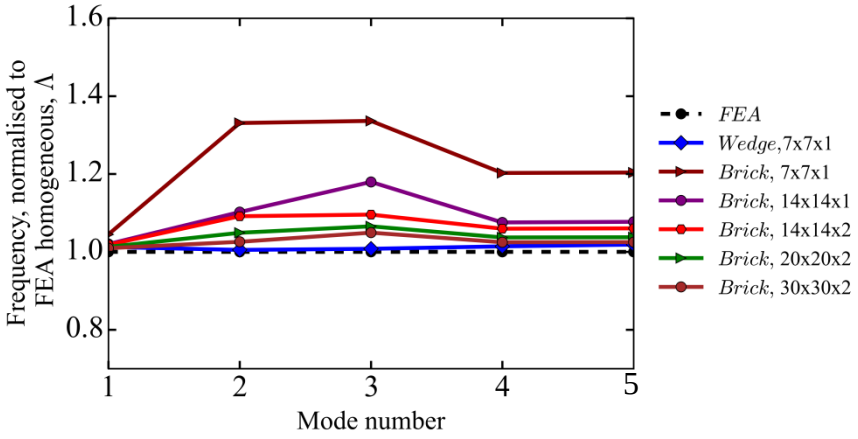

Figure 7-6: Normalised frequency of homogeneous plates with various line divisions and brick element in comparison with a plate with 15-node wedge element. Frequencies of five modes normalised to the frequencies obtained from FEA homogeneous plate with NCy=1, AR=8.083 and Sy=0.866 mm

7.5 Validation of the 3D-MPFEM and 15-node wedge element

A square homogeneous plate with the depth of 0.866 mm and the aspect ratio of 10 was modelled using the 3D-MPFEM in which the length and width of the plates were divided into 20 equal divisions and one division throughout the depth of the plate. This line division constitutes a plate with 400 elements (15-node wedge), and the first eight dimensionless modal frequencies were obtained for this plate with unconstrained boundary conditions, see table 7-3. Also, a plate with the dimensions mentioned above was modelled, and the first eight dimensionless modal frequencies were obtained by FEA with 334080 brick elements (20-node).

As stated explicitly in chapter two, as yet there is not an exact solution available for a two dimensional Mindlin plate with FFFF boundary conditions, however, there are some limited results available in the literature which used the Ritz method that could be used for verification of the 3D-MPFEM. Eftekhari et al. (2013) used a method termed the mixed finite element differential quadrature formulation (Mixed FE-DQ) and derived the first eight non-dimensional frequency parameters for plates with different boundary conditions. They also provided results based on the Pb2-Ritz method that was previously developed by Liew et al. (1993) in which two-dimensional polynomials were used as the admissible displacement and rotation functions in this Rayleigh-Ritz based method. Table 7-3 provides the results for the homogeneous isotropic plate with aspect ratio equal to 10:1 in which the data in the second and third columns are extracted from the work of Eftekhari et al. (2013).

Table 7-3: non-dimensional frequency parameters for an unconstrained square homogeneous plate with the aspect ratio equal to 10 using various numerical methods.

					Relative difference of 3D-MPFEM with		
Mode Number	FE-DQ	Pb2-Ritz	3D-Plate FEA	3D-MPFEM	FE-DQ	Pb2-Ritz	3D-Plate FEA
1	1.2887	1.2887	1.2891	1.2877	-0.0008	-0.0008	-0.0011
2	1.9194	1.9194	1.9205	1.9141	-0.0027	-0.0027	-0.0033
3	2.3633	2.3633	2.3654	2.3588	-0.0019	-0.0019	-0.0028
4	3.2343	3.2344	3.2376	3.2273	-0.0022	-0.0022	-0.0032
5	3.2344	3.2344	3.2381	3.2280	-0.0020	-0.0020	-0.0031
6	5.6082	5.6084	5.6222	5.5929	-0.0027	-0.0028	-0.0052
7	5.6082	5.6084	5.6222	5.5951	-0.0023	-0.0024	-0.0048
8	5.6449	5.6450	5.6557	5.6330	-0.0021	-0.0021	-0.0040

The relative difference of the values of the first eight modal frequencies, obtained by using 3D-MPFEM, with the results from FEA, FE-DQ and Pb2-Ritz methods, which are provided in table 7-3, verify the accuracy of the 3D-MPFEM with an error of less than -0.0052.

7.6 Conclusions

A set of algorithms which incorporate the linear isotropic micropolar theory into the conventional finite element method were developed for modal analysis of 3D plates. In the development of the finite element algorithms, both 15-node wedge and 8-node brick elements were used in the implementation of the algorithms as described in this chapter, and the method was named 3D-MPFEM or MPFEM for short. The micro-inertia and mass matrices were then incorporated into the algorithms. The micropolar elastic constants in a heterogeneous plate facilitate investigating size effects in such plates and enable the comparison of the predicted modal frequencies with those of actual plates with various types of heterogeneities which will be covered in chapters eight and nine.

Homogeneous plates modelled with 15-node wedge and 8-node brick elements were compared and the advantages of 15-node wedge element were discussed. The application of the wedge element was then favoured over the use of brick element because of its versatility and robustness in modelling and modal analysis.

The application of the 15-node wedge element in modal analysis especially in heterogeneous plates has not been previously studied by researchers; therefore, the 3D-MPFEM is a novel approach in the dynamic analysis of such plates which is capable of forecasting the size effects anticipated in them.

In the next two chapters, heterogeneous plates with cylindrical and spherical voids and inclusions will be modelled, and the modal frequencies acquired by FE modal analysis will be compared with the results which are generated using the 3D-MPFEM which uses the advantages of 15-node wedge element in modelling of nonhomogeneous plates.

8 Size Effects in 3D Heterogeneous Plates with Cylindrical Voids or Inclusions

In this chapter, the free vibration of unconstrained square plates is studied with specific focus again being on the size effect phenomenon in heterogeneous materials. Plates with cylindrical-type voids and inclusions were modelled, the cross section of which resemble beam categories similar to those studied in chapter three which are then extruded in the direction that is normal to the x-y plane. The general methodology of studying the size effect is unchanged which means that the overall properties of the plates such as modulus of elasticity, Poisson's ratio and the mass density were kept unchanged for all plate types. Unlike the previous chapters, here the longitudinal and transverse modes were not categorically segregated or studied separately and therefore the full spectrum of the modal frequencies was investigated. The main reason is that the first eight mode shapes appear in sequence and only include transverse modes. The longitudinal modes, in horizontal directions (in x-z plane), parallel to the plane of the plate appear after the eighth modal frequency for which the micropolar theory is incapable of anticipating size effects correctly anyway. Secondly, in relation to the plate's longitudinal vibration, the micropolar theory is again incapable of anticipating any size effect.

In fact, the beam models which were studied in chapter three, are extruded to construct three dimensional plate models which allows the use of two micropolar constants (l_b and N) that were already obtained for the 2D materials thereby permitting the identification of the remaining micropolar constants (l_t and Ψ) and study the size effect in 3D heterogeneous materials. Therefore, going from 2D beams' modal analysis to 3D heterogeneous plates' modal analysis seems to be a logical progression. The other important point which must be addressed here is that in the application of the 3D-MPFEM, isotropic micropolar plates are created and analysed while FE method creates 3D plate models with cylindrical extrusions which are anisotropic, although this thesis has attempted to reduce the anisotropic effect to as minimum as practically possible. The issue of the degree of anisotropy of heterogeneous plate models with cylindrical voids and inclusions will be addressed in section 8.2.2.

8.1 Finite element modelling of plates with cylindrical voids or inclusions and mesh refinement

Cylindrical type voids or inclusions were considered for modelling the heterogeneous plates. Therefore, plates with voids and one isotropic matrix material, plates with two isotropic materials comprised of stiff matrix but compliant inclusions, and finally plates with compliant matrix and stiff inclusions were all modelled. The surface conditions of the top and bottom surfaces of the plates were considered to be either continuous or textured. Therefore, six plate types in total were modelled as follows:

1. Plates with cylindrical voids and continuous boundaries (CYVOCB)
2. Plates with cylindrical voids and textured boundaries (CYVOTB)
3. Plates with cylindrical compliant inclusions and continuous boundaries (CYCICB)
4. Plates with cylindrical compliant inclusions and textured boundaries (CYCITB)
5. Plates with cylindrical inclusions, compliant matrix and continuous boundaries (CYCMCB)
6. Plates with cylindrical inclusions, compliant matrix and textured boundaries (CYCMTB)

Referring back to chapters four to six, the micropolar constants were only obtainable for the first, third and sixth plates types of the above list which are distinguished as CYVOCB, CYCICB and CYCMTB.

The FEA results are presented for all of the above categories while, in this chapter, the 3D-MPFEM results for the plate types CYVOCB, CYCICB and CYCMTB are presented and discussed.

8.1.1 Unit-cells with cylindrical void or inclusions

For each plate type, specific three-dimensional unit cells were modeled using 20-node Solid element type with ANSYS APDL version 17, see the semi unit-cells (half sized) in figure 8-1. The line divisions are the same as the earlier beam models in their 2D forms presented in chapter three and the only difference is that the unit-cells are three-dimensional here, this being achieved by extruding the 2D plane models in the z direction with the extended lines in the direction of S_z being divided into 14 equal divisions. The sign conventions are according to figure 7-1. The Cartesian coordinates may also be indicated by integers 1, 2 and 3. By repeatedly regenerating the unit cells as needed, plate types of required thickness and aspect ratios were modeled. The height of the unit cells remained

unchanged at 0.866 mm, and the aspect ratio (length or width to height ratio) for all plates was 8.083:1 which resulted in modelling the smallest squared plate samples so that they contained seven cylindrical voids or inclusions along the plate edge and one unit-cell through the plate thickness which thus form a plate model with 49 unit-cells in total; and this is increased by eight times when the plate depth is multiplied by two for the second smallest plate and so forth. The length and width of unit cells were equal to 1 mm, and the successive layers of voids and inclusions were such that the center points of every three neighboring cylinders forms an equilateral triangle. This, as the heterogeneity arrangement, was aimed at reducing or avoiding the anisotropic characteristics of the material as much as practically possible. Voids and inclusions in plate models are unidirectional and normal to the length of the plates (they are extruded in z direction). Therefore, the plates are squared which eliminates the need for a separate investigation into the importance of cylinder orientation in a plane parallel to the mid-plane. Inclusion and matrix are of two isotropic materials with a matrix to inclusion stiffness ratio of 10:1 for the third and fourth plate types (CYCICB and CYCITB) and 1:10 for the fifth and sixth plates plate categories (CYCMCB and CYCMTB).

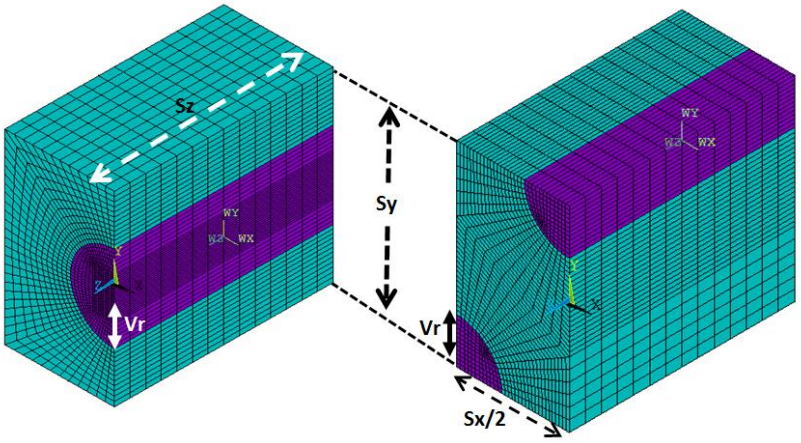

Figure 8-1: Representation of half unit cells of two isotropic materials with void or inclusion's volume fraction 15%. The unit cell on the left is used to model 3D plates with continuous boundaries e.g., CYCICB (with inclusions) or CYVOCB (without inclusions) and the unit cell on the right-hand side is used for plates with textured boundaries (e.g., CYCMTB).

8.1.2 Mesh refinement of the unit-cells

Two plate models with continuous and textured boundary surfaces and containing compliant inclusions were studied and presented here to show that the plate models under investigation satisfy the requirements of mesh convergence. The modal frequencies of plates with $NCy = 1$, $AR = 8.083:1$, $S_y = 0.866mm$ and $V_f = 0.15$ ($r = 0.2\,mm$) with cylindrical inclusions

were studied for mesh convergence while changing the element density of the unit-cell as the average error are provided in tables 8-1 and 8-2:

Table 8-1: Mesh convergence for the plate samples with compliant inclusions and continuous boundaries (CYCICB) and $V_f = 0.15$

Number of elements in one unit-cell	**Number of nodes in one unit-cell**	**Average error for the primary mode**	**Average error for ten modes**	**Average error for 33 modes**
128	773	1.94E-04	2.63E-04	2.87E-04
624	3141	2.94E-05	5.65E-05	4.97E-05
3744	19980	4.90E-06	3.18E-05	2.39E-05
10240	45077	3.27E-06	3.09E-05	2.23E-05
34944	149405	1.50E-07	2.80E-06	2.20E-06

Table 8-2: Mesh convergence for the plate samples with compliant inclusions and textured boundaries (CYCITB) and $V_f = 0.15$

Number of elements in one unit-cell	Number of nodes in one unit-cell	Average error for the primary mode	Average error for ten modes	Average error for 33 modes
100	1124	7.65E-05	2.66E-04	3.56E-04
288	2788	1.86E-05	1.23E-04	1.29E-04
1734	12124	1.10E-06	2.95E-05	2.66E-05
4431	26816	2.07E-06	1.28E-05	1.10E-05
18270	94932	1.96E-06	1.35E-06	1.07E-06

As seen in tables 8-1 and 8-2, plates with about 3000 to 10,000 elements per unit cells satisfy the mesh convergence for the primary and first ten modes. The FEA plate models were created so that they contained elements per unit cells as given in the fourth row of tables 8-1 and 8-2. The average errors in these tables are small values but the relative error simultaneously increases with mode number which must be noted if higher mode numbers are to be investigated.

8.2 Adjusting the modulus of elasticity (E) and mass density (ρ) of the unit-cells with cylindrical voids or inclusions

Now that the heterogeneous plates are modelled, the matrix and inclusions Young's modulus and material density must be adjusted so that the overall homogenised properties of the plate remain unchanged. However, by adjusting the material properties, some degree of anisotropy in plate properties will occur which are also noted and quantified in this section.

8.2.1 Obtaining modulus of elasticity (E) and mass density (ρ)

The cylinders' radius varied from 0.1 to 0.3 mm, in 0.05 mm intervals, giving void or inclusions volume fractions of 4, 8 15, 23 and 33 percent respectively. In this chapter as

previously, volume fraction, void radius or normalised void radius are used interchangeably, and their relations are provided in table 8-3 for clarification.

By regenerating and repeated reflection of the unit cells in x, y and z directions, plates with continuous and textured boundaries of minimum one to maximum of four unit cells in the plate depth were created. This modelling procedure provides plates of four sizes and varying volume fractions for each of the three plate types as introduced earlier in section 8.1. This procedure was performed while keeping the overall material properties namely the mass of the unit cells and elastic modulus of the plates unchanged at 2700 kg/m^3 and 7E10 Pa for density and Young's modulus respectively. Therefore, it is believed that changing the volume fraction of each plate of any specified size or type won't affect the overall homogenised material properties of the plate samples. The correction of elastic modulus was done by performing tensile test simulations using FEA, and the correction of density was done by keeping the mass and volume of the unit cells constant but changing the density of the constituent isotropic materials. The corrected materials properties are provided in table 8-4, 8-5 and 8-6. Figure 8-2 illustrates the cross-section of example plates and the arrangement of unit cells for two plate types.

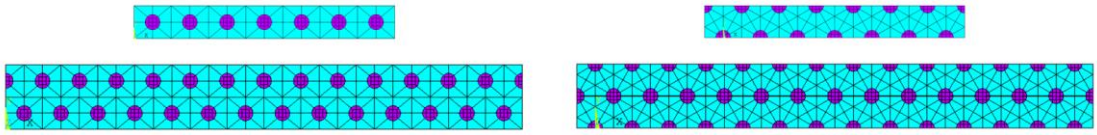

Figure 8-2 : Models' cross sections with periodically located cylindrical voids or inclusions showing the arrangement of unit cells in plates; a) Plate size 1 with 7 unit cells with continuous boundaries (top, left); b) Plate size 2 with 14 unit cells in length and width with continuous boundaries (bottom, left); c) Plate size 1 with 7 unit cells with textured boundaries (top, right); d) Plate size 2 with 14 unit cells in length and width with textured boundaries (bottom, right)

Table 8-3: Volume fraction and normalised equivalent of *cylindrical* void or inclusions

Void/inclusion radius, r, [mm]	0.1	0.15	0.2	0.25	0.3
Cylindrical void or inclusion volume fraction, %	4%	8%	15%	23%	33%
Normalised radius, V_r/S_y	0.12	0.17	0.23	0.29	0.35

Table 8-4: Corrected modulus of elasticity for plate's matrix. Inclusions modulus is either 0.1 or 10 times the values of this table depending on plate type. These FE plate types are those for which micropolar solutions were obtained

	The modulus of elasticity of matrix, MPa					
	Plates with Continuous boundaries				Plates with Textured boundaries	
Cylindrical void or inclusion radius, mm	Plates with cylindrical voids and continuous boundaries (CYVOCB)	Relative diff. with the homogen-eous beam	Plates with cylindrical compliant inclusions and continuous boundaries (CYCICB)	Relative diff. with the homoge-eous beam	Plates with cylindrical inclusions, compliant matrix and textured boundaries (CYCMTB)	Relative diff. with the homoge-neous beam
0	7.00E+04	3.16E-05	7.000E+04	2.30E-05	7.000E+04	4.07E-05
0.1	7.75E+04	8.36E-05	7.56E+04	5.33E-05	6.57E+04	7.40E-05
0.15	8.80E+04	5.63E-05	8.31E+04	7.31E-05	6.12E+04	9.22E-05
0.2	1.05E+05	9.27E-05	9.48E+04	7.31E-05	5.56E+04	8.92E-05
0.25	1.31E+05	2.60E-05	1.12E+05	8.36E-05	4.91E+04	4.37E-05
0.3	1.75E+05	3.16E-05	1.37E+05	2.30E-05	4.19E+04	4.07E-05

Table 8-5: Corrected modulus of elasticity for plate's matrix. Inclusions modulus is either 0.1 or 10 times the values of this table. These FE plate types are those for which micropolar solutions were not obtained

	The modulus of elasticity of matrix, MPa					
	Plates with Continuous boundaries		Plates with Textured boundaries			
Cylindrical void or inclusion radius, mm	Plates with compliant matrix and continuous boundaries (CYCMCB)	Relative diff. with the homoge-neous beam	Plates with cylindrical voids and textured boundaries (CYVOTB)	Relative diff. with the homoge-neous beam	Plates with cylindrical and compliant inclusions and textured boundaries (CYCITB)	Relative diff. with the homoge-neous beam
0	7.00E+04	4.38E-05	7.00E+04	1.25E-05	7.00E+04	8.36E-05
0.1	6.59E+04	7.75E-05	7.77E+04	4.28E-05	7.57E+04	5.36E-05
0.15	6.15E+04	5.16E-05	8.82E+04	1.25E-05	8.32E+04	2.60E-05
0.2	5.60E+04	7.49E-05	1.05E+05	1.39E-05	9.47E+04	8.66E-05
0.25	4.95E+04	8.01E-05	1.30E+05	2.30E-05	1.11E+05	8.31E-05
0.3	4.22E+04	4.38E-05	1.72E+05	1.25E-05	1.37E+05	8.36E-05

Table 8-6: Corrected density of the plate's unit cell by void or inclusions radius

cylindrical voids or inclusion radius, mm	The mass density of matrix and inclusions, kg/m^3		
	Plates with cylindrical voids	Plates with cylindrical inclusions	
	For matrix	For matrix	For inclusions
0	2700.00	2700.00	N/A
0.1	2801.64	2546.94	6766.11
0.15	2939.97	2672.70	3007.16
0.2	3158.29	2871.18	1691.53
0.25	3491.67	3174.25	1082.58
0.3	4008.87	3644.43	751.79

8.2.2 The effect of anisotropy in plates with cylindrical voids or inclusions

The tensile test simulations on the plate models were carried out in x-direction based on which the modulus of elasticity of the matrix material was adjusted and provided in tables 8-4 and 8-5 for various volume fractions. The moduli of elasticity of inclusions were also assumed to be different from the modulus of elasticity of matrix material by a factor of ten depending on the plate model types. Although the macroscopic modulus of elasticity in

the x-direction, E_x , is unchanged and equal to 70E3 MPa, the corresponding modulus of elasticity in the z-direction, E_z , (perpendicular to the x-direction) for various volume fractions changes which indicate that the plate models will demonstrate some degrees of anisotropy. The degree of anisotropy (DA) was obtained by tensile test simulations in the z-direction, and the relative difference of E_z to E_x was calculated for various volume fractions. However, the anisotropy in plate models varies with volume fraction as seen in table 8-7:

Table 8-7: The degree of anisotropy in heterogeneous plate models with cylindrical voids and inclusions

	The relative degree of anisotropy [(Ez-Ex)/Ez]		
Volume fraction	**Plates with compliant inclusions and continuous boundaries**	**Plates with voids and continuous boundaries**	**Plates with compliant matrix and textured boundaries**
0.00	0.00	0.00	0.00
0.04	0.04	0.06	0.20
0.08	0.09	0.13	0.34
0.15	0.15	0.22	0.46
0.23	0.21	0.31	0.53
0.33	0.28	0.41	0.58

The values in table 8-7 indicate that the plates with void or compliant inclusions and volume fraction of less than 0.15 can be assumed to be relatively isotropic, and the plates with higher volume fractions as plates with a higher degree of anisotropy. On the contrary, the plates with a compliant matrix exhibit a higher degree of anisotropy even for lower volume fractions. Therefore, the dynamic behaviours of the heterogeneous plate models with a lower degree of anisotropy (DA) are expected to be explained by the results from 3D-MPFEM which only models isotropic micropolar plates. The results for heterogeneous plates are compared and discussed in section 8.5.

8.3 Modal analysis procedure and mode shapes

In finite element modal analysis, the PCG Lanczos solver and distributed memory were used for modal analysis of plates. This method is as accurate as Block Lanczos and is widely used for models with a large number of degrees of freedom. A detailed comparison between the two methods and their applicability are given in reference (Beisheim 2007).

The first 8 mode shapes using finite element analysis are shown in figures 8-3-a to 8-3-h and as it can be seen every mode has its own distinct shape. The first mode is known as the twist

mode (figure 8-3-a), the second mode is known as the saddle type mode or hyperbolical surface (figure 8-3-b) and the mode shape in figure 8-3-c is known as the ellipsoidal surfaced type mode. The rest of modes show very distinct mode shapes in which the number of transverse lobes (waves) increases with the mode number. The twisting modes are shear deformation dominated such as in mode one where l_t is the key influencing parameter in their dynamic behaviour while modes two and three are bending deformation dominated in which l_b is the principal influencing parameter rather than l_t. Thus, from the transverse mode four onward, the dynamic behaviour of the plate models, both shear and bending deformations are the prevailing factors. However, the longitudinal modes in an FFFF boundary condition case appear usually after mode 8 which are therefore not presented in this chapter.

The non-dimensional modal frequencies for homogeneous plates (Ω) which are given in table 8-8 and used for normalisation of the plate modal frequencies in the figures provided in sections 8.4 and 8.5, are derived using equation (8.1) as follows:

$$\Omega = \frac{\omega LW}{\pi^2}\sqrt{\frac{\rho d}{D}} \tag{8.1}$$

where L is the plate length, W (=L) is the plates width, d is the plate depth which may also be shown by "h" while D is the flexural rigidity:

$$D = \frac{Ed^3}{[12(1-\nu^2)]} \tag{8.2}$$

Table 8-8 : The non-dimensional frequencies (Ω) for homogeneous plates with AR=8.083:1

Mode	**1**	**2**	**3**	**4**	**5**	**6**	**7**	**8**
ANSYS FEA	1.266325	1.889482	2.321783	3.138321	3.138415	5.388943	5.389036	5.395208
MPFEM	1.265003	1.884909	2.317066	3.130562	3.130925	5.36872	5.369923	5.378121

In this chapter, the finite element results are only presented when being compared to the predictions of 3D-MPFEM in the sections that follow. However, the FEA and 3D-MPFEM results are listed in Appendix E.1 and E.2.

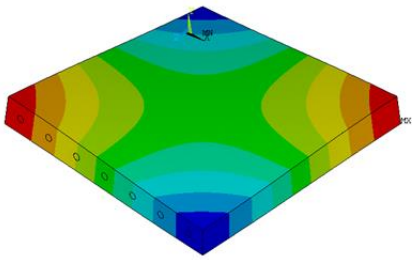

a) Mode 1, Twist shape

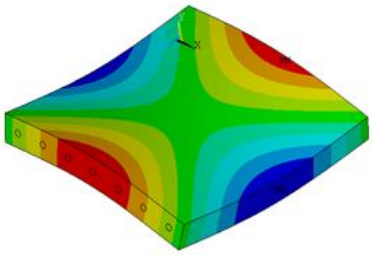

b) Mode 2, (hyperbolical surface) Saddle shape

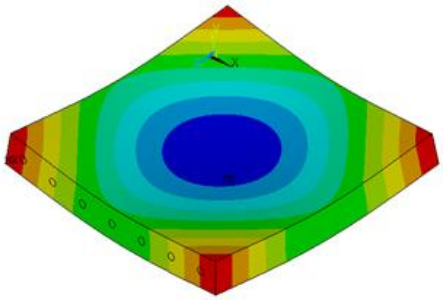

c) Mode 3, (ellipsoidal surfaced) Bending Type

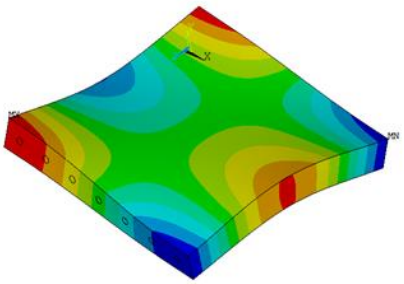

d) : Mode 4

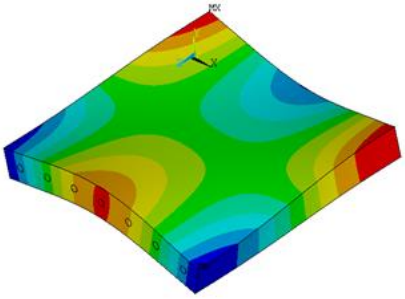

e) Mode 5

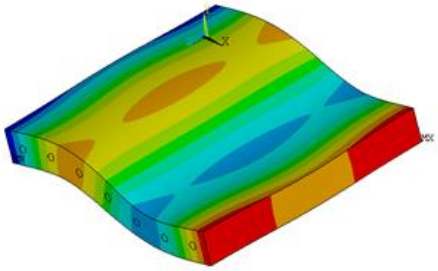

f) Mode 6

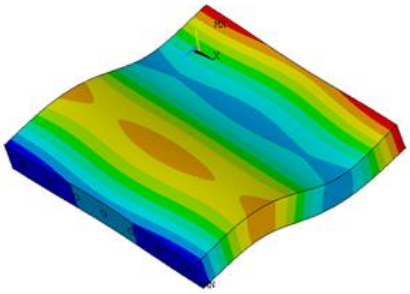

g) Mode 7

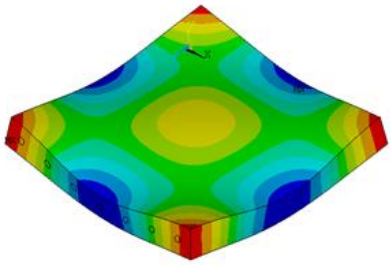

h) Mode 8

Figure 8-3: The first 8 mode shapes (a to h) of a sample plate with cylindrical inclusions of volume fraction equal to 0.15 and continuous boundaries (NCy=1) generated by FEA. Note that the first eight mode shapes of the homogeneous plate as well as other plate models with textured boundaries are similar to the mode shape figures here also.

The mode shapes of the micropolar plates were also extracted using the 3D-MPFEM. As an example, the first eight mode shapes for a plate model with the depth of 2 unit cells; $h = 2 \times 0.866;\ V_f = 0.15; l_b = 0.6084\ ; l_t = 2 \times l_b\ , N = 0.0507\ , \Psi = 1.5, \nu_m = 0.3\ , E_m = 7 \times 10^{10}\ MPa$, corresponding to CYVOCB are provided in figures 8-4-a to 8-4-h. The

micropolar plate mode shapes generated were qualitatively similar to those in figures 8-3-a to 8-3-h for plates modelled using FEA which indicate that 3D-MPFEM identifies the first mode as twisting, second and third modes as bending and the rest of the transverse modes are dominated by both shear and bending deformation.

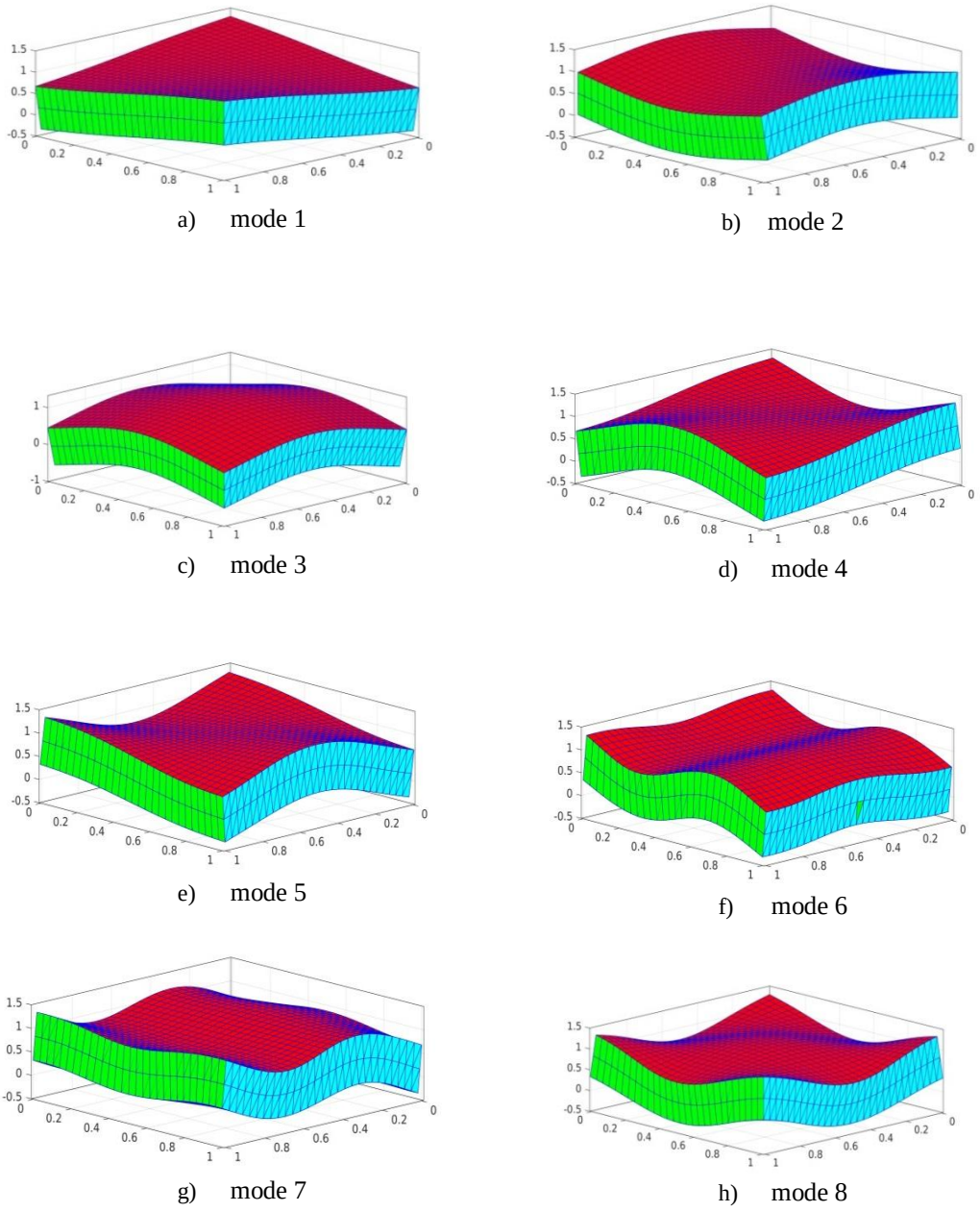

a) mode 1 b) mode 2

c) mode 3 d) mode 4

e) mode 5 f) mode 6

g) mode 7 h) mode 8

Figure 8-4: MPFEM extracted mode shapes for a plate model with the depth of 2 unit cells; $h = 2 \times 0.866$; $V_f = 0.15$; $l_b = 0.6084$; $l_t = 2 \times l_b$, $N = 0.0507$, $\Psi = 1.5$, $\nu_m = 0.3$, $E_m = 7 \times 10^{10}\ MPa$,

8.4 Micropolar elastic constants

Here, in the three-dimensional modal analysis, the micropolar Poisson's ratio is assumed to be equal to 0.3, micropolar modulus of elasticity, E_m, equal to 7E10 Pa; the characteristic length in bending and the coupling number are as given in tables 4-3 and 6-1 and were obtained from the two dimensional plane stress case, the method of which is provided in chapters 4 and 5, and for greater accuracy, these two constants were obtained by considering only the beam models of depth 2, 3 and 4 array of voids or inclusions. Finally the polar ratio is assumed to be 1.5 as already indicated.

The modal analysis of micropolar plates with three unit cells in height and cylindrical voids, as will be explained in section 8.4.1, indicates that the characteristic length of torsion must forecast the behavior of higher modes as well as the first mode which is twisting dominated. Therefore, three values for the characteristic length of torsion $l_t = 2l_b$, $l_t = l_b$ and $l_t = 0.5l_b$ had been tried and its influence on the frequency predictions are investigated and qualitatively illustrated.

In modal analysis of a micropolar plate, small displacements in the absence of any external load with FFFF (unconstrained plate edges) boundary conditions are sought in order to investigate size effect predictions by micropolar theory when the microstructural dimensions are comparable to the overall size of the plate. It will be shown in the details given in this chapter and in chapter nine, that for specific non-homogeneous plates, the micropolar theory is capable of predicting size effect for the first few modal frequencies, that means the first 5 to 8 modes, but the micropolar theory lacks the ability to be reliable in predicting the frequencies of higher modes. It will also be shown in section 8.4.1 that selecting a characteristic length of torsion, l_t, equal to twice the characteristic length of bending, l_b , as has been used in other literature (Hassanpour and Heppler 2017), where it may be a valid estimation in static cases, may also be valid for lower mode numbers in the dynamic case.

As an extra verification of the characteristic length of bending which was identified through equation (4.46), by replacing the flexural rigidity, D, with $D + \gamma d$ in equation (8.1), a very useful and alternative equation for calculating the characteristic length of bending in plates can be derived as:

$$\Omega = \frac{\omega LW}{\pi^2}\sqrt{\frac{\rho d}{D + \gamma^* d}} \tag{8.3}$$

where $D + \gamma^* d$ is termed the flexural rigidity of the micropolar plate here, which was first derived by Gauthier et al. (1975) to relate the curvature to bending in a micropolar plate with small displacement, and is identified with $\overline{\overline{D}}$ here, and d is the depth of the plate. The extra micropolar term $\gamma^* d$ reflects the effect of micropolar constituent parameter,γ^*, in flexural rigidity of micropolar plates. $\overline{\overline{D}}$ is reducible to D when γ^* approaches zero for the flexural rigidity in a classical material.

By replacing D from equation (8.2), γ^* from equation (7.5) and knowing that $E_{mf} \approx E_m$:

$$\overline{\overline{D}} = \frac{E_{mf} d^3}{[12(1 - \nu_m{}^2)]} + \left(\frac{2E_m l_b^2}{1 + \upsilon_m}\right) d \tag{8.4}$$

Thus:

$$\overline{\overline{D}} = \frac{E_{mf} d^3}{[12(1 - \nu_m{}^2)]} \left\{1 + 24(1 - \upsilon_m)\left(\frac{l_b^2}{d^2}\right)\right\} \tag{8.5}$$

in the context of a square plate in which:

$$LW = L^2 = A^* \tag{8.6}$$

where A^* is the mid plane surface area of the plate.

Note that h and d are used interchangeably throughout for the depth (or height) of the plate; Therefore, by replacing $\overline{\overline{D}}$ from equation (8.5) and substituting into equation (8.3) and re-arranging:

$$\rho A^* \omega^2 = \frac{\pi^4 \Omega^2 E_{mf}}{12(1 - \nu_m{}^2)(AR)^2} \left\{1 + 24(1 - \upsilon_m)\left(\frac{l_b}{d}\right)^2\right\} \tag{8.7}$$

Equation (8.7) thus relates the characteristic length of bending, l_b , non-dimensional frequency parameter of the plate (applicable to mode two only), Ω, micropolar flexural modulus, E_{mf}, and plate dimensions, to the product of plate's mass density, ρ, multiplied by the mid plane surface area of the plate and the squared frequency. Thus, if this product is determined for plates of various sizes and plotted against the plate's reciprocal size measure, $(1/d^2)$, then it is possible to obtain E_{mf} or Ω from the intercept and the characteristic length from the slope. Thus equation (8.7) generates the same characteristic length of bending as equation (4.46).

Note that the equation (8.7) is not reducible to equation (4.46) because here ω is the transverse frequency of a rectangular plate and Ω is the non-dimensional frequency parameter of the plate. Therefore, equation (8.7) is only introduced and used as an alternative method to confirm the values obtained for the l_b.

8.4.1 Qualitative illustration of the influence of Ψ and l_t on modal frequencies

As referred to in chapters 4, 5 and 6, and based on the method introduced in reference (Hassanati and Wheel 2018) for the determination of elastic constants in two-dimensional beam models, l_b and N where determined for various beam models and these material property constants of l_b and N were used for plate models in this chapter accordingly because the heterogeneous plate types in this chapter are created by extruding the 2D beam models which were previously modelled and presented in chapter three.

The assumed values of l_t and Ψ, appear to be satisfactory for static cases (Altenbach and Eremeyev 2009; V. a. Eremeyev, Lebedev, and Altenbach 2013; Kouhia and Niemi 2013; V. A. Eremeyev, Skrzat, and Stachowicz 2016a) or even modal analysis (Steinberg and Kvasov 2015), but in this work, these assumptions have proved to have some shortcomings which are illustrated here.

These maximum values of l_t and Ψ qualitatively forecast the results for the first two modal frequencies, but are less reliable for the third mode and beyond. As is shown in figures 8-5, 8-6, and 8-7, by keeping the polar ratio at 1.5 but decreasing, l_t, to the values listed below, some improvement is achievable for mode three but at the expense of other modal frequencies. As an example, the plate samples CYVOCB with NCy = 3 and volume fractions, 0.4, 0.15 and 0.33 were investigated with following constants:

a) $\Psi = 1.5$, $l_t = 2l_b$, see figure 8-5
b) $\Psi = 1.5$, $l_t = l_b$, see figure 8-6
c) $\Psi = 1.5$, $l_t = 0.5l_b$, see figure 8-7

As seen in figure 8-5, by setting the value of $l_t = 2l_b$, the isotropic micropolar plate assumption leads to underestimating the modal frequencies at mode three compared with the FEA results for the heterogeneous plate models with higher volume fraction cylindrical voids which represent materials with a higher level of anisotropy. Nevertheless, decreasing the value of l_t causes an increase in the modal frequency at mode three for isotropic micropolar plates but then underestimates the primary and second modal frequencies for all volume fractions, as seen in figures 8-6 and 8-7.

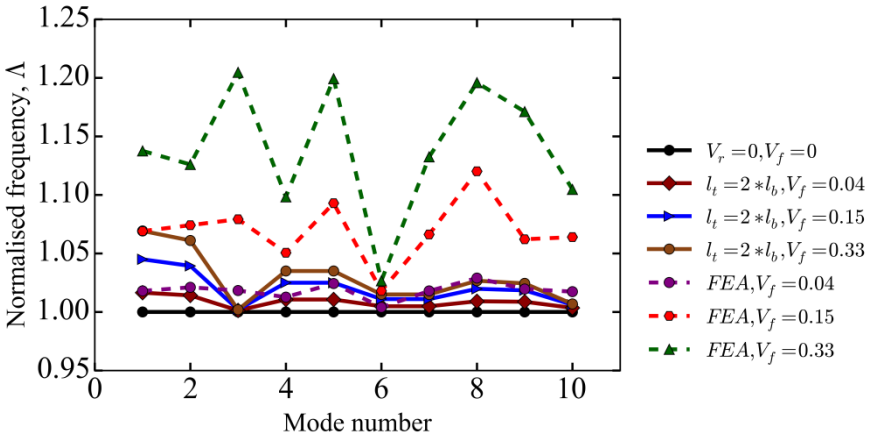

Figure 8-5: Changes of normalised frequencies of a micropolar plate (CYVOCB) with $l_t = 2 * l_b$, Ψ=1.5, NCy=3, $S_y = 0.866$ mm and AR=8.083 in comparison with corresponding FEA results (dotted lines).

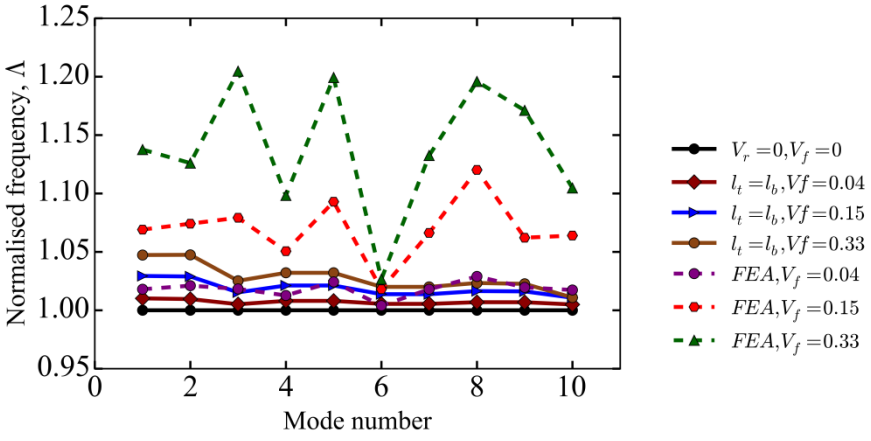

Figure 8-6: Changes of normalised frequencies of a micropolar plate (CYVOCB) with $l_t = l_b$, Ψ=1.5, NCy=3, $S_y = 0.866$ and AR=8.083 in comparison with corresponding FEA results (dotted lines).

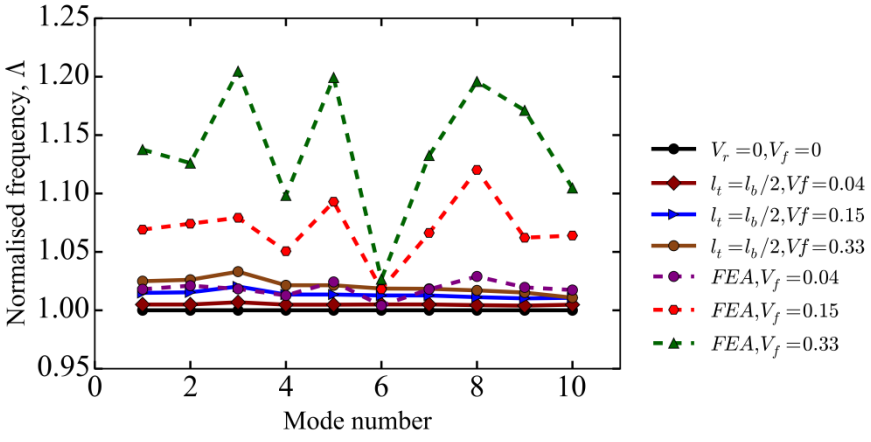

Figure 8-7: Changes of normalised frequencies of a micropolar plate (CYVOCB) with $l_t = l_b/2$, Ψ=1.5, NCy=3, $S_y = 0.866$ and AR=8.083 in comparison with corresponding FEA results (dotted lines).

In addition, a set of numerical analyses indicated that the smallest plate samples with higher volume fraction are more sensitive to the value of coupling number. The results in figures 8-8 and 8-9 indicate that the normalised frequencies produce more acceptable results for higher volume fractions when the characteristic length of torsion is set to twice the value of l_b. However, at mode three, the frequency values are under estimated as shown previously in figure 8-5.

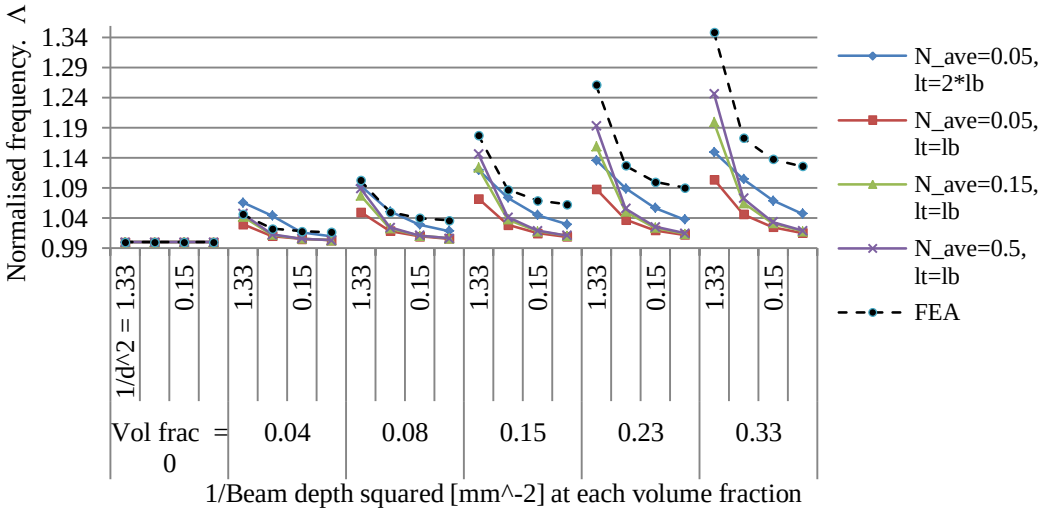

Figure 8-8: The influence of $\boldsymbol{l_t}$ and N on the primary modal frequencies of plates with CYVOCB

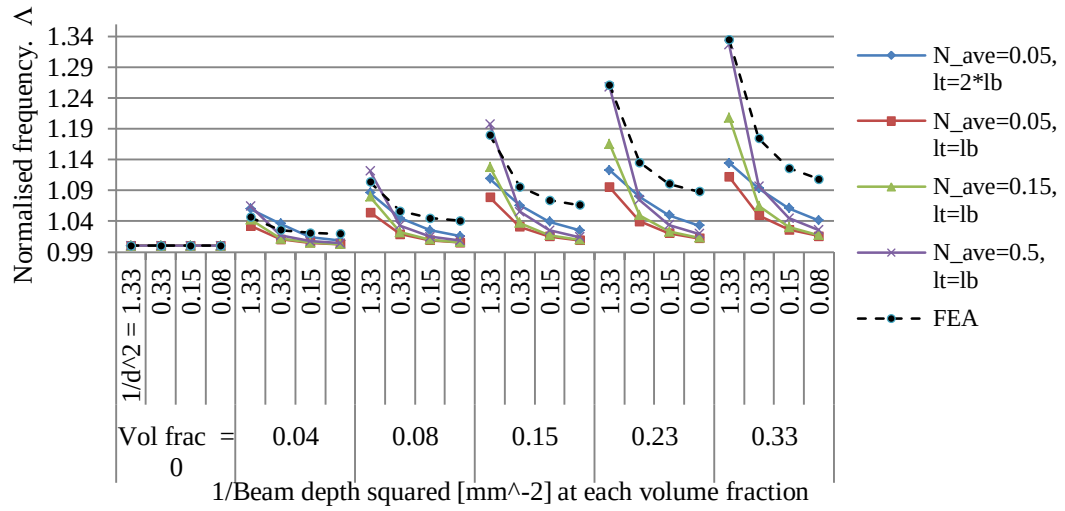

Figure 8-9: The influence of $\boldsymbol{l_t}$ and N on the second modal frequencies of plates with CYVOCB

8.5 Detailed results and discussions

In this section, the finite element results and the size effect predictions for plates with cylindrical voids or inclusions are presented, these results are also compared with those obtained by 3D-MPFEM and the size effect predictions for plates are discussed.

8.5.1 Plates with continuous boundaries

8.5.1.1 Plates with cylindrical voids and continuous boundaries (CYVOCB)

The modal frequencies obtained by finite element analysis were normalised by the values in table 8-8. Figure 8-10 shows the normalised modal frequencies for the primary mode of all four plate sizes, using FEA and indicates that the variation of normalised modal frequencies with the inverse of the squared sample depth, is approximately linear and this linear behavior is valid for all cylindrical void volume fractions. As the graph in figure 8-10 reveals, the size effect is highest for the smallest plate sample sizes, and thus more pronounced. The size effect reduces as the depth of the plate increases. This phenomenon is unique for every mode number and thus for every mode the gradient of the line varies which can be characterised as the behaviour of plates in such specific modal frequency. Of course, as the void's volume fraction increases, so does the gradient of the line which connects these normalised frequencies. This is precisely what was expected because adding more layers to the sample and reducing the void radius, will definitely reduce the sudden changes in stress gradients at each unit-cell throughout the depth of the plate and therefore, if one extrapolates the lines in the figure 8-10, the normalised frequency parameter of the plates will finally approach unity value and exhibit the behaviour of a homogeneous plate if the ratio of the volume fraction to the plate's depth is reduced to near zero.

It must be noted here that the plates with one layer of voids are structurally different from other specimens with more than one layer in the depth of the plate. In the 3-dimensional plate modeling, as explained in the previous section, the arrangement of the cylindrical voids in the material are such that they form an equilateral triangle with 60° angle to avoid anisotropic behavior but the smallest samples lack this fundamental arrangement. For this very reason, at some modes where bending is involved (other than mode one which is the first twisting mode) the normalised frequencies for the smallest sized sample do not correlate with other larger samples. This inconsistency of the modal frequencies of the smallest samples occurs for the higher modes too.

Figure 8-11 shows the normalised modal frequencies for the primary mode of all four plate sizes, exploiting the micropolar theory with the micropolar constants identified (E_m, l_b, N) or assumed (l_t, Ψ) previously. By comparing these data with the corresponding results in figure 8-10 for the finite element models, it can be concluded that for the primary modal frequencies:

- Micropolar plate theory can anticipate the size effect although the micropolar results are not correlated on a straight line.
- The normalised modal frequencies obtained for micropolar plates are slightly lower than the results from finite element modal analysis,
- The micropolar theory underestimates the modal frequencies for the smallest samples in comparison with the finite element modal analysis and this is understood to be due to the structural characteristics of the void arrangements which do not form equilateral triangles as seen in plates with two or more layers.

Figure 8-12 shows the FEA results for the first five normalised modal frequencies of five volume fractions which vary with mode number. The finite element predictions show that the homogeneous plates are not size dependent, as expected, these being represented by dotted lines with the value of unity. The results which were generated using the micropolar theory like the finite element results clearly demonstrate the size effect in a micropolar plate for only the first 2 modes, after which the normalised frequencies quickly reduced to near the homogenised case, see figure 8-13 . This suggests that the micropolar theory is not applicable to higher modal frequencies. It must also be noted that although mode shapes appear in sequential order, every modal frequency which is generated for the micropolar plate must be compared with the same mode number (mode shapes) of the FEA models because every modal frequency in the plate vibration is associated with a distinct shape.

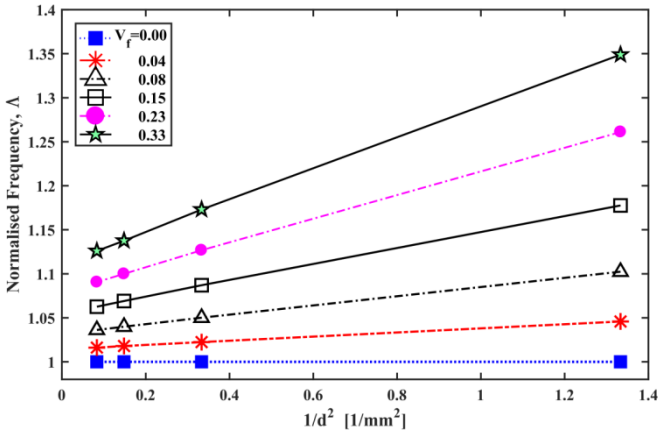

Figure 8-10: Normalised primary modal frequency of four plate sizes for plates with cylindrical voids and continuous boundaries using FEA (CYVOCB). $V_f = 0\ to\ 33\%$ ($V_r/S_y = 0.12\ to\ 0.35$)

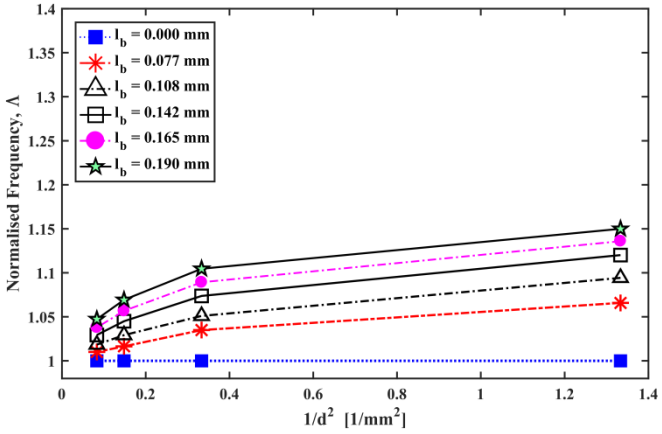

Figure 8-11: Normalised primary modal frequency of four plate sizes for plates with cylindrical voids and continuous boundaries using the micropolar theory (for CYVOCB).
($l_b = 0\ to\ 0.190\ mm\ corresponds\ to\ V_f = 0\ to\ 33\%$)

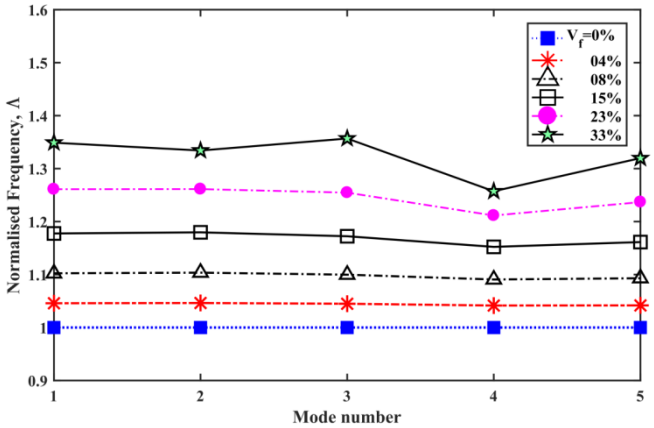

Figure 8-12: The first five normalised transverse modal frequencies of the smallest plate sample with voids and continuous boundaries using FEA. $V_f = 0\ to\ 33\%$ ($V_r/S_y = 0.12\ to\ 0.35$)

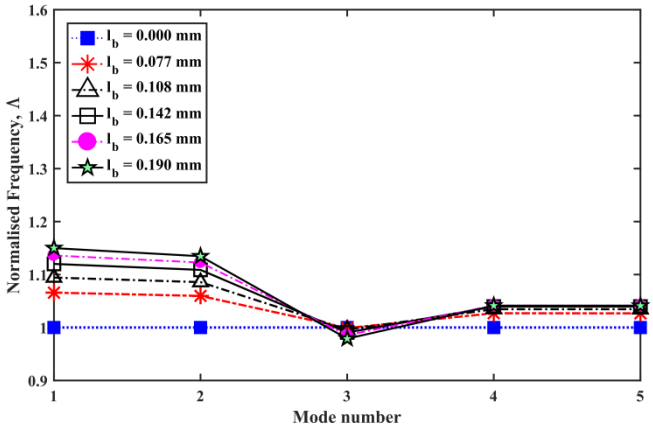

Figure 8-13: The first five normalised transverse modal frequencies of the smallest plate sample with voids and continuous boundaries using the micropolar theory.
($l_b = 0\ to\ 0.190\ mm\ corresponds\ to\ V_f = 0\ to\ 33\%$)

In figure 8-14 and 8-15 the primary and second modal frequencies for all plate depths and void volume fractions using FEA and micropolar theory for plates with voids and continuous boundaries are compared directly which clearly indicate that as the void volume fraction increases and plate sample size (depth) reduces, so the difference between the FEA and micropolar results is accentuated. The values of DA listed in table 8-7 are directly related to V_f. Therefore, the increased difference between FEA and 3D-MPFEM results at higher V_f is due to increasing anisotropy in the plate models. The results indicate clearly that the micropolar theory is able to predict modal frequencies in good agreement with FEA results for the first two modal frequencies and below volume fraction of 0.15 when the degree of anisotropy is low.

The FEA and micropolar dimensionless parameters of eight modes are provided in the Appendix E.

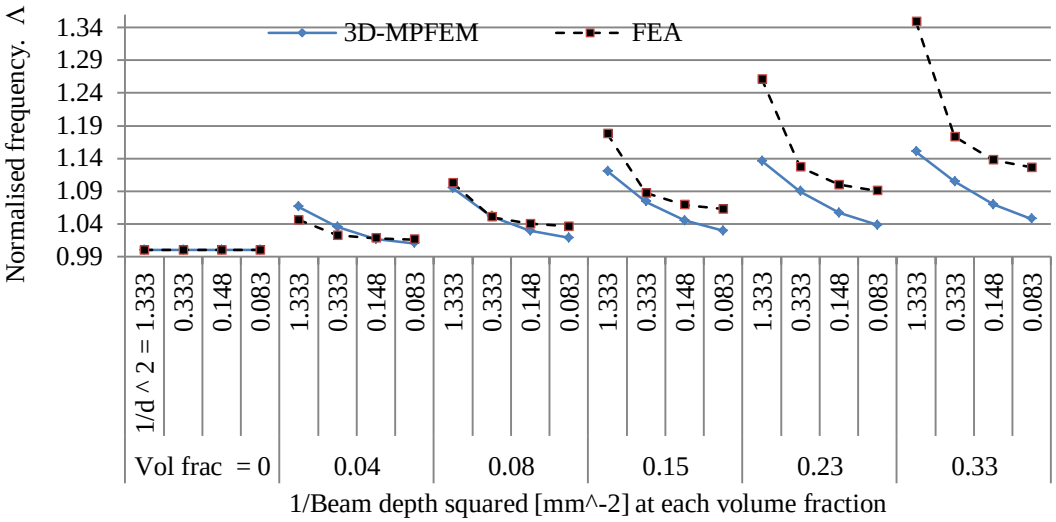

Figure 8-14: Primary normalised modal frequencies, mode 1, for plates with voids and continuous boundaries, CYVOCB

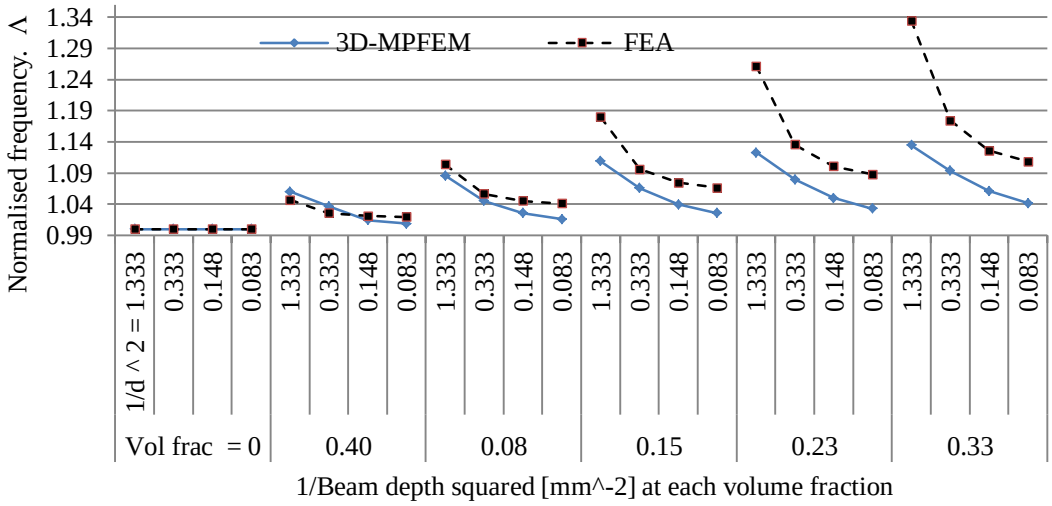

Figure 8-15: Second normalised modal frequencies, mode 1, for plates with voids and continuous boundaries, CYVOCB

The numerical results (modal frequency of plates) for the first 8 normalised modal frequencies of four plate sizes with cylindrical voids and continuous boundaries for $V_f = 0\ to\ 33\%$ ($V_r/S_y = 0.12\ to\ 0.35$) obtained using finite element for CYVOCB which are tabulated in table E-1 in Appendix E and indicate that the size effects at higher modes are qualitatively similar to the FE results for the smaller sample, as seen in figure 8-12, with considers the changes in volume fraction and the plate size.

8.5.1.2 Plates with cylindrical inclusions of compliant material (CYCICB)

The finite element results for plates with cylindrical inclusions of a compliant material show similar behavior to plates with cylindrical voids although the normalised frequencies are different. The main difference is that the gradients quantifying the size effect seem to be smaller than the plates with voids. The numerical results for eight normalised modal frequencies of this type of plates are given in Appendix E and the explanations provided in section 8.5.1.1 also appear to be valid for plates with cylindrical compliant inclusions (CYCICB) as well. The normalised modal frequencies presented in figure 8-16 indicate that the variation of frequency of the primary mode is linear with the inverse of the squared sample depth which is also valid for plates with cylindrical voids. The results for the primary mode also indicate that the gradient of the lines decreases with reducing volume fraction. This dynamic behaviour of plates with cylindrical and compliant inclusions has been observed already in the dynamic analysis of plates with cylindrical voids and continues boundaries; however, by direct comparison of the results in figure 8-16 and 8-10 it can be argued that the existence of inclusions in the plate models mitigates the size effect in comparison with plates with cylindrical voids.

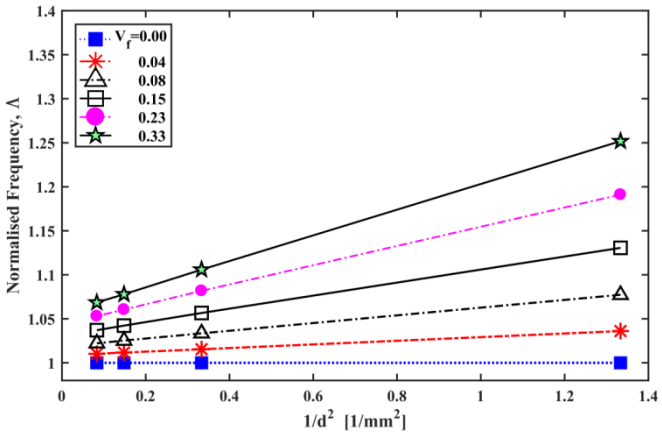

Figure 8-16: Normalised primary modal frequency of four plate sizes for plates with cylindrical compliant inclusions and continuous boundaries using FEA (CYCICB). $V_f = 0\ to\ 33\%$ ($V_r/S_y = 0.12\ to\ 0.35$)

The modal analysis results obtained by applying the micropolar theory show similar dynamic behaviour for the three largest plate samples for the normalised primary frequency values of the plate with cylindrical compliant inclusions and continuous boundaries (CYCICB) with the micropolar constants assumed or identified previously, as seen in figure 8-17. The size effect in the primary modal frequency of the plate samples using 3D-MPFEM is in close agreement with those obtained by finite element analysis except for the smallest plate model.

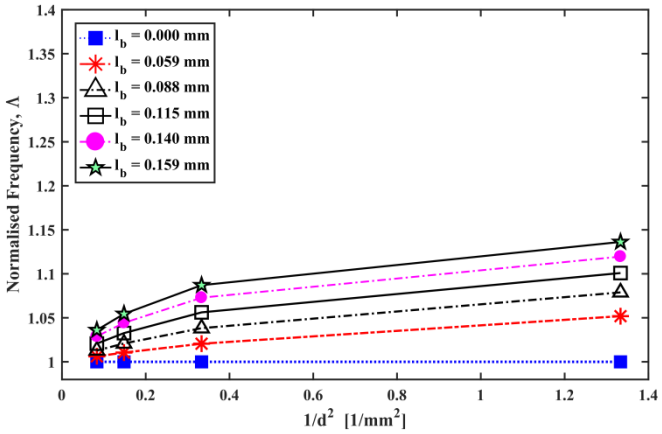

Figure 8-17: Normalised primary modal frequency of four plate sizes for plates with cylindrical compliant inclusions and continuous boundaries using MPFEM (CYCICB).
($l_b = 0\ to\ 0.159\ mm\ corresponds\ to\ V_f = 0\ to\ 33\%$)

Once again, similar to the results derived for plates with voids (CYVOCB), the underestimations in normalised values for the smallest plate sample, as shown in figure 8-17, are due to the void arrangements which do not form equilateral triangles as seen in plates with two or more layers. Thus, the normalised frequency values do not form a straight line and show underestimations in normalised frequency values which were obtained by using 3D-MPFEM.

The values of normalised modal frequencies of the first five normalised transverse modal frequencies of the smallest plate sample with compliant inclusions and continuous boundaries using FEA do not show sensitivity to mode number for the first three modal frequencies, as seen figure 8-18.

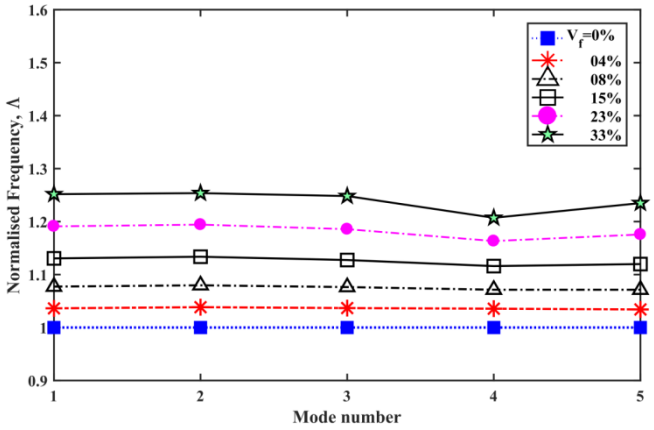

Figure 8-18: The first five normalised transverse modal frequencies of the smallest plate sample with compliant inclusions and continuous boundaries using FEA. $V_f = 0\ to\ 33\%$ ($V_r/S_y = 0.12\ to\ 0.35$)

The normalised frequency values obtained by applying the micropolar theory were not able to predict size effect at higher mode numbers beyond the second and tend to reach unity, see figure 8-19.

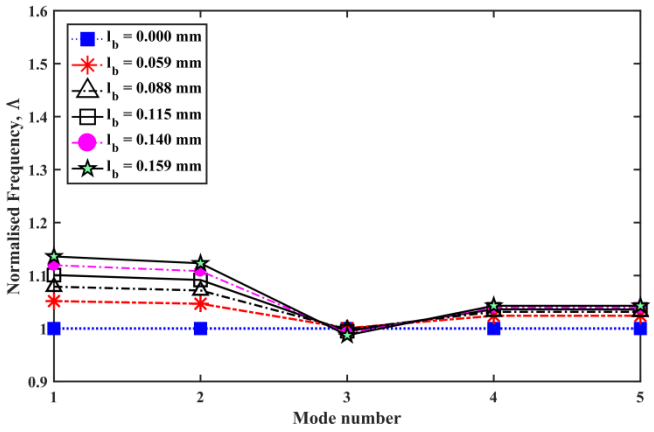

Figure 8-19: The first five normalised transverse modal frequencies of the smallest plate sample with compliant inclusions and continuous boundaries using MPFEM.
($l_b = 0\ to\ 0.159\ mm\ corresponds\ to\ V_f = 0\ to\ 33\%$)

Note that, the micropolar plates which are modelled and analysed by 3D-MPFEM are isotropic while the representative plates which are modelled by FEA are not isotropic despite arranging the cylindrical inclusions in an equilateral triangles form. However, the first two normalised frequencies, which were obtained by using the available micropolar constants, show some agreement with the FEA results and the size effect is clearly forecast. Figure 8-20 shows the primary normalised modal frequencies for plates with compliant inclusions and continuous boundaries, which indicate that the micropolar plate models significantly under-estimates the normalised frequency values predicted by FEA for the smallest sample size when the volume fraction is greater than 0.15. Again, as explained in the previous section, the increased difference between FEA and 3D-MPFEM at higher V_f is due to increasing anisotropy in the plate models with compliant inclusions and continuous boundaries. However, the 3D-MPFEM results here are in better agreement with the FEA results because the degree of anisotropy, as provided in table 8-7, is lower compared with plates with voids.

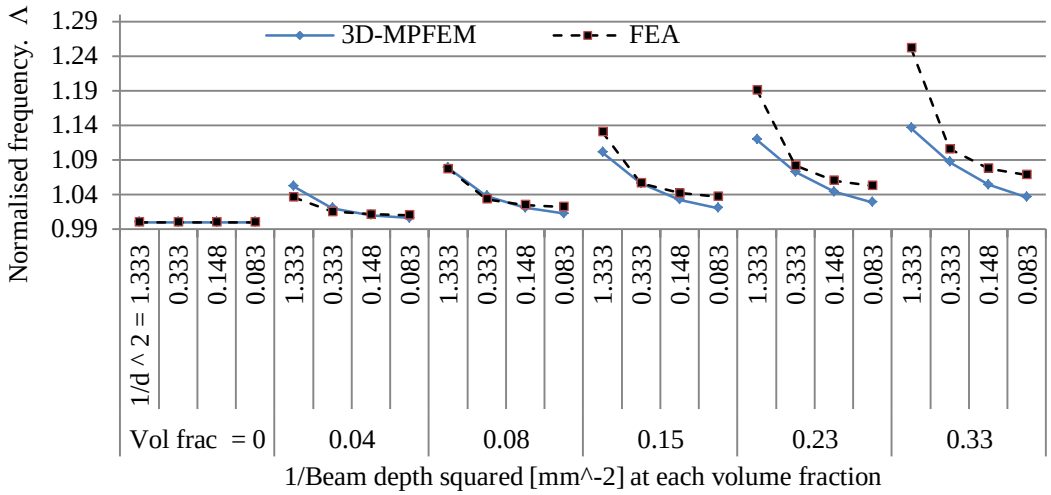

Figure 8-20: Primary normalised modal frequencies, mode 1, for plates with compliant inclusions and continuous boundaries, CYCICB

The first 8 normalised modal frequencies of four plate sizes with cylindrical inclusions and continuous boundaries for $V_f = 0\ to\ 33\%$ ($V_r/S_y = 0.12\ to\ 0.35$) using finite element analysis (CYCICB) are tabulated in table E.2 in Appendix E and indicate that the size effect at higher modes for the three larger sizes are qualitatively similar to the FEA results for the smaller sample, as seen in figure 8-18.

8.5.1.3 Plates with cylindrical inclusions of stiff material but compliant matrix (SYCMCB)

Plates with cylindrical inclusions of stiff material but compliant matrix, (SYCMCB), show a different size effect in modal frequencies in comparison with plates with voids and /or compliant inclusions, as the gradient of the lines which connect the normalised modal frequencies at each volume fraction is negative, as seen in figure 8-21. This type of size effect could not be predicted by the micropolar theory either because the micropolar constant the coupling number, N, could not be obtained for a material with such heterogeneities using the analytical method which was provided in chapter five.

Figure 8-21 shows the normalised primary modal frequency of four plate sizes for plates with cylindrical inclusions, compliant matrix and continuous boundaries (CYCMCB) using FEA. The negative slope of the lines indicates that increasing volume fraction causes a decrease in Λ at a given mode number for larger sample sizes with more than two unit-cells across the depth of the plates. However, the size effect although inverted nevertheless remains approximately linear across the plate samples.

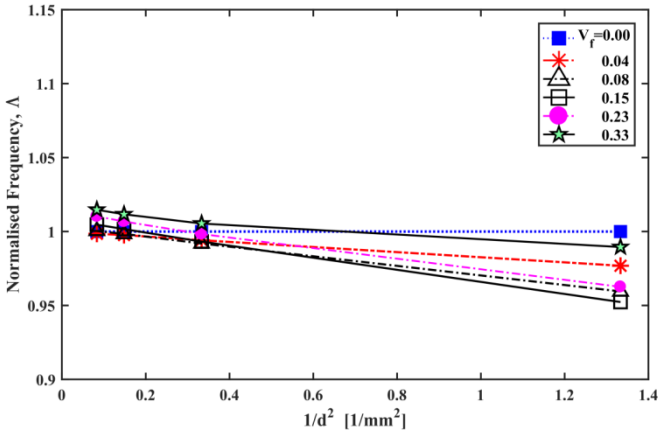

Figure 8-21: Normalised primary modal frequency of four plate sizes for plates with cylindrical compliant matrix and continuous boundaries using FEA (CYCMCB). $V_f = 0\ to\ 33\%$ ($V_r/S_y = 0.12\ to\ 0.35$)

Increasing the volume fraction in plates with cylindrical inclusions, compliant matrix and continuous boundaries (CYCMCB), as seen in figure 8-22, does not always have an inverse effect on the normalised frequencies as can be seen for volume fractions greater than 0.15.

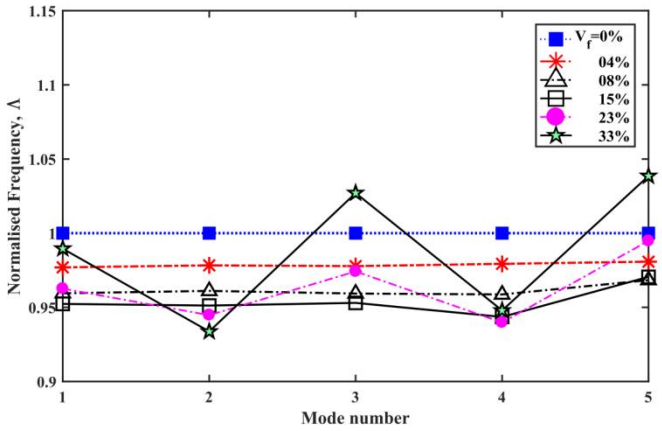

Figure 8-22: The first five normalised transverse modal frequencies of the smallest plate sample with compliant matrix and continuous boundaries using FEA. $V_f = 0\ to\ 33\%$ ($V_r/S_y = 0.12\ to\ 0.35$)

The opposite scale effect in the dynamic behaviour of the plate sample with compliant matrix and continuous boundaries could be due to the material's matrix which is more compliant than the previous models, in sections 8.5.1.1 and 8.5.2.1, and that in beam models with or less than four layers of unit cells in depth of the beams, the compliant matrix may dictate the overall behaviour of the structure and generate inverse size effects on normalised frequencies. This phenomenon has also been seen in the 2D beams with similar material properties, Figure 3-9 and 3-10. Therefore, it must be noted that the plates with similar

macroscopic properties may demonstrate different dynamic behaviour due to their micro-structurally related size effects.

8.5.2 Plates with textured boundaries

8.5.2.1 Plates with textured boundaries and voids (CYVOTB)

The FEA results for the plates with cylindrical voids and textured boundaries showed a specific size effect for which 3D-MPFEM results are again not available for comparison because of the negative gradient in the graph for normalised frequency against the inverse of the plates depth squared as seen in figure 8-23. This figure shows how the normalised frequency changes with the plates sample size while figure 8-24 provides the five normalised modal frequencies of the smallest CYVOTB plate.

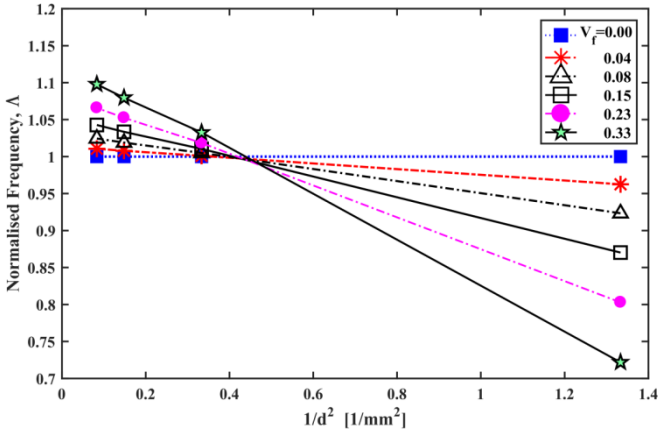

Figure 8-23: Normalised primary modal frequency of four plate sizes for plates with cylindrical voids and textured boundaries using FEA (CYVOTB). $V_f = 0\ to\ 33\%$ ($V_r/S_y = 0.12\ to\ 0.35$)

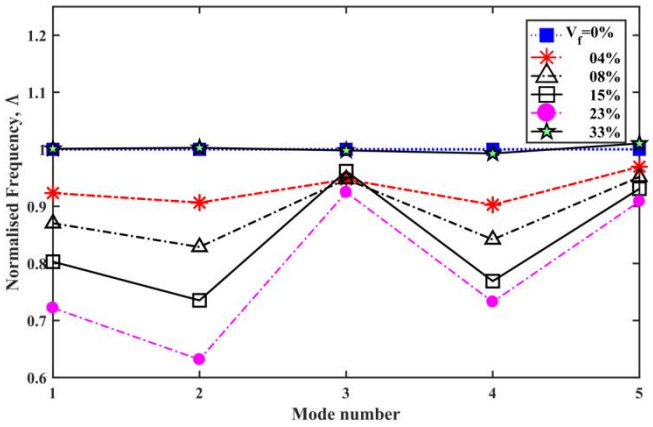

Figure 8-24: The first five normalised transverse modal frequencies of the smallest plate sample with voids and textured boundaries using FEA. $V_f = 0\ to\ 33\%$ ($V_r/S_y = 0.12\ to\ 0.35$)

Similar to the dynamic behaviour of the beams with textured boundaries as presented in chapter three, opposite scale effects in specimens with textured edges may occur in heterogeneous plate models because the material near the surface region of the sample is compromised. Also, as has already been explained in the previous section, the compliant matrix may dictate the overall dynamic behaviour of the plate structure when there are four or less than four layers of unit cells are present across the depth of the specimen. However, if the structure's boundary is intercepted by voids or compliant inclusions (See also section 8.5.2.2), the near-surface region becomes even more compliant, and this compromises the rigidity of the plate's boundaries. On the contrary, the near-surface area becomes stiffer than internal sections of the specimen if more rigid inclusions intercept the surface of the plate, (See section 8.5.2.3). The samples with one layer of unit-cells across the depths of the plate models show even more pronounced response because the microstructural arrangements of the inclusions will be no longer present.

8.5.2.2 Plates with textured boundaries and compliant inclusions (CYCITB)

Plates with compliant inclusions and textured boundaries showed similar dynamic behaviour as the plates with voids as explained in the previous section for which the micropolar constants cannot be identified. Therefore, the micropolar results are once again not available for comparison with the FEA results. In figure 8-25 the results include the normalised primary modal frequency values of four plate sizes for plates with cylindrical compliant inclusions and textured boundaries using FEA (CYCITB) which indicate that the size effect also inverts at a specific plate depth (here plate with NCy = 2) but remains linear across the samples.

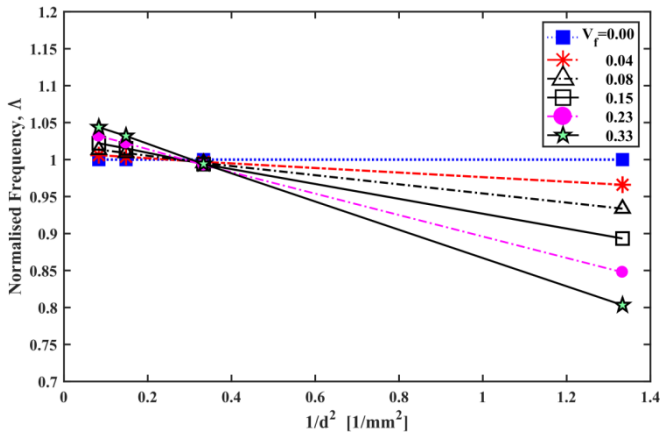

Figure 8-25: Normalised primary modal frequency of four plate sizes for plates with cylindrical compliant inclusions and textured boundaries using FEA (CYCITB). $V_f = 0\ to\ 33\%$ ($V_r/S_y = 0.12\ to\ 0.35$)

The FEA numerical results for the first eight non-dimensional bending modal frequencies of four plate sizes for plates with compliant inclusions and textured boundaries (CYCITB) are provided in Appendix table E-5 which also confirm the inversion of size effect at this specific plate depth. As an example, the first five normalised modal frequencies of the smallest plate sample with compliant inclusions and textured boundaries using FEA are provided in figure 8-26, which show that the normalised frequencies are all below unity values for the smallest plate sample.

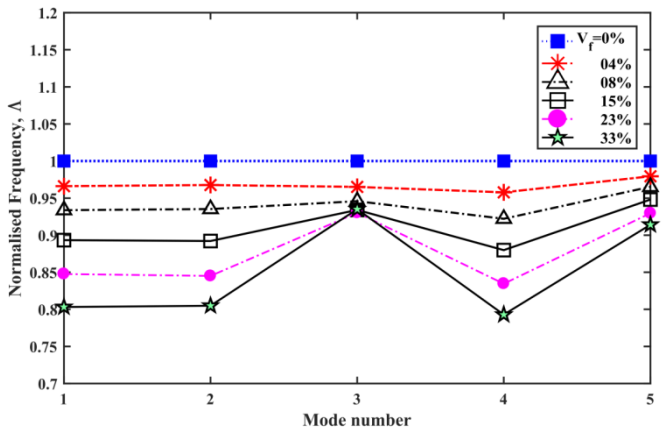

Figure 8-26: The first five normalised transverse modal frequencies of the smallest plate sample with compliant inclusions and textured boundaries using FEA. $V_f = 0\ to\ 33\%$ ($V_r/S_y = 0.12\ to\ 0.35$)

8.5.2.3 Plates with textured boundaries and compliant matrix (CYCMTB)

Unlike the plates with compliant inclusions or voids and textured boundaries, the micropolar constants can be obtained for the plates with textured boundaries and compliant matrix according to the methodology given in chapter five.

The finite element results for plates with textured boundaries and compliant matrix (CYCMTB) are provided in figure 8-27 to 8-29 and in table E-6 in Appendix E.

The FEA results for plates with stiff cylindrical inclusions and compliant matrix (CYCMTB) show similar behavior as plates with cylindrical voids or inclusions but continuous boundaries. However, here the plate models demonstrated lower size effect in comparison with CYVOCB or CYCICB. The results in figure 8-27 indicate that the gradient in the primary normalised frequency results for CYCMTB plates are slightly smaller than the results for CYCICB and CYVOCB. The normalised modal frequencies presented in figure 8-27 indicate that the variation of normalised modal frequencies of the primary mode is approximately linear with the inverse of the squared sample depth. The results for the primary mode also indicate that the gradient of the lines decreases with reducing the volume fraction.

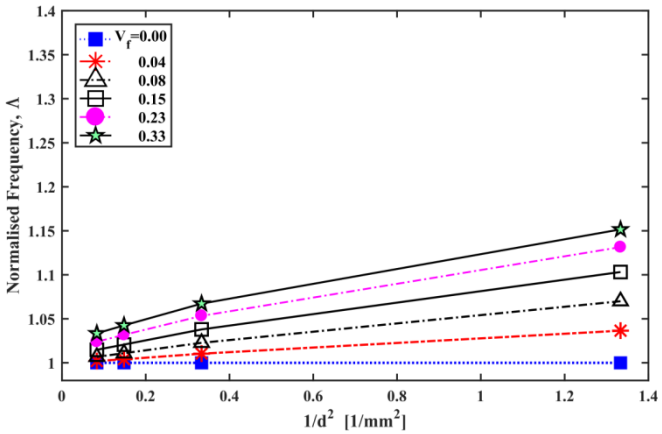

Figure 8-27: Normalised primary modal frequency of four plate sizes for plates with compliant matrix and textured boundaries using FEA (CYCMTB). $V_f = 0\ to\ 33\%$ ($V_r/S_y = 0.12\ to\ 0.35$)

The values of normalised modal frequencies of the first five normalised modal frequencies of the smallest plate sample with compliant matrix and textured boundaries generated using FEA demonstrate a great deal of sensitivity to mode number as seen in figure 8-28 which remains pronounced for higher modes too. This figure indicates that there is an increase in normalised frequency at modes three and five compared to CYCICB and CYVOCB. Note that figure 8-28 provides normalised frequencies at five different modes for the smallest plate sample and is not showing the gradient of changes at any specific mode for all plate sizes as seen in figure 8-27.

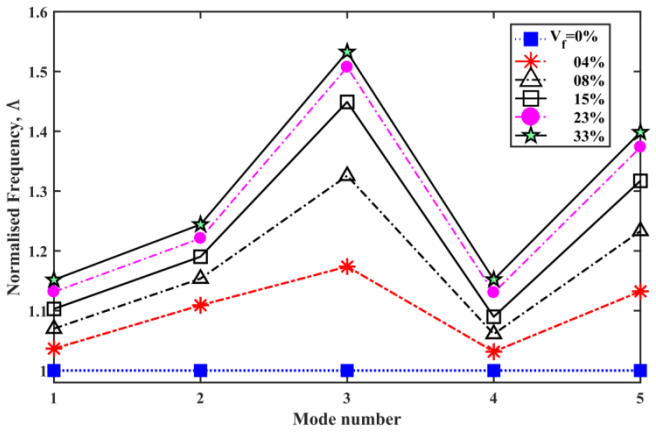

Figure 8-28: The first five normalised transverse modal frequencies of the smallest plate sample with compliant matrix and textured boundaries using FEA. $V_f = 0\ to\ 33\%$ ($V_r/S_y = 0.12\ to\ 0.35$)

As mentioned earlier in this chapter, the linear isotropic micropolar theory is not applicable for calculating the modal frequencies at higher mode numbers because, as said, the micropolar plate models are isotropic in contrast with the anisotropic models which were generated by FEA. However, the first two normalised frequencies, which were obtained by using the available micropolar constants, are in close agreement with the FEA results and the size effect is forecast. Figure 8-29 shows the primary normalised modal frequencies for plates with compliant matrix and textured boundaries, CYCMTB, which again indicate that the micropolar theory under-estimates the normalised frequency values for the smallest sample size when the volume fraction is higher than 0.15. In this figure, the 3D-MPFEM results are in better agreement with FEA results although the plates are more anisotropic, nevertheless this might be due to inverse effect of the plate's textured boundaries.

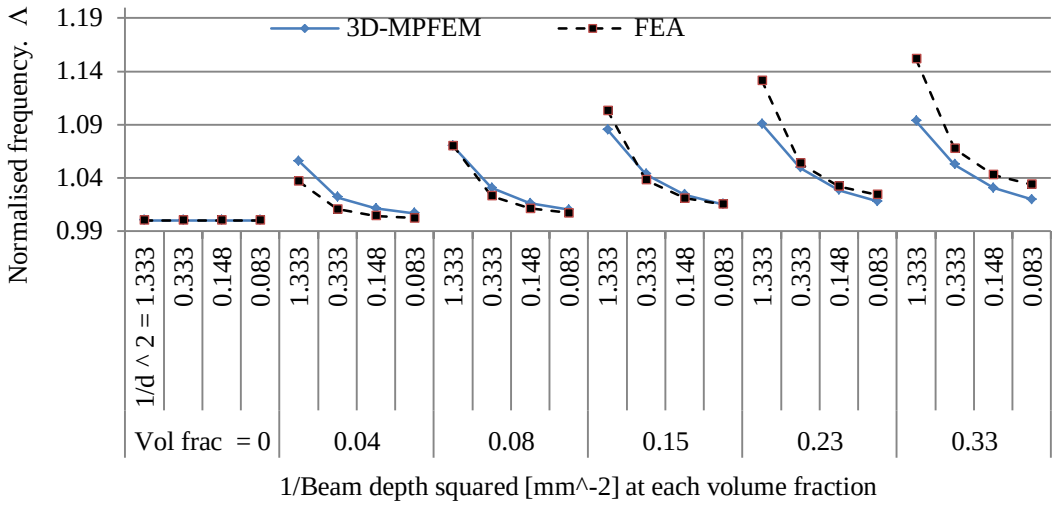

Figure 8-29: Primary normalised modal frequencies, mode 1, for plates with compliant matrix and textured boundaries, CYCMTB

8.6 Conclusions

In this chapter, six types of heterogeneous plate models were created using FEA as listed in section 8.1. The models were generated such that the sizes of the microstructures were comparable to the overall size of the plates. The size effects due to these microstructures were investigated by their effect on modal frequencies in the free vibration of plates with FFFF boundary conditions (unconstrained edges) in the absence of external loads.

Using the results from the finite element analysis, two of the micropolar constants, the characteristic length of bending and coupling number, were obtained from the dynamic behaviour of beams in a 2-dimensional case as discussed in chapters 4 and 5. The modulus of elasticity values were obtained from the tensile analysis. The polar ratio was considered constant and equal to 1.5, and the characteristic length of torsion was kept as twice the value of the characteristic length of bending throughout the entire modal analysis of the micropolar plates. However, the effect of changes in polar ratio or characteristic length of torsion was briefly investigated and it was concluded that reducing the ratio of l_t/l_b to e.g. 0.5 may only correct the underestimation of the modal frequency of mode three to some extent, but it causes severe under estimation in the value of the primary modal frequency of the plate. The under estimation of the normalised frequency parameters, especially at mode 3, by the 3D-MPFEM, may well be due to the orientation of the cylindrical voids or inclusions in one direction of the square heterogeneous plates which might indicate the effect of anisotropy in the material. If this is the case, then next chapter describes the influence of spherical voids or

inclusions in modal frequencies of the square plates which indeed negates the anisotropy issues associated with the direction of the cylindrical voids or inclusions.

The three-dimensional micropolar finite element approach, incorporating the micropolar theory was used to model a set of micropolar plates corresponding to the previously modelled non-homogeneous plates using FEA. Using the 3D-MPFEM algorithms, modal frequencies were generated for the micropolar plates. The size effects in micropolar plates were investigated. The results of the 3D-MPFEM analysis were in approximate agreement with FEA results for the first five modal frequencies though the degree of agreement appeared to decrease as V_f increased and the plate became more anisotropic.

In general, the micropolar theory was capable of anticipating size effect qualitatively in non-homogeneous plates in modal analysis, and the accuracy of the results greatly depends on the precise values of micropolar constants used in the analysis and the degree of anisotropy (DA) of the plate properties. The heterogeneous plate models, as explained in section 8.2.2 showed some degree of anisotropy which is also related to the volume fraction. Plates with lower volume fractions were considered to be mildly anisotropic, and therefore the dynamic behaviour of such heterogeneous plates could be better explained by the isotropic plate models generated by applying the micropolar theory.

Although the size effect can be anticipated by micropolar theory, nevertheless, for the smallest sample models where the structural depth of the plates was comprised of just one unit cell, the frequencies were underestimated and the reason may be, for example, that for such models, despite unit-cell similarities, the equilateral triangle arrangements for the neighbouring voids or inclusions was removed indicating that in such structures the strain gradient through the depths of the plate changes more abruptly than anticipated which thus affect the results.

In the next chapter, the heterogeneous models will include plates with spherical voids or compliant inclusions in which the effect of the material anisotropy is expected to be reduced and the application of the linear isotropic micropolar theory to such plates will be investigated accordingly. Therefore, the linear isotropic micropolar theory is also expected to answer the question of the underestimation in the value of the modal frequencies at mode three observed in this chapter.

9 Size Effects in 3D Heterogeneous Plates with Spherical Voids or Inclusions

In the previous chapter, the study of plates with cylindrical-type voids or inclusions showed some underestimation in calculating the normalised values of the modal frequencies of heterogeneous plates especially at mode three despite the anticipation of noticeable size effects. These underestimations, however, were presumed to result from the orientation of the voids or inclusions being in one direction which caused some anisotropy effects in the plate models that also increased with volume fraction. In this chapter, the free vibration of unconstrained square plates with spherical-type voids and inclusions is investigated. Modelling these non-homogeneous plates with spherical voids or inclusions is intended to decrease the degree of anisotropy (DA) which justifies the application of the linear isotropic micropolar theory to analyse such plate models. The degree of anisotropy of these plates are obtained and discussed in section 9.2.2.

The plates were modelled so that the centre point of any particular void or inclusion is located at the same distance from all neighbouring spheres in a square-pyramidal geometry or a so called body-centred cubic arrangement when there are at least two unit-cells included in the depth of the plate models. Like the previous chapters, the general methodology of studying size effects is unaltered which means that the overall properties of the plate's material are kept unchanged for all plate types. The plates with compliant matrix and stiff inclusions where not included here because this chapter is only investigating spherical heterogeneity types to find answers to some of the questions raised in the previous chapter; the other reason is that the plate models with cylindrical inclusions, complaint matrix and textured boundaries showed smaller size effects compared to the other plate types.

9.1 Finite element modelling of plates with spherical voids or inclusions

Spherical type voids or inclusions were considered for modelling the plates. Therefore, plates with voids consisting of one isotropic material forming the matrix and plates with two isotropic materials comprising the stiff matrix and compliant inclusions were modelled and numerically analysed. The surface conditions of the top and bottom faces of the plates were considered to be either continuous or textured. Therefore, four plate types, in total, were studied as follows:

a) Plates with spherical voids and continuous boundaries (SPVOCB)

b) Plates with spherical voids and textured boundaries (SPVOTB)

c) Plates with spherical compliant inclusions and continuous boundaries (SPCICB)

d) Plates with spherical compliant inclusions and textured boundaries (SPCITB)

FEA results are presented for all of the above categories while the micropolar results for the plate types SPVOCB and SPCICB are presented and discussed because the micropolar constants were only identifiable for plates with continuous boundaries.

9.1.1 Unit-cells in construction of plates with spherical voids or inclusions

For each plate type with spherical voids or inclusions, specific three-dimensional unit-cells were modelled using 20-node Solid elements of tetrahedron type; see the semi unit-cells in figure 9-1 and a full sized plate with continuous surfaces in figure 9-2 along with a full sized plate with textured boundaries in figure 9-3. In the smallest plate samples, there are five unit-cells along the plate edge and one unit-cell through the plate thickness which form a plate with 25 unit-cells in total; and this is increased by eight times when the plate depth is multiplied by two for the second smallest plate and so forth.

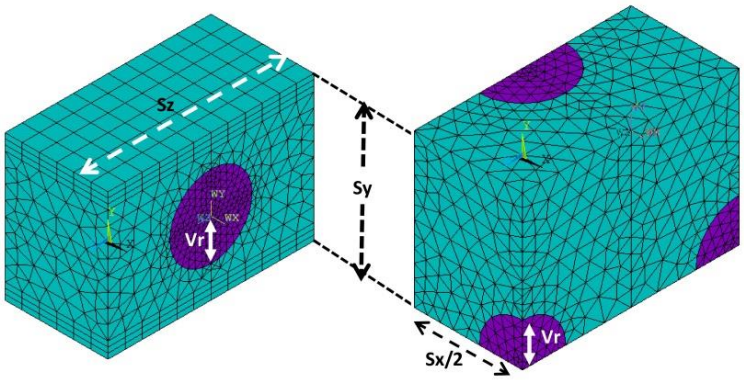

Figure 9-1: Representation of half unit cells of two isotropic materials with void or inclusion's volume fraction of 4.7%. The unit-cell on the left is used to model 3D plates with continuous boundaries, e.g., SPCICB (with inclusions) or SPVOCB (without inclusions) and the unit cell on the right-hand side is used for plates with textured boundaries (e.g., SPCITB).

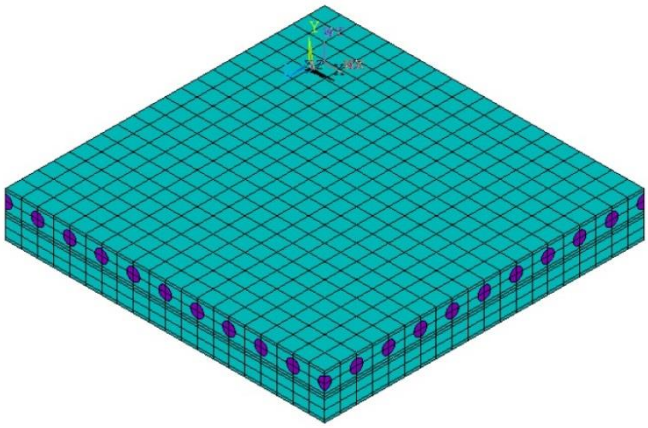

Figure 9-2: A completed plate model with compliant inclusions ($V_f = 0.047$) and continuous boundaries (e.g. top and bottom surfaces are not textured), NCy=2, d=0.7071*2 mm, AR=7.072

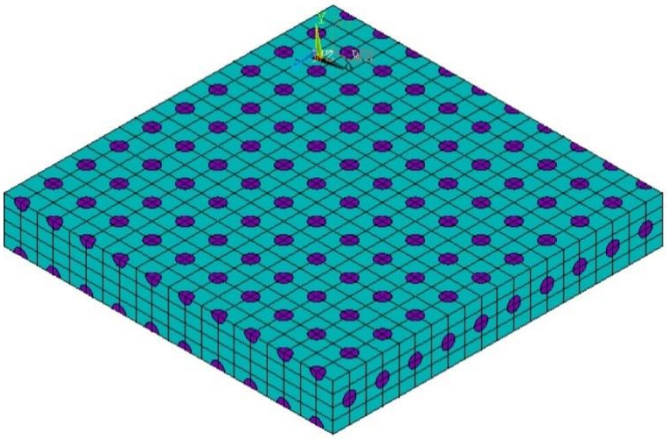

Figure 9-3: A completed plate model with compliant inclusions ($V_f = 0.047$) textured boundaries (e.g. top and bottom surfaces are textured), NCy=2, d=0.7071*2 mm, AR=7.072

Similar to the models presented in chapter eight, the void or inclusion radius varies from 0.1 to 0.3 in 0.05 mm intervals but for the spherical type void and inclusions within unit-cells, this, when compared with cylindrical type voids, generated lower volume fractions ranging between 0.6 and 16%.

At first, for both plate types (with continuous or textured boundaries), a quarter-sized unit-cell was modelled which was then repeatedly reflected to form a complete unit-cell. The unit-cell was then regenerated in all coordinate directions as required to form a full plate model with desired heterogeneity and dimensions. A completed plate model is arranged such that the voids or inclusions construct a uniform arrangement in which every five spheres (four spheres in one layer and one from the next layer) form a pyramidal, body-centred cubic arrangement where the spheres are located at the vertices. In order to achieve such

arrangements, the depth of the unit-cell is set at 0.7071mm and the plate aspect ratio at 7.072. The length and width of unit-cells were equal to 1 mm. This heterogeneity arrangement attempted to minimise the anisotropy of the material.

In modelling the quarter unit-cell for the plates with textured boundaries, the quarter circle arcs and the lines together with the circle edge lines were segmented into six element divisions, and the remaining lines were divided into 3 to 5 divisions as shown in figure 9-1 on the right. Then, using tetrahedron elements, the whole quarter cell was meshed. The same method was used to model the quarter unit cells for the plates with continuous boundaries except for one difference, that is to generate solid brick elements on one side of the quarter cell, as shown in figure 9-1 on the left, due to element connectivity when regenerating next layer of unit-cells. Therefore, a six by six area meshed with three divisions of brick in depth was utilised. The sizes of the three divisions in depth vary as the radius of the void or inclusion increase, as seen in figure 9-4:

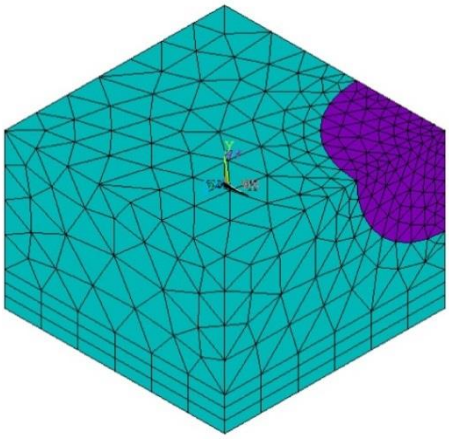

Figure 9-4: A quarter cell for plates with compliant inclusions and continuous boundaries

By repeatedly regenerating the unit-cells as needed, plate types of required thickness and aspect ratios were modelled.

In the case of plates with inclusions, similar to previous models, inclusion and matrix are both of two isotropic materials with a matrix to inclusion stiffness ratio of 10:1.

9.1.2 Mesh convergence in modal analysis

Two plate models with continuous and textured boundary surfaces and containing compliant inclusions with spherical geometries were studied and presented here to show that the plate models under study satisfy the requirements of mesh convergence. The modal frequencies of plates with $NCy = 1, AR = 7.072{:}1,\ S_y = 0.7071\ mm$ and $V_f = 0.047$ $(r = 0.2\ mm)$ with

spherical inclusions were numerically investigated for mesh convergence while changing the element density of the unit-cell (mesh density) as follows:

Table 9-1: Mesh convergence for the plate samples with spherical compliant inclusions and continuous boundaries (SPCICB) and $V_f = 0.05$

Number of elements in one unit-cell	Number of nodes in one unit-cell	The average error for the primary mode	The average error for ten modes	The average error for 33 modes
1216	2261	1.25E-03	1.61E-03	2.34E-03
3016	5341	1.49E-04	1.09E-04	2.85E-04
9128	14421	1.58E-04	7.38E-05	8.15E-05
18464	29061	1.27E-04	5.67E-05	4.33E-05
136424	136424	1.25E-05	2.46E-06	3.25E-06

Table 9-2: Mesh convergence for the plate samples with spherical compliant inclusions and textured boundaries (SPCITB) and $V_f = 0.05$

Number of elements in one unit-cell	Number of nodes in one unit-cell	The average error for the primary mode	The average error for ten modes	The average error for 33 modes
1604	2727	3.35E-03	2.74E-03	2.87E-03
2312	3981	1.37E-03	1.09E-03	1.17E-03
4892	8015	4.33E-04	3.57E-04	3.82E-04
14752	22371	2.98E-04	2.39E-04	2.57E-04
121916	175922	1.13E-05	1.00E-06	1.26E-06

As seen in tables 9-1 and 9-2, SPCICB and SPCITB plates with 18,464 and 14572 elements per unit cells provide convergence error of less than 0.03% and, therefore, used for meshing the plate models. Although the average error in these tables are small values, as explained in the previous chapter, section 8.1, the relative error simultaneously increases with mode number which must be noted if higher modes numbers are investigated.

9.2 Adjusting the modulus of elasticity (E) and mass density (ρ) of the unit-cells in plates with spherical voids and inclusions

9.2.1 Obtaining the modulus of elasticity (E) and mass density (ρ)

The sphere radius within the unit-cells varied from 0.1 to 0.3 mm, in 0.05mm intervals, to account for void or inclusions volume fractions of 0.6, 2, 4.7, 9.3 and 16% respectively. The volume fraction, void radius or normalised void radius, V_r/S_y, are as previously used interchangeably, see table 9-3.

Having modelled and meshed the unit-cells, complete plate models were created by regenerating and repeated reflection of the unit-cells in x, y and z directions similar to the methodology of chapter eight. The overall material properties such as the mass of the unit-cells and elastic modulus of the plate remained unchanged and set at 2700 kg/m3 and 7×10^{10} Pa for density and Young's modulus respectively. The correction of elastic modulus was therefore done by performing FEA static tensile test simulations, and correction of the density was done by keeping the mass and volume of the unit cells constant but changing the density of the constituent isotropic materials. The materials corrected properties of the plate models are provided in table 9-4 and 9-5.

Table 9-3: Volume fraction and normalised equivalent of *spherical* void or inclusions

Void/inclusion radius, r, [mm]	0.1	0.15	0.2	0.25	0.3
Spherical void or inclusion volume fraction, %	0.59%	2.00%	4.74%	9.26%	15.99%
Normalised radius, V_r/S_y	0.14	0.21	0.28	0.35	0.42

Table 9-4: Corrected modulus of elasticity for plate's matrix. The young modulus is 0.1 times the values of the matrix for plates with compliant inclusions

	The modulus of elasticity of matrix, MPa							
	Plates with Continuous boundaries				**Plates with Textured boundaries**			
Void or inclusion radius, mm	**Plates with SPVOCB**	**Relative diff. with homogeneous beam**	**Plates with SPCICB**	**Relative diff. with homogeneous beam**	**Plates with SPVOTB**	**Relative diff. with homogeneous beam**	**Plates with SPCITB**	**Relative diff. with homogeneous beam**
0	7.00E+04	0	7.00E+04	0	7.00E+04	0	7.00E+04	0
0.1	7.08E+04	1.94E-04	7.07E+04	4.39E-06	7.08E+04	2.60E-04	7.07E+04	2.60E-04
0.15	7.29E+04	1.61E-04	7.23E+04	1.69E-04	7.29E+04	5.90E-04	7.23E+04	9.46E-05
0.2	7.70E+04	3.67E-04	7.57E+04	4.66E-04	7.70E+04	9.46E-05	7.57E+04	4.58E-04
0.25	8.44E+04	4.99E-04	8.16E+04	5.65E-04	8.44E+04	4.91E-04	8.15E+04	8.87E-04
0.3	9.72E+04	3.67E-04	9.13E+04	7.96E-04	9.71E+04	4.99E-04	9.12E+04	9.20E-04

Table 9-5: Corrected density of the plate's unit cell by spherical void or inclusions radius

Spherical voids or inclusion radius, mm	**The mass density of matrix and inclusions, kg/m^3**				
	Plates with voids		**Plates with inclusions**		
	For matrix	**Relative difference with homogeneous beam**	**For matrix**	**For inclusions**	**Relative difference with homogeneous beam**
0	2700	0	2700.00	N/A	0
0.1	2716.09	1.85E-07	2469.17	41434.61	1.85E-07
0.15	2755.08	1.85E-07	2504.62	12276.92	1.85E-07
0.2	2834.32	1.85E-07	2576.66	5179.33	1.85E-07
0.25	2975.41	1.85E-07	2704.91	2651.81	1.85E-07
0.3	3214.08	1.85E-07	2921.89	1534.62	1.85E-07

9.2.2 The effect of anisotropy in plates with spherical voids or inclusions

Although the voids and inclusions are modelled such as to decrease the degree of anisotropy (DA) of the plates, the plate models might still be considered as non-homogeneous and the degree of anisotropy of such plate models must therefore be investigated. The method of obtaining the DA of the plate models considered here are analogous to what was explained in section 8.2.2 for plates with cylindrical voids or inclusions in chapter eight. Therefore, the degree of anisotropy (DA) was obtained by tensile test simulations in the z-direction, and the relative difference of E_z to E_x was calculated for various volume fractions as provided in table 9-6:

Table 9-6: The degree of anisotropy in heterogeneous plate models with spherical voids and inclusions

	The relative degree of anisotropy (DA) [(Ez-Ex)/Ez]	
Volume fraction	**Plates with compliant inclusions**	**Plates with voids**
0.00	0.000	0.000
0.006	0.001	0.001
0.020	0.003	0.001
0.047	0.005	0.002
0.093	0.010	0.003
0.160	0.020	0.018

The values of DA, as seen in table 9-6, are minimal and indicate that the anisotropy in these plate models is practically negligible even for high volume fractions of 0.16 and therefore the plates may be considered as isotropic even though they are still heterogeneous at the macroscopic scale. Consequently, the application of the isotropic 3D-MPFEM to the investigation of the dynamic behaviour of non-homogeneous plates with spherical void and inclusions seems logical.

9.3 Modal analysis procedure and mode shapes of plate models

The PCG Lanczos method and distributed memory were again used for the modal analysis of plates. The first 8 mode shapes are shown in figures 9-5-a to 9-5-h. Mode shapes of plates with spherical voids and inclusions are similar to those of cylindrical shaped voids and inclusions shown in figures 8-3-a to 8-3-h in chapter eight. Thus similarly, the first mode is distinctively the twisting mode which is shearing deformation dominated where the

influencing parameter in the dynamic behaviour of the plate is the characteristic length in torsion, l_t. The second and third are bending dominated modes in which the determining micropolar constant is l_b. After mode three, some mode shapes appear in pairs with very close frequencies, but opposite mode shapes, and some does not. For example modes four and five are similar in which the plate's dynamic behaviour is influenced by both l_b and l_t; modes six and seven are again bending deformation dominated; mode eight which is both bending and shear deformation dominated.

The non-dimensional modal frequencies (Ω) for homogeneous plates are provided in table 9-7 and used for normalisation of modal frequencies (see figures 9-6 to 9-26) which are derived using the equation (8.1).

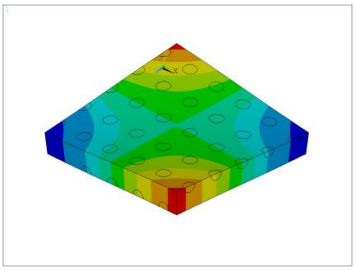

a) Mode 1, Twist shape (Shear dominated)

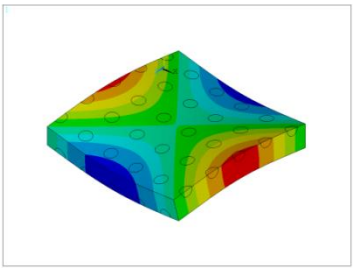

b) Mode 2, (hyperbolical surface) Saddle shape

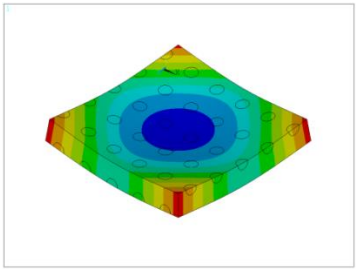

c) : Mode 3, (ellipsoidal surfaced) Bending Type

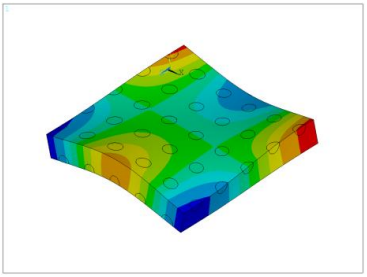

d) Mode 4

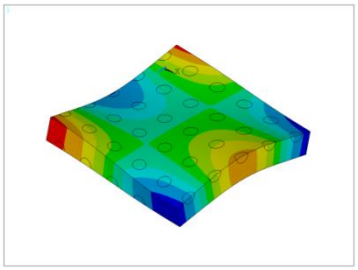

e) Mode 5

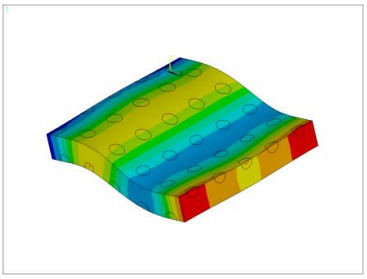

f) Mode 6

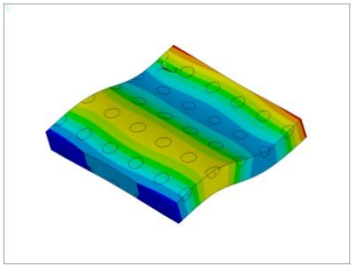

g) Mode 7

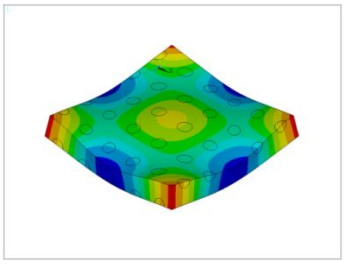

h) Mode 8

Figure 9-5: The first 8 mode shapes (a to h) of a sample plate with spherical inclusions of volume fraction equal to 0.05 and textured boundaries (NCy=1). Note that the first eight mode shapes of the homogeneous plate as well as other plate models with continuous boundaries are similar to the mode shape figures here also.

Table 9-7 : The non-dimensional frequencies (Ω) for homogeneous plates with AR=7.072:1

Mode	1	2	3	4	5	6	7	8
ANSYS FE	1.2483145	1.8623777	2.2832388	3.0602078	3.060611	5.1799099	5.203043	5.207992
MPFEM	1.2466034	1.8571328	2.2792083	3.0502382	3.0508554	5.1773338	5.181014	5.183083

9.4 Results and size effect forecast for plates with spherical voids or inclusions

The numerical results for the plates with continuous and textured boundaries using FEA and the linear isotropic micropolar theory are tabulated and provided in Appendix F which includes the eight modal frequencies for the plate models. The isotropic micropolar plate models (referred to as 3D-MPFEM models) contain eight 15-node wedge elements per unit-cell as described in the section 7.3.1 of chapter 7, so the mesh densities of the plates are the same. The height of the unit cells remained unchanged at 0.7071 mm, and the aspect ratio (length or width to height ratio) for all plates was 7.072:1 which resulted in modelling the smallest squared plate samples such that they contained 10 divisions along the plate edges (x-z plane) and one division through the plate thickness thus forming a plate with 200 wedge elements in total. This is increased by eight times when the plate depth is multiplied by two for the second smallest plate and so forth. In the next sections, the normalised frequency values, Λ, of the plates with spherical voids and inclusions which are obtained by using both FEA and 3D-MPFEM are presented, compared and discussed accordingly.

9.4.1 The micropolar constants for the plate models

To identify some of the micropolar constants, three-dimensional slender beams with spherical voids and inclusions were modelled with one unit-cell in depth and ten unit cells in length representing the smallest beam sample with twice the aspect ratio of the plates (2×7.072) using FEA. Then beams with two, three and four unit cells in depth were created with the same aspect ratio. The unit-cells geometry, mesh density and the material properties are the same as the plate models which are already discussed in sections 9.1 and 9.2 but instead of plates, 3D beam models were generated. The reason is to obtain the lateral modal frequencies in the x-y plane of beams with spherical voids and inclusions, and subsequently use these frequencies to identify the l_b and N by applying the methods in chapters 4 and 5. The algorithm for identifying the coupling number, N, as described in chapter 5, is only capable of estimating the coupling number by matching the first two flexural frequencies of beams obtained through FEA with two-dimensional micropolar beam models and using the linear regression methods. Therefore, the first two bending modal frequencies were used to obtain the characteristic length of bending, l_b, using equation (4.46). The characteristic lengths of bending was then compared with those obtained from using equation (8.7) at mode two (because mode one of the plates is a twist mode). Interestingly, the characteristic length using either equations (4.46) or (8.7) show approximately similar values as seen in

table 9-8. However, the values obtained from beam models and equation (4.46) appear to vary more linearly with the void radius and, therefore, are used for the plate analysis.

Table 9-8: Characteristic length of bending for plates with spherical voids and inclusions

Specimen	Equation	R=0.1 , mm	R=0.15 , mm	R=0.2 , mm	R=0.25 , mm	R=0.3 , mm
SPVOCB	(8.7)	0.017	0.034	0.044	0.062	0.076
BVOCB	(4.46)	0.017	0.032	0.048	0.064	0.078
SPCICB	(8.7)	0.016	0.029	0.041	0.050	0.060
BCICB	(4.46)	0.017	0.029	0.043	0.061	0.067

The micropolar Poisson's ratio, micropolar modulus of elasticity and the polar ratio, Ψ, were all kept constant at 0.3, 7×10^{10} Pa and 1.5 respectively. The coupling number, N, was obtained by the iteration method as described in chapter five and values were found to be insensitive to void or inclusion radius, being 0.030 and 0.031 for SPVOCB and SPCICB plate models respectively. The low values of the coupling number are due to the shape and arrangements of the spherical voids and inclusions in the vicinity of the plate matrix. Finally the value of the characteristics length of torsion, l_t , is chosen as equal to twice the value of characteristics length of bending. It must be remembered that this value of l_t might influence the modal frequencies differently especially the primary mode which is dominated by shear deformation.

As an example, the plate samples SPVOCB with NCy = 3 and volume fractions, 0.01, 0.05 and 0.16 were investigated and compared with 3D-MPFEM results with input parameters of $\Psi = 1.5$ and various values of l_t equal to $2l_b$, $1.5l_b$, l_b and $0.5l_b$. This is aimed to qualitatively illustrate the influence of the changes of l_t on the primary mode in particular (the twist mode) and then see the outcome of such changes in l_t on the higher frequencies.

As seen in figure 9-6, by setting the value of $l_t = 2l_b$, micropolar theory overestimates the modal frequencies of mode one compared to the FEA results for the heterogeneous plate models even though the level of anisotropy in plate models is low. Although, decreasing the value of l_t causes a decrease in the modal frequency at mode one for isotropic micropolar plates but then underestimates the second modal frequency and overestimates the third modal frequencies for all volume fractions, as seen in figures 9-7 and 9-8 while, on the other hand, the value of $l_t = 2l_b$ provides better agreement with the finite element results at mode two and three.

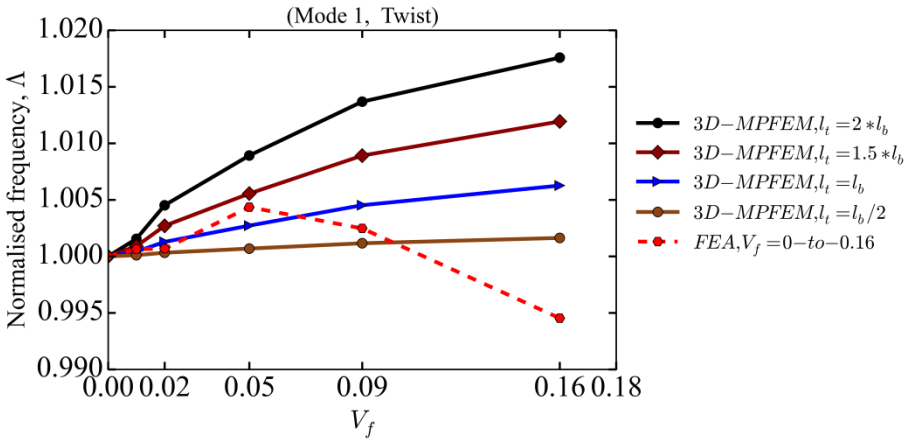

Figure 9-6: The overestimation of the normalised primary frequencies of SPVOCB plates using FEA and 3D-MPFEM for the plate with NCy=3 when $l_t = 2l_b$.
($V_f = 0.006, 0.05$ *and* 0.16 *corresponds to* $l_b = 0.017, 0.048$ *and* 0.078 *mm*)

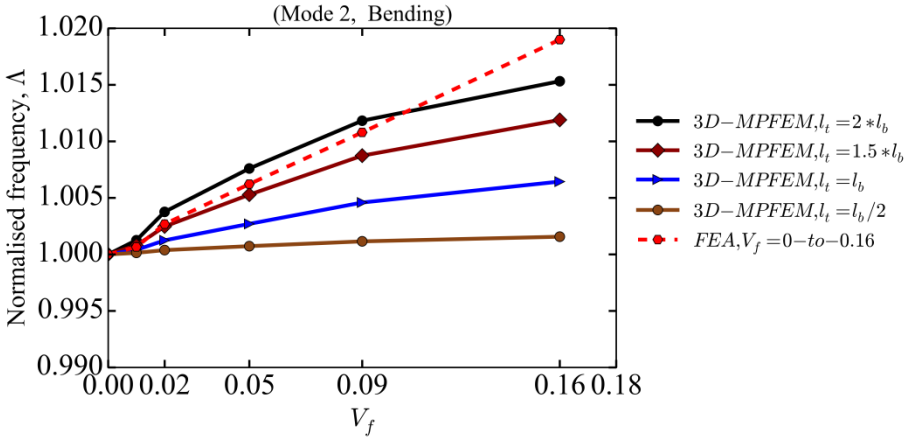

Figure 9-7: The normalised frequencies of the second mode of SPVOCB plates with NCy=3 using FEA which show better agreement with the 3D-MPFEM results when $l_t = 2l_b$.
($V_f = 0.006, 0.05$ *and* 0.16 *corresponds to* $l_b = 0.017, 0.048$ *and* 0.078 *mm*)

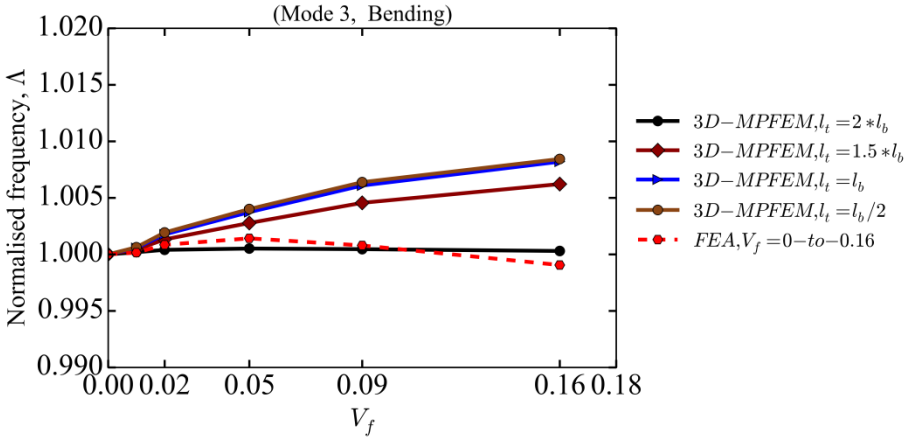

Figure 9-8: The normalised frequencies of the third mode of SPVOCB plates with NCy=3 using FEA which show better agreement with the 3D-MPFEM results when $l_t = 2l_b$.
($V_f = 0.006, 0.05$ *and* 0.16 *corresponds to* $l_b = 0.017, 0.048$ *and* 0.078 *mm*)

For further clarifications, the results in figures 9-9 to 9-12 show the changes of the normalised frequency with mode number and indicate that the 3D-MPFEM produces more acceptable results for higher volume fractions when the value of l_t is set to equal $2l_b$. However, at mode one and especially the highest volume fraction, the frequency values are overestimated.

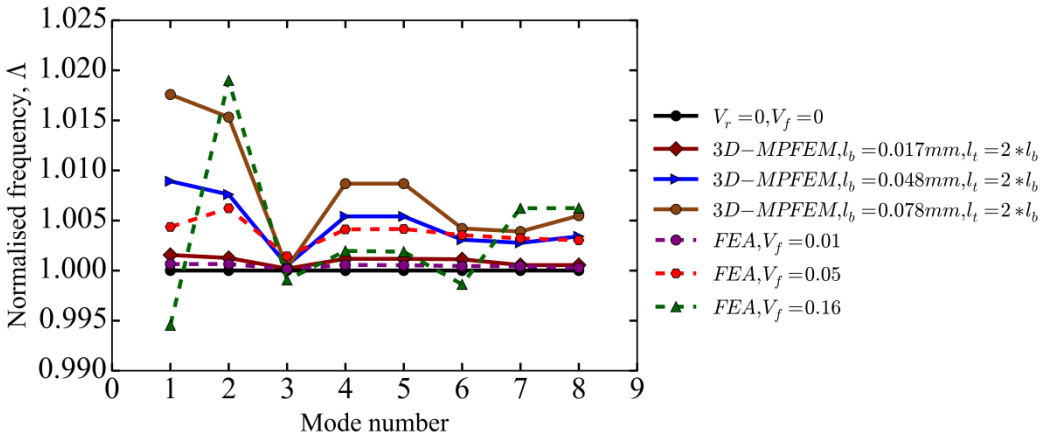

Figure 9-9: The normalised frequencies of SPVOCB plates using FEA and 3D-MPFEM for the plate with NCy=3, Ψ=1.5, d=0.866mm and AR=8.083. ANSYS results reduction at mode three are similar to MPFEM when $l_t = 2l_b$.

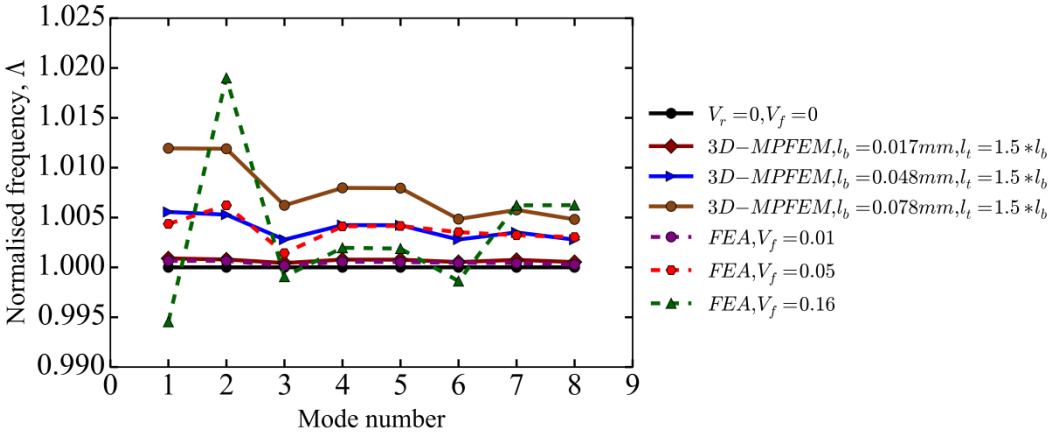

Figure 9-10: Changes of normalised frequencies of a micropolar plate (SPVOCB) with $l_t = (3/2)l_b$, Ψ=1.5, NCy=3, $S_y = 0.866mm$ and AR=8.083 in comparison with corresponding FEA results.

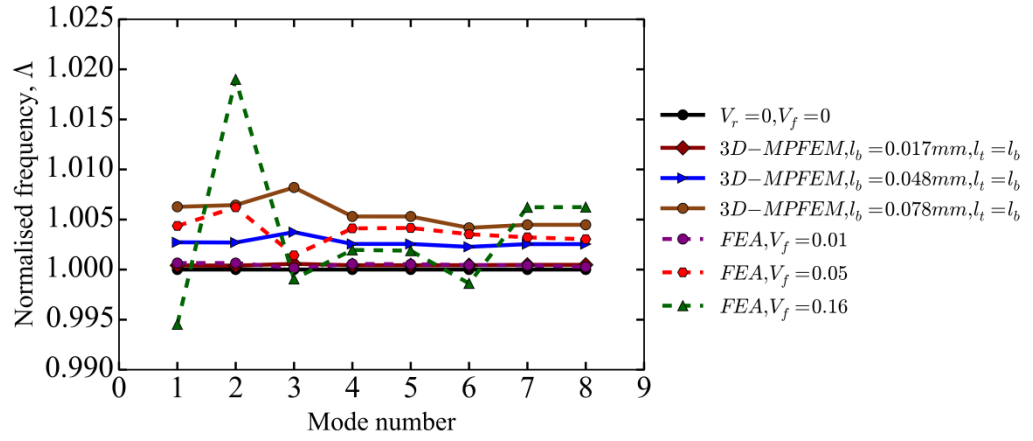

Figure 9-11: Changes of normalised frequencies of a micropolar plate (SPVOCB) with $l_t = l_b$, Ψ=1.5, NCy=3, $S_y = 0.866mm$ and AR=8.083 in comparison with corresponding FEA results.

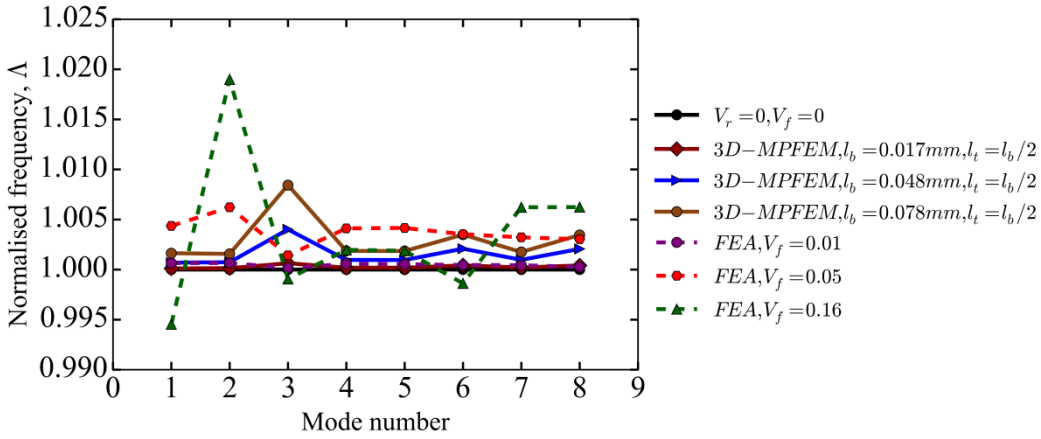

Figure 9-12: Changes of normalised frequencies of a micropolar plate (SPVOCB) with $l_t = (1/2)l_b$, Ψ=1.5, NCy=3, $S_y = 0.866mm$ and AR=8.083 in comparison with corresponding FEA results.

9.4.2 Plates with continuous boundaries

Now that the plate models and micropolar constants for the heterogeneous plates with continuous boundaries are defined, the modal frequencies are to be obtained using FEA and compared to 3D-MPFEM results in this section. The comparison of the results aims to answer some of the questions surrounding the shortcomings which were raised in chapter eight, especially the underestimation of modal frequency at mode three.

9.4.2.1 Plates with spherical voids and continuous boundaries (SPVOCB)

The size effect governing the changes in normalised modal frequency values for the plates with spherical voids and inclusions rapidly diminishes as the plate's depth increases, but is still pronounced for the smallest plate samples. This is, indeed, due to the square pyramidal void and inclusion geometrical configuration, or body-centred cubic, which is not present in

the smallest plate sample. Despite the somewhat smaller size effects in the dynamic behaviour of the plate models of thickness of two or more unit cells, the rate of changes of the normalised frequencies with size remains approximately linear, except at the largest volume fraction, and the gradient remain positive which is an indication of the applicability of micropolar theory to this case; see figure 9-13 and 9-14. The 3D-MPFEM results for the corresponding SPVOCB plates showed convincing agreement with the FEA results except in the high volume fraction cases for the smallest plate samples; see figure 9-15. It must be remembered that the primary modal frequency is associated with a twist mode which is shear deformation dominated and therefore different to the bending modes. The 3D-MPFEM results for the second mode, which is a saddle type mode and therefore predominantly bending, showed an even better agreement with the FEA results but the difference at the highest volume fraction for the smallest plate models remains quite marked; see figure 9-16. In fact the second mode is influenced by the value of characteristic length of bending, l_b, for identification of which an analytical method was developed and l_b was obtained according to equation (4.46) which was also confirmed by equation (8.7), where the l_b values are believed to be accurate. On the contrary, the primary frequency is merely influenced by the value of the characteristic length in torsion, l_t, for which a value of $2l_b$ is assumed.

In general, the results obtained by the micropolar plate simulations for the SPVOCB representative plate models, compared with the results of the CYVOCB plates presented in Chapter 8, in figures 8-14 and 8-15, are more in agreement with the FEA results, due to the presence of a lower degree of anisotropy in the plate models containing spherical void.

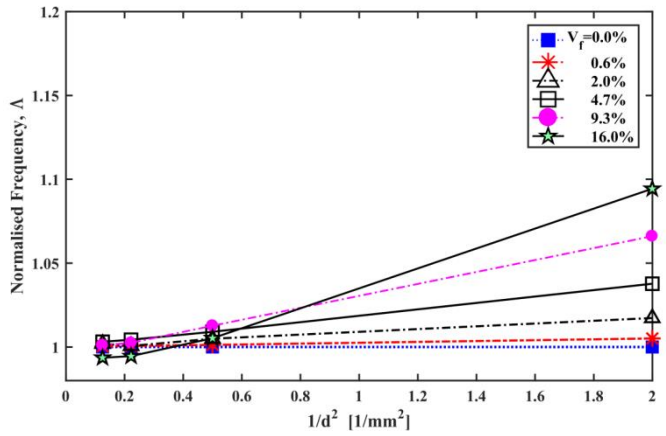

Figure 9-13: Normalised primary modal frequency of four sizes of plates with spherical voids and continuous boundaries using FEA (SPVOCB). $V_f = 0\ to\ 16\%$ ($V_r/S_y = 0\ to\ 0.42$)

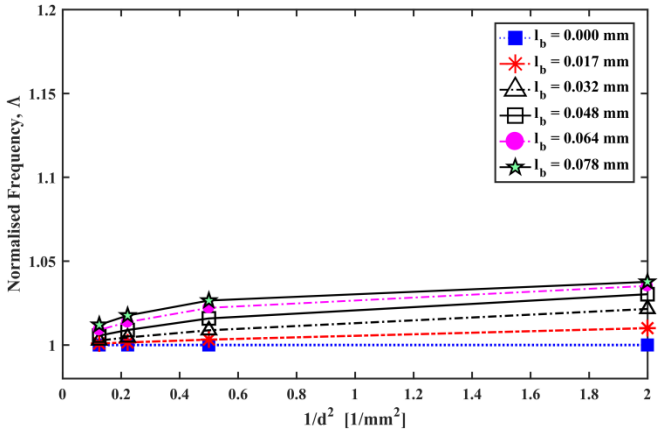

Figure 9-14: Normalised primary modal frequency of four sizes of plates with spherical voids and continuous boundaries using 3D-MPFEM (SPVOCB).
($l_b = 0$ *to* 0.078 *mm corresponds to* $V_f = 0$ *to* 16%)

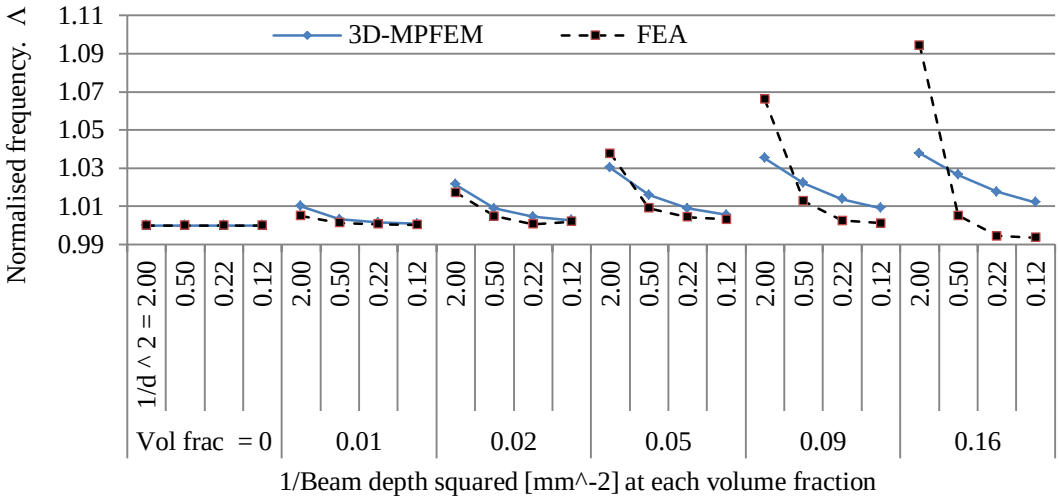

Figure 9-15: Primary normalised modal frequencies, mode 1, for plates with spherical voids and continuous boundaries, SPVOCB

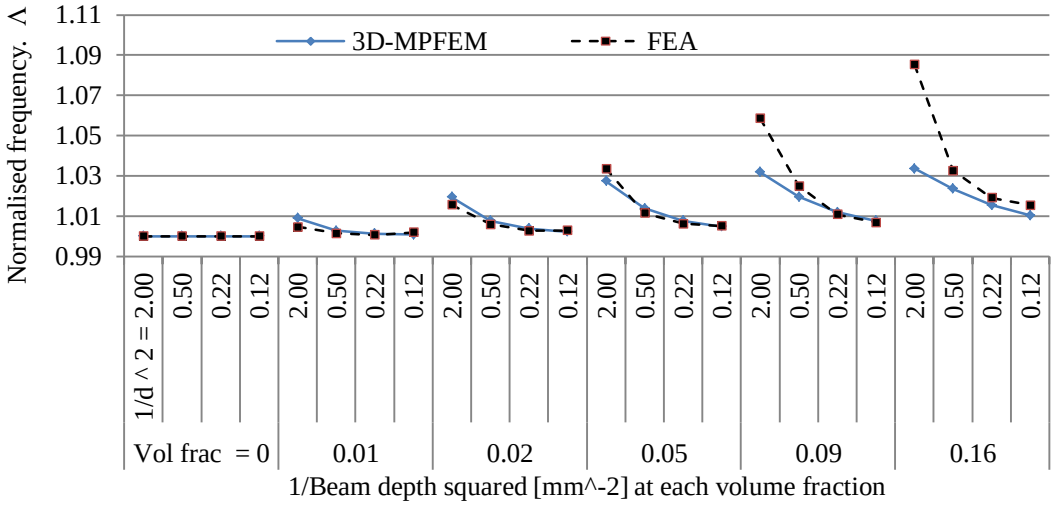

Figure 9-16: Second normalised modal frequencies, mode 2, for plates with spherical voids and continuous boundaries, SPVOCB

The FEA results indicated that the size effect for the smallest plate samples is more pronounced than in the larger samples, especially for the plates with higher void volume fraction, as explained. The FEA results, figure 9-17, show a gradual decline in normalised modal frequencies as the mode number increases while the 3D-MPFEM results at mode three show an inverted size effect, see figure 9-18. This is believed to occur because the characteristic length of torsion, l_t, is taken as equal to twice the value of l_b. A lower value of l_t would compensate this shortcoming but would then affect the other modal frequencies more significantly and would thus result in their severe underestimation. However, the 3D-MPFEM results for the plates with more than one unit-cell in depth show similar dynamic behaviour to the FEA, as previously shown in figure 9-9 for the normalised frequencies of SPVOCB plates with NCy=3.

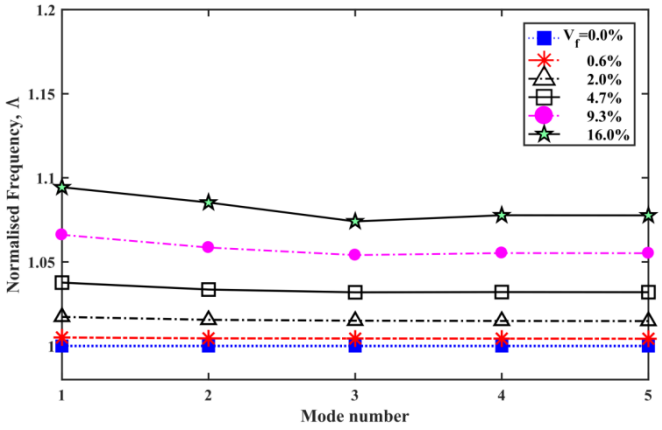

Figure 9-17: The first five normalised flexural modal frequencies of the smallest plate sample with voids and continuous boundaries using FEA. $V_f = 0\ to\ 16\%$ ($V_r/S_y = 0\ to\ 0.42$)

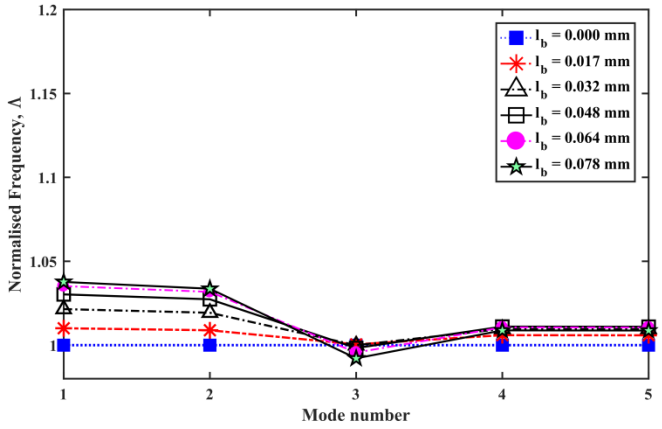

Figure 9-18: The first five normalised flexural modal frequencies of the smallest plate sample with voids and continuous boundaries using 3D-MPFEM. ($l_b = 0\ to\ 0.078\ mm\ corresponds\ to\ V_f = 0\ to\ 16\%$)

9.4.2.2 Plates with spherical inclusions of compliant material (SPCICB)

The numerical results using the FEA and 3D-MPFEM procedure for the plates with spherical compliant inclusions show plate dynamic behaviour similar to the plates with voids. The results also indicate that plates with SPCICB show slightly lower normalised frequencies in comparison with those for plates with SPVOCB, as seen in figures 9-19 to 9-23. Thus the explanations regarding the dynamic behaviour of plates with voids and continuous boundaries in section 9.4.2.1 are valid for the plate models considered in this section as well. The normalised modal frequencies in figure 9-19 indicate that the size effect rapidly diminishes as the plate's depth increases, but is still pronounced for the smallest plate samples. This is, indeed, due to the fact that firstly the degree of anisotropy (DA) in SPCICB plates is minimal thus ignorable. Secondly, the body-centred geometrical configuration of inclusions (pyramidal arrangements of inclusions) is not present in the smallest plate sample.

The FEA results, with an exception of the plates with largest volume fraction as seen in figure 9-19, for SPCICB plates indicate that size effect in plates with two or more unit cells in depth is somewhat smaller yet readily discernible, thus the micropolar theory is applicable, see figure 9-20.

The numerical results indicated that size effect for the smallest plate samples is more pronounced than expected especially for the plates with higher void volume fraction, as explained.

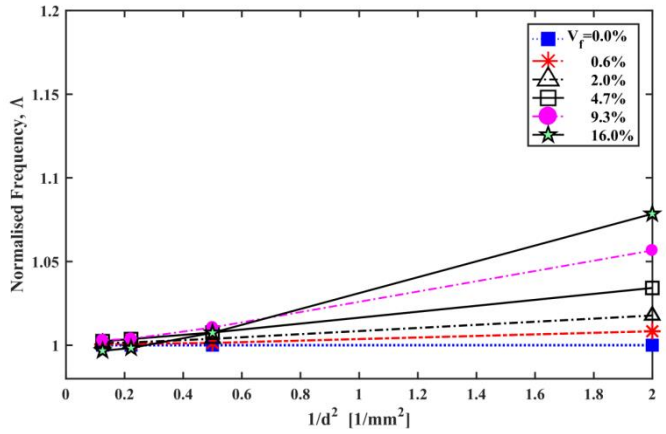

Figure 9-19: Normalised primary modal frequency of four plate sizes for plates with spherical compliant inclusions and continuous boundaries using FEA (SPCICB). $V_f = 0\ to\ 16\%$ ($V_r/S_y = 0\ to\ 0.42$)

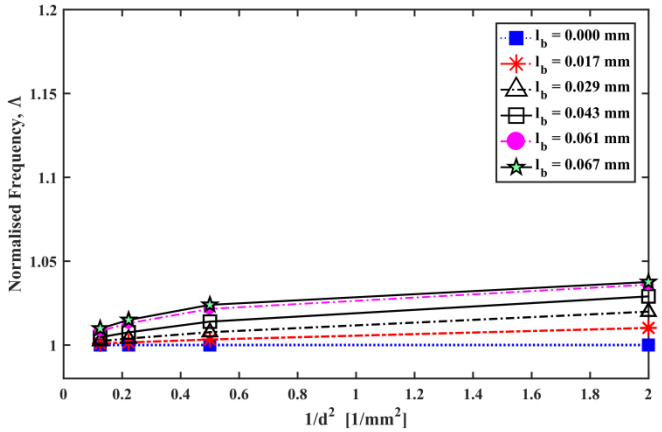

Figure 9-20: Normalised primary modal frequency of four plate sizes for plates with spherical compliant inclusions and continuous boundaries using 3D-MPFEM (SPCICB).
($l_b = 0\ to\ 0.067\ mm\ corresponds\ to\ V_f = 0\ to\ 16\%$)

The FEA results, figure 9-21, show a gradual decline in normalised modal frequencies as the mode number increase which indicates that the first five modal frequencies are less sensitive to the actual mode numbers while the 3D-MPFEM results show an inverted size effect at mode three, see figure 9-22. However, the 3D-MPFEM results for the plate with more than one unit-cell in depth show similar dynamic behaviour to the FEA results as previously shown in figure 9-9 for plates with voids.

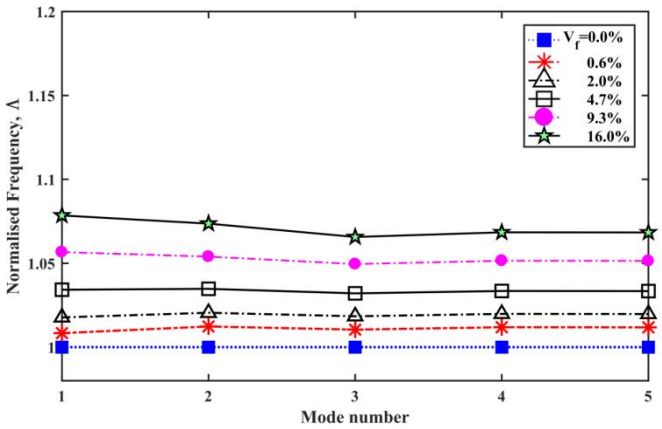

Figure 9-21: The first five normalised flexural modal frequencies of the smallest plate sample with compliant inclusions and continuous boundaries using ANSYS. $V_f = 0\ to\ 16\%\ (V_r/S_y = 0\ to\ 0.42)$

It must be noted that the 3D-MPFEM results do not show any size effect in normalised modal frequencies above mode five, therefore are not shown here. However, the first eight

non-dimensional modal frequencies predicted for the plates with SPCICB are provided in Appendix F, table F-2.

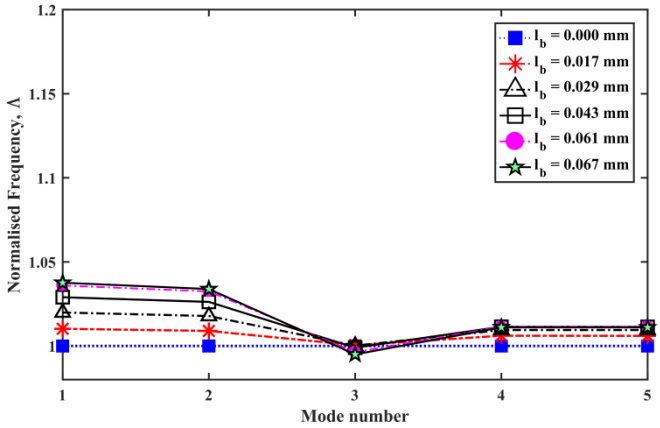

Figure 9-22: The first five normalised flexural modal frequencies of the smallest plate sample with compliant inclusions and continuous boundaries using MPFEM.
($l_b = 0\ to\ 0.067\ mm\ corresponds\ to\ V_f = 0\ to\ 16\%$)

The 3D-MPFEM results for the corresponding SPCICB plates showed convincing agreement with the FEA results except in the high volume fraction cases for the smallest plate samples; see figure 9-23. However, the results obtained by the micropolar plate simulations for the SPCICB plate models are more in agreement with the FEA results, due to having a very low degree of anisotropy in the plate models containing spherical inclusions.

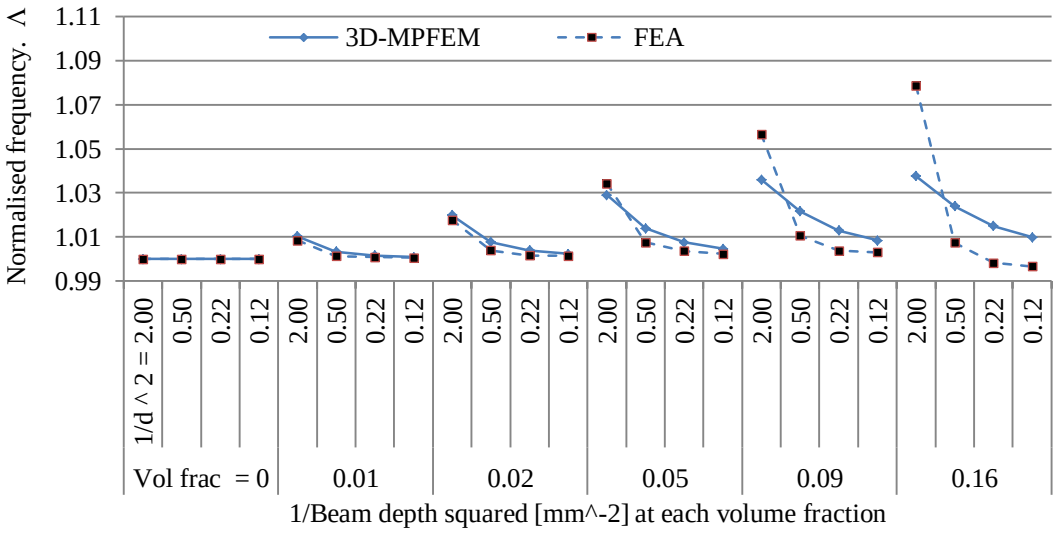

Figure 9-23: Primary normalised modal frequencies, mode 1, for plates with spherical compliant matrix and continuous boundaries, SPCICB

9.4.3 Plates with textured boundaries

The plate models with texture boundaries and spherical voids or inclusions show a different size effect for which the micropolar constants were not available; therefore 3D-MPFEM results are not obtained, but the size effect of such plate models is discussed in this section. Furthermore, the first eight non-dimensional modal frequencies of plates with textured boundaries were obtained using FEA and these are provided in Appendix F.

9.4.3.1 Plates with textured boundaries and voids (SPVOTB)

Figure 9-24 shows the inverse size effect on normalised frequencies for the primary mode of plate specimens with spherical voids and textured boundaries, SPVOTB, when the voids intersect the plate surfaces. The size effect clearly inverts but its variation remains approximately linear across the three larger samples. Figure 9-25 shows changes in Λ with mode number for the plates with the depth of one unit-cell. Here, a distinctly different size effect indicating that increasing volume fraction causes a decrease in normalised frequency, Λ, at a given model number is seen for this plates size.

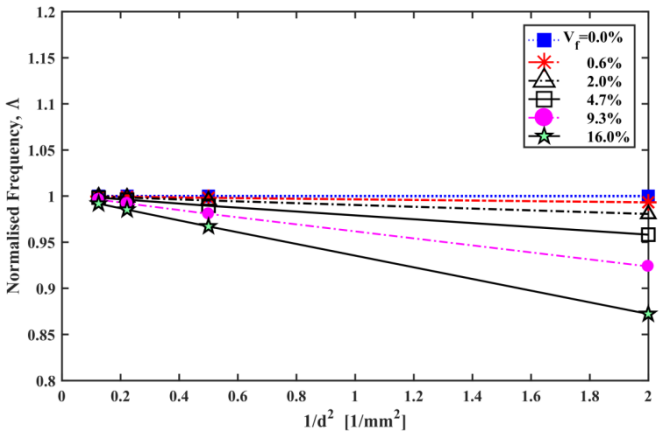

Figure 9-24: Normalised primary modal frequency of four plate sizes for plates with spherical voids and textured boundaries using FEA (SPVOTB). $V_f = 0\ to\ 16\%$ ($V_r/S_y = 0\ to\ 0.42$)

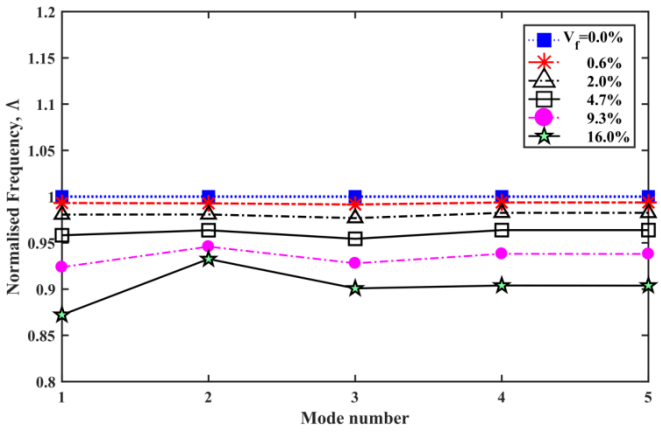

Figure 9-25: The first five normalised flexural modal frequencies of the smallest plate sample with voids and textured boundaries using FEA. $V_f = 0\ to\ 16\%$ ($V_r/S_y = 0\ to\ 0.42$)

9.4.3.2 Plates with textured boundaries and compliant inclusions (SPCITB)

Plates with spherical compliant inclusions and textured boundaries, SPCITB showed similar behaviour as the plates with spherical voids and textured boundaries, as summarised in figure 9-26.

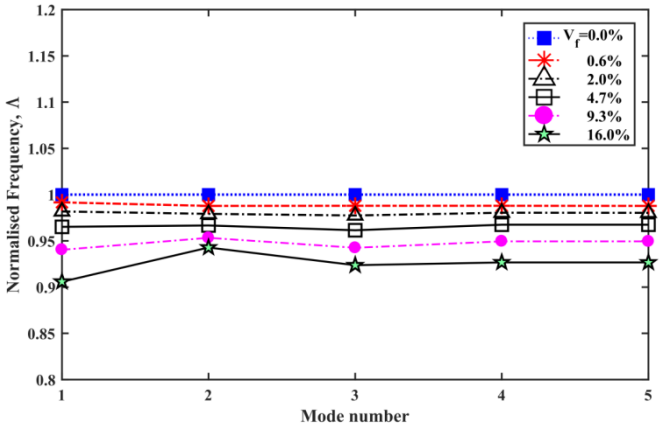

Figure 9-26: The first five normalised flexural modal frequencies of the smallest plate sample with compliant inclusions and textured boundaries using FEA. $V_f = 0\ to\ 16\%$ ($V_r/S_y = 0\ to\ 0.42$)

9.5 Conclusions

In this chapter, two types of heterogeneous plate models were created using the finite element method. The models were generated for plates with spherical voids or compliant inclusions and with both textured and continuous boundaries. The size effects due to the

various microstructures were investigated by its effect on modal frequencies in the free vibration of plates with FFFF boundary conditions in the absence of external loads.

Using finite element modelling capabilities, the spherical type void and inclusions in a body-centred arrangement were located in the plate models so that it causes a considerable reduction in the overall plate material's anisotropy which resulted in a more convincing agreement with the 3D micropolar results for beams with either voids or compliant inclusions in which the surfaces were continuous. However, the micropolar constant (Coupling number), N, could not be obtained for plates with textured surface configurations using the parameter identification algorithm as described in chapter five; therefore, the 3D-MPFEM procedure was not applied to such plate models. The crucial point in the analysis of plates with spherical void or inclusions is that although the observed size effects were attenuated in most cases, particularly plates with two or more unit cells in depth even at relatively low heterogeneity levels, there is still noticeable size effect which can be anticipated.

A set of three-dimensional beams with spherical voids and inclusions were also modelled by using finite element modelling and the transverse flexural modal frequencies of the beams were used to estimate the characteristic lengths which were then validated with the values which were obtained with a corresponding equation for plates in chapter eight, see equation (8.7). The coupling number was obtained from the dynamic behaviour of beams in a two-dimensional case. The modulus of elasticity values were obtained from the simulated static tensile analysis. The polar ratio was kept at equal to 1.5, and the characteristic length of torsion was kept as twice the value of the characteristic length of bending throughout all modal analyses.

In chapter eight, the underestimation of the normalised frequency parameters, especially at mode 3, by the 3D-MPFEM, which was understood to be due to the unidirectional orientation of the voids or inclusions within the square plates was still present for plate models in this chapter but it diminished quickly upon increasing the plate's depth.

Using 3D-MPFEM method, modal frequencies were generated for the micropolar plates. The size effects in micropolar plates were investigated. The results of 3D-MPFEM analysis were in qualitative and approximate quantitative agreement with the FEA results for the first five modal frequencies. The analysis of size effects in plates with spherical voids or inclusions in this chapter had two significant benefits. Firstly, the study showed the size effects in the

dynamic behaviour of heterogeneous materials declines with reducing the anisotropy of material due to changes in the geometry of the constituent unit-cells. Secondly, the size effect analysis made it possible to present the extent to which the linear isotropic micropolar theory applies to the heterogeneous materials.

In general, the micropolar theory was qualitatively capable of anticipating size effects in non-homogeneous plates with spherical voids or inclusions in dynamic analysis and this suggests that the micropolar theory is applicable to such problems in heterogeneous plates with a small degree of anisotropy (DA) below 0.15. Nevertheless, the 3D-MPFEM algorithm can be improved by modifying its element stiffness matrix to account for heterogeneous plates with higher DA and this is suggested for future research work.

The disagreement between the FEA and 3D-MPFEM results was still present for the smallest plate models. This might well be because the smallest plate models were comprised of one unit-cell in depth. Therefore, the body-centred cubic arrangement of the voids and inclusions did not exist for the smallest plate models which caused such disagreement between the results.

The mode shapes were also categorised and distinguished from each other based on their deformation knowing that in some modes the dynamic behaviour was predominantly controlled by shear deformation; therefore, the characteristic length of torsion is the determinative parameter in such cases. As an example mode one was categorised as the twist mode. On the contrary, mode two and three, as tangible examples, showed a tendency of being influenced by the characteristic length of bending rather than torsion. Clearly, there were some modes whose modal frequency was greatly influenced by both shearing and bending deformation e.g., modes four and five.

In summary, the numerical results indicate that the forecast size effect depends on:

- Plate depths
- Void/inclusions volume fraction
- The relative stiffness of matrix and inclusions
- Plate surface topology

These conditions are similar to the conclusions which were made in studying the beams with voids and inclusions as well as the plates with cylindrical voids and inclusions.

10 Summary and Suggestions for Future Work

10.1 Modelling specimens with heterogeneities and analysis approach

In order to study and quantify the size effect in the dynamic behaviour of nonhomogeneous materials, modal analysis of 2D beam and 3D plate models with unconstrained boundary conditions and small displacements was selected as a consistent approach to the problem. In this project, unlike the conventional approach by researchers, the models were created so that changing the depth of the specimen caused no changes in the aspect ratio of the specimens. Maintaining constant aspect ratio is important because in the homogeneous case all sizes of sample exhibit the same frequency spectrum while in heterogeneous case, in contrast, normalised frequency values not only exhibit sensitivity to the volume fraction of voids and inclusions but also to the sample's size as quantified by its depth. So the changes in volume fraction and the specimen size were both used to quantify size effects while the overall homogenized material properties of specimens were maintained. This yields a novel analysis approach which is not readily achieved by laboratory based methods and thus the best tool for doing this was indeed through finite element modelling and numerical analysis. Consequently, the results are very useful in understanding the size effect in the dynamic behaviour of nonhomogeneous materials. Another importance of this work is that unlike most previous studies of size effects which involve static loading, here an extensive investigation into size effects has been carried out in dynamic cases. The finite element models represented simple though realistic heterogeneities with various types of physical material configurations, void and inclusions, their shape and location within the specimen and also cases where they were exposed at the specimen's exterior surfaces.

The finite element analysis results revealed novel types of size effects which were not conventionally forecast by existing theoretical means. Initial numerical analysis indicated that 2D beams with voids or compliant inclusions and continuous boundaries exhibited similar dynamic behaviour and size effects while the beams with similar heterogeneities but textured boundaries behaved in a completely opposite manner and the size effect actually reversed.

3D square plate models with cylindrical voids and inclusions were modelled and analysed numerically by the finite element method and confirmed the same dynamic behaviour and size effects as seen in the 2D beam models. However, since the direction of the cylindrical

voids or inclusions in these plates was identified as a source of anisotropy within the material of the plates despite their square shape, additional more isotropic models with spherical voids and compliant inclusions were modelled and analysed which once again confirmed the size effect in their dynamic behaviour.

As the classical theory of elasticity for beams, namely Euler-Bernoulli and Timoshenko beams theories, failed to explain any size effect in 2D heterogeneous beam models, the Eringen non-local Timoshenko beam theory, a more advanced model with inherent length scale, was thus used to investigate size effect in the beam's dynamic behaviour. However, the analytically obtained results of the Eringen non-local Timoshenko beam theory again failed to explain the size effects which are exhibited by beam models. Consequently, the micropolar theory of Eringen, a higher order and more advanced theory, was chosen to investigate if the size effect in the dynamic behaviour of beams and plates can be explained by such more generalised continuum mechanics and, if so, to what extent is the theory applicable and can it capture the size effect.

10.2 Micropolar theory and size effect

The Eringen micropolar theory had been previously applied to the investigation of size effects in heterogeneous beams in the static case of three points bending by incorporating the theory into a CVFEM which showed satisfactory agreement with the FEA and laboratory test results. Therefore, the already available CVFEM stiffness matrix, as well as the mass and inertia matrices, were taken into account and incorporated into the calculations for modal analysis and obtain mode shapes. The micropolar theory was also incorporated into the conventional finite element method as an alternative procedure, namely 2D-MPFEM, which was used to confirm the CVFEM results. The traditional finite element method is computationally faster than the control volume finite element method. Therefore the study of 3D heterogeneous plates has been conducted by the micropolar finite element method alone.

Useful equations were analytically derived which can estimate the characteristic length of bending by knowing only the overall 2D beam dimensions and the primary modal frequencies of four beam sizes. The coupling number was then obtained numerically by iteration, and this was only possible for beams with voids or compliant inclusions and continuous boundaries as well as beams with a compliant matrix and textured boundaries. So, the micropolar theory was capable of being used to obtain the characteristic length of bending and coupling number in the 2D modal analysis and forecast the size effect in certain

cases for example, the coupling number is not obtainable by the iteration procedure, as described in chapter five, for beam models with voids or compliant inclusions and textured boundaries or models with compliant matrix and continuous boundaries.

The numerical iteration process for obtaining the coupling number considers only the first two modal frequencies. However, the values of coupling number did not show severe sensitivity with changes in volume fraction and are about 0.05 for 2D beams and plates with cylindrical voids or inclusions for which it was also obtainable. The coupling number values obtained are in broad agreement with statically obtained values determined previously. The coupling numbers obtained from 2D iterative analysis were used in subsequent 3D analysis.

A shortcoming of the micropolar theory is that the size effect actually seen in longitudinal modal frequencies though smaller is not anticipated at all.

Turning to the different plate types, in the three-dimensional micropolar finite element method, 3D-MPFEM, 8-nodes brick element or 15-node wedge element were uses for meshing along with the micropolar theory in the dynamic analysis of 3D plate models which has not been attempted for modal analysis before and is the novelty of this method.

The finite element results for the plates with spherical voids or compliant inclusions showed size effects which confirmed the dynamic behaviour as seen in previous heterogeneous models of 2D beams. Because of the geometrical shape and arrangement of the spheres in the plate models which suppressed the effect of any material anisotropy, the size effect was also reduced but nonetheless is still identifiable. The coupling numbers for these plate models were obtained by modelling 2D micropolar beams with the same void distribution and using the numerical iterative method. Lower values for coupling number of about 0.03 were obtained for such beams. The 3D-MPFEM results satisfactorily anticipated the size effects seen in the plates although the issue with the smallest plate models was still present and this was caused by the fact that in the smallest plate samples the body-centred cubic arrangement of the voids or inclusions was not really present.

The polar ratio and the characteristic length of torsion were not obtained numerically for two reasons. Firstly, modal analysis and iteration for N for the three-dimensional micropolar models are not expedient as it takes significant computational time and resources. Secondly, if the values of the characteristic length of torsion are based on the previous micropolar constants and another iteration process, in addition to numerical difficulties, any under or overestimation of the previous micropolar constants will be reflected and amplified for the

polar ratio and the characteristic length of torsion. Therefore, the values of these remaining micropolar constants l_t and Ψ were taken from the literature as equal to $2l_b$ and 1.5 respectively. The influence of these assumed values of the micropolar constants in predicting the FEA results is closely related to the mode number at which the modal frequency is compared. For example, the frequency at mode one which is shear dominated is more related to the value of coupling number where the optimum value for the polar ratio is 1.5. At modes two to five, when the characteristic length of torsion is set to twice the value of l_b, the predictions of micropolar theory were in good agreement with the FEA results especially if the degree of anisotropy of the plate materials remains below 0.15, particularly at mode three which is highly sensitive to the degree of anisotropy.

10.3 Project achievements and future work

The finite element and micropolar results helped greatly in investigating the size effect in the dynamic behaviour of materials through modal analysis of 2D beams and 3D plates with free boundary conditions in the absence of external loads. However, this paves the way to extend future work for other type of boundary conditions and constrained specimen edges as well as applying external load and studying the modal analysis. However, it must be noted that prescribing boundary conditions may not be mathematically straight forward. The complexity of partial constrains which are present in static cases are eliminated in unconstrained boundary condition cases involving dynamic behaviour.

The equations derived for obtaining the characteristic length of bending via modal frequencies of beams and plates are very useful and may be beneficial for research activities in future work. Moreover, the benefit of these equations is that by only obtaining the first modal frequency of slender beams or plates, the characteristic length of bending of the sample will be determined and can be used as a benchmark for verification of results for future work.

The coupling numbers for the specimens were obtained by numerical iterations based on the first two modal frequencies of 2D beam models. The values for the coupling number remain to be further studied and be analytically obtained independently from other constants as it is evident that the coupling number plays a significant role in the outcome of the analyses.

The results indicate that the micropolar type theories do not apply to the specimens with textured boundaries; therefore alternative advanced theories are required.

The algorithms for micropolar finite element method are defined for dynamic analysis of 2D beam and 3D plate models and are excellent candidates to be modified, improved and adapted for static problems such as 3D bending and also for other types of dynamic analysis such as forced vibration with a combination of boundary conditions.

The matrix of material properties which is termed as $\mathbb{D}$ matrix in this work is based on the isotropic micropolar theory which can be used for the isotropic and mildly anisotropic materials. However, the $\mathbb{D}$ matrix could be modified for application of orthotropic and highly anisotropic materials which expands the applicability of the 3D-MPFEM greatly.

The FEA results for both 2D beams and 3D plates form an invaluable database of results:

- Against which the predictions of other more generalised continuum theories can be tested;
- Which can be used for future investigation into the dynamic behaviour of 2D beams and 3D plates at higher modes because considerable time and HPC resources were used in obtaining the modal frequency data and archiving them including mode shapes for future use;
- The FEA data base can be expanded to additionally include results for dynamic cases with other type of boundary conditions and static cases as well;
- The FEA results provide a lot more information than experimental results with regard to the frequency spectrum, mode shapes, and variety of sample models which are useful in terms of reducing research time and the economic allocation of resources.

As further recommendations, from the theoretical and practical point of views this work can be expanded to investigate and study:

- Other more generalised continuum theories and their applications in predicting size effect in heterogeneous materials and compare the results with the already existing FEA results, for example investigation of the influence of the samples' surface conditions using other continuum theories;
- Other material and sample models with different type of heterogeneities such as in predicting the dynamic behaviour of foam core materials used in the construction of sandwich panel materials;
- The dynamic behaviour of highly anisotropic materials;
- The dynamic behaviour of other practical loaded heterogeneous materials;

- The influence of various types of boundary conditions in the dynamic behaviour of heterogeneous materials.

APPENDICES

Appendix A

A) Exact Analytical Solution of the Timoshenko beam theory with FF boundary conditions by separation of variables

The Timoshenko beam theory in terms of transverse deflection $\boldsymbol{W}$ can be written as in equation A.1, see references (Han, S., Benaroya, and Wei 1999), (Carcorze-soto 2010), (Manevich and Zbigniew 2011):

$$EI\frac{\partial^4 \boldsymbol{W}}{\partial x^4} + \rho A\frac{\partial^2 \boldsymbol{W}}{\partial t^2} - \left(\frac{\rho EI}{\hat{\kappa}G} + \rho I\right)\frac{\partial^4 \boldsymbol{W}}{\partial x^2 \partial t^2} + \left(\frac{\rho^2 I}{\hat{\kappa}G}\right)\frac{\partial^4 \boldsymbol{W}}{\partial t^4} = 0 \tag{A.1}$$

Note that equation (A.1) can be stated in terms of beam rotation, $\boldsymbol{\theta}$, by simply replace $\boldsymbol{W}$ with $\boldsymbol{\theta}$. The abovementioned equation is a fourth order differential equation which may also be stated in form of a quadratic equation form. Thus, the following characteristics equation is derived as in (Han, S., Benaroya, and Wei 1999; Carcorze-soto 2010):

$$(EI)k^2 + \left[-\rho I\lambda^2\left(1 + \frac{E}{\hat{\kappa}G}\right)\right]k - \rho A\lambda^2 + \frac{\rho^2 I\lambda^4}{\hat{\kappa}G} = 0 \tag{A.2}$$

According to (Doschoris 2016) the roots of the equation (A.2) are:

$$k = [k_1 k_2] = \left[\frac{-b + \sqrt{b^2 - 4ac}}{2a} \quad \frac{-b - \sqrt{b^2 - 4ac}}{2a}\right] \tag{A.3}$$

The solutions of equation (A.1) may also be written in form of displacement or rotation as in equations A.4 and A.5:

$$\boldsymbol{W} = \left(A_1 e^{sx} + A_2 e^{-sx} + A_3 e^{isx} + A_4 e^{-isx}\right)\left(T_0 e^{i\lambda t}\right) \tag{A.4}$$

$$\boldsymbol{\theta} = \left(B_1 e^{sx} + B_2 e^{-sx} + B_3 e^{isx} + B_4 e^{-isx}\right)\left(T_0 e^{i\lambda t}\right) \tag{A.5}$$

where s is the square root ($\sqrt{k}$) of the second order form of the differential equation (A.1) and T_0 is constant for time function. A_i *and* B_i are interrelated in following forms:

$$B_1 = \left(s + \frac{\rho\lambda^2}{\hat{\kappa}Gs}\right)A_1 \ , \quad B_2 = \left(-s - \frac{\rho\lambda^2}{\hat{\kappa}Gs}\right)A_2,$$
$$B_3 = \left(is - i\frac{\rho\lambda^2}{\hat{\kappa}Gs}\right)A_3 \ \ and \ \ B_4 = \left(-is + i\frac{\rho\lambda^2}{\hat{\kappa}Gs}\right)A_4 \tag{A.6}$$

Thus:

$$\boldsymbol{W} = \left(A_1T_0e^{i\lambda t}e^{sx} + A_2T_0e^{i\lambda t}e^{-sx} + A_3T_0e^{i\lambda t}e^{isx} + A_4T_0e^{i\lambda t}e^{-isx}\right) \tag{A.7}$$

$$\boldsymbol{\theta} = \left(\left(s + \frac{\rho\lambda^2}{\hat{\kappa}Gs}\right)A_1e^{sx} + \left(-s - \frac{\rho\lambda^2}{\hat{\kappa}Gs}\right)A_2e^{-sx} + \left(is_1 - i\frac{\rho\lambda^2}{\hat{\kappa}Gs}\right)A_3e^{isx} + \left(-is + i\frac{\rho\lambda^2}{\hat{\kappa}Gs}\right)A_4e^{-isx}\right)\left(T_0e^{i\lambda t}\right) \tag{A.8}$$

The boundary conditions for a free-free beam must be so that to satisfy the end conditions at x=0 and x=L so moment and shear force at both ends must equal zero:

$$Moment = 0 \ \rightarrow \left[\frac{\partial\boldsymbol{\theta}}{\partial x}\right] = 0 \ at \ x = 0 \ and \ L \tag{A.9}$$

$$Shear \ force = 0 \ \rightarrow \left[\frac{\partial\boldsymbol{W}}{\partial x} - \boldsymbol{\theta}\right] = 0 \ at \ x = 0 \ and \ L \tag{A.10}$$

This is the same as stating that second and the third derivatives of the displacement function **W** must be equal zero at x=0 and x=L.

$$\begin{Bmatrix} \boldsymbol{W}''_{(x=0)} = 0 \\ \boldsymbol{W}'''_{(x=0)} = 0 \\ \boldsymbol{W}''_{(x=L)} = 0 \\ \boldsymbol{W}'''_{(x=L)} = 0 \end{Bmatrix}$$ or it can be written as $$\begin{Bmatrix} \left[\frac{\partial \boldsymbol{\theta}}{\partial x}\right]_{x=0} = 0 \\ \left[\frac{\partial \boldsymbol{W}}{\partial x} - \boldsymbol{\theta}\right]_{x=0} = 0 \\ \left[\frac{\partial \boldsymbol{\theta}}{\partial x}\right]_{x=L} = 0 \\ \left[\frac{\partial \boldsymbol{W}}{\partial x} - \boldsymbol{\theta}\right]_{x=L} = 0 \end{Bmatrix}$$ or in matrix form we get the following equation:

$$\begin{bmatrix} s^2 + \frac{\rho\lambda^2}{\hat{\kappa}G} & s^2 + \frac{\rho\lambda^2}{\hat{\kappa}G} & -s^2 + \frac{\rho\lambda^2}{\hat{\kappa}G} & -s^2 + \frac{\rho\lambda^2}{\hat{\kappa}G} \\ -\frac{\rho\lambda^2}{\hat{\kappa}Gs} & \frac{\rho\lambda^2}{\hat{\kappa}Gs} & \left(\frac{\rho\lambda^2}{\hat{\kappa}Gs}\right)i & -\left(\frac{\rho\lambda^2}{\hat{\kappa}Gs}\right)i \\ (e^{sl}s^2 + \frac{e^{sl}\rho\lambda^2}{\hat{\kappa}G}) & (\frac{s^2}{e^{sl}} + \frac{\rho\lambda^2}{\hat{\kappa}Ge^{sl}}) & (-e^{isl}s^2 + \frac{e^{isl}\rho\lambda^2}{\hat{\kappa}G}) & (-\frac{s^2}{e^{isl}} + \frac{\rho\lambda^2}{\hat{\kappa}Ge^{isl}}) \\ -\frac{\rho\lambda^2 e^{sl}}{\hat{\kappa}Gs} & \frac{\rho\lambda^2}{\hat{\kappa}Gse^{sl}} & \left(\frac{\rho\lambda^2 e^{isl}}{\hat{\kappa}Gs}\right)i & -\left(\frac{\rho\lambda^2}{\hat{\kappa}Gs_1 e^{isl}}\right)i \end{bmatrix} \begin{bmatrix} A_1 \\ A_2 \\ A_3 \\ A_4 \end{bmatrix} = 0 \quad \text{(A.11)}$$

The above determinant consists of both real and imaginary parts. After solving the above 4by4 determinant and applying lengthy but simple multiplications and collection of variables, the real portions of the final equation will cancel each other out and only the imaginary parts will remain as follows:

$$\left\{\left[\cos(sl) \times (\frac{1}{e^{sl}} + e^{sl})\right] - 2\right\} \mathrm{i} \frac{4\rho^4}{\hat{\kappa}^4 G^4 s^2}\lambda^8 + [(\frac{1}{e^{sl}} - e^{sl}) \times \sin(sl)]i \frac{8\rho^3}{\hat{\kappa}^3 G^3}\lambda^6 + [2 - \cos(sl) \times (\frac{1}{e^{sl}} + e^{sl})]i \frac{4s^2\rho^2}{\hat{\kappa}^2 G^2}\lambda^4 = 0 \quad \text{(A.12)}$$

Appendix B

B) FEA Numerical Results (Transverse Frequencies) for 2D Beams with Voids and Inclusions

Table B-1: FEA results for the first ten non-dimensional bending modal frequencies, λ, of four beam sizes for beams with voids and continuous boundaries.

V_r/S_y	$1/d^2$	Mode 1	Mode 2	Mode 3	Mode 4	Mode 5	Mode 6	Mode 7	Mode 8	Mode 9	Mode 10
0.12	1.33	4.76955	7.68132	10.35591	12.76693	14.93788	16.88913	18.61605	19.99604	22.62761	23.77287
	0.33	4.68729	7.57493	10.25310	12.69255	14.91404	16.94335	18.80583	20.52301	22.11161	23.58229
	0.15	4.66959	7.54856	10.22110	12.65790	14.87917	16.91035	18.77657	20.49923	22.09501	23.57460
	0.08	4.66333	7.53907	10.20920	12.64431	14.86449	16.89507	18.76115	20.48404	22.08054	23.56148
0.17	1.33	4.90166	7.84884	10.51240	12.87028	14.94866	16.75620	18.25124	19.27956	23.33800	24.05576
	0.33	4.72757	7.63200	10.31759	12.75624	14.97082	16.98881	18.83670	20.53666	22.10554	23.55362
	0.15	4.68756	7.57440	10.25109	12.68880	14.90873	16.93700	18.79930	20.51731	22.10779	23.58129
	0.08	4.67318	7.55331	10.22584	12.66164	14.88138	16.91078	18.77521	20.49630	22.09079	23.56949
0.23	1.33	5.06288	8.02794	10.63599	12.87575	14.78071	16.35164	17.54079	18.26429	22.58100	22.85800
	0.33	4.78076	7.70206	10.38746	12.81145	15.00121	16.98756	18.79922	20.45959	21.98596	23.38806
	0.15	4.71149	7.60675	10.28491	12.71812	14.92935	16.94617	18.79525	20.49900	22.07450	23.53231
	0.08	4.68620	7.57108	10.24467	12.67837	14.89384	16.91758	18.77564	20.48990	22.07746	23.54905
0.29	1.33	5.22486	8.15349	10.61435	12.65910	14.31213	15.59849	16.50500	17.02099	20.76968	21.14741
	0.33	4.83872	7.76881	10.43623	12.82049	14.95620	16.87921	18.62170	20.20869	21.65796	22.97855
	0.15	4.73769	7.63848	10.31101	12.72910	14.91850	16.90907	18.72915	20.40219	21.94600	23.37150
	0.08	4.70036	7.58842	10.25926	12.68512	14.88911	16.89905	18.74183	20.44008	22.01115	23.46609
0.35	1.33	5.35391	8.14392	10.37197	12.11473	13.47552	14.48776	15.17417	15.55343	18.77221	19.31754
	0.33	4.89192	7.80981	10.42461	12.72609	14.76084	16.57268	18.19838	19.66493	20.99083	22.18467
	0.15	4.76152	7.65909	10.31068	12.69310	14.83683	16.77533	18.53948	20.15453	21.63943	23.00600
	0.08	4.71287	7.59915	10.25851	12.66461	14.84301	16.82350	18.63439	20.29934	21.83652	23.25743

Table B-2: FEA results for the first ten non-dimensional bending modal frequencies, λ, of four beam sizes for beams with compliant inclusions and continuous boundaries.

V_r/S_y	$1/d^2$	Mode 1	Mode 2	Mode 3	Mode 4	Mode 5	Mode 6	Mode 7	Mode 8	Mode 9	Mode 10
0.12	1.33	4.75123	7.66769	10.35911	12.79741	15.00668	17.01499	18.84630	20.49177	22.19597	23.59273
	0.33	4.68110	7.56720	10.24600	12.68789	14.91294	16.94646	18.81348	20.53531	22.12848	23.60351
	0.15	4.66748	7.54630	10.21966	12.65800	14.88127	16.91468	18.78318	20.50804	22.10581	23.58711
	0.08	4.66249	7.53830	10.20903	12.64515	14.86659	16.89853	18.76588	20.49005	22.08768	23.56959
0.17	1.33	4.84870	7.79438	10.48399	12.89362	15.05104	16.97843	18.66707	19.97418	22.70293	23.81555
	0.33	4.71030	7.60966	10.29603	12.74053	14.96462	16.99474	18.85674	20.57241	22.15847	23.62528
	0.15	4.68058	7.56559	10.24292	12.68337	14.90744	16.94082	18.80887	20.53297	22.12978	23.60976
	0.08	4.66978	7.54912	10.22220	12.65969	14.88186	16.91418	18.78177	20.50613	22.10393	23.58594
0.23	1.33	4.96849	7.94033	10.61103	12.96234	15.02517	16.80993	18.27300	19.25911	23.40805	23.92484
	0.33	4.74841	7.66251	10.35388	12.79499	15.00981	17.02668	18.87283	20.57082	22.13765	23.58338
	0.15	4.69778	7.58987	10.27030	12.71048	14.93192	16.96124	18.82433	20.54298	22.13400	23.60783
	0.08	4.67937	7.56279	10.23785	12.67553	14.89668	16.92727	18.79279	20.51494	22.11055	23.59024
0.29	1.33	5.09188	8.07596	10.70363	12.96512	14.89632	16.50033	17.72840	18.48490	22.82080	23.10764
	0.33	4.78987	7.71682	10.40761	12.83679	15.03172	17.02332	18.84050	20.50669	22.03927	23.44780
	0.15	4.71681	7.61537	10.29664	12.73282	14.94694	16.96665	18.81872	20.52549	22.10404	23.56488
	0.08	4.69009	7.57735	10.25318	12.68902	14.90650	16.93228	18.79233	20.50866	22.09828	23.57190
0.35	1.33	5.19900	8.18027	10.75120	12.91266	14.70869	16.14526	17.19202	17.80838	21.86749	22.21757
	0.33	4.82774	7.76310	10.44718	12.85702	15.02368	16.98069	18.75855	20.38153	21.86718	23.22472
	0.15	4.73465	7.63768	10.31667	12.74478	14.94674	16.95144	18.78654	20.47502	22.03434	23.47507
	0.08	4.70048	7.59047	10.26515	12.69652	14.90715	16.92448	18.77513	20.48139	22.06051	23.52323

Table B-3: FEA results for the first ten non-dimensional bending modal frequencies, λ, of four beam sizes with compliant matrix and textured boundaries

V_r/S_y	$1/d^2$	Mode 1	Mode 2	Mode 3	Mode 4	Mode 5	Mode 6	Mode 7	Mode 8	Mode 9	Mode 10
0.12	1.33	4.72946	7.63167	10.31391	12.74914	14.96101	16.97705	18.82349	20.52080	22.08456	23.51864
	0.33	4.67474	7.55630	10.23092	12.66928	14.89158	16.92312	18.78891	20.51027	22.10379	23.58024
	0.15	4.66415	7.54046	10.21133	12.64735	14.86851	16.90006	18.76707	20.49073	22.08789	23.56936
	0.08	4.66041	7.53475	10.20404	12.63884	14.85907	16.88991	18.75639	20.47983	22.07692	23.55855
0.17	1.33	4.79981	7.73649	10.44016	12.88522	15.09868	17.11120	18.95153	20.64153	22.19873	23.62610
	0.33	4.69361	7.58611	10.26980	12.71521	14.94282	16.97809	18.84626	20.56862	22.16152	23.63539
	0.15	4.67256	7.55394	10.22929	12.66920	14.89381	16.92850	18.79839	20.52477	22.12430	23.60763
	0.08	4.66512	7.54233	10.21420	12.65134	14.87374	16.90666	18.77518	20.50069	22.09963	23.58306
0.23	1.33	4.86778	7.83361	10.54994	12.99331	15.19525	17.19013	19.00983	20.67820	22.21484	23.62362
	0.33	4.71272	7.61511	10.30545	12.75433	14.98271	17.01645	18.88109	20.59805	22.18360	23.64764
	0.15	4.68105	7.56693	10.24559	12.68764	14.91352	16.94881	18.81879	20.54492	22.14375	23.62573
	0.08	4.66980	7.54951	10.22324	12.66163	14.88488	16.91839	18.78735	20.51312	22.11233	23.59574
0.29	1.33	4.92902	7.91767	10.63896	13.07209	15.25356	17.22171	19.01125	20.64896	22.15520	23.53770
	0.33	4.73121	7.64217	10.33705	12.78652	15.01227	17.04078	18.89797	20.60541	22.17930	23.62915
	0.15	4.68972	7.57979	10.26091	12.70387	14.92945	16.96357	18.83174	20.55554	22.15156	23.63006
	0.08	4.67484	7.55698	10.23220	12.67124	14.89453	16.92768	18.79602	20.52104	22.11932	23.60152
0.35	1.33	4.97450	7.97691	10.69532	13.11107	15.26453	17.19681	18.94450	20.53606	21.99261	23.32542
	0.33	4.74526	7.66210	10.35901	12.80674	15.02757	17.04848	18.89564	20.59065	22.14966	23.58161
	0.15	4.69628	7.58920	10.27154	12.71418	14.93820	16.96979	18.83470	20.55444	22.14572	23.61878
	0.08	4.67845	7.56215	10.23804	12.67693	14.89946	16.93139	18.79821	20.52143	22.11778	23.59761

Note: Micropolar theory does not apply to the FEA results which are provided in the next three tables A-4 to A-6.

Table B-4: FEA results for the first ten non-dimensional bending modal frequencies, λ, of four beam sizes for beams with voids and textured boundaries.(BVOTB)

V_r/S_y	$1/d^2$	Mode 1	Mode 2	Mode 3	Mode 4	Mode 5	Mode 6	Mode 7	Mode 8	Mode 9	Mode 10
0.12	1.33	4.46441	7.24540	9.85519	12.26018	14.47163	16.50739	18.39289	20.12539	21.73600	23.21958
	0.33	4.60562	7.44731	10.08676	12.49434	14.68954	16.69718	18.54218	20.24584	21.82513	23.29161
	0.15	4.63202	7.48910	10.14213	12.56149	14.76677	16.78308	18.63534	20.34500	21.92897	23.39882
	0.08	4.64149	7.50434	10.16279	12.58724	14.79742	16.81836	18.67507	20.38892	21.97680	23.45007
0.17	1.33	4.27663	6.96480	9.51273	11.88429	14.08302	16.11926	18.00429	19.74958	21.35540	22.80511
	0.33	4.56247	7.37419	9.98165	12.35565	14.51631	16.48902	18.29906	19.96798	21.51278	22.94510
	0.15	4.61224	7.45512	10.09246	12.49481	14.68218	16.67992	18.51339	20.20437	21.77018	23.22299
	0.08	4.62983	7.48425	10.13333	12.54755	14.74686	16.75653	18.60175	20.30415	21.88082	23.34353
0.23	1.33	4.04846	6.61526	9.07218	11.38240	13.54270	15.55583	17.42541	19.15406	20.73298	22.13102
	0.33	4.51730	7.29154	9.85333	12.17503	14.27896	16.19256	17.94243	19.55080	21.03488	22.40625
	0.15	4.59282	7.41882	10.03480	12.41198	14.57147	16.53972	18.34305	20.00390	21.54037	22.96538
	0.08	4.61897	7.46373	10.10043	12.49993	14.68284	16.67507	18.50235	20.18680	21.74599	23.19222
0.29	1.33	3.78355	6.19944	8.53137	10.74385	12.82918	14.78308	16.60534	18.28903	19.82041	21.16942
	0.33	4.47136	7.19942	9.69922	11.94638	13.96812	15.79559	17.45799	18.97892	20.37611	21.66117
	0.15	4.57417	7.38000	9.96771	12.30975	14.42940	16.35513	18.11472	19.73186	21.22556	22.60968
	0.08	4.60907	7.44257	10.06307	12.44213	14.60163	16.56870	18.36993	20.02824	21.56182	22.98364
0.35	1.33	3.48557	5.72363	7.89873	9.97832	11.95237	13.81322	15.55441	17.16643	18.63458	19.88314
	0.33	4.42469	7.09477	9.51141	11.65692	13.56704	15.27907	16.82599	18.23326	19.51922	20.69549
	0.15	4.55550	7.33585	9.88499	12.17779	14.24130	16.10705	17.80524	19.36103	20.79465	22.12091
	0.08	4.59927	7.41832	10.01628	12.36601	14.49158	16.42196	18.18530	19.80557	21.30176	22.68774

Table B-5: FEA results for the first ten non-dimensional bending modal frequencies, λ, of four beam sizes for beams with compliant inclusions and textured boundaries.(BINTB)

V_r/S_y	$1/d^2$	Mode 1	Mode 2	Mode 3	Mode 4	Mode 5	Mode 6	Mode 7	Mode 8	Mode 9	Mode 10
0.12	1.33	4.51605	7.31346	9.92525	12.32020	14.51296	16.52368	18.37101	20.07825	21.65362	23.10773
	0.33	4.62023	7.46881	10.11317	12.52394	14.72092	16.72917	18.57365	20.27577	21.85259	23.31579
	0.15	4.63989	7.50100	10.15721	12.57900	14.78618	16.80380	18.65686	20.36677	21.95054	23.41972
	0.08	4.64696	7.51275	10.17367	12.60016	14.81200	16.83433	18.69210	20.40672	21.99502	23.46844
0.17	1.33	4.38917	7.12858	9.70687	12.09052	14.28881	16.31732	18.19235	19.93034	21.53995	23.02279
	0.33	4.59087	7.42067	10.04633	12.43873	14.61784	16.60902	18.43752	20.12493	21.68840	23.13980
	0.15	4.62722	7.47983	10.12715	12.53970	14.73738	16.74548	18.58920	20.29018	21.86562	23.32748
	0.08	4.64006	7.50115	10.15704	12.57818	14.78444	16.80109	18.65318	20.36220	21.94526	23.41396
0.23	1.33	4.24250	6.90973	9.43976	11.79736	13.98606	16.01594	17.89808	19.64316	21.25236	22.71077
	0.33	4.55888	7.36509	9.96417	12.32776	14.47681	16.43768	18.23620	19.89442	21.42958	22.85352
	0.15	4.61286	7.45437	10.08864	12.48650	14.66840	16.66021	18.48755	20.17250	21.73271	23.18058
	0.08	4.63166	7.48616	10.13421	12.54645	14.74312	16.74971	18.59164	20.29067	21.86418	23.32400
0.29	1.33	4.10052	6.69304	9.16710	11.48629	13.64945	15.66161	17.52834	19.25456	20.83378	22.23871
	0.33	4.53107	7.31325	9.88238	12.21129	14.32302	16.24554	18.00582	19.62655	21.12520	22.51347
	0.15	4.60140	7.43215	10.05220	12.43293	14.59577	16.56743	18.37441	20.03931	21.58029	23.01028
	0.08	4.62554	7.47396	10.11375	12.51586	14.70108	16.69548	18.52494	20.21162	21.77315	23.22181
0.35	1.33	3.98470	6.51302	8.93458	11.21201	13.34051	15.32128	17.15460	18.84169	20.37054	21.71070
	0.33	4.50910	7.26928	9.80900	12.10299	14.17684	16.06054	17.78247	19.36602	20.82885	22.18260
	0.15	4.59236	7.41294	10.01850	12.38116	14.52356	16.47363	18.25860	19.90183	21.42191	22.83222
	0.08	4.62075	7.46328	10.09433	12.48530	14.65772	16.63844	18.45375	20.12634	21.67416	23.10977

Table B-6: FEA results for the first ten non-dimensional bending modal frequencies, λ, of four beam sizes for beams with compliant matrix and continuous boundaries.(BCMCB)

V_r/S_y	$1/d^2$	Mode 1	Mode 2	Mode 3	Mode 4	Mode 5	Mode 6	Mode 7	Mode 8	Mode 9	Mode 10
0.12	1.33	4.61383	7.47353	10.14126	12.58521	14.82253	16.87804	18.78383	20.71425	21.76321	23.53297
	0.33	4.64432	7.50988	10.17193	12.60087	14.81635	16.84333	18.70668	20.42775	22.02311	23.50382
	0.15	4.65070	7.51966	10.18426	12.61496	14.83147	16.85889	18.72219	20.44272	22.03715	23.51663
	0.08	4.65276	7.52278	10.18824	12.61963	14.83670	16.86457	18.72822	20.44895	22.04354	23.52292
0.17	1.33	4.55692	7.38608	10.03265	12.46490	14.69803	16.75459	18.66406	20.56475	21.67034	23.43582
	0.33	4.63126	7.48793	10.14103	12.56132	14.76882	16.78869	18.64621	20.36279	21.95542	23.43536
	0.15	4.64474	7.50934	10.16924	12.59501	14.80651	16.82899	18.68752	20.40367	21.99423	23.47059
	0.08	4.64938	7.51694	10.17967	12.60816	14.82223	16.84705	18.70767	20.42549	22.01731	23.49433
0.23	1.33	4.49132	7.28276	9.90045	12.31340	14.53530	16.58635	18.49186	20.33557	21.59447	23.28639
	0.33	4.61766	7.46393	10.10556	12.51390	14.70954	16.71840	18.56605	20.27438	21.86057	23.33626
	0.15	4.63864	7.49819	10.15218	12.57135	14.77586	16.79121	18.64278	20.35213	21.93648	23.40755
	0.08	4.64596	7.51066	10.17003	12.59467	14.80461	16.82512	18.68142	20.39501	21.98266	23.45596
0.29	1.33	4.42665	7.17754	9.76069	12.14632	14.34703	16.38025	18.26414	20.01883	21.59575	23.10994
	0.33	4.60665	7.44292	10.07226	12.46671	14.64790	16.64239	18.47642	20.17232	21.74750	23.21389
	0.15	4.63395	7.48873	10.13647	12.54816	14.74441	16.75106	18.59380	20.29446	21.87053	23.33409
	0.08	4.64343	7.50553	10.16136	12.58175	14.78687	16.80226	18.65327	20.36154	21.94411	23.41255
0.35	1.33	4.36876	7.07890	9.62276	11.97163	14.13677	16.13128	17.96091	19.58367	21.71911	22.96106
	0.33	4.59933	7.42714	10.04481	12.42512	14.59054	16.56852	18.38565	20.06448	21.62267	23.07231
	0.15	4.63134	7.48230	10.12432	12.52869	14.71644	16.71377	18.54664	20.23714	21.80307	23.25671
	0.08	4.64233	7.50251	10.15534	12.57171	14.77211	16.78225	18.62765	20.33008	21.90677	23.36949

Appendix C

C) Solution to Small scale effects on Non-Local Timoshenko beam for free-free boundary conditions:

C.1 Eringen Nonlocal Effect In x Direction

A modified Timoshenko beam theory based on Eringen's nonlocal theory has been used in nanotechnology in recent years. Wang et al. (2007) incorporated the Eringen small scale coefficient $e_0\bar{a}$ into the moment in the Timoshenko beam model. Here, the work of Wang et al., which was briefly discussed earlier in chapter two, is extended to include the free-free boundary condition:

Normal and shear stresses can be stated in following forms:

$$\boldsymbol{\sigma}_{xx} - (e_0\bar{a})^2 \frac{d^2\boldsymbol{\sigma}_{xx}}{dx^2} = E\boldsymbol{\varepsilon}_{xx} \tag{C.1}$$

$$\boldsymbol{\sigma}_{xy} = G\boldsymbol{\gamma}_{xy} \tag{C.2}$$

where $(e_0\bar{a})$ has the dimension of length and referred to as α "Alpha" which stand for small length scale parameter; "e_0" is the small length scale coefficient which is dimensionless; "$\bar{a}$" is internal characteristic length. Wang et al did not consider the nonlocal effect into shear constitutive relations. However, the influence of the Eringen's nonlocal small length scale parameter, α, in both horizontal and vertical stress components will be discussed in appendix C.2 and the nonlocal Timoshenko beam will be solved for such assumptions.

The term α can be identified by the curve fitting methods. However, the constituent terms in α such as $\bar{a}$ or e_0 have their mechanical definitions too. For example "$\bar{a}$" as the internal characteristic length can be related to molecular bonds or granular size or distance in materials. Some researchers have attempted to obtain e_0 analytically. In a very recent work Wang et al modelled a beam by dividing it into finite rigid elements (segments), elastic rotational springs and lumped masses where the segments join together and by applying

Hamilton principle to their model, they were able to obtain the small length scale coefficient "e_0" by analytical method and showed that e_0 is approximately equals to 0.408 or $\frac{1}{\sqrt{6}}$ for vibration of nonlocal Euler beams when there is no load applied on the beam eg. Initial axial stress ratio is zero$^{\boldsymbol{\sigma}_0}/_{\breve{\boldsymbol{\sigma}}_m} = 0$, and for initial stress ration from -1 to +1, e_0 changes from 0.5 to 0.289 and found that e_0 is independent from vibration modes (Z. Zhang, Challamel, and Wang 2013),(Zhen Zhang, Wang, and Challamel 2015).

The shear force and bending moment with taking the effect of the Eringen small length scale parameter in x coordinates may be stated as in (Wang, Zhang, and He 2007):

$$\boldsymbol{Q} = \hat{\kappa}GA\left(\boldsymbol{\theta} + \frac{d\boldsymbol{W}}{dx}\right) \tag{C.3}$$

$$\boldsymbol{M} = EI\frac{d\boldsymbol{\theta}}{dx} - (e_0\bar{a})^2(\rho A\omega^2\boldsymbol{W} + \rho I\omega^2\frac{d\boldsymbol{\theta}}{dx}) \tag{C.4}$$

Thus the governing equations of nonlocal Timoshenko may be modified as:

$$EI\frac{d^2\boldsymbol{\theta}}{dx^2} - \hat{\kappa}GA\left(\boldsymbol{\theta} + \frac{d\boldsymbol{W}}{dx}\right) + \rho I\omega^2\boldsymbol{\theta} - (e_0\bar{a})^2\left(\rho A\omega^2\frac{d\boldsymbol{W}}{dx} + \rho I\omega^2\frac{d^2\boldsymbol{\theta}}{dx^2}\right) = 0 \tag{C.5}$$

$$\hat{\kappa}GA\left(\frac{d\boldsymbol{\theta}}{dx} + \frac{d^2\boldsymbol{W}}{dx^2}\right) + \rho A\omega^2\boldsymbol{W} = 0 \tag{C.6}$$

Considering the following non-dimensional parameters:

$\overline{x} = \frac{x}{L}$, $\overline{\boldsymbol{W}} = \frac{\boldsymbol{W}}{L}$, $\lambda^2 = \omega^2\frac{\rho AL^4}{EI}$, λ is frequency parameter. $\hat{\Omega} = \frac{EI}{\hat{\kappa}GAL^2}$ Shear deformation parameters, $\alpha = e_0\bar{a}/L$ as scaling effect parameter and finally $\hat{\xi} = \frac{L\sqrt{A}}{\sqrt{I}}$ which is the slenderness ratio.

Thus according to Wang et al (2007) the Timoshenko governing equations for beams can be rewritten in a non-dimensional form as follows:

$$\hat{\Omega}\left(1 - \frac{\alpha^2\lambda^2}{\hat{\xi}^2}\right)\frac{d^2\boldsymbol{\theta}}{d\overline{x}^2} + \left(\frac{\lambda^2\hat{\Omega}}{\hat{\xi}^2} - 1\right)\boldsymbol{\theta} - \left(\alpha^2\lambda^2\hat{\Omega} + 1\right)\frac{d\overline{\boldsymbol{W}}}{d\overline{x}} = 0 \tag{C.7}$$

$$\left(\frac{d\boldsymbol{\theta}}{d\overline{x}}+\frac{d^2\overline{\boldsymbol{W}}}{d\overline{x}^2}\right)+\lambda^2\hat{\Omega}\overline{\boldsymbol{W}}=0 \tag{C.8}$$

The equations (C.7) and (C.8) can be decoupled in term of $\overline{w}$ and θ as follows:

$$\left(1-\frac{\alpha^2\lambda^2}{\hat{\xi}^2}\right)\frac{d^4\overline{\boldsymbol{W}}}{d\overline{x}^4}+\lambda^2\left(\hat{\Omega}+\frac{1-\hat{\Omega}\alpha^2\lambda^2}{\hat{\xi}^2}+\alpha^2\right)\frac{\boldsymbol{d^2\overline{W}}}{d\overline{x}^2}+\lambda^2\left(\frac{\lambda^2\hat{\Omega}}{\hat{\xi}^2}-1\right)\overline{\boldsymbol{W}}=0 \tag{C.9}$$

$$\left(1-\frac{\alpha^2\lambda^2}{\hat{\xi}^2}\right)\frac{d^4\boldsymbol{\theta}}{d\overline{x}^4}+\lambda^2\left(\hat{\Omega}+\frac{1-\hat{\Omega}\alpha^2\lambda^2}{\hat{\xi}^2}+\alpha^2\right)\frac{d^2\boldsymbol{\theta}}{d\overline{x}^2}+\lambda^2\left(\frac{\lambda^2\hat{\Omega}}{\hat{\xi}^2}-1\right)\boldsymbol{\theta}=0 \tag{C.10}$$

The solutions of the above equations are:

$$\overline{\boldsymbol{W}}=C_1 sinh(\beta\overline{x})+C_2 cosh(\beta\overline{x})+C_3 sin(\gamma\overline{x})+C_4 cos(\gamma\overline{x}) \tag{C.11}$$

$$\boldsymbol{\theta}=D_1 sinh(\beta\overline{x})+D_2 cosh(\beta\overline{x})+D_3 sin(\gamma\overline{x})+D_4 cos(\gamma\overline{x}) \tag{C.12}$$

where:

$$a=\left(1-\frac{\alpha^2\lambda^2}{\hat{\xi}^2}\right),\ b=\lambda^2\left(\hat{\Omega}+\frac{1-\hat{\Omega}\alpha^2\lambda^2}{\hat{\xi}^2}+\alpha^2\right)\ and\ c=\lambda^2\left(\frac{\lambda^2\hat{\Omega}}{\hat{\xi}^2}-1\right) \tag{C.13}$$

$$\binom{\beta}{\gamma}=\left(\frac{\pm b+\sqrt{b^2-4ac}}{2a}\right)^{1/2} \tag{C.14}$$

According to Wang et al. (2007) the constants $C_i\ and\ D_i$ are not independent and related as follows:

$$D_1 = C_1 \widehat{\Psi}_\beta \tag{C.15}$$

$$D_2 = C_2 \widehat{\Psi}_\beta \tag{C.16}$$

$$D_3 = C_3 \widehat{\Psi}_\gamma \tag{C.17}$$

$$D_4 = -C_4 \widehat{\Psi}_\gamma \tag{C.18}$$

$$\widehat{\Psi}_\beta = -\frac{\beta^2 + \lambda^2 \hat{\Omega}}{\beta} \tag{C.19}$$

$$\widehat{\Psi}_\gamma = \frac{\gamma^2 + \lambda^2 \hat{\Omega}}{\gamma} \tag{C.20}$$

Wang et al. (2007) have provided the solutions of the above equations for various boundary conditions except for beam model with free-free boundary conditions. To apply the boundary conditions for free-free beam, the bending moment and shear forces at either edges of the beam must be equal to zero as follows:

$$\overline{\boldsymbol{M}} = \frac{\boldsymbol{M}L}{EI} = \left(1 - \frac{\alpha^2 \lambda^2}{\hat{\xi}^2}\right) \frac{d\boldsymbol{\theta}}{d\overline{x}} - \alpha^2 \lambda^2 \overline{\boldsymbol{W}} = 0 \qquad at\ \overline{x} = 0\ and\ at\ \overline{x} = 1 \tag{C.21}$$

$$\overline{\boldsymbol{Q}} = \frac{\boldsymbol{Q}}{\hat{\kappa} GA} = \boldsymbol{\theta} + \frac{d\overline{\boldsymbol{W}}}{d\overline{x}} = 0 \qquad \text{at } \overline{x} = 0\ and\ at\ \overline{x} = 1 \tag{C.22}$$

Thus the eigenvalue problem for a free- free beam can be solved as follows:

$$\begin{bmatrix} H_1 & 0 & H_2 & 0 \\ 0 & H_3 & 0 & -H_4 \\ H_1\cosh\beta & H_1\sinh\beta & H_2\cos\gamma & H_2\sin\gamma \\ H_3\sinh\beta & H_3\cosh\beta & H_4\sin\gamma & -H_4\cos\gamma \end{bmatrix} \times \begin{Bmatrix} C_1 \\ C_2 \\ C_3 \\ C_4 \end{Bmatrix} = 0 \quad \text{(C.23)}$$

$$H_1 = \alpha^2\lambda^2 + \left(\frac{\alpha^2\lambda^2}{\hat{\xi}^2} - 1\right)\beta\widehat{\Psi}_\beta \quad \text{(C.24)}$$

$$H_2 = \alpha^2\lambda^2 + \left(\frac{\alpha^2\lambda^2}{\hat{\xi}^2} - 1\right)\gamma\widehat{\Psi}_\gamma \quad \text{(C.25)}$$

$$H_3 = \widehat{\Psi}_\beta + \beta \quad \text{(C.26)}$$

$$H_4 = \widehat{\Psi}_\gamma - \gamma \quad \text{(C.27)}$$

In order to make sure that both sides of equation (C.23) equal zero then the determinant of the matrix must equal zero:

$$\begin{vmatrix} H_1 & 0 & H_2 & 0 \\ 0 & H_3 & 0 & -H_4 \\ H_1\cosh\beta & H_1\sinh\beta & H_2\cos\gamma & H_2\sin\gamma \\ H_3\sinh\beta & H_3\cosh\beta & H_4\sin\gamma & -H_4\cos\gamma \end{vmatrix} = \begin{vmatrix} 0 \\ 0 \\ 0 \\ 0 \end{vmatrix} \quad \text{(C.28)}$$

Solution of the above equation equals:

$$2H_1H_2H_3H_4(\cosh\beta\cos\gamma - 1) + [(H_2H_3)^2 - (H_1H_4)^2]\sinh\beta\sin\gamma = 0 \quad \text{(C.29)}$$

$$(\cosh\beta\cos\gamma - 1) + ([(H_2H_3)^2 - (H_1H_4)^2]/2H_1H_2H_3H_4)\sinh\beta\sin\gamma = 0 \quad \text{(C.30)}$$

C.2 The Effect of Eringen Small Length Scale parameter, α, in both Normal and Shear Stress Components (x and y components of stresses)

In this appendix section the Eringen's nonlocal effect assumed also considered to influence in y direction too. Hosseini et al. (2013) has influenced the Eringen's material constant $(e_0\bar{a})$ in shear stress as well as the normal stress in an investigation of surface Effects on free vibration of Nano beams. Reddy (2007) has also referred to the stress resultant in x-y as shear forces. Thus, the shear stress and strain relationship which was previously defined in equation (C.2) may be written with nonlocal effect as:

$$\boldsymbol{\sigma}_{xy} - (e_0\bar{a})^2 \frac{d^2\boldsymbol{\sigma}_{xy}}{dx^2} = G\boldsymbol{\gamma}_{xy} = 2G\boldsymbol{\varepsilon}_{xy} \tag{C.31}$$

Bending moment and shear forces are:

$$\boldsymbol{M} = \int_A \boldsymbol{\sigma}_{xx} z dA \qquad [N.m] \tag{C.32}$$

$$\boldsymbol{Q} = \int_A \boldsymbol{\sigma}_{xy} dA \qquad [N] \tag{C.33}$$

So, by multiplying equation (C.1) by ydy and integrating over the cross section of the beam, A:

$$\boldsymbol{M} - (e_0\bar{a})^2 \frac{d^2\boldsymbol{M}}{dx^2} = EI\frac{d\boldsymbol{\theta}}{dx} \tag{C.34}$$

Therefore, constitutive equations must be obtained and solved for this new assumption accordingly. Thus the Timoshenko governing equations can be written as:

$$\frac{d}{dx}\boldsymbol{M} = \boldsymbol{Q} - \rho I\omega^2\boldsymbol{\theta} \tag{C.35}$$

$$\frac{d}{dx}\boldsymbol{Q} = -\rho h\frac{\partial^2\boldsymbol{W}}{\partial t^2} \tag{C.36}$$

Or:

$$\frac{d\boldsymbol{M}}{dx} = \boldsymbol{Q} - \rho I\omega^2\boldsymbol{\theta} \tag{C.37}$$

And

$$\frac{d\boldsymbol{Q}}{dx} = -\rho A\omega^2\boldsymbol{W} \tag{C.38}$$

Therefore:

$$\boldsymbol{M} = EI\frac{d\boldsymbol{\theta}}{dx} + (e_0\bar{a})^2\frac{d^2\boldsymbol{M}}{dx^2} = EI\frac{d\boldsymbol{\theta}}{dx} + (e_0\bar{a})^2\left(\frac{d\boldsymbol{Q}}{dx} - \rho I\omega^2\frac{d\boldsymbol{\theta}}{dx}\right) \tag{C.39}$$

Thus:

$$\boldsymbol{M} = EI\frac{d\boldsymbol{\theta}}{dx} + (e_0\bar{a})^2\left(-\rho A\omega^2\boldsymbol{W} - \rho I\omega^2\frac{d\boldsymbol{\theta}}{dx}\right) \tag{C.40}$$

So:

$$\boldsymbol{M} = EI\frac{d\boldsymbol{\theta}}{dx} + (e_0\bar{a})^2\left(\rho A\omega^2\boldsymbol{W} + \rho I\omega^2\frac{d\boldsymbol{\theta}}{dx}\right) \tag{C.41}$$

Now by integrating equation (C.31) over area, A:

$$\int_A \boldsymbol{\sigma}_{xy}\,dA - (e_0\bar{a})^2\int_A \frac{d^2\boldsymbol{\sigma}_{xy}}{\partial x^2}dA = G\int_A \boldsymbol{\gamma}_{\boldsymbol{xy}}dA \tag{C.42}$$

$$\boldsymbol{Q} - (e_0\bar{a})^2\frac{d^2\boldsymbol{Q}}{dx^2} = G\int_A\left(\boldsymbol{\theta} + \frac{d\boldsymbol{W}}{dx}\right)dA = \hat{\kappa}GA(\boldsymbol{\theta} + \frac{d\boldsymbol{W}}{dx}) \tag{C.43}$$

Thus

$$\boldsymbol{Q} = \hat{\kappa}GA\left(\boldsymbol{\theta} + \frac{d\boldsymbol{W}}{dx}\right) + (e_0\bar{a})^2\frac{d^2\boldsymbol{Q}}{dx^2} \tag{C.44}$$

Taking derivatives from both sides of equation (C.38) with respect to x:

$$\frac{d^2\boldsymbol{Q}}{dx^2} = -\rho I\omega^2\frac{\partial \boldsymbol{W}}{\partial x} \tag{C.45}$$

Now (C.45) into (C.44):

$$\boldsymbol{Q} = \hat{\kappa}GA\left(\boldsymbol{\theta} + \frac{d\boldsymbol{W}}{dx}\right) - (e_0\bar{a})^2\left(\rho A\omega^2\frac{d\boldsymbol{W}}{dx}\right) \tag{C.46}$$

Taking derivatives from equation (C.41) with respect to x:

$$\frac{d\boldsymbol{M}}{dx} = EI\frac{d^2\boldsymbol{\theta}}{dx^2} - (e_0\bar{a})^2\left(\rho A\omega^2\frac{d\boldsymbol{W}}{dx} + \rho I\omega^2\frac{d^2\boldsymbol{\theta}}{dx^2}\right) \tag{C.47}$$

Taking derivatives from equation (C.46) with respect to x:

$$\frac{d\boldsymbol{Q}}{dx} = \hat{\kappa}GA\left(\frac{d\boldsymbol{\theta}}{dx} + \frac{d^2\boldsymbol{W}}{dx^2}\right) - (e_0\bar{a})^2\left(\rho A\omega^2\frac{d^2\boldsymbol{W}}{dx^2}\right) \tag{C.48}$$

Now by substitution equations (C.47) and (C.48) in the equations (C.37) and (C.38), the Timoshenko constitutive equations can be written as:

$$EI\frac{d^2\boldsymbol{\theta}}{dx^2} - \hat{\kappa}GA\left(\boldsymbol{\theta} + \frac{d\boldsymbol{W}}{dx}\right) + \rho I\omega^2\boldsymbol{\theta} - (e_0\bar{a})^2\left(\rho I\omega^2\frac{d^2\boldsymbol{\theta}}{dx^2}\right) = 0 \tag{C.49}$$

$$\hat{\kappa}GA\left(\frac{d\boldsymbol{\theta}}{dx} + \frac{d^2\boldsymbol{W}}{dx^2}\right) + \rho A\omega^2\boldsymbol{W} - (e_0\bar{a})^2\left(\rho A\omega^2\frac{d^2\boldsymbol{W}}{dx^2}\right) = 0 \tag{C.50}$$

Now by normalisation we derive:

$$\hat{\Omega}\left(1-\frac{\alpha^2\lambda^2}{\hat{\xi}^2}\right)\frac{d^2\boldsymbol{\theta}}{dx^2}+\left(\frac{\lambda^2\hat{\Omega}}{\hat{\xi}^2}-1\right)\boldsymbol{\theta}-\frac{d\overline{\boldsymbol{W}}}{d\bar{x}}=0 \tag{C.51}$$

$$\frac{d\boldsymbol{\theta}}{d\bar{x}}+\left(1-\alpha^2\lambda^2\hat{\Omega}\right)\frac{d^2\overline{\boldsymbol{W}}}{d\bar{x}^2}+\lambda^2\hat{\Omega}\overline{\boldsymbol{W}}=0 \tag{C.52}$$

Equations (C.51) and (C.52) then decoupled in term of $\overline{\boldsymbol{W}}$ and $\boldsymbol{\theta}$ as follows:

$$\left(1-\alpha^2\lambda^2(\hat{\Omega}-\frac{\alpha^2\lambda^2\hat{\Omega}-1}{\hat{\xi}^2})\right)\frac{d^4\overline{\boldsymbol{W}}}{d\bar{x}^4}+\lambda^2\left(\hat{\Omega}+\frac{1-2\hat{\Omega}\alpha^2\lambda^2}{\hat{\xi}^2}+\alpha^2\right)\frac{d^2\overline{\boldsymbol{W}}}{d\bar{x}^2} \tag{C.53}$$
$$+\lambda^2\left(\frac{\lambda^2\hat{\Omega}}{\hat{\xi}^2}-1\right)\overline{\boldsymbol{W}}=0$$

And in terms of rotation:

$$\left(1-\alpha^2\lambda^2(\hat{\Omega}-\frac{\alpha^2\lambda^2\hat{\Omega}-1}{\hat{\xi}^2})\right)\frac{d^4\boldsymbol{\theta}}{d\bar{x}^4}+\lambda^2\left(\hat{\Omega}+\frac{1-2\hat{\Omega}\alpha^2\lambda^2}{\hat{\xi}^2}+\alpha^2\right)\frac{d^2\boldsymbol{\theta}}{d\bar{x}^2} \tag{C.54}$$
$$+\lambda^2\left(\frac{\lambda^2\hat{\Omega}}{\hat{\xi}^2}-1\right)\boldsymbol{\theta}=0$$

Thus the general solutions for the above decoupled equations are:

$$\overline{\boldsymbol{W}}=A_1sinh(\beta\bar{x})+A_2cosh(\beta\bar{x})+A_3sin(\gamma\bar{x})+A_4cos(\gamma\bar{x}) \tag{C55}$$

$$\boldsymbol{\theta}=B_1sinh(\beta\bar{x})+B_2cosh(\beta\bar{x})+B_3sin(\gamma\bar{x})+B_4cos(\gamma\bar{x}) \tag{C.56}$$

The solution of either of the above equations a set of new variables are defined which are different from Appendix C.1 but the rest of procedure is the same and final equation will be similar to the equation (C.30). Therefore, equation (C.30) should be used with the following parameters:

$$a = \left(1 - \frac{\alpha^2\lambda^2}{\hat{\xi}^2}\right)\left(1 - \alpha^2\lambda^2\hat{\Omega}\right) \tag{C.57}$$

$$b = \lambda^2\left(\hat{\Omega} + \frac{1 - 2\Omega\alpha^2\lambda^2}{\hat{\xi}^2} + \alpha^2\right) \tag{C.58}$$

$$c = \lambda^2\left(\frac{\lambda^2\hat{\Omega}}{\hat{\xi}^2} - 1\right) \tag{C.59}$$

So

$$\binom{\beta}{\gamma} = \left(\frac{\pm b + \sqrt{b^2 - 4ac}}{2a}\right)^{1/2} \tag{C.60}$$

$$B_1 = A_1\widehat{\Psi}_\beta \tag{C.61}$$

$$B_2 = A_2\widehat{\Psi}_\beta \tag{C.62}$$

$$B_3 = A_3\widehat{\Psi}_\gamma \tag{C.63}$$

$$B_4 = -A_4\widehat{\Psi}_\gamma \tag{C.64}$$

$$\widehat{\Psi}_\beta = -\frac{\beta^2 + \lambda^2\hat{\Omega}(1 - \alpha^2\beta^2)}{\beta} \tag{C.65}$$

$$\widehat{\Psi}_\gamma = \frac{\gamma^2 - \lambda^2\hat{\Omega}(1 + \alpha^2\beta^2)}{\gamma} \tag{C.66}$$

$$H_1 = \left(1 - \frac{\alpha^2\lambda^2}{\hat{\xi}^2}\right)\beta\widehat{\Psi}_\beta - \alpha^2\lambda^2 \tag{C.67}$$

$$H_2 = \left(1 - \frac{\alpha^2\lambda^2}{\hat{\xi}^2}\right)\gamma\widehat{\Psi}_\gamma - \alpha^2\lambda^2 \tag{C.68}$$

$$H_3 = \widehat{\Psi}_\beta + (1 - \alpha^2\lambda^2\hat{\Omega})\beta \tag{C.69}$$

And

$$H_4 = \widehat{\Psi}_\gamma - (1 - \alpha^2\lambda^2\hat{\Omega})\gamma \tag{C.70}$$

C.3 Extracting the Timoshenko Beam Mode Shapes

The mode shapes for the modal frequencies in both local and nonlocal Timoshenko beam will be the same (Wang, Zhang, and He 2007). Thus the displacement and the three consecutive derivatives of it are as:

$$\overline{\boldsymbol{W}} = C_1 sinh(\beta\overline{x}) + C_2 cosh(\beta\overline{x}) + C_3 sin(\gamma\overline{x}) + C_4 cos(\gamma\overline{x}) \tag{C.71}$$

$$\overline{\boldsymbol{W}}'(x) = C_1\beta cosh(\beta\overline{x}) + C_2\beta sinh(\beta\overline{x}) + C_3\gamma cos(\gamma\overline{x}) - C_4\gamma sin(\gamma\overline{x}) \tag{C.72}$$

$$\overline{\boldsymbol{W}}''(x) = C_1\beta^2 sinh(\beta\overline{x}) + C_2\beta^2 cosh(\beta\overline{x}) - C_3\gamma^2 sin(\gamma\overline{x}) - C_4\gamma^2 cos(\gamma\overline{x}) \tag{C.73}$$

$$\overline{\boldsymbol{W}}'''(x) = C_1\beta^3 cosh(\beta\overline{x}) + C_2\beta^3 sinh(\beta\overline{x}) - C_3\gamma^3 cos(\gamma\overline{x}) + C_4\gamma^3 sin(\gamma\overline{x}) \tag{C.74}$$

From the equations (C.71) to (C.74), at x=0 then the second and third derivatives must also be equal to zero: $\boldsymbol{W}''(0) = 0$ and $\boldsymbol{W}'''(0) = 0$. Thus, in other to achieve such conditions then:

$$H_1 C_1 + H_2 C_3 = 0 \tag{C.75}$$

And,

$$H_3 C_2 - H_4 C_4 = 0 \tag{C.76}$$

The variables H_1 to H_4 in equations (C.75) and (C.76) can be derived from equations (C.23) to (C.27) as the final equation can be used to obtain the mode shapes in either local or nonlocal Timoshenko beams. Thus:

$$C_4 = \frac{H_3}{H_4} C_2 \tag{C.77}$$

And,

$$C_3 = \frac{-H_1}{H_2} C_1 \tag{C.78}$$

And so at x=L or $\bar{x} = 1$, $\overline{\mathbf{W}}''(1) = 0$ and $\overline{\mathbf{W}}'''(1) = 0$

$$\overline{\boldsymbol{W}}''(1) = C_1\beta^2 sinh(\beta) + C_2\beta^2 cosh(\beta) - C_3\gamma^2 sin(\gamma) - C_4\gamma^2 cos(\gamma) = 0 \tag{C.79}$$

Sunstituting C_3 and C_4 into equation (C.79):

$$\begin{aligned}\overline{\boldsymbol{W}}''(1) = C_1\beta^2 sinh(\beta) + C_2\beta^2 cosh(\beta) - \left(\frac{-H_1}{H_2} C_1\right)\gamma^2 sin(\gamma) \\ - \left(\frac{H_3}{H_4} C_2\right)\gamma^2 cos(\gamma) = 0\end{aligned} \tag{C.80}$$

Thus

$$C_1\left[\beta^2 sinh(\beta) + \left(\frac{H_1}{H_2}\right)\gamma^2 sin(\gamma)\right] + C_2[\beta^2 cosh(\beta) - (\frac{H_3}{H_4})\gamma^2 cos(\gamma)] = 0 \tag{C.81}$$

$$\frac{C_2}{C_1} = -\frac{\left[\beta^2 sinh(\beta) + \left(\frac{H_1}{H_2}\right)\gamma^2 sin(\gamma)\right]}{[\beta^2 cosh(\beta) - (\frac{H_3}{H_4})\gamma^2 cos(\gamma)]} \tag{C.82}$$

Substitute (C.77) and (C.78) into the equation (C.71):

$$\overline{\boldsymbol{W}} = C_1 sinh(\beta\overline{x}) + C_2 cosh(\beta\overline{x}) + \frac{-H_1}{H_2} C_1 sin(\gamma\overline{x}) + \frac{H_3}{H_4} C_2 cos(\gamma\overline{x}) \qquad \text{(C.83)}$$

By rearranging equation (C.83):

$$\overline{\boldsymbol{W}} = C_1 sinh(\beta\overline{x}) - \frac{H_1}{H_2} C_1 sin(\gamma\overline{x}) + C_2 cosh(\beta\overline{x}) + \frac{H_3}{H_4} C_2 cos(\gamma\overline{x}) \qquad \text{(C.84)}$$

Thus

$$\overline{\boldsymbol{W}} = \left[sinh(\beta\overline{x}) - \frac{H_1}{H_2} sin(\gamma\overline{x})\right] + \frac{C_2}{C_1}\left[cosh(\beta\overline{x}) + \frac{H_3}{H_4} cos(\gamma\overline{x})\right] \qquad \text{(C.85)}$$

For $C_1 = 1$ in equation (C.82) and replacing C_1/C_2 in equation (C.85):

$$\begin{aligned}\overline{\boldsymbol{W}} = &\left[sinh(\beta\overline{x}) - \frac{H_1}{H_2} sin(\gamma\overline{x})\right] \\ &- \frac{\left[\beta^2 sinh(\beta) + \left(\frac{H_1}{H_2}\right)\gamma^2 sin(\gamma)\right]}{\left[\beta^2 cosh(\beta) - \left(\frac{H_3}{H_4}\right)\gamma^2 cos(\gamma)\right]}\left[cosh(\beta\overline{x})\right. \\ &\left. + \frac{H_3}{H_4} cos(\gamma\overline{x})\right]\end{aligned} \qquad \text{(C.86)}$$

The mode shapes at each modal frequency of a Timoshenko beam with a defined aspect ratio can be extracted using the equation (C.86).

Appendix D

D) Numerical Results (Longitudinal and Transverse) for 2D beams Using MPFEM and CVFEM

D.1) Longitudinal Modal Frequencies Using MPFEM in Comparison with FEA Results

Table D-1: Longitudinal frequency of beams with voids and continuous boundaries using MPFEM with corresponding FEA results

		Longitudinal Frequency, ω, [Rad/s] of Beams With Voids and Continuous Boundaries Using MPFEM					Longitudinal Frequency, ω, [Rad/s] of Beams With Voids and Continuous Boundaries Using FEA				
V_r/S_y	$1/d^2$	Mode 1	Mode 2	Mode 3	Mode 4	Mode 5	Mode 1	Mode 2	Mode 3	Mode 4	Mode 5
0	1.33	1775482	3547265	5310760	7060279	8785975	1776747	3549673	5314249	7064185	8789925
	0.33	887740.6	1773582	2655268	3529714	4351582	888373	1774836	2657121	3532105	4394956
	0.15	591996	1182027	1768671	2349671	2896848	592249	1183224	1771418	2354737	2929969
	0.08	444360.4	886747.8	1326985	1762730	2184207	444187	887418	1328561	1766053	2197481
0.12	1.33	1775484	3547360	5310805	7060403	8786580	1776206	3545099	5297398	7018695	8682608
	0.33	887741	1773589	2655292	3529779	4392354	888310	1774284	2655161	3527217	4384821
	0.15	591827	1182389	1770183	2353147	2928101	592228	1183042	1770771	2353160	2926752
	0.08	443870	886791	1327634	1764849	2196043	444175	887330	1328247	1765286	2195923
0.17	1.33	1775484	3547354	5310816	7060433	8786700	1775069	3535542	5261715	6919986	8443910
	0.33	887742	1773591	2655298	3529797	4392406	888166	1773159	2651316	3517723	4365174
	0.15	591828	1182390	1770188	2353160	2928132	592180	1182690	1769596	2350307	2920977
	0.08	443871	886792	1327637	1764859	2196066	444153	887167	1327719	1764004	2193341
0.23	1.33	1775485	3547380	5310825	7060459	8786802	1773209	3519614	5201478	6751597	8042289
	0.33	887742	1773592	2655304	3529812	4392447	887952	1771437	2645309	3502782	4334116
	0.15	591828	1182391	1770192	2353171	2928158	592118	1182181	1767818	2345959	2912137
	0.08	443871	886793	1327640	1764867	2196088	444128	886947	1326940	1762107	2189495
0.29	1.33	1775485	3547404	5310831	7060475	8786864	1770501	3496473	5112980	6501714	7457890
	0.33	887742	1773593	2655307	3529821	4392474	887663	1769087	2637065	3482223	4291290
	0.15	591828	1182392	1770194	2353177	2928176	592029	1181465	1765368	2339959	2899929
	0.08	443871	886793	1327642	1764873	2196100	444085	886620	1325840	1759436	2184098
0.35	1.33	1775485	3547430	5310836	7060489	8786915	1766505	3461463	4975208	6090417	6550472
	0.33	887742	1773574	2655310	3529829	4392498	887255	1765707	2625203	3452598	4229696
	0.15	591828	1182393	1770196	2353183	2928190	591900	1180416	1761723	2331005	2881682
	0.08	443871	886794	1327644	1764877	2196111	444025	886130	1324131	1755239	2175553

Table D-2: Longitudinal frequency of beams with compliant inclusions and continuous boundaries using MPFEM with corresponding FEA results

		Longitudinal Frequency, ω, [Rad/s] of Beams With Compliant Inclusions and Continuous Boundaries Using MPFEM					Longitudinal Frequency, ω, [Rad/s] of Beams With Compliant Inclusions and Continuous Boundaries Using FEA				
V_r/S_y	$1/d^2$	Mode 1	Mode 2	Mode 3	Mode 4	Mode 5	Mode 1	Mode 2	Mode 3	Mode 4	Mode 5
0	1.33	1775482	3547265	5310760	7060279	8785975	1776747	3549673	5314249	7064185	8789925
	0.33	887740.6	1773582	2655268	3529714	4351582	888373	1774836	2657121	3532105	4394956
	0.15	591996	1182027	1768671	2349671	2896848	592249	1183224	1771418	2354737	2929969
	0.08	444360.4	886747.8	1326985	1762730	2184207	444187	887418	1328561	1766053	2197481
0.12	1.33	1775484	3547297	5310806	7060404	8786587	1776558	3544006	5291491	7004118	8659109
	0.33	887741	1773589	2655291	3529777	4392354	888581	1774604	2655104	3526186	4382101
	0.15	591827	1182389	1770182	2353144	2928093	592423	1183375	1771136	2353392	2926676
	0.08	443870	886790	1327632	1764845	2196034	444331	887619	1328636	1765726	2196357
0.17	1.33	1775484	3547363	5310812	7060423	8786660	1776269	3540581	5277951	6965602	8563479
	0.33	887741	1773590	2655296	3529790	4392376	888587	1774290	2653779	3522643	4374410
	0.15	591827	1182390	1770186	2353154	2928136	592441	1183306	1770771	2352368	2924446
	0.08	443870	886791	1327635	1764854	2196056	444339	887588	1328466	1765255	2195332
0.23	1.33	1775484	3547360	5310819	7060440	8786729	1775616	3533456	5249865	6885491	8365621
	0.33	887742	1773591	2655300	3529801	4392417	888549	1773586	2651039	3515555	4359324
	0.15	591828	1182391	1770189	2353163	2928139	592445	1183124	1769992	2350339	2920179
	0.08	443871	886792	1327638	1764861	2196072	444352	887525	1328152	1764394	2193504
0.29	1.33	1775485	3547380	5310825	7060459	8786801	1774705	3523780	5211965	6778614	8111655
	0.33	887742	1773592	2655304	3529812	4392446	888530	1772694	2647439	3506162	4339356
	0.15	591828	1182391	1770191	2353171	2928157	592470	1182916	1768999	2347674	2914537
	0.08	443871	886793	1327640	1764867	2196087	444380	887469	1327756	1763269	2191079
0.35	1.33	1775485	3547410	5310833	7060479	8786876	1773831	3513765	5172928	6671863	7876098
	0.33	887742	1773593	2655308	3529823	4392479	888543	1771758	2643512	3495845	4317491
	0.15	591828	1182392	1770194	2353178	2928158	592522	1182703	1767868	2344558	2907858
	0.08	443871	886793	1327642	1710455	2196101	444431	887418	1327291	1761868	2187975

Table D-3: Longitudinal frequency of beams with compliant matrix and textured boundaries using MPFEM with corresponding FEA results

		Longitudinal Frequency, ω, [Rad/s] of Beams With Compliant Matrix and Textured Boundaries Using MPFEM					Longitudinal Frequency, ω, [Rad/s] of Beams With Compliant Matrix and Textured Boundaries Using FEA				
V_r/S_y	$1/d^2$	Mode 1	Mode 2	Mode 3	Mode 4	Mode 5	Mode 1	Mode 2	Mode 3	Mode 4	Mode 5
0	1.33	1775482	3547265	5310760	7060279	8785975	1776747	3549673	5314249	7064185	8789925
	0.33	887740.6	1773582	2655268	3529714	4351582	888373	1774836	2657121	3532105	4394956
	0.15	591996	1182027	1768671	2349671	2896848	592249	1183224	1771418	2354737	2929969
	0.08	444360.4	886747.8	1326985	1762730	2184207	444187	887418	1328561	1766053	2197481
0.12	1.33	1775484	3547306	5310814	7060422	8786663	1776830	3548222	5307315	7043690	8730560
	0.33	887741	1773589	2655294	3529785	4392408	888511	1774939	2656827	3530847	4391909
	0.15	591827	1182389	1770183	2353148	2928102	592353	1183382	1771517	2354624	2929421
	0.08	443870	886791	1327633	1764847	2196039	444263	887547	1328697	1766125	2197389
0.17	1.33	1775484	3547258	5310813	7060424	8786668	1776625	3546062	5299417	7024014	8690672
	0.33	887741	1773590	2655295	3529789	4392382	888500	1774702	2655928	3528577	4387226
	0.15	591827	1182390	1770185	2353152	2928113	592364	1183338	1771297	2353993	2928081
	0.08	443870	886791	1327635	1764852	2196050	444275	887547	1328621	1765873	2196837
0.23	1.33	1775484	3547353	5310813	7060426	8786673	1775948	3541505	5284281	6987847	8620718
	0.33	887742	1773590	2655296	3529792	4392398	888366	1774056	2653957	3524021	4378381
	0.15	591827	1182390	1770186	2353156	2928124	592280	1183054	1770556	2352448	2925180
	0.08	443871	886791	1327636	1764856	2196060	444225	887390	1328256	1765132	2195481
0.29	1.33	1775484	3547347	5310814	7060426	8786674	1775301	3535877	5264826	6940628	8531183
	0.33	887742	1773590	2655297	3529793	4392396	888294	1773378	2651608	3518345	4367093
	0.15	591827	1182390	1770187	2353158	2928127	592269	1182874	1769893	2350777	2921822
	0.08	443871	886792	1327637	1764857	2196063	444228	887327	1327984	1764438	2194047
0.35	1.33	1775484	3547345	5310814	7060427	8786675	1774166	3528325	5240057	6881805	8417683
	0.33	887742	1773590	2655297	3529794	4392397	888032	1772211	2648250	3510793	4352667
	0.15	591827	1182390	1770187	2353158	2928128	592150	1182444	1768774	2348380	2917392
	0.08	443871	886792	1327637	1764858	2196065	444130	887055	1327374	1763240	2191950

D.2) Transverse Modal Frequencies for 2D beams Using MPFEM

Table D-4: MPFEM results for the first ten non-dimensional bending modal frequencies, λ, of four beam sizes for beams with voids and continuous boundaries. (BVOCB)

V_r/S_y	$1/d^2$	Mode 1	Mode 2	Mode 3	Mode 4	Mode 5	Mode 6	Mode 7	Mode 8	Mode 9	Mode 10
0.12	1.33	4.76512	7.61965	10.27137	12.67763	14.96468	17.05317	18.86293	20.62313	22.26413	23.79808
	0.33	4.69153	7.57112	10.23810	12.66757	14.88220	16.90693	18.75617	20.43925	22.06997	23.58142
	0.15	4.67259	7.55084	10.22108	12.65493	14.87333	16.90203	18.76617	20.48682	22.07861	23.56709
	0.08	4.66537	7.54166	10.21185	12.64671	14.86651	16.89664	18.76221	20.48462	22.08058	23.56086
0.17	1.33	4.83584	7.65801	10.29792	12.74810	14.95530	16.99660	18.87115	20.63319	22.27322	23.80628
	0.33	4.72206	7.60101	10.26264	12.68602	14.89492	16.98578	18.79962	20.51875	22.11474	23.59822
	0.15	4.68809	7.56979	10.23970	12.67151	14.88754	16.91367	18.77417	20.63529	22.10398	23.58359
	0.08	4.67456	7.55407	10.22539	12.66006	14.87904	16.90809	18.77243	20.49323	22.08611	23.53795
0.23	1.33	4.91133	7.69002	10.32157	12.75489	14.96626	17.00478	18.96640	20.64210	22.28124	23.81351
	0.33	4.76159	7.63369	10.28690	12.70119	14.89833	16.93912	18.80516	20.52612	22.12187	23.60411
	0.15	4.70947	7.59326	10.26057	12.68848	14.90078	16.92161	18.75008	20.57493	22.16682	23.58377
	0.08	4.68754	7.57039	10.24183	12.67503	14.89210	16.91910	18.78092	20.49537	22.14981	23.59664
0.29	1.33	4.96123	7.70703	10.33621	12.76455	14.97427	17.01124	18.91516	20.64771	22.28628	23.81806
	0.33	4.79185	7.65574	10.30249	12.70784	14.87844	16.93753	18.81053	20.53166	22.12700	23.60878
	0.15	4.72676	7.61059	10.27495	12.69940	14.90850	16.91802	18.83010	20.53452	22.12564	23.61271
	0.08	4.69830	7.58308	10.25384	12.68535	14.90063	16.92567	18.78420	20.55882	22.11459	23.59468
0.35	1.33	5.00907	7.71788	10.34909	12.77350	14.98126	17.01692	18.90854	20.65250	22.29057	23.82193
	0.33	4.82502	7.67712	10.31697	12.70557	14.68714	16.91550	18.81526	20.53662	22.13155	23.61291
	0.15	4.74674	7.62892	10.28919	12.70935	14.91433	16.99867	18.81913	20.53473	22.12665	23.60558
	0.08	4.71104	7.59718	10.26642	12.69556	14.90857	16.93073	18.77999	20.49967	22.10444	23.59532

Table D-5: MPFEM results for the first ten non-dimensional bending modal frequencies, λ, of four beam sizes for beams with compliant inclusions and continuous boundaries.(BINCB)

V_r/S_y	$1/d^2$	Mode 1	Mode 2	Mode 3	Mode 4	Mode 5	Mode 6	Mode 7	Mode 8	Mode 9	Mode 10
0.12	1.33	4.72890	7.60088	10.26148	12.69004	14.90897	16.96877	18.86443	20.62369	22.26475	23.79880
	0.33	4.67735	7.55619	10.22575	12.65856	14.87622	16.90469	18.76902	20.48875	22.16388	23.59163
	0.15	4.66562	7.54185	10.21188	12.64654	14.86615	16.89616	18.76171	20.48422	22.08042	23.65958
	0.08	4.66130	7.53596	10.20538	12.64015	14.86022	16.89084	18.75701	20.48013	22.07695	23.55851
0.17	1.33	4.79161	7.63833	10.28541	12.65615	14.96247	17.01410	18.86947	20.62968	22.27013	23.80355
	0.33	4.70150	7.58224	10.24835	12.67632	14.88943	16.91133	18.70040	20.53129	22.12483	23.58034
	0.15	4.67748	7.55727	10.22794	12.66158	14.87954	16.90769	18.77115	20.49053	22.07494	23.65976
	0.08	4.66822	7.54570	10.21652	12.65162	14.87142	16.90143	18.76682	20.48898	22.08453	23.56394
0.23	1.33	4.85343	7.66669	10.30417	12.74833	14.95821	16.99868	18.87257	20.63566	22.27546	23.80830
	0.33	4.73042	7.60855	10.26855	12.69018	14.89729	16.94838	18.80060	20.52058	22.11657	23.59957
	0.15	4.69247	7.57488	10.24446	12.67559	14.89090	16.91622	18.77501	20.51604	22.10252	23.65977
	0.08	4.67718	7.55750	10.22899	12.66347	14.88213	16.91083	18.77475	20.49491	22.08574	23.58239
0.29	1.33	4.90837	7.68940	10.32106	12.79044	14.96622	17.00478	18.86849	20.64200	22.28116	23.81344
	0.33	4.75969	7.63246	10.28617	12.70102	14.89919	16.93968	18.80522	20.52613	22.12187	23.60413
	0.15	4.70837	7.59218	10.25973	12.68790	14.90041	16.92169	18.77769	20.60004	22.19558	23.65984
	0.08	4.68686	7.56960	10.24111	12.67444	14.89165	16.91880	18.78081	20.49615	22.17514	23.59828
0.35	1.33	4.95446	7.70938	10.33727	12.76698	14.97627	17.01310	18.84863	20.64880	22.28732	23.81903
	0.33	4.78530	7.65295	10.30163	12.70997	14.89459	16.94241	18.81199	20.53288	22.12818	23.60994
	0.15	4.72262	7.60727	10.27293	12.69855	14.90864	16.92415	18.86878	20.54169	22.13154	23.65985
	0.08	4.69564	7.58033	10.25169	12.68394	14.89989	16.92563	18.78555	20.48271	22.15448	23.59742

Table D-6: MPFEM results for the first ten non-dimensional bending modal frequencies, λ, of four beam sizes with compliant matrix and textured boundaries (BCMTB)

V_r/S_y	$1/d^2$	Mode 1	Mode 2	Mode 3	Mode 4	Mode 5	Mode 6	Mode 7	Mode 8	Mode 9	Mode 10
0.12	1.33	4.73198	7.60680	10.26819	12.69702	14.91708	16.97845	18.87151	20.63001	22.27057	23.66279
	0.33	4.67796	7.55749	10.22776	12.66113	14.87919	16.90795	18.77263	20.49378	22.07772	23.62816
	0.15	4.66587	7.54235	10.21266	12.64764	14.86755	16.89783	18.76363	20.48638	22.08283	23.56387
	0.08	4.66143	7.53621	10.20578	12.64071	14.86096	16.89176	18.75812	20.48143	22.07843	23.56017
0.17	1.33	4.76403	7.62634	10.27953	12.69736	14.87073	16.96512	18.87075	20.63016	22.24991	23.66280
	0.33	4.68972	7.57073	10.23949	12.67038	14.88600	16.91221	18.77243	20.50951	22.10374	23.66024
	0.15	4.67156	7.54995	10.22079	12.65540	14.87453	16.90387	18.76865	20.49019	22.08479	23.56010
	0.08	4.66474	7.54094	10.21129	12.64650	14.86670	16.89726	18.76326	20.48611	22.08254	23.56352
0.23	1.33	4.80922	7.64620	10.29016	12.78410	14.95564	16.99908	18.86999	20.63077	22.27107	23.66281
	0.33	4.70944	7.58966	10.25403	12.68019	14.89171	16.90657	18.80874	20.51960	22.11495	23.60418
	0.15	4.68153	7.56214	10.23258	12.66553	14.88274	16.91012	18.77262	20.48896	22.14362	23.58712
	0.08	4.67063	7.54892	10.21998	12.65494	14.87444	16.90409	18.76908	20.49076	22.08555	23.56272
0.29	1.33	4.82916	7.65268	10.29370	12.74307	14.95163	16.99339	18.86895	20.63101	22.27121	23.66281
	0.33	4.71960	7.59810	10.25982	12.68350	14.89272	16.97499	18.79691	20.51637	22.11253	23.59607
	0.15	4.68689	7.56817	10.23791	12.66972	14.88582	16.91205	18.77267	20.43529	22.10181	23.58168
	0.08	4.67385	7.55306	10.22420	12.65877	14.87772	16.90677	18.77112	20.49196	22.08488	23.53265
0.35	1.33	4.83959	7.65556	10.29536	12.73834	14.95063	16.99209	18.86797	20.63112	22.27128	23.66281
	0.33	4.72534	7.60253	10.26272	12.68496	14.89273	16.93957	18.73094	20.51581	22.11211	23.59529
	0.15	4.68999	7.57150	10.24074	12.67184	14.88730	16.91280	18.77175	20.50748	22.09818	23.58059
	0.08	4.67573	7.55540	10.22651	12.66080	14.87939	16.90808	18.77204	20.49225	22.08297	23.57254

D.3) Transverse Modal Frequencies for 2D beams Using CVFEM

Table D-7: CVFEM results for the first ten non-dimensional bending modal frequencies, λ, of four beam sizes for beams with voids and continuous boundaries. (BVOCB)

V_r/S_y	$1/d^2$	Mode 1	Mode 2	Mode 3	Mode 4	Mode 5	Mode 6	Mode 7	Mode 8	Mode 9	Mode 10
0.12	1.33	4.75637	7.59068	10.21280	12.58191	14.83105	16.73721	18.57903	20.25346	21.79828	23.22596
	0.33	4.68916	7.56458	10.22432	12.64295	14.84286	16.84883	18.67776	20.35837	21.94411	23.40409
	0.15	4.67151	7.54830	10.21598	12.64573	14.85819	16.87886	18.73272	20.44081	22.01811	23.49184
	0.08	4.66444	7.53964	10.20804	12.64007	14.85567	16.87998	18.73792	20.45078	22.03528	23.50243
0.17	1.33	4.82571	7.62610	10.23582	12.64875	14.80303	16.78384	18.58474	20.25889	21.80268	23.22954
	0.33	4.71946	7.59345	10.24690	12.65860	14.85219	16.73529	18.71317	20.40353	21.96680	23.41491
	0.15	4.68695	7.56691	10.23375	12.66084	14.87027	16.88774	18.73750	20.40843	22.03857	23.50013
	0.08	4.67359	7.55184	10.22102	12.65231	14.86642	16.88890	18.74484	20.45536	22.03627	23.48191
0.23	1.33	4.89978	7.65585	10.25707	12.65005	14.81051	16.78698	18.59033	20.26497	21.80785	23.23402
	0.33	4.75875	7.62521	10.26963	12.67185	14.85405	16.87464	18.71564	20.40768	21.97046	23.41640
	0.15	4.70825	7.58999	10.25379	12.67652	14.88179	16.89372	18.67238	20.53295	22.12210	23.49860
	0.08	4.68654	7.56794	10.23689	12.66626	14.87796	16.89789	18.75087	20.45506	22.10400	23.52893
0.29	1.33	4.94893	7.67196	10.27074	12.65827	14.81722	16.79191	18.59367	20.26935	21.81167	23.23741
	0.33	4.78885	7.64674	10.28445	12.67772	14.83656	16.87312	18.71981	20.41183	21.97414	23.41954
	0.15	4.72549	7.60708	10.26770	12.68676	14.88868	16.88974	18.79038	20.48019	22.05546	23.53306
	0.08	4.69727	7.58048	10.24856	12.67600	14.88566	16.90343	18.75304	20.52779	22.05965	23.52488
0.35	1.33	4.99620	7.68236	10.28297	12.66622	14.82330	16.79652	18.59503	20.27322	21.81505	23.24041
	0.33	4.82187	7.66765	10.29826	12.67535	14.67203	16.85808	18.72366	20.41567	21.97752	23.42249
	0.15	4.74542	7.62518	10.28153	12.69614	14.89387	16.68189	18.77758	20.47919	22.05506	23.51637
	0.08	4.70998	7.59443	10.26080	12.68566	14.89286	16.90762	18.74842	20.45925	22.05012	23.52442

Table D-8: CVFEM results for the first ten non-dimensional bending modal frequencies, λ, of four beam sizes for beams with compliant inclusions and continuous boundaries.(BINCB)

V_r/S_y	$1/d^2$	Mode 1	Mode 2	Mode 3	Mode 4	Mode 5	Mode 6	Mode 7	Mode 8	Mode 9	Mode 10
0.12	1.33	4.72170	7.57633	10.20897	12.59875	14.76897	16.76765	18.58888	20.27545	21.80808	23.46034
	0.33	4.67518	7.55071	10.21431	12.63773	14.84205	16.85283	18.69499	20.38844	21.89480	23.42504
	0.15	4.66459	7.53964	10.20765	12.63903	14.85369	16.87676	18.73312	20.44407	22.02631	23.49088
	0.08	4.66039	7.53412	10.20211	12.63464	14.85133	16.87714	18.73684	20.45163	22.03824	23.50780
0.17	1.33	4.78258	7.60866	10.22594	12.56844	14.81827	16.85586	18.58464	20.25868	21.87438	23.46020
	0.33	4.69909	7.57548	10.23410	12.65100	14.84919	16.85236	18.64205	20.42563	21.99335	23.40545
	0.15	4.67638	7.55466	10.22265	12.65204	14.86388	16.88383	18.73686	20.44360	22.01467	23.43303
	0.08	4.66729	7.54364	10.21259	12.64473	14.86017	16.88417	18.74172	20.45413	22.03804	23.50421
0.23	1.33	4.84297	7.63420	10.24143	12.64686	14.80493	16.78422	18.58646	20.26062	21.80416	23.46021
	0.33	4.72777	7.60078	10.25244	12.66228	14.85404	16.88769	18.71330	20.40452	21.96770	23.41481
	0.15	4.69132	7.57191	10.23833	12.66462	14.87322	16.88978	18.73784	20.46793	22.03638	23.50025
	0.08	4.67621	7.55522	10.22449	12.65549	14.86916	16.89116	18.74656	20.45635	22.03532	23.50665
0.29	1.33	4.89703	7.65550	10.25680	12.65038	14.81073	16.78726	18.59051	20.26506	21.80796	23.46027
	0.33	4.75687	7.62403	10.26899	12.67177	14.85492	16.87530	18.71585	20.40784	21.97063	23.41660
	0.15	4.70716	7.58896	10.25303	12.67605	14.88157	16.89395	18.72123	20.56827	22.00172	23.49938
	0.08	4.68586	7.56716	10.23621	12.66574	14.87760	16.89770	18.75089	20.45590	22.13799	23.53097
0.35	1.33	4.94270	7.67492	10.27237	12.66142	14.81987	16.79444	18.59583	20.27094	21.81319	23.46034
	0.33	4.78238	7.64417	10.28390	12.68014	14.85095	16.87777	18.72173	20.41357	21.97586	23.42127
	0.15	4.72138	7.60389	10.26593	12.68625	14.88922	16.89599	18.38906	20.48869	22.06310	23.48966
	0.08	4.69462	7.57779	10.24655	12.67483	14.88525	16.90380	18.75481	20.44418	22.15225	23.52833

Table D-9: CVFEM results for the first ten non-dimensional bending modal frequencies, λ, of four beam sizes with compliant matrix and textured boundaries (BCMTB)

V_f/S_y	$1/d^2$	Mode 1	Mode	Mode 3	Mode 4	Mode 5	Mode 6	Mode 7	Mode 8	Mode 9	Mode 10
0.12	1.33	4.72512	7.58322	10.21713	12.60747	14.77863	16.78034	18.59846	20.27179	21.81651	23.46050
	0.33	4.67584	7.55220	10.21678	12.64111	14.84618	16.85761	18.70041	20.39525	21.95234	23.34324
	0.15	4.66485	7.54019	10.20859	12.64045	14.85562	16.87922	18.73610	20.44757	22.03033	23.63363
	0.08	4.66053	7.53440	10.20260	12.63540	14.85243	16.87864	18.73877	20.45404	22.04114	23.51119
0.17	1.33	4.75603	7.59925	10.22335	12.60221	14.74273	16.76272	18.58975	20.26358	21.80796	23.46029
	0.33	4.68745	7.56467	10.22672	12.64732	14.84872	16.85649	18.69422	20.40684	22.90858	23.41549
	0.15	4.67051	7.54756	10.21608	12.64694	14.86053	16.88227	18.73717	20.44649	22.02660	23.63355
	0.08	4.66382	7.53900	10.20773	12.64036	14.85672	16.88188	18.74071	20.45448	22.03993	23.50817
0.23	1.33	4.79968	7.61544	10.22939	12.70649	14.80616	16.79492	18.58405	20.25813	21.80221	23.46019
	0.33	4.70695	7.58255	10.23910	12.65389	14.85027	16.84716	18.72621	20.40679	21.96980	23.45297
	0.15	4.68042	7.55941	10.22699	12.65548	14.86633	16.88529	18.73716	20.44098	22.09237	23.63348
	0.08	4.66968	7.54679	10.21585	12.64767	14.86258	16.88595	18.74283	20.45449	22.03743	23.50140
0.29	1.33	4.81895	7.62063	10.23146	12.64327	14.79917	16.78034	18.58238	20.25666	21.80063	23.46016
	0.33	4.71699	7.59053	10.24405	12.65603	14.84994	16.92840	18.71037	20.40108	21.96451	23.41257
	0.15	4.68575	7.56527	10.23194	12.65902	14.86850	16.88606	18.73592	20.59770	22.03622	23.63345
	0.08	4.67289	7.55083	10.21981	12.65100	14.86507	16.88754	18.74348	20.45403	22.03498	23.47842
0.35	1.33	4.82903	7.62289	10.23246	12.63645	14.79713	16.77727	18.58160	20.25602	21.79994	23.46015
	0.33	4.72267	7.59471	10.24653	12.65695	14.84936	16.87791	18.70780	20.39957	21.96306	23.41024
	0.15	4.68883	7.56852	10.23456	12.66081	14.86952	16.88626	18.73447	20.43049	22.03189	23.63344
	0.08	4.67476	7.55312	10.22199	12.65277	14.86635	16.88831	18.74372	20.45354	22.03242	23.51065

Appendix E

E) Numerical Results for Square Plates with Cylindrical Voids and Inclusions

In this section the finite element results using ANSYS for all plate models and MPFEM results for plates with CYVOCB, CYCICB and CYCMTB are provided. Only eight dimensionless modal frequencies, Ω, are listed in this appendix. The rest of modal frequencies up to mode number 33 and mode shapes are stored in an Excel database separately future work. Note that the first twisting mode is also included in the tables along with the transverse mode (not to be confused with bending modes).

E.1) FEA results for square plates with cylindrical voids and inclusions

a) FEA results for plates with CYVOCB

Table E-1: FEA results for the first eight non-dimensional transverse modal frequencies, Ω, of four plate sizes for plates with voids and continuous boundaries (CYVOCB)

V_r/S_y	$1/d^2$	Mode 1	Mode 2	Mode 3	Mode 4	Mode 5	Mode 6	Mode 7	Mode 8
0.12	1.33	1.32439	1.97707	2.42605	3.26842	3.26956	5.56322	5.59149	5.60799
	0.33	1.29461	1.93783	2.37172	3.19401	3.22234	5.44374	5.50546	5.56343
	0.15	1.28905	1.92922	2.36426	3.17816	3.21470	5.41029	5.48582	5.55132
	0.08	1.28680	1.92595	2.35610	3.17161	3.20771	5.39820	5.47563	5.54595
0.17	1.33	1.39586	2.08510	2.55332	3.42297	3.43057	5.74501	5.82232	5.88602
	0.33	1.32968	1.99618	2.44054	3.26395	3.32731	5.51294	5.64152	5.78506
	0.15	1.31675	1.97446	2.41637	3.22837	3.30398	5.44143	5.59565	5.75681
	0.08	1.31215	1.96682	2.40791	3.21547	3.29505	5.41587	5.57830	5.74625
0.23	1.33	1.49117	2.22880	2.72196	3.61649	3.64457	5.91532	6.10596	6.27711
	0.33	1.37643	2.07085	2.54383	3.35704	3.47024	5.59850	5.82152	6.09364
	0.15	1.35371	2.02951	2.50572	3.29689	3.42986	5.48596	5.74573	6.04352
	0.08	1.34572	2.01441	2.49207	3.27447	3.41483	5.44458	5.71707	6.02398
0.29	1.33	1.59691	2.38331	2.91319	3.80216	3.88169	5.95041	6.36623	6.76122
	0.33	1.42688	2.14561	2.67596	3.45219	3.63571	5.65741	6.01135	6.46441
	0.15	1.39278	2.07966	2.62382	3.36506	3.57490	5.51443	5.90564	6.33990
	0.08	1.38106	2.05565	2.60550	3.33385	3.55342	5.46001	5.86641	6.29245
0.35	1.33	1.70819	2.52099	3.15041	3.94553	4.14188	5.74997	6.55930	6.71095
	0.33	1.48547	2.21845	2.86293	3.55440	3.84082	5.67518	6.22222	6.58083
	0.15	1.44047	2.12749	2.79698	3.44677	3.76377	5.53239	6.10299	6.45191
	0.08	1.42586	2.09455	2.77353	3.40894	3.73670	5.47563	6.05904	6.40129

b) FEA results for plates with CYCICB

Table E-2: FEA results for the first eight non-dimensional transverse modal frequencies, Ω, of four plate sizes for plates with compliant inclusions and continuous boundaries (CYCICB)

V_r/S_y	$1/d^2$	Mode 1	Mode 2	Mode 3	Mode 4	Mode 5	Mode 6	Mode 7	Mode 8
0.12	1.33	1.31207	1.96200	2.40683	3.24567	3.25021	5.55827	5.56631	5.56813
	0.33	1.28587	1.92534	2.35825	3.18106	3.20186	5.43439	5.47460	5.51481
	0.15	1.28105	1.91793	2.34841	3.16560	3.18840	5.40790	5.45587	5.50153
	0.08	1.27924	1.91524	2.34538	3.16060	3.18452	5.39778	5.44823	5.49654
0.17	1.33	1.36411	2.04025	2.49908	3.36242	3.36265	5.69552	5.73456	5.76472
	0.33	1.30878	1.96560	2.40347	3.22510	3.26755	5.48301	5.56437	5.66209
	0.15	1.29824	1.94949	2.38369	3.19793	3.24752	5.42782	5.52545	5.63576
	0.08	1.29441	1.94371	2.37673	3.18652	3.23997	5.40770	5.51072	5.62606
0.23	1.33	1.43165	2.14189	2.61784	3.50269	3.51438	5.83953	5.94215	6.03122
	0.33	1.33794	2.01706	2.46694	3.28418	3.35848	5.54109	5.67813	5.85972
	0.15	1.31977	1.98758	2.43411	3.23440	3.32375	5.45237	5.61374	5.81453
	0.08	1.31331	1.97709	2.42334	3.21918	3.31122	5.42024	5.58979	5.79838
0.29	1.33	1.50817	2.25630	2.75296	3.65090	3.68947	5.95080	6.16284	6.35711
	0.33	1.36987	2.07270	2.54642	3.34771	3.46348	5.59593	5.80231	6.09752
	0.15	1.34284	2.02692	2.49983	3.27438	3.40406	5.47663	5.71095	6.02907
	0.08	1.33355	2.01041	2.48369	3.25356	3.39249	5.43196	5.67710	6.00410
0.35	1.33	1.58508	2.36887	2.89790	3.78836	3.87556	6.01205	6.37511	6.73372
	0.33	1.40035	2.12532	2.64033	3.40650	3.57591	5.63525	5.92322	6.36945
	0.15	1.36480	2.06247	2.58381	3.31834	3.50828	5.49238	5.80763	6.27423
	0.08	1.35308	2.03981	2.56375	3.28775	3.48474	5.44173	5.77121	6.22606

c) FEA results for plates with CYCMCB (For which micropolar constants are not available)

Table E-3: FEA results for the first eight non-dimensional transverse modal frequencies, Ω, of four plate sizes for plates with compliant matrix and continuous boundaries (CYCMCB)

V_r/S_y	$1/d^2$	Mode 1	Mode 2	Mode 3	Mode 4	Mode 5	Mode 6	Mode 7	Mode 8
0.12	1.33	1.23704	1.84852	2.27024	3.07338	3.07805	5.28954	5.30301	5.31268
	0.33	1.25889	1.95283	2.39442	3.12155	3.22485	5.33630	5.41059	5.70950
	0.15	1.26325	1.96942	2.42228	3.13250	3.25512	5.35266	5.43722	5.80111
	0.08	1.26436	1.97408	2.43299	3.13658	3.26507	5.36033	5.44939	5.83409
0.17	1.33	1.21498	1.81589	2.22727	3.00864	3.03908	5.14998	5.22114	5.29557
	0.33	1.25609	1.98625	2.50710	3.11041	3.32674	5.28818	5.44482	5.97914
	0.15	1.26419	2.00909	2.56775	3.13120	3.38445	5.32222	5.49687	6.03398
	0.08	1.26679	2.01723	2.59946	3.14450	3.40484	5.33525	5.51578	6.13843
0.23	1.33	1.20589	1.79723	2.21257	2.96116	3.04598	4.99098	5.18743	5.39944
	0.33	1.25764	1.99973	2.65914	3.10448	3.45200	5.23862	5.50265	5.98475
	0.15	1.26830	2.02654	2.74910	3.13333	3.53253	5.29199	5.57617	6.05360
	0.08	1.27224	2.03595	2.78096	3.14431	3.56179	5.31285	5.60261	6.07949
0.29	1.33	1.21890	1.78507	2.26178	2.94948	3.12207	4.83120	5.23376	5.58560
	0.33	1.26414	2.00200	2.81701	3.10653	3.58222	5.19538	5.57774	5.97979
	0.15	1.27483	2.03219	2.92337	3.13936	3.67508	5.26625	5.66124	6.05972
	0.08	1.27932	2.04003	2.95225	3.14891	3.70791	5.29393	5.68900	6.07197
0.35	1.33	1.25306	1.76422	2.38460	2.97472	3.25937	4.68165	5.35406	5.56577
	0.33	1.27318	2.00087	2.94759	3.11457	3.69214	5.16367	5.65255	5.97540
	0.15	1.28106	2.03360	3.05359	3.14613	3.78252	5.24831	5.73137	6.06166
	0.08	1.28500	2.04312	3.09265	3.15897	3.81084	5.29423	5.76150	6.09673

d) FEA results for plates with CYVOTB (Micro polar constants not available)

Table E-4: FEA results for the first eight non-dimensional transverse modal frequencies, Ω, of four plate sizes for plates with voids and textured boundaries (CYVOTB)

V_r/S_y	$1/d^2$	Mode 1	Mode 2	Mode 3	Mode 4	Mode 5	Mode 6	Mode 7	Mode 8
0.12	1.33	1.21885	1.81492	2.23401	2.98461	3.08701	5.00831	5.23544	5.42015
	0.33	1.26756	1.89442	2.31705	3.11517	3.17046	5.26551	5.39736	5.50331
	0.15	1.27620	1.90891	2.33448	3.13956	3.18705	5.32467	5.43049	5.52247
	0.08	1.27971	1.91418	2.34102	3.15002	3.19381	5.34709	5.44524	5.53010
0.17	1.33	1.16917	1.71273	2.19954	2.83301	3.04268	4.64714	5.07989	5.41933
	0.33	1.27245	1.89765	2.33923	3.10207	3.21758	5.15633	5.41746	5.65648
	0.15	1.29021	1.92925	2.36953	3.15033	3.25175	5.27354	5.48606	5.69500
	0.08	1.29736	1.94041	2.38037	3.17083	3.26552	5.31582	5.51479	5.71018
0.23	1.33	1.10204	1.56585	2.20052	2.64208	2.98665	4.21954	4.87480	5.05230
	0.33	1.27939	1.89413	2.39386	3.09122	3.28342	5.03514	5.44879	5.82643
	0.15	1.30873	1.94830	2.43502	3.16872	3.33998	5.22016	5.55998	5.93177
	0.08	1.32042	1.96708	2.45031	3.20119	3.36267	5.28776	5.60952	5.95639
0.29	1.33	1.01673	1.38897	2.23290	2.41272	2.92117	3.74149	4.58959	4.61902
	0.33	1.28955	1.88377	2.48681	3.08605	3.37111	4.90624	5.49508	5.77238
	0.15	1.33278	1.96362	2.53855	3.19744	3.45499	5.17061	5.66114	6.01441
	0.08	1.34975	1.99095	2.55757	3.24301	3.48790	5.26540	5.73312	6.11074
0.35	1.33	0.91404	1.19296	2.14695	2.29899	2.85157	3.23143	4.04923	4.32341
	0.33	1.30750	1.86523	2.62631	3.08994	3.49302	4.75587	5.56858	5.69491
	0.15	1.36712	1.97300	2.68978	3.24036	3.60940	5.11251	5.80221	6.03902
	0.08	1.39016	2.00961	2.71286	3.30182	3.65462	5.23976	5.90134	6.17517

e) FEA results for plates with CYCITB (Micro polar constants not available)

Table E-5: FEA results for the first eight non-dimensional transverse modal frequencies, Ω, of four plate sizes for plates with compliant inclusions and textured boundaries (CYCITB)

V_r/S_y	$1/d^2$	Mode 1	Mode 2	Mode 3	Mode 4	Mode 5	Mode 6	Mode 7	Mode 8
0.12	1.33	1.22327	1.82841	2.24067	3.00586	3.07401	5.08335	5.23163	5.35579
	0.33	1.26231	1.89090	2.31349	3.11017	3.14922	5.29482	5.37104	5.45052
	0.15	1.27107	1.90273	2.32935	3.13563	3.16719	5.34292	5.41046	5.47353
	0.08	1.27388	1.90691	2.33357	3.14378	3.17299	5.35970	5.42218	5.48154
0.17	1.33	1.18233	1.76727	2.19607	2.89405	3.02919	4.84314	5.10925	5.37987
	0.33	1.26048	1.89486	2.32011	3.09055	3.17112	5.21894	5.36416	5.54155
	0.15	1.27764	1.91786	2.34613	3.13813	3.20498	5.30536	5.43737	5.58190
	0.08	1.28309	1.92596	2.35569	3.15336	3.21626	5.33721	5.46055	5.59601
0.23	1.33	1.13121	1.68575	2.16865	2.76145	2.97552	4.57575	4.95734	5.31187
	0.33	1.25856	1.89677	2.34142	3.06968	3.20100	5.13511	5.35879	5.66260
	0.15	1.28559	1.93329	2.37771	3.14248	3.25373	5.26344	5.47194	5.72353
	0.08	1.29420	1.94605	2.39069	3.16522	3.27106	5.31094	5.50723	5.74474
0.29	1.33	1.07342	1.59680	2.16008	2.61917	2.91761	4.31172	4.78577	5.06624
	0.33	1.25701	1.89536	2.37919	3.04976	3.23824	5.05048	5.35654	5.77500
	0.15	1.29468	1.94620	2.42457	3.14862	3.31138	5.22124	5.51274	5.89167
	0.08	1.30648	1.96373	2.44059	3.17875	3.33483	5.28359	5.56081	5.92040
0.35	1.33	1.01708	1.52084	2.17092	2.48819	2.86887	4.09473	4.62241	4.83753
	0.33	1.25892	1.89262	2.43521	3.03731	3.28800	4.97455	5.36893	5.73942
	0.15	1.30679	1.95611	2.48843	3.16010	3.38112	5.18139	5.56635	5.97264
	0.08	1.32173	1.97811	2.50766	3.19762	3.41194	5.25685	5.62712	6.04848

f) FEA results for plates with CYCMTB

Table E-6: FEA results for the first eight non-dimensional transverse modal frequencies, Ω, of four plate sizes for plates with compliant matrix and textured boundaries (CYCMTB)

V_f/S_y	$1/d^2$	Mode 1	Mode 2	Mode 3	Mode 4	Mode 5	Mode 6	Mode 7	Mode 8
0.12	1.33	1.31260	2.09565	2.72556	3.23740	3.55381	5.48947	5.69220	6.22072
	0.33	1.27952	2.01528	2.51757	3.16992	3.35747	5.39764	5.53417	6.08326
	0.15	1.27148	1.99607	2.47579	3.15139	3.31220	5.37650	5.48825	5.97075
	0.08	1.26887	1.98891	2.46114	3.14566	3.29649	5.36890	5.47350	5.92826
0.17	1.33	1.35490	2.17988	3.07763	3.32969	3.87065	5.60757	5.95387	6.40082
	0.33	1.29513	2.06754	2.74562	3.20646	3.56192	5.41891	5.68551	6.18411
	0.15	1.28008	2.04248	2.67193	3.16842	3.48611	5.37503	5.59532	6.11830
	0.08	1.27497	2.03362	2.63937	3.15585	3.45919	5.35387	5.55321	6.09342
0.23	1.33	1.39685	2.24892	3.36427	3.42042	4.13370	5.72390	6.18806	6.55180
	0.33	1.31430	2.09898	2.97939	3.24190	3.76598	5.44407	5.83476	6.25873
	0.15	1.29251	2.06739	2.88975	3.19070	3.67016	5.37844	5.71945	6.16891
	0.08	1.28508	2.05617	2.85704	3.17414	3.63645	5.35519	5.68099	6.13918
0.29	1.33	1.43276	2.30688	3.49934	3.54682	4.31055	5.82403	6.36316	6.67184
	0.33	1.33387	2.11999	3.16789	3.27767	3.93212	5.46782	5.97180	6.31596
	0.15	1.30643	2.08095	3.07677	3.21440	3.82885	5.38296	5.83666	6.20599
	0.08	1.29679	2.06711	3.04330	3.19270	3.79281	5.35190	5.78996	6.16800
0.35	1.33	1.45817	2.35077	3.55833	3.61527	4.38889	5.89851	6.46273	6.74544
	0.33	1.35136	2.13445	3.28444	3.31177	4.04169	5.48900	6.07326	6.36188
	0.15	1.32006	2.08908	3.19868	3.23688	3.93374	5.38947	5.92901	6.23413
	0.08	1.30868	2.07314	3.17163	3.21146	3.90526	5.35278	5.87761	6.19199

E.2) 3D-MPFEM results for square plates with cylindrical voids and inclusions

a) 3D-MPFEM results for CYVOCB plates

Table E-7: MPFEM results for the first eight non-dimensional transverse modal frequencies, Ω, of four plate sizes for plates with voids and continuous boundaries (CYVOCB)

V_r/S_y	$1/d^2$	Mode 1	Mode 2	Mode 3	Mode 4	Mode 5	Mode 6	Mode 7	Mode 8
0.12	1.33	1.34818	1.99758	2.31508	3.21474	3.21489	5.41980	5.42041	5.47858
	0.33	1.32077	1.95327	2.32982	3.23478	3.23511	5.45393	5.45508	5.55006
	0.15	1.28586	1.91157	2.32003	3.16387	3.16423	5.39480	5.39600	5.42723
	0.08	1.27780	1.90102	2.31935	3.15251	3.15288	5.38619	5.38740	5.41200
0.17	1.33	1.38426	2.04650	2.30792	3.23880	3.23888	5.41202	5.41213	5.50402
	0.33	1.32958	1.96999	2.32043	3.21162	3.21196	5.42818	5.42933	5.48389
	0.15	1.30195	1.93266	2.32113	3.18528	3.18564	5.41087	5.41208	5.45544
	0.08	1.28835	1.91466	2.32055	3.16843	3.16880	5.39850	5.39971	5.43455
0.23	1.33	1.41695	2.09010	2.29547	3.25468	3.25469	5.35160	5.34996	5.51277
	0.33	1.35822	2.00841	2.31918	3.23756	3.23789	5.44360	5.44473	5.51353
	0.15	1.32190	1.95909	2.32173	3.20870	3.20906	5.42783	5.42903	5.48449
	0.08	1.30216	1.93271	2.32161	3.18737	3.18773	5.41284	5.41405	5.45989
0.29	1.33	1.43699	2.11622	2.28383	3.26060	3.26056	5.24178	5.23649	5.48425
	0.33	1.37786	2.03476	2.31759	3.25364	3.25397	5.45120	5.45231	5.53170
	0.15	1.33674	1.97884	2.32180	3.22458	3.22495	5.43888	5.44008	5.50353
	0.08	1.31290	1.94686	2.32218	3.20102	3.20138	5.42300	5.42420	5.47747
0.35	1.33	1.45468	2.13851	2.26842	3.25993	3.25981	5.01303	5.00119	5.15428
	0.33	1.39729	2.06082	2.31516	3.26787	3.26819	5.45505	5.45613	5.54751
	0.15	1.35258	1.99999	2.32148	3.24006	3.24042	5.44905	5.45024	5.52149
	0.08	1.32488	1.96271	2.32254	3.21514	3.21550	5.43327	5.43448	5.49499

b) **3D-MPFEM results for CYCICB plates**

Table E-8: MPFEM results for the first eight non-dimensional transverse modal frequencies, Ω, of four plate sizes for plates with compliant inclusions and continuous boundaries (CYCICB)

V_r/S_y	$1/d^2$	Mode 1	Mode 2	Mode 3	Mode 4	Mode 5	Mode 6	Mode 7	Mode 8
0.12	1.33	1.33058	1.97322	2.31853	3.20628	3.20646	5.42193	5.42265	5.47214
	0.33	1.29112	1.91857	2.32031	3.17074	3.17109	5.39994	5.40112	5.43597
	0.15	1.27828	1.90164	2.31943	3.15331	3.15367	5.38682	5.38802	5.41319
	0.08	1.27295	1.89479	2.31873	3.14490	3.14526	5.38027	5.38147	5.40101
0.17	1.33	1.36483	2.02013	2.31356	3.22911	3.22922	5.42540	5.42586	5.49522
	0.33	1.31332	1.94816	2.32080	3.19607	3.19642	5.41805	5.41922	5.46646
	0.15	1.29133	1.91865	2.32061	3.17192	3.17229	5.40101	5.40221	5.43854
	0.08	1.28127	1.90544	2.31986	3.15812	3.15848	5.39061	5.39181	5.42034
0.23	1.33	1.39260	2.05771	2.30564	3.24384	3.24390	5.40569	5.40559	5.50895
	0.33	1.33612	1.97875	2.32030	3.21806	3.21840	5.43237	5.43352	5.49145
	0.15	1.30626	1.93835	2.32134	3.19069	3.19105	5.41487	5.41607	5.46237
	0.08	1.29126	1.91843	2.32083	3.17262	3.17298	5.40171	5.40291	5.44032
0.29	1.33	1.41620	2.08915	2.29627	3.25494	3.25495	5.35829	5.35684	5.51433
	0.33	1.35711	2.00691	2.31932	3.23686	3.23719	5.44339	5.44452	5.51288
	0.15	1.32100	1.95788	2.32175	3.20783	3.20820	5.42725	5.42845	5.48355
	0.08	1.30150	1.93183	2.32159	3.18657	3.18693	5.41226	5.41346	5.45892
0.35	1.33	1.43724	2.11688	2.28758	3.26530	3.26526	5.29562	5.29207	5.51041
	0.33	1.37512	2.03096	2.31839	3.25324	3.25357	5.45265	5.45376	5.53219
	0.15	1.33387	1.97492	2.32206	3.22261	3.22298	5.43786	5.43906	5.50199
	0.08	1.31058	1.94373	2.32222	3.19870	3.19906	5.42142	5.42262	5.47506

c) 3D-MPFEM results for CYCMTB plates

Table E-9: MPFEM results for the first eight non-dimensional transverse modal frequencies, Ω, of four plate sizes for plates with compliant matrix and textured boundaries (CYCMTB)

V_r/S_y	$1/d^2$	Mode 1	Mode 2	Mode 3	Mode 4	Mode 5	Mode 6	Mode 7	Mode 8
0.12	1.33	1.33537	1.97948	2.31923	3.21414	3.21429	5.42850	5.42918	5.48307
	0.33	1.29226	1.91994	2.32067	3.17329	3.17364	5.40208	5.40327	5.44037
	0.15	1.27875	1.90217	2.31960	3.15438	3.15475	5.38774	5.38894	5.41516
	0.08	1.27320	1.89506	2.31883	3.14547	3.14583	5.38076	5.38196	5.40206
0.17	1.33	1.35311	2.00396	2.31675	3.22488	3.22501	5.43087	5.43144	5.49264
	0.33	1.30347	1.93487	2.32097	3.18642	3.18677	5.41157	5.41275	5.45609
	0.15	1.28517	1.91052	2.32024	3.16381	3.16417	5.39496	5.39616	5.42816
	0.08	1.27724	1.90023	2.31941	3.15204	3.15240	5.38591	5.38712	5.41179
0.23	1.33	1.37252	2.03062	2.31142	3.23279	3.23289	5.42115	5.42150	5.49850
	0.33	1.31973	1.95677	2.32067	3.20226	3.20260	5.42214	5.42330	5.47334
	0.15	1.29545	1.92409	2.32082	3.17719	3.17755	5.40491	5.40611	5.44524
	0.08	1.28399	1.90898	2.32014	3.16214	3.16251	5.39369	5.39490	5.42592
0.29	1.33	1.37955	2.04015	2.30819	3.23430	3.23439	5.40966	5.40982	5.49862
	0.33	1.32711	1.96677	2.32027	3.20839	3.20873	5.42574	5.42690	5.47957
	0.15	1.30056	1.93088	2.32096	3.18316	3.18352	5.40921	5.41042	5.45237
	0.08	1.28748	1.91355	2.32041	3.16699	3.16735	5.39735	5.39856	5.43235
0.35	1.33	1.38291	2.04467	2.30622	3.23465	3.23473	5.40069	5.40067	5.49788
	0.33	1.33103	1.97208	2.31999	3.21140	3.21174	5.42734	5.42849	5.48253
	0.15	1.30339	1.93466	2.32099	3.18629	3.18665	5.41143	5.41263	5.45601
	0.08	1.28945	1.91615	2.32054	3.16962	3.16998	5.39933	5.40053	5.43577

Appendix F

F) Numerical Results for Plates with Spherical Voids and Inclusions

F.1) FEA results for plates with spherical void and inclusions

a) Plates with continuous boundaries

1. FEA Results for SPVOCB

Table F-1: FEA results for the first eight non-dimensional transverse modal frequencies, Ω, of four plate sizes for plates with spherical voids and continuous boundaries (SPVOCB)

V_r/S_y	$1/d^2$	Mode 1	Mode 2	Mode 3	Mode 4	Mode 5	Mode 6	Mode 7	Mode 8
0.14	2.00	1.25460	1.87174	2.29551	3.07401	3.07401	5.21956	5.22346	5.22347
	0.50	1.24989	1.86585	2.28760	3.06430	3.06430	5.20527	5.21292	5.21295
	0.22	1.24909	1.86449	2.28579	3.06232	3.06248	5.20222	5.20927	5.20945
	0.12	1.24871	1.86580	2.28536	3.06172	3.06172	5.20163	5.20811	5.21254
0.21	2.00	1.26984	1.89219	2.31968	3.10619	3.10619	5.26250	5.26252	5.26778
	0.50	1.25441	1.87414	2.29439	3.07449	3.08189	5.22116	5.22870	5.23536
	0.22	1.24913	1.86827	2.28737	3.06748	3.06803	5.21089	5.21655	5.21703
	0.12	1.25077	1.86750	2.28616	3.06607	3.06607	5.20838	5.21329	5.21337
0.28	2.00	1.29535	1.92583	2.35836	3.15872	3.15872	5.32114	5.32115	5.34477
	0.50	1.25964	1.88469	2.30183	3.08726	3.08750	5.23957	5.24708	5.24898
	0.22	1.25371	1.87486	2.28867	3.07319	3.07358	5.21821	5.22378	5.22386
	0.12	1.25221	1.87166	2.28448	3.06890	3.06907	5.21212	5.21562	5.21613
0.35	2.00	1.33078	1.97230	2.40886	3.22975	3.22976	5.39288	5.39292	5.44605
	0.50	1.26413	1.90971	2.31300	3.10117	3.10669	5.25622	5.27542	5.29800
	0.22	1.25137	1.88338	2.28723	3.07493	3.07647	5.21865	5.23210	5.23259
	0.12	1.24971	1.87514	2.28063	3.06673	3.06992	5.16960	5.21580	5.21962
0.42	2.00	1.36610	2.02218	2.45469	3.29849	3.29849	5.45087	5.45087	5.53646
	0.50	1.25483	1.92406	2.31499	3.10061	3.10061	5.24191	5.29861	5.29861
	0.22	1.24145	1.89867	2.28328	3.06661	3.06662	5.19266	5.23942	5.24056
	0.12	1.24034	1.89092	2.27207	3.05428	3.06007	5.18325	5.21849	5.22316

2. FEA Results for SPCICB

Table F-2: FEA results for the first eight non-dimensional transverse modal frequencies, Ω, of four plate sizes for plates with spherical inclusions and continuous boundaries (SPCICB)

V_r/S_y	$1/d^2$	Mode 1	Mode 2	Mode 3	Mode 4	Mode 5	Mode 6	Mode 7	Mode 8
0.14	2.00	1.25870	1.88618	2.30922	3.09695	3.09695	5.26192	5.27574	5.27574
	0.50	1.24997	1.86622	2.28828	3.06482	3.06482	5.20527	5.21368	5.21368
	0.22	1.24938	1.86533	2.28705	3.06374	3.06374	5.20458	5.21238	5.21238
	0.12	1.24897	1.86425	2.28587	3.06229	3.06230	5.20213	5.20924	5.20945
0.21	2.00	1.27042	1.90143	2.32754	3.12136	3.12136	5.30026	5.30600	5.30602
	0.50	1.25306	1.87155	2.29309	3.07233	3.07233	5.21774	5.22627	5.22627
	0.22	1.25030	1.87003	2.29008	3.06720	3.07205	5.21085	5.21738	5.22251
	0.12	1.25001	1.86619	2.28627	3.06464	3.06465	5.20608	5.21225	5.21226
0.28	2.00	1.29101	1.92802	2.35861	3.16312	3.16313	5.35303	5.35303	5.36233
	0.50	1.25771	1.88107	2.30074	3.08411	3.08414	5.23580	5.24567	5.24567
	0.22	1.25284	1.87293	2.29018	3.07230	3.07231	5.21782	5.22505	5.22505
	0.12	1.25126	1.87050	2.28684	3.06797	3.07850	5.21143	5.21652	5.23799
0.35	2.00	1.31896	1.96385	2.39864	3.21826	3.21826	5.40934	5.40934	5.44137
	0.50	1.26148	1.89485	2.30960	3.09673	3.09673	5.25277	5.26946	5.26946
	0.22	1.25302	1.88051	2.29004	3.07552	3.07610	5.20090	5.22224	5.23390
	0.12	1.25202	1.87676	2.28557	3.06976	3.07000	5.21192	5.22127	5.22182
0.42	2.00	1.34629	2.00049	2.43545	3.27014	3.27015	5.45512	5.45516	5.51028
	0.50	1.25754	1.91087	2.31560	3.09971	3.09971	5.24927	5.29040	5.29043
	0.22	1.24614	1.88808	2.28872	3.07046	3.07265	5.20520	5.23876	5.24004
	0.12	1.24420	1.88858	2.28066	3.06360	3.07381	5.20000	5.22435	5.24166

b) Plates with textured boundaries

1. FEA Results for SPVOTB

Table F-3: FEA results for the first eight non-dimensional transverse modal frequencies, Ω, of four plate sizes for plates with spherical voids and textured boundaries (SPVOTB)

V_f/S_y	$1/d^2$	Mode 1	Mode 2	Mode 3	Mode 4	Mode 5	Mode 6	Mode 7	Mode 8
0.14	2.00	1.23975	1.84974	2.26590	3.04128	3.04128	5.17174	5.17341	5.17342
	0.50	1.24591	1.85974	2.27925	3.05434	3.05504	5.18970	5.19557	5.19618
	0.22	1.24734	1.86173	2.28224	3.05791	3.05791	5.19490	5.20134	5.20138
	0.12	1.24777	1.86257	2.28298	3.05914	3.05927	5.19694	5.20342	5.20346
0.21	2.00	1.22404	1.82743	2.23233	3.00706	3.00706	5.11664	5.11664	5.12208
	0.50	1.24241	1.85514	2.26925	3.04504	3.04700	5.17497	5.17798	5.18014
	0.22	1.24630	1.85995	2.27429	3.05402	3.05502	5.18964	5.19275	5.19358
	0.12	1.24775	1.86255	2.27959	3.05834	3.05852	5.19552	5.19933	5.19944
0.28	2.00	1.19608	1.79544	2.18114	2.94996	2.94996	5.02908	5.02908	5.03510
	0.50	1.23520	1.84800	2.25187	3.02731	3.03175	5.14538	5.14698	5.15034
	0.22	1.24332	1.85929	2.26644	3.04780	3.04944	5.17671	5.17724	5.18530
	0.12	1.24629	1.86198	2.27164	3.05442	3.05476	5.18817	5.18836	5.18863
0.35	2.00	1.15313	1.76257	2.12056	2.87111	2.87113	4.90743	4.92467	4.92474
	0.50	1.22425	1.84295	2.23079	3.00505	3.01200	5.10789	5.10830	5.11567
	0.22	1.23851	1.86012	2.25334	3.03882	3.03962	5.15909	5.15940	5.16006
	0.12	1.24367	1.86407	2.26126	3.04974	3.05027	5.17701	5.17768	5.17824
0.42	2.00	1.08870	1.73749	2.05852	2.76643	2.76643	4.72406	4.81656	4.81657
	0.50	1.20723	1.84285	2.20782	2.97615	2.98594	5.05417	5.06988	5.08300
	0.22	1.22987	1.86320	2.23752	3.02591	3.02642	5.13254	5.14209	5.14310
	0.12	1.23805	1.87048	2.24864	3.04275	3.04344	5.16183	5.16755	5.16874

2. FEA Results for SPCITB

Table F-4: FEA results for the first eight non-dimensional transverse modal frequencies, Ω, of four plate sizes for plates with spherical inclusions and textured boundaries (SPCITB)

V_r/S_y	$1/d^2$	Mode 1	Mode 2	Mode 3	Mode 4	Mode 5	Mode 6	Mode 7	Mode 8
0.14	2.00	1.23781	1.84061	2.25791	3.02359	3.02359	5.12084	5.12085	5.12307
	0.50	1.16990	1.85684	2.26746	2.98296	3.05086	5.14625	5.18307	5.18470
	0.22	1.24645	1.85457	2.28083	3.05361	3.05667	5.10011	5.19512	5.19731
	0.12	1.24810	1.86258	2.28324	3.05781	3.05872	5.19545	5.20193	5.20224
0.21	2.00	1.22559	1.82446	2.23393	3.00067	3.00067	5.09126	5.09127	5.09798
	0.50	1.19418	1.84581	2.23914	2.77189	3.04326	5.16890	5.17193	5.31164
	0.22	1.24611	1.85966	2.27779	3.05380	3.05389	5.18635	5.19130	5.19135
	0.12	1.24742	1.86178	2.28254	3.05732	3.05747	5.19310	5.19823	5.20613
0.28	2.00	1.20478	1.80105	2.19750	2.96111	2.96111	5.03712	5.03713	5.04382
	0.50	1.24879	1.89306	2.26019	3.03242	3.04972	5.15140	5.15178	5.16761
	0.22	1.25508	1.86564	2.27198	3.04920	3.06375	5.17851	5.18153	5.18171
	0.12	1.24644	1.86155	2.27554	3.05500	3.05525	5.18891	5.19181	5.19210
0.35	2.00	1.17388	1.77619	2.15415	2.90613	2.90613	4.96002	4.96881	4.96883
	0.50	1.22911	1.84453	2.24348	3.01469	3.02018	5.12352	5.12551	5.13182
	0.22	1.26686	1.85894	2.26554	3.04231	3.06940	5.16825	5.16882	5.17605
	0.12	1.24436	1.86254	2.26829	3.05123	3.05169	5.18146	5.18368	5.18416
0.42	2.00	1.13075	1.75673	2.11094	2.83640	2.83642	4.84260	4.89817	4.89817
	0.50	1.21687	1.84287	2.22665	2.99348	3.00140	5.08554	5.09761	5.10763
	0.22	1.23367	1.85949	2.24999	3.03213	3.03213	5.14507	5.15497	5.15497
	0.12	1.23975	1.86542	2.25854	3.04457	3.04519	5.16745	5.17422	5.17508

F.2) MPFEM results for plates with spherical void and Inclusions and Continuous Boundaries

1. MPFEM Results for SPVOCB

Table F-5: MPFEM results for the first eight non-dimensional transverse modal frequencies, Ω, of four plate sizes for plates with spherical voids and continuous boundaries (SPVOCB)

V_r/S_y	$1/d^2$	Mode 1	Mode 2	Mode 3	Mode 4	Mode 5	Mode 6	Mode 7	Mode 8
0.14	2.00	1.25917	1.87357	2.28025	3.06832	3.06886	5.19063	5.19413	5.20775
	0.50	1.25065	1.86212	2.27995	3.05728	3.05790	5.18281	5.18949	5.19113
	0.22	1.24854	1.85946	2.27965	3.05380	3.05442	5.18315	5.18383	5.18590
	0.12	1.24773	1.85847	2.27949	3.05237	3.05299	5.18088	5.18272	5.18479
0.21	2.00	1.27341	1.89301	2.27901	3.07975	3.08025	5.19612	5.19947	5.21899
	0.50	1.25759	1.87111	2.28037	3.06660	3.06720	5.18952	5.19619	5.20333
	0.22	1.25224	1.86412	2.28013	3.05965	3.06027	5.18825	5.19032	5.19171
	0.12	1.24999	1.86127	2.27987	3.05622	3.05684	5.18569	5.18682	5.18776
0.28	2.00	1.28432	1.90794	2.27537	3.08391	3.08438	5.18680	5.18980	5.22142
	0.50	1.26638	1.88279	2.28007	3.07510	3.07570	5.19473	5.20140	5.21261
	0.22	1.25773	1.87124	2.28038	3.06673	3.06735	5.19328	5.19535	5.20075
	0.12	1.25358	1.86584	2.28023	3.06153	3.06215	5.18963	5.19170	5.19425
0.35	2.00	1.29051	1.91605	2.26919	3.08256	3.08301	5.10459	5.10038	5.19953
	0.50	1.27424	1.89336	2.27907	3.08044	3.08104	5.19630	5.20295	5.21767
	0.22	1.26366	1.87909	2.28026	3.07276	3.07338	5.19711	5.19918	5.20749
	0.12	1.25781	1.87135	2.28039	3.06682	3.06744	5.19334	5.19541	5.20086
0.42	2.00	1.29357	1.91956	2.26125	3.07700	3.07741	4.51421	4.50051	4.49229
	0.50	1.27966	1.90066	2.27774	3.08302	3.08363	5.19449	5.20111	5.21984
	0.22	1.26852	1.88558	2.27989	3.07671	3.07733	5.19911	5.20118	5.21149
	0.12	1.26159	1.87634	2.28035	3.07082	3.07144	5.19595	5.19802	5.20541

2. MPFEM Results for SPCICB

Table F-6: MPFEM results for the first eight non-dimensional transverse modal frequencies, Ω, of four plate sizes for plates with spherical inclusions and continuous boundaries (SPCICB)

V_r/S_y	$1/d^2$	Mode 1	Mode 2	Mode 3	Mode 4	Mode 5	Mode 6	Mode 7	Mode 8
0.14	2.00	1.25934	1.87377	2.28032	3.06877	3.06930	5.19101	5.19450	5.20851
	0.50	1.25068	1.86214	2.27997	3.05736	3.05797	5.18288	5.18955	5.19129
	0.22	1.24855	1.85947	2.27965	3.05382	3.05444	5.18320	5.18386	5.18593
	0.12	1.24773	1.85848	2.27949	3.05238	3.05300	5.18090	5.18273	5.18480
0.21	2.00	1.27137	1.89015	2.27954	3.07923	3.07973	5.19681	5.20018	5.21912
	0.50	1.25613	1.86917	2.28039	3.06502	3.06563	5.18848	5.19515	5.20162
	0.22	1.25139	1.86303	2.28006	3.05846	3.05907	5.18738	5.18945	5.19011
	0.12	1.24946	1.86060	2.27981	3.05537	3.05599	5.18505	5.18559	5.18712
0.28	2.00	1.28275	1.90576	2.27693	3.08498	3.08545	5.19396	5.19714	5.22370
	0.50	1.26396	1.87951	2.28034	3.07346	3.07407	5.19405	5.20071	5.21133
	0.22	1.25602	1.86898	2.28039	3.06486	3.06547	5.19203	5.19410	5.19867
	0.12	1.25240	1.86432	2.28016	3.05996	3.06058	5.18850	5.19057	5.19223
0.35	2.00	1.29143	1.91739	2.27092	3.08539	3.08584	5.15118	5.15194	5.21689
	0.50	1.27348	1.89228	2.27945	3.08079	3.08139	5.19732	5.20397	5.21859
	0.22	1.26275	1.87784	2.28040	3.07229	3.07291	5.19699	5.19906	5.20735
	0.12	1.25706	1.87034	2.28043	3.06614	3.06676	5.19293	5.19500	5.20025
0.42	2.00	1.29346	1.91994	2.26785	3.08401	3.08445	5.07433	5.06654	5.18617
	0.50	1.27651	1.89636	2.27893	3.08256	3.08316	5.19735	5.20399	5.22019
	0.22	1.26522	1.88112	2.28029	3.07457	3.07519	5.19834	5.20041	5.20978
	0.12	1.25889	1.87273	2.28046	3.06827	3.06888	5.19438	5.19645	5.20280

References

A. Riahi Dehkordi. 2008. “3D Finite Element Cosserat Continuum Simulation of Layered Geomaterials.” *PhD Thesis, University of Toronto*, 122–47.

Abadikhah, H., and P. D. Folkow. 2017. “A Systematic Approach to Derive Dynamic Equations for Homogeneous and Functionally Graded Micropolar Plates.” *Procedia Engineering* 199: 1429–34. https://doi.org/10.1016/j.proeng.2017.09.389.

Abadikhah, Hossein, and Peter D. Folkow. 2015. “A Hierarchy of Dynamic Equations for Micropolar Plates.” *Journal of Sound and Vibration* 357: 427–36. https://doi.org/10.1016/j.jsv.2015.08.005.

Aifantis, Elias C. 2011. “On the Gradient Approach – Relation to Eringen’s Nonlocal Theory.” *International Journal of Engineering Science* 49: 1367–77. https://doi.org/10.1016/j.ijengsci.2011.03.016.

Aksencer, Tolga, and Metin Aydogdu. 2011. “Levy Type Solution Method for Vibration and Buckling of Nanoplates Using Nonlocal Elasticity Theory.” *Physica E: Low-Dimensional Systems and Nanostructures* 43 (4): 954–59. https://doi.org/10.1016/j.physe.2010.11.024.

Altenbach, Holm, and Victor A. Eremeyev. 2009. “On the Linear Theory of Micropolar Plates.” *ZAMM Zeitschrift Fur Angewandte Mathematik Und Mechanik* 89 (4): 242–56. https://doi.org/10.1002/zamm.200800207.

Apuzzo, A, R Barretta, S A Faghidian, R Luciano, and F Marotti De Sciarra. 2018. “Free Vibrations of Elastic Beams by Modified Nonlocal Strain Gradient Theory.” *International Journal of Engineering Science* 133: 99–108.

Asghari, M., M. H. Kahrobaiyan, M. Rahaeifard, and M. T. Ahmadian. 2011. “Investigation of the Size Effects in Timoshenko Beams Based on the Couple Stress Theory.” *Archive of Applied Mechanics* 81 (7): 863–74. https://doi.org/10.1007/s00419-010-0452-5.

Askes, Harm. 2009. “Gradient Elasticity and Flexural Wave Dispersion in Carbon Nanotubes.” *PHYSICAL REVIEW* 80 (19): 1–8. https://doi.org/10.1103/PhysRevB.80.195412.

Askes, Harm, and Elias C Aifantis. 2011. “Gradient Elasticity in Statics and Dynamics : An Overview of Formulations , Length Scale Identification Procedures , Finite Element Implementations and New Results.” *International Journal of Solids and Structures* 48: 1962–90. https://doi.org/10.1016/j.ijsolstr.2011.03.006.

Askes, Harm, Duc C.D. Nguyen, and Andy Tyas. 2011. “Increasing the Critical Time Step: Micro-Inertia, Inertia Penalties and Mass Scaling.” *Computational Mechanics* 47 (6): 657–67. https://doi.org/10.1007/s00466-010-0568-z.

Avcar, Mehmet. 2014. “Vibrations of a Free-Free Beam.” *International Journal of Mechanics and Applications* 4 (3): 94–100.

Bathe, K. 2006. *Finite Element Procedures*. 2nd ed. K.J.Bsthe, Watertown, MA. http://web.mit.edu/kjb/www/Books/FEP_2nd_Edition_4th_Printing.pdf.

Beisheim, Jeff. 2007. “Introducing the PCG Lanczos Eigensolver.” *ANSYS Advantage* I (1): 42–43.

Beveridge, A. J., M. A. Wheel, and D. H. Nash. 2013a. “The Micropolar Elastic Behaviour of Model Macroscopically Heterogeneous Materials.” *International Journal of Solids and Structures* 50 (1): 246–55. https://doi.org/10.1016/j.ijsolstr.2012.09.023.

Beveridge, A J, M A Wheel, and D H Nash. 2013b. “A Higher Order Control Volume Based Finite Element Method to Predict the Deformation of Heterogeneous Materials.” *Computers & Structures* 129 (0): 54–62. https://doi.org/http://dx.doi.org/10.1016/j.compstruc.2013.08.006.

Borst, R. de, and L. J. Sluys. 1991. “Localisation in a Cosserat Continuum under Static Aod Dynamic Loading Conditions.” *Computer Methods in Applied Mechanics and Engineering* 84 (3): 805–27. https://doi.org/10.1016/0045-7825(91)90185-9.

Buhan, P. de, J.Fréard, D. Garnier, and S. Maghous4. 2002. “Failure Properties of Fractured Rock Masses as Anisotropic Homogenized Media.” *J. Eng. Mech.* 128 (August): 869–75.

Carcorze-soto, Jorge Luis. 2010. “Dynamic Stress Predictions of a Viscously Damped Timoshenko Beam At Resonant Conditions” 2010 (December).

Colorado, University of. 2010. “Lumped and Consisitent Mass Matrices.” *Introduction To Finite Element Mehtods*, 31.1-31.23. https://doi.org/10.1097/OLQ.0b013e31815fd412.

Dasgupta, Abhijit. 2000. “Eigenstrain Techniques for Modeling Adaptive Structures: II. Active Damping.” *Journal of Intelligent Material Systems and Structures* 11 (8): 631–41. https://doi.org/10.1106/NYLF-WKYV-UUWX-RPV9.

Della, Christian N, and Dongwei Shu. 2006. “Natural Frequency of Beams with Embedded Piezoelectric Sensors and Actuators.” *Institute of Physics Publishing* 15: 529–37. https://doi.org/10.1088/0964-1726/15/2/036.

Dolph, C. L. 1954. “On the Timoshenko Theory of Transverse Beam Vibrations.” *Quarterly of Applied Mathematics* 12 (2): 175–87. https://doi.org/10.1090/qam/62620.

Doschoris, Michael. 2016. “Towards a Generalization of the Separation of Variables Technique.” *METHODS AND APPLICATIONS OF ANALYSIS* 19 (January 2012): 381–402. https://doi.org/10.4310/MAA.2012.v19.n4.a4.

Eftekhari, S. A., and A. A. Jafari. 2013. “A Simple and Accurate Mixed FE-DQ Formulation for Free Vibration of Rectangular and Skew Mindlin Plates with General Boundary Conditions.” *Meccanica* 48 (5): 1139–60. https://doi.org/10.1007/s11012-012-9657-8.

Eisenberg, M. A., and L. E. Malverns. 1973. “On Finite Element Integration in Natural Co-Ordinates.” *International Journal for Numerical Methods in Engineering* 7 (July): 574–75. https://doi.org/doi/pdf/10.1002/nme.1620070421.

Elishakoff, Isaac, Julius Kaplunov, and Evgeniya Nolde. 2015. “Celebrating the Centenary of Timoshenko’s Study of Effects of Shear Deformation and Rotary Inertia.” *Applied Mechanics Reviews* 67 (6): 060802-060802–11. https://doi.org/10.1115/1.4031965.

Eremeyev, Victor a., Leonid P Lebedev, and Holm Altenbach. 2013. *Foundations of Micropolar Mechanics*. https://doi.org/10.1007/978-3-642-28353-6.

Eremeyev, Victor A., Andrzej Skrzat, and Feliks Stachowicz. 2016a. “On Finite Element Computations of Contact Problems in Micropolar Elasticity.” *Advances in Materials Science and Engineering* 2016. https://doi.org/10.1155/2016/9675604.

Eremeyev, Victor A, Andrzej Skrzat, and Feliks Stachowicz. 2016b. “On Finite Element Computations of Contact Problems in Micropolar Elasticity.” *Advances in Materials Science and Engineering* 2016: 1–9. http://dx.doi.org/10.1155/2016/9675604.

Eringen, A. C. 1966. “Linear Theory of Micropolar Elasticity.” *Journal of Mathematics and Mechanics* 15 (6): 909–23.

Eringen, A. Cemal. 1972. “Nonlocal Polar Elastic Continua.” *International Journal of Engineering Science* 10 (1): 1–16. https://doi.org/10.1016/0020-7225(72)90070-5.

Faghidian, S Ali. 2018. “Integro-Differential Nonlocal Theory of Elasticity.” *International Journal of Engineering Science* 129: 96–110.

Fatemi, J, F V A N Keulen, and P R Onck. 2002. “Generalized Continuum Theories : Application to Stress Analysis in Bone.” *Meccanica* 37 (4–5): 385–96.

Felippa, Carlos A., Qiong Guo, and K. C. Park. 2015. “Mass Matrix Templates: General Description and 1D Examples.” *Archives of Computational Methods in Engineering* 22 (1): 1–65. https://doi.org/10.1007/s11831-014-9108-x.

Fernández-Sáez, J., R. Zaera, J. A. Loya, and J. N. Reddy. 2016. “Bending of Euler-Bernoulli Beams Using Eringen’s Integral Formulation: A Paradox Resolved.” *International Journal of Engineering Science* 99: 107–16. https://doi.org/10.1016/j.ijengsci.2015.10.013.

Frame, Jamie Campbell. 2013a. “A Computational and Experimental Investigation into the Micropolar Elastic Behaviour of Cortical Bone.” *PhD Thesis, University Of Strathclyde*, 67–97.

———. 2013b. “A Computational and Experimental Investigation into the Micropolar Elastic Behaviour of Cortical Bone.” *PhD Thesis, University Of Strathclyde*, 29–110.

Franco-Villafañe, J. A., and R. A. Méndez-Sánchez. 2016. “On the Accuracy of the Timoshenko Beam Theory Above the Critical Frequency: Best Shear Coefficient.” *Journal of Mechanics* 32 (05): 515–18. https://doi.org/10.1017/jmech.2015.104.

Fu, Guangyang, Shenjie Zhou, and Lu Qi. 2019. “A Size-Dependent Bernoulli-Euler Beam Model Based on Strain Gradient Elasticity Theory Incorporating Surface Effects.” *ZAMM - Journal of Applied Mathematics and Mechanics* 99 (6): 1–22. https://doi.org/10.1002/zamm.201800048.

Garcea, G., A. Madeo, and R. Casciaro. 2012. “The Implicit Corotational Method and Its Use in the Derivation of Nonlinear Structural Models for Beams and Plates.” *Journal of Mechnaics of Materials and Structures* 7 (6): 509–38.

Gauthier, R. D., and W. E. Jahsman. 1975. “A Quest for Micropolar Elastic Constants.” *Journal of Applied Mechanics, Transactions ASME* 42 (2): 369–74. https://doi.org/10.1115/1.3423583.

Gherlone, Marco. 2013. “On the Use of Zigzag Functions in Equivalent Single Layer Theories for Laminated Composite and Sandwich Beams: A Comparative Study and

Some Observations on External Weak Layers." *Journal of Applied Mechanics* 80 (6): 1–19. https://doi.org/10.1115/1.4023690.

Gitman, Inna M, Harm Askes, Ellen Kuhl, and Elias C Aifantis. 2010. "Stress Concentrations in Fractured Compact Bone Simulated with a Special Class of Anisotropic Gradient Elasticity." *International Journal of Solids and Structures* 47 (9): 1099–1107. https://doi.org/10.1016/j.ijsolstr.2009.11.020.

Goda, I., M. Assidi, and J. F. Ganghoffer. 2014. "A 3D Elastic Micropolar Model of Vertebral Trabecular Bone from Lattice Homogenization of the Bone Microstructure." *Biomech. Model. Mechanobiol.,* 42 (Jan): 53–83. https://doi.org/10.1007/s10237-013-0486-z.

Godio, Michele, Ioannis Stefanou, Karam Sab, Jean Sulem, Michele Godio, Ioannis Stefanou, Karam Sab, et al. 2015. "Dynamic Finite Element Formulation for Cosserat Elastic Plates To Cite This Version : HAL Id : Hal-01114343 Dynamic Finite Element Formulation for Cosserat Elastic Plates."

Gortsas, Theodore V, Stephanos V Tsinopoulos, Dimitrios Rodopoulos, and Demosthenes Polyzos. 2018. "Strain Gradient Elasticity and Size Effects in the b Ending of Fib Er Composite Plates." *International Journal of Solids and Structures* 143: 103–12.

Groh, R. M J, and P. M. Weaver. 2015. "On Displacement-Based and Mixed-Variational Equivalent Single Layer Theories for Modelling Highly Heterogeneous Laminated Beams." *International Journal of Solids and Structures* 59: 147–70. https://doi.org/10.1016/j.ijsolstr.2015.01.020.

Hadjesfandiari, Ali R, Arezoo Hajesfandiari, and Gary F Dargush. 2016. "Pure Plate Bending in Couple Stress Theories." *ArXiv:1606.02954v1 [Physics.Gen-Ph]*, 1–38.

Han, S., M., H. Benaroya, and T. Wei. 1999. "Dynamics of Transversely Vibrating Beams Using Four Engineering Theories." *Journal of Sound and Vibrarion* 225: 935–88. https://doi.org/jsvi.1999.225.

Hanukah, Eli. 2014. "Mass Matrix Integration Scheme for Fifteen-Node Wedge Element," 1–8. https://doi.org/10.11205/jalp1953.2006.100.

Hassanati, B., and M. Wheel. 2019. "Quantifying Numerically Forecast Size Effects in the Free Vibration of Heterogeneous Beams." *International Journal of Mechanical Sciences* 152: 298–311. https://doi.org/10.1016/j.ijmecsci.2019.01.009.

Hassanati, B, and M Wheel. 2018. "Size Effects on Free Vibration of Heterogeneous Beams." *2017 International Conference on Engineering Vibration, ICoEV 2017* 148: 1–7. https://doi.org/10.1051/matecconf/201814807003.

Hassanpour, Soroosh, and Glenn R. Heppler. 2017. "Micropolar Elasticity Theory: A Survey of Linear Isotropic Equations, Representative Notations, and Experimental Investigations." *Mathematics and Mechanics of Solids* 22 (2): 224–42. https://doi.org/10.1177/1081286515581183.

Huebner, Kenneth H., Donald L. Dewhirst, Douglas E. Smith, and Ted G. Byrom. 2001. "The Finite Element Method for Engineers." *John Wiley &Sons, INC* Forth ed,: 151–61.

Kaltenbacher, Manfred. 2015. *Numerical Simulation of Mechatronic Sensors and Actuators: Finite Elements for Computational Multiphysics, Third Edition*. *Numerical Simulation of Mechatronic Sensors and Actuators: Finite Elements for Computational Multiphysics, Third Edition*. https://doi.org/10.1007/978-3-642-40170-1.

Kouhia, Reijo, and Antti H Niemi. 2013. "On the Numerical Solution of a Micropolar Continuum Model." *Proceedings of the 26th Nordic Seminar on Computational Mechanics*, no. 3: 128–31.

Lakes, R. 1996. "Experimental Methods for Study of Cosserat Elastic Solids and Other Generalized Elastic Continua." *Continuum Models for Materials with Micro-Structure*, no. 1: 1–22. http://scholar.google.com/scholar?hl=en&btnG=Search&q=intitle:Experimental+Methods+for+Study+of+Cosserat+Elastic+Solids+and+Other+Generilzed+Elastic+Continua#0.

Lam, D C C, F Yang, A C M Chong, J Wang, and P Tong. 2003. "Experiments and Theory in Strain Gradient Elasticity." *Journal of the Mechanics and Physics of Solids* 51: 1477–1508. https://doi.org/10.1016/S0022-5096(03)00053-X.

Li, Lei, and Shuisheng Xie. 2004. "Finite Element Method for Linear Micropolar Elasticity and Numerical Study of Some Scale Effects Phenomena in MEMS." *International Journal of Mechanical Sciences* 46: 1571–87. https://doi.org/10.1016/j.ijmecsci.2004.10.004.

Liew, K. M., K. C. Hung, and M. K. Lim. 1995. "Vibration of Mindlin Plates Using Boundary Characteristic Orthogonal Polynomials." *Journal of Sound and Vibration* 182 (1): 77–90.

Liew, K. M., Y. Xiang, and S. Kitipornchai. 1993. "Transverse Vibration of Thick Rectangular Plates-IV. Influence of Isotropic in-Plane Pressure." *Computers and Structures* 49 (1): 69–78. https://doi.org/10.1016/0045-7949(93)90125-W.

———. 1995. "Research on Thick Plate Vibration: A Literature Survey." *Journal of Sound and Vibration* 180 (1): 163–76. https://doi.org/10.1006/jsvi.1995.0072.

Lim, C. W., S. Kitipornchai, and K. M. Liew. 1998. "Numerical Aspects for Free Vibration of Thick Plates Part II: Numerical Efficiency and Vibration Frequencies." *Computer Methods in Applied Mechanics and Engineering* 156: 31–44.

Lim, C. W., K. M. Liew, and S. Kitipornchai. 1998. "Numerical Aspects for Free Vibration of Thick Plates Part I: Formulation and Verification." *Computer Methods in Applied Mechanics and Engineering* 156 (1–4): 15–29. https://doi.org/10.1016/S0045-7825(97)00198-9.

Liu, Huimin, Fanming Liu, Xin Jing, Zhenpeng Wang, and Linlin Xia. 2017. "Three-Dimensional Vibration Analysis of Rectangular Thick Plates on Pasternak Foundation with Arbitrary Boundary Conditions." *Shock and Vibration* 2017: 1–10. https://doi.org/10.1155/2017/3425298.

Lombardo, Mariateresa, and Harm Askes. 2012. "Higher-Order Gradient Continuum Modelling of Periodic Lattice Materials." *Computational Materials Science* 52 (1): 204–8. https://doi.org/10.1016/j.commatsci.2011.05.025.

Lurie, S, and Y Solyaev. 2018. “Revisiting Bending Theories of Elastic Gradient Beams.” *International Journal of Engineering Science* 126: 1–21.

Manevich, A, and Kolakowski Zbigniew. 2011. “Free and Forced Oscillations of Timoshenko Beam Made of Viscoelastic Material.” *Journal of Theoretical and Applied Mechanics* 49 (2011): 3–16.

McGregor, M., and M. A. Wheel. 2014. “On the Coupling Number and Characteristic Length of Micropolar Media of Differing Topology.” *Proceedings of the Royal Society A: Mathematical, Physical and Engineering Sciences* 470 (20140150): 1–19. https://doi.org/10.1098/rspa.2014.0150.

Méndez-Sánchez, R. A., A. Morales, and J. Flores. 2005. “Experimental Check on the Accuracy of Timoshenko’s Beam Theory.” *Journal of Sound and Vibration* 279 (1–2): 508–12. https://doi.org/10.1016/j.jsv.2004.01.050.

Mindlin, R. D. 1986. “Flexural Vibrations of Rectangular Plates with Free Edges.” *Mechanics Research Communications*. https://doi.org/10.1016/0093-6413(86)90049-2.

Mindlin, R. D., and H. Deresiewicz. 1955. “Thickness-Shear and Flexural Vibrations of Rectangular Crystal Plates.” *Journal of Applied Physics* 26 (12): 1435–42. https://doi.org/10.1063/1.1721928.

Mindlin, R. D., and N. N. Eshel. 1968. “On First Strain-Gradient Theories in Linear Elasticity.” *International Journal of Solids and Structures* 4: 109–24.

Mindlin, Raymond D. 1951. “Thickness-Shear and Flexural Vibrations of Crystal Plates.” *Journal of Applied Physics* 22 (3): 316–23. https://doi.org/10.1063/1.1699948.

Nakamura, S, and R S Lakes. 1995. “Finite Element Analysis of Saint-Venant End Effects in Micropolar Elastic Solids.” *Engineering Computations* 12: 571–87.

———. 2003. “Finite Element Analysis of Saint-Venant End Effects in Micropolar Elastic Solids Adapted from Engineering Computations, 12, 571-587, (1995),” 1–10. https://www.semanticscholar.org/paper/Finite-element-analysis-of-Saint-Venant-end-effects-Lakes/2f596539beac0b6368b768bd160dc10768acd3c1#similar-papers.

Nakamura, Sachio, Robert Benedict, and Roderic Lakes. 1984. “Finite Element Method for Orthotropic Micropolar Elasticity.” *Int. J. Engng Sci.* 22 (3): 319–30.

Neff, Patrizio, Jena Jeong, and Hamidréza Ramézani. 2009. “Subgrid Interaction and Micro-Randomness – Novel Invariance Requirements in Infinitesimal Gradient Elasticity.” *International Journal of Solids and Structures* 46 (25–26): 4261–76. https://doi.org/10.1016/j.ijsolstr.2009.07.014.

Park, H. C., and R. S. Lakes. 1986. “Cosserat Micromechanics of Human Bone: Strain Redistribution by a Hydration Sensitive Constituent.” *J. Biomech.* 19 (5): 385–397.

Pasternak, E, and H.-B. Mühlhaus. 2005. “Generalised Homogenisation Procedures for Granular Materials.” *Journal of Engineering Mathematics* 52 (1): 199–229. https://doi.org/10.1007/s10665-004-3950-z.

Providas, E, and M A Kattis. 2002. “Finite Element Method in Plane Cosserat Elasticity.” *Computers and Structures* 80: 2059–69.

R. S. Lakes. 1991. “Experimental Micro Mechanics Methods for Conventional and Negative Poisson’s Ratio Cellular Solids as Cosserat Continua.” *The International Journal on the Biology of Stress* 113 (1): 148–55.

Rabboh, Saber A, Nadia E Bondok, Tamer S Mahmoud, and Heba I El Kholy. 2013. “The Effect of Functionally Graded Materials into the Sandwich Beam Dynamic Performance.” *Mater. Sci. Appl.* 2013 (November): 751–60.

Rafii-tabar, Hashem, Esmaeal Ghavanloo, and S Ahmad Fazelzadeh. 2016. “Nonlocal Continuum-Based Modeling of Mechanical Characteristics of Nanoscopic Structures.” *Physics Reports* 638: 1–97.

Reddy, J. N. 2007. “Nonlocal Theories for Bending, Buckling and Vibration of Beams.” *International Journal of Engineering Science* 45 (2–8): 288–307. https://doi.org/10.1016/j.ijengsci.2007.04.004.

Riahi, Azadeh, and John H. Curran. 2009. “Full 3D Finite Element Cosserat Formulation with Application in Layered Structures.” *Applied Mathematical Modelling* 33 (8): 3450–64. https://doi.org/10.1016/j.apm.2008.11.022.

S. Forest, and K. Sab. 1998. “Cosserat Overall Modeling of Heterogeneous Materials.” *Mechanics Research Communications* 25 (4): 449–54.

Salerno, Ginevra, and Gianmarco De Felice. 2009. “Continuum Modeling of Periodic Brickwork.” *International Journal of Solids and Structures* 46 (5): 1251–67. https://doi.org/10.1016/j.ijsolstr.2008.10.034.

Sanchez-Molina, David. 2014. “A Microcontinuum Model for Mechanical Properties of Esophageal Tissue: Experimental Methodology and Constitutive Analysis.” *Ann. Biomed. Eng.* 42 (1): 62–72.

Sawant, Prof S H. 2013. “Experimental Verification of Transverse Vibrations of Free-Free Beam.” *International Journal of Advanced Research in Electrical, Electronics and Instrumentation Engineering* 2 (9): 4536–41.

Schulze, Stefan-H., Matthias Pander, Konstantin Naumenko, and Holm Altenbach. 2012. “Analysis of Laminated Glass Beams for Photovoltaic Applications.” *International Journal of Solids and Structures* 49 (15–16): 2027–36. https://doi.org/http://dx.doi.org/10.1016/j.ijsolstr.2012.03.028.

Sh. Hosseini-Hashemi, M. Fakher, R.Nazemnezhad. 2013. “Surface Effects on Free Vibration Analysis of Nanobeams Using Nonlocal Elasticity: A Comparison Between Euler-Bernoulli and Timoshenko.” *Journal of Solid Mechanics* 5 (3): 290–304.

Shen, H. S., J. Yang, and L. Zhang. 2001. “Free and Forced Vibration of Reissner-Mindlin Plates with Free Edges Resting on Elastic Foundations.” *Journal of Sound and Vibration* 244 (2): 299–320. https://doi.org/10.1006/jsvi.2000.3501.

Shimpi, R. P., and H. G. Patel. 2006. “Free Vibrations of Plate Using Two Variable Refined Plate Theory.” *Journal of Sound and Vibration* 296 (4–5): 979–99. https://doi.org/10.1016/j.jsv.2006.03.030.

Stefanou, I., J. Sulem, and I. Vardoulakis. 2008. “Three-Dimensional Cosserat Homogenization of Masonry Structures: Elasticity.” *Acta Geotech.* 3: 71–83.

https://doi.org/10.1007/s11440-007-0051-y.

Steinberg, Lev, and Roman Kvasov. 2015. “Analytical Modeling of Vibration of Micropolar Plates.” *Applied Mathematics* 06 (05): 817–36. https://doi.org/10.4236/am.2015.65077.

Stephen, N. G. 1981. “Considerations on Second Order Beam Theories.” *International Journal of Solids and Structures* 17 (3): 325–33. https://doi.org/10.1016/0020-7683(81)90066-4.

Stephen, N G, and S Puchegger. 2006. “On the Valid Frequency Range of Timoshenko Beam Theory.” *Journal of Sound and Vibration* 297: 1082–87. https://doi.org/10.1016/j.jsv.2006.04.020.

Stricklin, James A. 1968. “Integration of Area Coordinates in Matrix Structural Analysis.” *American Institute of Aeronautics and Astronautics (AIAA)*, no. October: 2023. https://doi.org/10.2514/3.55425.

Strutt, John William, and Baron Rayleigh. 1877. “N0095130_PDF_1_340.Pdf.” MacMillian and Co.

Sulem, Jean, Ioannis Stefanou, and Emmanuil Veveakis. 2011. “Stability Analysis of Undrained Adiabatic Shearing of a Rock Layer with Cosserat Microstructure.” *Granul. Matter* 13 (3): 261–268. https://doi.org/10.1007/s10035-010-0244-1.

Tang, Hongxiang, and Chunhong Song. 2016. “Cosserat Continuum Model and Its Application to the Studies of Progressive Failure.” *The 15th Asian Regional Conference on Soil Mechanics and Geotechnical Engineering*, 703–8. https://doi.org/http://doi.org/10.3208/jgssp.CHN-57.

Tekoğlu, Cihan, and Patrick R. Onck. 2008. “Size Effects in Two-Dimensional Voronoi Foams : A Comparison between Generalized Continua and Discrete Models.” *Journal of the Mechanics and Physics of Solids* 56: 3541–64. https://doi.org/10.1016/j.jmps.2008.06.007.

Toupin, R A. 1964. “Theories of Elasticity with Couple-Stress.” *Arch. Ration. Mech. Analysis.* 17: 85–112.

Trinh, Duy Khanh, J Ralf, Nicolas Auffray, Stefan Diebels, and Samuel Forest. 2012. “Evaluation of Generalized Continuum Substitution Models for Heterogeneous Materials.” *Journal for Multiscale Computational Engineering* 10 (6): 527–49.

Vardoulakis, I. 1989. “Shear-Banding and Liquefaction in Granular Materials on the Basis of a Cosserat Continuum Theory.” *Ingenieur-Archiv* 59 (2): 106–13.

Veveakis, Emmanuil, Ioannis Stefanou, Jean Sulem, Emmanuil Veveakis, Ioannis Stefanou, and Jean Sulem. 2013. “Failure in Shear Bands for Granular Materials : Thermo-Hydro-Chemomechanical Effects.” *HAL Archives-Ouverts* 3 (2): 31–36. https://doi.org/10.1680/geolett.12.00063.

Vladimir, Nikola, and Marko Tomic. 2015. “Timoshenko Beam Theory 93 Years Later – over Bridges to Nanotubes and Ultra Large Ships,” no. January.

Wang, C M, Y Y Zhang, and X Q He. 2007. “Vibration of Nonlocal Timoshenko Beams.” *Nanotechnology* 18 (10): 1–9. https://doi.org/10.1088/0957-4484/18/10/105401.

Waseem, A., A. J. Beveridge, M. A. Wheel, and D. H. Nash. 2013. “The Influence of Void Size on the Micropolar Constitutive Properties of Model Heterogeneous Materials.” *European Journal of Mechanics, A/Solids* 40: 148–57. https://doi.org/10.1016/j.euromechsol.2013.01.002.

Wheel, M.a., J.C. Frame, and P.E. Riches. 2015. “Is Smaller Always Stiffer? On Size Effects in Supposedly Generalised Continua.” *International Journal of Solids and Structures* 67–68: 84–92. https://doi.org/10.1016/j.ijsolstr.2015.03.026.

Wheel, M A. 2008. “A Control Volume-Based Finite Element Method for Plane Micropolar Elasticity.” *Int. J. Numer. Meth. Engng* 75 (February): 992–1006. https://doi.org/10.1002/nme.

Wu, Jiu Hui, A. Q. Liu, and H. L. Chen. 2007. “Exact Solutions for Free-Vibration Analysis of Rectangular Plates Using Bessel Functions.” *Journal of Applied Mechanics* 74 (6): 1247. https://doi.org/10.1115/1.2744043.

Xiang, Y., S. K. Lai, L. Zhou, and C. W. Lim. 2010. “DSC-Ritz Element Method for Vibration Analysis of Rectangular Mindlin Plates with Mixed Edge Supports.” *European Journal of Mechanics, A/Solids* 29 (4): 619–28. https://doi.org/10.1016/j.euromechsol.2009.12.007.

Xing, Yufeng, and Bo Liu. 2009. “Closed Form Solutions for Free Vibrations of Rectangular Mindlin Plates.” *Acta Mechanica Sinica/Lixue Xuebao* 25 (5): 689–98. https://doi.org/10.1007/s10409-009-0253-7.

Zhang, Z., N. Challamel, and C. M. Wang. 2013. “Calibration of Eringen’s Small Length Scale Coefficient for Initially Stressed Vibrating Nonlocal Euler Beams Based on Microstructured Beam Model.” *Journal of Applied Physics* 114 (11): 1–6. https://doi.org/10.1063/1.4821246.

Zhang, Zhen, C M Wang, and Noël Challamel. 2015. “Eringen’s Length-Scale Coefficients for Vibration and Buckling of Nonlocal Rectangular Plates with Simply Supported Edges.” *Journal of Engineering Mechanics* 141 (2): 04014117-1–10. https://doi.org/10.1061/(ASCE)EM.1943-7889.0000838.

Zienkiewicz, O. C., and R.L. Taylor. 2000. “Finite Element Procedures for Solids and Structures - NonlinearAnalysis,” no. 73.

Zienkiewicz, O.C., R.L. Taylor, and J.Z. Zhu. 2013. *The Finite Element Method: Its Basis and Fundamentals*. *Butterworth-Heinemann*. 7th ed. https://doi.org/10.1016/B978-1-85617-633-0.00006-X.

Zienkiewicz, O C, and R L Taylor. n.d. “Method for Solid and Structural Mechanics UNESCO Professor of Numerical Methods in Engineering.” *Methods*.